Lawrence Berkeley Laboratory

UNIVERSITY OF CALIFORNIA

Materials & Molecular Research Division

MOLECULAR BEAM STUDIES OF ELECTRONIC STATE-SELECTIVE PHOTOCHEMISTRY

L.J. Butler
(Ph.D. Thesis)

October 1985

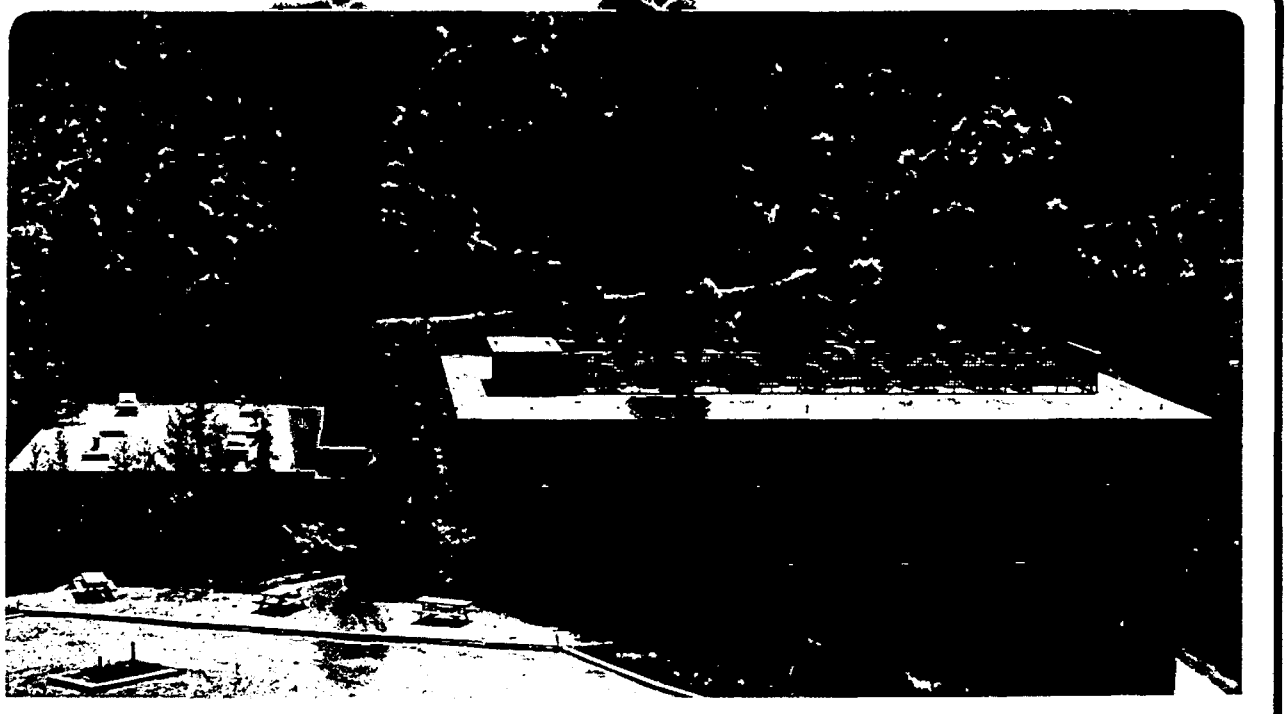

Prepared for the U.S. Department of Energy under Contract DE-AC03-76SF00098

DISCLAIMER

Molecular Beam Studies of Electronic State-Selective Photochemistry

Laurie Jeanne Butler
Ph.D. Thesis

Lawrence Berkeley Laboratory
University of California
Berkeley, California 94720

October 1985

This thesis is lovingly dedicated to my mother, whose intelligence and giving nature I hope will guide me always, and to my bright and funny father, whom I miss.

TABLE OF CONTENTS

MOLECULAR BEAM STUDIES OF ELECTRONIC STATE-SELECTIVE PHOTOCHEMISTRY

Laurie Jeanne Butler

Materials and Molecular Research Division
Lawrence Berkeley Laboratory
and
Department of Chemistry
University of California
Berkeley, California 94720

ABSTRACT

The evolution of a specifically excited molecule to its final fragmentation products is studied here for three photochemical systems by the crossed laser-molecular beam technique. Measurement of product velocity distributions and polarization dependences allows elucidation of details of all pathways from excitation through fragmentation.

The photodissociation of CH_2BrI has been studied at 248.5, 210, and 193.3 nm. Excitation at 210 nm, an n(Br) $\rightarrow$ σ^*(C-Br) transition, results in breaking of the stronger C-Br bond, and no fission of the weaker C-I bond, in contrast to conclusions based on previous studies of the UV photodissociation of polyhalomethanes. Some concerted elimination of electronically excited IBr also occurs at 210 nm and at 193 nm. Excitation at 193 nm, a Rydberg transition on the I atom, results in both bond fission channels (C-Br fission being dominant) to form spin-orbit excited halogen atom products with an isotropic polarization dependence. Excitation at 248.5 nm, a n(I) $\rightarrow$ σ^*(C-I) transition with some overlap of a n(Br) $\rightarrow$ σ^*(C-Br) transition, results in primary C-I fission to form both $I(^2P_{1/2})$ and $I(^2P_{3/2})$ product with the same

parallel anisotropy and some C-Br fission. The iodine product spin-orbit state branching ratio is discussed in relation to models for transitions between diabatic electronic states.

The dissociation of nitromethane following excitation of the $\pi^* \leftarrow \pi$ transition at 193 nm has been investigated by product emission spectroscopy and molecular beam photofragmentation translational energy spectroscopy. The only primary process is shown to be cleavage of the C-N bond to give CH_3 and NO_2 radicals; there are two distinct mechanisms by which CH_3 and NO_2 are produced. The dominant mechanism releases a relatively large fraction of the total available energy to translation and probably gives NO_2 radicals in a vibrationally excited $^2B_2$ state. The studies show there is little transfer of energy from the excited NO_2 group to the alkyl group during dissociation for the dominant mechanism.

Dissociation pathways of a vibrationally excited molecule in the ground electronic state have been studied in the infrared multiphoton dissociation of diethyl ether. Partitioning of the energy to translation is compared for the radical channel $C_2H_5OC_2H_5 \rightarrow C_2H_5O + C_2H_5$, for which the distribution of translational energies is in agreement with predictions of statistical unimolecular rate theory, and the concerted channel $C_2H_5OC_2H_5 \rightarrow C_2H_5O + C_2H_4$, for which the high translational energy release with a relatively narrow distribution results from the recoil of the products from each other down the exit barrier. Applying statistical unimolecular rate theory, we estimate the average energy levels from which the molecules dissociate using the measured translational energy distribution of the radical channel.

Yuan T. Lee

ACKNOWLEDGMENTS

I wish to thank Professor Lee for all the encouragement and support he has given me during my graduate work. We all admire him for his intelligence, enthusiasm, and dedication to science. As his students we benefit greatly from his commitment to educating young scientists. I hope he knows how much his integrity as a person as well as a scientist have meant to me.

My gratitude to the co-workers on the experiments in this thesis. I had the rare opportunity to undertake the CH_2BrI study in Chapter 1 by myself until the last part at 210 nm when I was joined by two young and able students, Eric Hintsa and Stacey Shane. Doug Krajnovich was a tremendous mentor on the nitromethane experiment (Chapter 2) my first year here--he wrote the Appendices of that paper which are included for completeness. I also gratefully thank our co-author's from Columbia, Professor Richard Bersohn and Dr. G. Ondrey, for allowing us to include the nitromethane paper in its entirety, as all the fluorescence measurements were performed in their laboratory. I learned a great deal from the joint effort on this system. Staff scientist Rick Buss took the data on diethyl ether with me (Chapter 3) and introduced me patiently to RRKM theory. Rick Brudzynski was a great help in making that original manuscript more clear and readable. I learned much from working on a few completed experiments not included in this thesis but listed in Appendix D, particularly the glyoxal experiment and writeup with John Hepburn and the editing of Doug Krajnovich's thesis chapter on $1,2\text{-}C_2F_4BrI$ to a paper with the small addition of my work at

266 nm; I hope that addition repaid him a little for all his help and instruction my first two years in the group. I also learned a lot from working on two experiments which are an ongoing effort in the Lee group, Rich Brudzynski's studies of V→T energy transfer and our study of laser stabilization of a collision complex with Rick Buss and our great Swiss postdoc, Peter Felder.

The technical demands of the apparatus for the experiments included here cannot be met by one graduate student alone and the contributors are too many to name. I would, however, particularly like to acknowledge the many people involved in the design and construction of the new molecular beam photofragmentation apparatus on which the study in Chapter 1 was performed. The apparatus was designed and final assembly done by Doug Krajnovich, Alec Wodtke and myself. (My particular contributions are described in part in the Appendices for the benefit of those using the machine in the future and those wishing to build similar parts for their own lab.) We all learned a great deal from Professor Lee's extensive experience and previous designs. We are indebted to the skillful management and machinists of the U.C. Berkeley campus machine shop headed by Fred Wolff and Andy Anderson. In addition, two of the experiments in this thesis (Chapters 1 and 2) were aided by a laser loan and technical assistance from the San Francisco Laser Center headed by Andy Kung. I especially thank them for the help with Raman shifting.

Special thanks to Professor Bob Field and Professor Jim Kinsey for whom I worked as an undergraduate at MIT. The experience I gained in Bob Field's lab under the tutoring of his postdoc Carter Kittrell helped

me considerably in the laser part of the experiments in the Lee group. Thank you, Professor Field, for all your enthusiastic encouragement and for telling Professor Lee about me so I wouldn't have to speak for myself when I tried to join the Lee group. My deepest wishes for Professor Kinsey's good health; for me he has been a most wise and inspiring scientist.

There are several members of the Lee group with whom I did not work on a completed experiment but whose friendship and assistance helped my graduate work more than can be described. It was always easy to round up helpful co-workers to move lasers from lab to lab or lift flanges off the machine with me late at night--thank you, my friends, and good luck with all your work. Particular thanks to Mitchio Okumura for all the thoughtful discussions related to spectroscopy and properties of molecules in general, to Tim Minton for his mutual interest with me in the curve crossing in alkyl halides and for his starting me on Tellll-a-Graf, to Ralph Page for his explanations of optical properties from first principles, and to Rick Brudzynski for the many times he has answered questions with honesty and intelligence (check out all those relays in Appendix A, Brud, thanks for the clear explanation). Of all the people I worked with as a young student in the group I owe the most thanks to Doug Krajnovich--all who know him will tell you he is incredibly hardworking, careful, smart, and unselfish.

The manuscript was expertly prepared by Connie Silva; I thank her for her patience and care. Thank you also, Ann Weightman, for helping

me with all the details of filing and quite a bit of rush typing during the initial drafts. You keep the Lee group running!

This work was supported by the Office of Naval Research under Contract No. N0014-83-K-0069 and by the Director, Office of Energy Research, Office of Basic Energy Sciences, Chemical Sciences Division of the U.S. Department of Energy under Contract No. DE-AC03-76SF00098.

My graduate stipend and tuition were generously funded by the University of California Graduate Opportunity Fellowship 1981-82 and 1982-83 and by an IBM fellowship in 1985 for the last two months of my study. Many thanks to Proctor and Gamble for the funding and the American Chemical Society for the administering of the 1983-84 ACS Graduate Fellowship from which I benefited.

Personal thanks to my best friend, Janet Minton for her sweetness and friendship and the many times she took care of the Smuff when I would visit my husband in New York. All my love to my older sisters and brothers and my twin sister, Lynne. What can I say, Bling, we were in the womb together, I admire you with all my heart. Finally, to my friend and husband, Michael, I love you dearly and thank you for the mutual understanding of how we feel about our work. May there be many years of happiness filled with kittens and twin sisters and science in our future together.

CHAPTER ONE

THE ELECTRONIC STATE-SELECTIVE PHOTODISSOCIATION OF CH_2BrI AT 248, 210, AND 193 nm

ABSTRACT

The primary photodissociation channels of CH_2BrI following excitation at 193.3, 210, and 248.5 nm have been studied with the crossed laser-molecular beam technique. Product translational energy distributions and polarization dependences are derived for the primary dissociation processes observed. Excitation at 248.5 nm, which is assigned to excitation of primarily a $n(I) \rightarrow \sigma^*(C-I)$ transition with some contribution from an overlapping $n(Br) \rightarrow \sigma^*(C-Br)$ transition, results in only C-I bond fission and C-Br bond fission, with C-I bond fission the dominant channel. A parallel anisotropy is measured for both channels, $\beta = 1.0 \pm 0.1$ for C-I fission and $\beta = 0.6 \pm 0.1$ for C-Br fission. C-I bond fission produces I atoms in both the $^2P_{3/2}$ and spin-orbit excited $^2P_{1/2}$ state in a ratio of 1.0:0.75, both with the same parallel angular distribution. The spin-orbit state branching ratio of I atoms produced is discussed in relation to models for transitions between diabatic electronic states. Excitation at 193.3 nm, assigned to transition to primarily predissociated Rydberg levels on the I atom, leads to C-Br bond fission, some C-I bond fission, and significant concerted elimination of IBr. The angular distribution of scattered product is roughly isotropic with respect to the polarization of the light, consistent with the product channels resulting from excitation to a bound Rydberg state

that predissociates on a time scale slow with respect to the rotational period of the molecule. Analysis of the product translational energy ditributions for the dissociation products indicate that the IBr is formed electronically excited and that the halogen atom products are spin-orbit excited. Excitation at 210 nm, of the transition assigned as $n(Br) \rightarrow \sigma^*(C\text{-}Br)$ based on comparison with CH_3Br, results in selective breaking of the stronger C-X bond in the molecule, the C-Br bond, with a parallel polarization dependence, and no fission of the C-I bond. Some concerted elimination of IBr also occurs; the IBr velocity distribution indicates it is probably formed electronically excited as it was in the 193.3 nm photolysis. The concerted elimination of exclusively electronically excited IBr is discussed in terms of a simple least motion path in the LCAO-MO approximation. The selective breaking of the C-Br bond over the weaker C-I bond is discussed in contrast to previous broadband photolysis studies of polyhalomethanes in which only the weaker C-X bond broke, and compared to one state specific study of $1,2\text{-}C_2F_4BrI$ which resulted in both C-I and C-Br fission following an analogous excitation.

INTRODUCTION

The photodissociation of CH_2BrI was undertaken to investigate how the electronic nature of a particular state excited in a molecule influences the product channels by which the molecule dissociates. Although there are numerous dissociation channels for CH_2BrI which

are energetically allowed at all three excitation wavelengths of 193, 210 and 248 nm, see Fig. 1,[1] our results to follow show that excitation at each wavelength produces very different branching ratios between the possible dissociation channels. Specifically, for example, excitation at 210 nm of a transition assigned as $n(Br) \rightarrow \sigma^*(C-Br)$ results in primary C-Br fission but no primary C-I bond fission. This result contradicts the popular conclusion[2] from previous broadband experiments on photodissociation of polyhalomethanes that only the weakest C-X bond breaks in the primary dissociation event at excitation wavelengths > 2000Å.

A bromo-iodo alkane was chosen for this study as they have three distinct types of electronic transitions above 190 nm which are separated in frequency, two of which result in electronic states antibonding in the C-I or C-Br bond respectively. The assignment of the transitions as based on comparison with the spectra of CH_3I and CH_3Br are shown above the low resolution UV absorption spectrum of CH_2BrI shown in Fig. 2. The spectrum consists of a broad band peaking near 270 nm which is assigned to the promotion of a nonbonding electron on the iodine to an antibonding orbital on the C-I bond, a broad band peaking near 215 nm assigned to promotion of a nonbonding electron on the Br atom to an antibonding orbital on the C-Br bond, and sharp features around 190 nm corresponding to Rydberg transitions on the I atom. The features are similar in shape to the analogous transitions observed in CH_3I and CH_3Br respectively, but the broad bands are considerably more intense and shifted slightly to the red. The ultraviolet spectrum of CH_2BrI has been previously recorded by S.J. Lee

and R. Bersohn[3] from 200 nm to 350 nm. They attributed the shift in the absorption bands to the fact that the central carbon atom has more positive charge in this dihalomethane than it does in a monohalomethane, thus stabilizing the antibonding orbitals.

Two recent studies of bromo-iodo alkanes are particularly relevant to this study. Lee and Bersohn[3] investigated the photodissociation of CH_2BrI with a broad band light source extending from 240 to 340 nm with a FWHM of approximately 40 nm. They measured the mass spectrum of dissociation fragments and reported signal at I^+, Br^+, CH_2Br^+, and CH_2I^+, but not at IBr^+. There was no reported attempt to resolve HI^+ or $H^{81}Br^+$ from I^+ or Br^+. From their integrated signal at I^+ and Br^+, they derived a branching ratio between C-I and C-Br bond fission to be 6:1; the calculation involved the estimated factor that only 7 percent of the CH_2Br product formed gives signal at Br^+ and 20 percent of the CH_2I product formed gives signal at I^+. The anisotropy of the I atom signal showed a parallel dependence on the direction of the electric vector of the dissociating light. It was concluded that excitation in the n(I) $\rightarrow$ σ^*(C-I) band promotes only C-I bond fission; the C-Br fission was attributed to the bandwidth of the light partially overlapping the absorption band of the n(Br) $\rightarrow$ σ^*(C-Br) transition.

A recent study of the photodissociation of C_2F_5Br, C_2F_5I, and 1,2-C_2F_4BrI by Krajnovich et al.[4] investigated product channels resulting from excitation in the n(I) $\rightarrow$ σ^*(C-I) and in the n(Br) $\rightarrow$ σ^*(C-Br) absorption bands. The absorption spectra of Leone and coworkers[5] from 190-400 nm show that the two broad band components of the spectrum of 1,2-C_2F_4BrI are similar in shape and position to the n(I) $\rightarrow$ σ^*(C-I)

absorption in C_2F_5I (peaking near 270 nm) and the n(Br) → σ*(C-Br) absorption in C_2F_5Br (still rising at 193 nm) but are considerably more intense (particularly the n(Br) → σ*(C-Br) transition). The Rydberg transitions on the I atom are shifted to higher energies in the fluorinated halocarbons. Krajnovich et al. measured the product velocity and angular distributions for excitation of the species at selected UV laser wavelengths. When 1,2-C_2F_4BrI was excited at 248 nm and 266 nm, only C-I bond fission was observed as a primary dissociation channel and most or all of the iodine product was spin-orbit excited $I(^2P_{1/2})$. When the molecule was dissociated at 193 nm, some of the molecules underwent primary C-I bond fission and some underwent primary C-Br bond fission in a ratio of approximately 1.7:1. The results were interpreted in terms of a fast electronic energy transfer between the C-Br and C-I bonds after a local excitation of the C-Br bond at 193 nm. This interpretation was consistent with the polarization dependences, which showed that both bond fission channels resulted from a dipole transition moment aligned parallel to the breaking bonds, because the C-I and C-Br bonds are nearly parallel in 1,2-C_2F_4BrI.

CH_2BrI was chosen as a model system for three specific reasons (beyond the consideration that it is one of very few bromo-iodo alkanes obtainable in any quantity at a reasonable price). First, the absorption spectrum contains two bands corresponding to n → σ* transitions of the C-I and C-Br bonds respectively, which are resolved despite the shared carbon. Second, the angle between the C-I and C-Br bond is strongly bent, potentially allowing us to use the polarization

dependences of the dissociation channels to identify the particular electronic transition which resulted in each dissociation channel. Third, the molecule is small and the energetics relevant to the dissociation channels are fairly well known, so primary dissociation events can be distinguished from secondary or three-body dissociation events (where the final products are CH_2 + Br + I). Care should be taken in comparing the experimental results on CH_2BrI to those on 1,2-C_2F_4BrI. The absorbtion bands due to the $n \rightarrow \sigma^*$ transitions are shifted to longer wavelengths in CH_2BrI so, for instance, excitation at 193 nm promotes a $n(Br) \rightarrow \sigma^*(C-Br)$ in 1,2-C_2F_4BrI but promotes a Rydberg transition in CH_2BrI; one must excite CH_2BrI at 210 nm to excite the $n(Br) \rightarrow \sigma^*(C-Br)$ transition.

The results and analysis section will present the experimental data and elucidate how one extracts from the data which dissociation channels are and are not occurring and what the polarization dependence of the dissociation events are. For readers who wish to just read a summary of the experimental results, one is presented at the start of the discussion section. In the discussion section we will address ourselves to qualitatively rationalizing how the nature of the electronic state excited and the coupling to other states results in the specific primary dissociation channels observed.

EXPERIMENTAL

The molecular beam photofragmentation apparatus has been previously described in detail.[6] CH_2BrI was obtained from Fairfield Chemical

Company. The molecular beam was formed by bubbling argon through a reservoir of CH_2BrI maintained at 18°C. A total stagnation pressure of 300 torr was used (5 torr CH_2BrI, 295 Ar) behind a 0.125 mm diameter nozzle. The nozzle was heated to 135°-140°C to reduce the formation of clusters in the beam. The data was checked for contributions from dissociation of clusters by repeating several measurements under the same molecular beam conditions except the reservoir of CH_2BrI was lowered to 5°C to substantially reduce the partial pressure of CH_2BrI in the beam and thus reduce cluster formation. The peak velocity of the molecular beam was typically $6.15 \pm 0.07 \times 10^4$ cm/sec with a FWHM of about 10 percent. The beam passed through two skimmers and two differential pumping regions, the second skimmer defining the beam to a full angular divergence of 3.0° before the molecular beam crossed the laser 74 mm from the nozzle. At the crossing point the beam diameter was 3 mm. The beam source is rotated in a plane perpendicular to the laser beam.

For the experiments at 193.3 and 248.5 nm, excluding the polarization dependence at 248 nm, the photodissociating light source was arranged as follows. The photons from a pulsed Lambda Physik model EMG 103MSC excimer laser operated at 100-150 Hz were focused onto the interaction region of the molecular beam to an oblong 3 mm by 1 mm spot with a 240 mm focal length (f.l.) magnesium fluoride lens. For all the data presented, except where otherwise noted, the laser was not polarized. The laser beam crossed the molecular beam perpendicular to the source-detector plane so the electric vector direction was isotropic in that

plane. The c.m. angular distribution of scattered product must then by symmetry be isotropic in the source-detector plane, whether the absorption is anisotropic or not. Laser pulse energies at 193 nm, ArF gas mixture, were typically 100-150 mJ/pulse and at 248 nm, KrF gas mixture, were ~200 mJ/pulse, with pulse widths of 17 and 25 nsec respectively (quoted from Lambda Physik).

The photons for the 210 nm experiments were obtained by Raman shifting the 193.3 nm output of a Lambda Physik 102E excimer laser equipped with unstable resonator optics. The optical setup is shown in Figure 3. The unpolarized excimer laser beam was focused by a 50 cm f.l. lens into a 97 cm long Raman cell filled with 300 psig of H_2 gas. A second 50 cm f.l. lens placed 122 cm from the first lens produced a moderately converging beam of the fundamental and Ramam shifted frequencies. The light was dispersed with a quartz Pellin-Broca prism. The 210 nm Stokes shifted light was redirected along the axis of rotation of the beam source with a Suprasil right angle prism and focused onto the interaction region with a 240 mm f.l. MgF_2 lens to a ~3 mm^2 spot. This light passed through an aperture in a copper barricade which blocked the fundamental and undesired higher order Raman shifted frequencies. Typical pulse energies produced were 2 mJ/pulse of 210 nm light from 55 mJ/pulse of 193 nm input energy to the Raman cell. Some power was lost at the Pellin-Broca prism as the excimer laser beam was too large for this optic. The 210 nm light is primarily unpolarized as the fundamental is, but the horizontal component is transmitted more easily through the entrance and exit surfaces of the

Pellin-Broca resulting in the horizontal component having ~60 percent of the energy and the vertical having ~40 percent. For the polarization dependence measurements the quartz Pellin-Broca was replaced with a birefringent MgF_2 one as described below. The laser repetition rate was 30 Hz for most of the unpolarized light data and 25 Hz for the polarized light data. Following every 12 hours of data taking the laser windows were cleaned and the whole optics setup realigned to restore good pulse energies.

The excimer laser was polarized for the anisotropy measurements at all three wavelengths by passing the beam through one of two MgF_2 prisms. MgF_2 is birefringent; the propagation directions of the two outgoing linearly polarized beams differ from each other by a small angle and from the incoming beam by a large angle. The two output beams were >99.9 percent linearly polarized in orthogonal directions. Figure 4a shows a side view of the optical setup at 193 nm. The rectangular, unpolarized excimer beam is turned upwards by a turning mirror into the tilted face of a MgF_2 prism polarizer designed by Optics for Research. The prism turns the horizontally polarized component of the light 30-40° downward, redirecting it along the axis of rotation of the beam source, while the vertical component is deflected less and blocked before the entrance to the machine. For the setup at 210 nm, the quartz Pellin-Broca, as shown in Figure 3, is replaced by a MgF_2 Pellin-Broca by Quanta Ray. The optical axis of the Pellin-Broca is vertical; it disperses the light by wavelength and by direction of linear polarization. The desired wavelength and polarization

of light is directed along the axis of rotation of the beam source with the right angle prism after the Pellin-Broca. The micrometer which controls the tilt of the right angle prism was calibrated so that either the horizontally or the vertically polarized light at 210 nm could be directed to the interaction region of the laser and molecular beam while the apparatus was under vacuum. The data was thus taken with each polarization of light under exactly the same molecular beam conditions. Because the horizontally polarized light is better transmitted by the Pellin-Broca, only the shapes of the time-of-flight data, not the total signal intensities, can be compared for the two polarizations of the dissociating light unless one performs additional normalization to the photon intensity. Finally, the optical setup for the anisotropy measurements at 248 nm is shown in Figure 4b. Here the two linearly polarized components of the Lambda Physik 102E excimer beam, used with unstable resonator optics to improve the angular divergence of the beam, are dispersed by the MgF_2 Pellin-Broca and the horizontal component is redirected along the axis of rotation of the beam source. A first-order half wave retarder from Karl Lambrecht Co., consisting of two quartz retardation plates with an air space between them and the optical axes at 90° with respect to each other, is placed before the entrance to the machine. The difference in the thickness of the two plates corresponds to a retardation of one half of the 248.5 nm wavelength. This combination retarder is less angle and temperature dependent than multiple order retardation plates. The purity of rotation of the light was checked by resolving the light after the rotator into its

vertical and horizontal components with the Optics for Research MgF_2 prism. When the optical axis of the rotator was turned to be parallel with the electric vector ($\vec{E}$) of the horizontally polarized incoming light, the vertical component of the outgoing light completely disappeared. When the half wave retarder was rotated by 45° (rotates $\vec{E}$ vector by 90°) the horizontal component of the outgoing light disappeared completely.

Neutral dissociation products formed at the crossing point of the laser and molecular beam travel 36.6 cm to an electron bombardment ionizer. The dissociation products pass through a set of defining slits mounted on the walls of the differentially pumped detector chamber which limit the acceptance angle of the detector for products scattered from the interaction region to 1.5°. The neutral products are ionized by bombardment with 120 eV electrons. The ion fragments are mass selected with a quadrupole mass spectrometer and counted with a Daly detector and a multichannel scaler with respect to their flight time from the interaction region after the dissociating laser pulse. Tuning of the quadrupole to a well defined mass to charge ratio and measuring its resolution is facilitated by measuring the intensity of the beam profile at the mass fragments of CH_2BrI as a function of quadrupole settings. All time-of-flight (TOF) data presented for 248 nm unpolarized and 193 nm excitation wavelengths was signal averaged over at least 200,000 laser shots each. The TOF data taken with 210 nm and polarized 248 nm light (with the lower repetition 102E laser) were signal averaged for at least 50,000 counts each. Typical signal levels at

193 nm, for instance, ranged from 0.008 counts/laser pulse at CH_2Br^+ (from 120 to 330 μsec) to 2.2 counts/laser pulse at I^+ (from 400 to 800 μsec).

The polarization dependence measurements at 248 nm of the I^+ and CH_2I^+ signals were carefully executed to average out laser power differences between laser gas fills and within each gas fill. The signal at each angle was accumulated for the same number of laser shots as the signal at other angles within each gas fill. Nine separate data averaging periods of 7,500 laser shots each for CH_2I^+ and 6,000 laser shots each for I^+ were summed for each of the nine electric vector positions to obtain the angular distibution data shown in this paper. The order of signal accumulation in the gas fill for each polarization angle was varied to average out the 2-15 percent change in laser power between the beginning and the end of each gas fill. Because of these averaging techniques, no additional normalization to laser power was needed at the various polarization angles.

RESULTS AND ANALYIS:

I. Photodissociation of CH_2BrI at 248 nm

A. $$CH_2BrI \xrightarrow{248\ nm} CH_2Br + I(^2P_{3/2}) \quad (1a)$$
$$\hookrightarrow CH_2Br + I(^2P_{1/2}) \quad (1b)$$

The time-of-flight (TOF) spectra of m/e=95, $CH_2^{81}Br^+$, and m/e=127, I^+, are shown in Figs. 5 and 6, respectively. Both sets of TOF spectra

show two narrow and fast overlapping product distributions, as well as a slow hump with a peak flight time of ~650 μsec at the small laboratory angle. The I^+ TOF spectra also show a broad underlying signal. The slow hump at 650 μsec was determined to be contribution from dimer contamination in the molecular beam (see Section I.E) and the broad underlying signal in the I^+ TOF's is due to secondary photodissociation of CH_2I product (see Section I.G). The two sharp peaks in the I^+ and CH_2Br^+ TOF spectra are easily assigned to the momentum matched I and CH_2Br products from C-I bond fission, the faster one of the pair being products from bond fissions producing $I(^2P_{3/2})$ and the slower one of the pair being from fissions producing $I(^2P_{1/2})$. This assignment follows from the fact that the products from the bond fissions giving spin-orbit excited iodine atom product must channel 21.7 kcal/mole (the spin-orbit splitting of iodine) of the total available energy into electronic energy. Hence, less energy is available for translation and internal vibration and rotation, and these products have smaller center-of-mass recoil velocities and longer arrival time in the TOF spectra.[7]

The center-of-mass product recoil translational energy distribution, $P(E_T)$, for C-I bond fission in CH_2BrI excited at 248 nm can be derived from forward convolution fitting of either the CH_2Br^+ TOF or the sharp peaks in the I^+ TOF, as the CH_2Br and I center-of-mass (c.m.) product velocities are related simply by momentum conservation. The CH_2Br^+ TOF was used initially as it is not complicated by the underlying signal from secondary dissociation. The $P(E_T)$ shown in Fig. 7 gives the fit shown in solid line in Fig. 5. This total $P(E_T)$

must be divided into two component translational energy distributions, one for production of each spin-orbit state of I atom product, in order to determine a product channel branching ratio. This was done approximately by constraining the shape of each $P(E_T)$ to be similar. Although there is clearly uncertainty in the shape of the $P(E_T)$'s in the overlapping region, there is less uncertainty in the total area under each component $P(E_T)$, which determines the product channel branching ratio. Production of ground state iodine is clearly the favored channel. The $P(E_T)$'s and their fits shown in Figs. 5 and 6 give the relative probability of producing spin-orbit excited I atom product in the primary bond fission to forming ground state I atom product to be 0.75:1.[11]

There are several potential pitfalls in determining product channel branching ratios from the relative area of $P(E_T)$'s that fit measured TOF spectra of products, all of which are shown to be avoided in this work. Certainly the molecular beam velocity, flight path, and ion flight time must be carefully determined so the well known transformations from $P(E_T)$ to product laboratory TOF can be carried out. More importantly, if one is determining the product channel branching ratio from the TOF spectra of a product like CH_2Br, which has the potential of absorbing another photon and dissociating itself, one must be certain that one is not preferentially losing the CH_2Br produced in one channel over the other (this is possible because the internal state distribution of the CH_2Br product from each channel is different). Also it is possible that the more internally hot CH_2Br from dissociations producing ground state I atoms may be less likely to give

parent CH_2Br^+ when ionized. All these potential problems may be eliminated by showing that the $P(E_T)$'s derived from the CH_2Br^+ TOF also fit the momentum matched I^+ TOF features, as was done in Fig. 6. Apparently, the secondary photodissociation of CH_2Br by 248 nm photons does not depend strongly on the internal excitation of the radical. The only remaining uncertainty is whether the ionization cross section of $I(^2P_{1/2})$ is the same as that of $I(^2P_{3/2})$. This was explicitly checked with our ionizer conditions by photodissociating CF_3I at 248 nm and checking that the same weighting of the two dissociation channels (~7 percent $I(^2P_{3/2})$ is formed) fit both the CF_3^+ and the I^+ TOF spectra. Similar insensitivity of the ionization efficiency to the spin-orbit excitation of I has been noted by Gorry and coworkers[8c] for their ionizer conditions. Thus our product channel branching ratio of 0.75:1 for $I(^2P_{1/2}):I(^2P_{3/2})$ only contains the relatively small uncertainty of assigning overlapping portions of each component in the TOF spectra to one or the other channel. The branching ratio determination is normally dependent on the polarization dependence of the photon absorption which results in an anisotropy in the product angular distribution for each channel, but the dissociation to each spin-orbit state of I is shown to have the same anisotropy in Section I.H.

B. $$CH_2BrI \xrightarrow{248\ nm} CH_2I + Br\ (^2P_{3/2}, {}^2P_{1/2}) \qquad (2)$$

The TOF spectra of m/e=141, CH_2I^+, and m/e=81, $^{81}Br^+$, are shown in Figs. 8 and 9 respectively. The spin-orbit splitting of Br atoms is

10.54 kcal/mole compared to 21.7 kcal/mole for I atoms, so it is much harder to resolve the two component dissociation channels (as was achieved for C-I fission above) given the width of the product translational energy distribution caused by the range of internal excitation of the CH_2I product. The total $P(E_T)$ for C-Br bond fission to CH_2I + Br was derived via fitting of the CH_2I^+ TOF spectrum and is shown in Fig. 10. The corresponding fit obtained to the CH_2I product TOF is shown in solid line in Fig. 8. There is clearly a little uncertainty in the low energy side of the $P(E_T)$ due to contamination of the CH_2I^+ TOF by signal from dimers (see section I.E) This $P(E_T)$ was then used to predict where signal from the momentum matched Br product would appear in the Br^+ TOF. The predicted Br^+ distribution shown in solid line in Fig. 9 matches the shape and position of the spike in the Br^+ signal. We attribute the broad underlying signal in these TOF's to secondary dissociation, via absorption of a photon, of some of the CH_2Br product from C-I bond fission. This secondary photodissociation will be discussed later (see Section I.F). It should be noted that some of the faster signal in the peak of the Br^+ TOF spectra could be due to CH_2Br product giving Br^+ in the ionizer, but the fraction of this contribution should be fairly small or the shape of the fits would not match the shape of the observed peaks.

The relative intensities of the Br atom signal from C-Br bond fission and the I atom signal from C-I bond fission suggest that C-Br bond fission is a minor channel. This will be quantified in Section III.I.

C. Absence of Occurrence of $CH_2BrI \xrightarrow{248\ nm} CHI + HBr$ (3) and $CH_2BrI \xrightarrow{248\ nm} CHBr + HI$ (4)

Two independent techniques were used to check for the possibility of concerted dissociation channels forming HI or HBr. First one looks for signal at HI^+ and at $H^{81}Br^+$. If any is observed one must compare it to the shape of the signal at I^+ (or Br^+ respectively) to be certain it is not m/e=127 (or 81) leaking through when the quadrupole is set to pass m/e=128 (or 82).[12] This technique assumes that if any HI or HBr is formed, they will give some parent ion in the ionizer. Second one looks for differences in the spectra of CH_2I^+ and CHI^+ and of $CH_2^{81}Br^+$ and $CH^{81}Br^+$. CHBr would contribute to the $CH^{81}Br^+$ but not to the $CH_2^{81}Br^+$ TOF (and likewise for CHI). The TOF spectra taken at m/e=128, HI^+, and m/e=82, $H^{81}Br^+$, are shown in Fig. 11. The TOF spectra of m/e=140, CHI^+, and 94, $CH^{81}Br^+$, are shown in Fig. 12. The very small signal at HBr^+ around 300 μsec measured at 20° could easily be due to leaking of the Br^+ through the quadrupole and the similarity of the CHI^+ and CH_2I^+ shown in Figs. 12 and 8 affirm that no HBr production is evident. Similarly there is no evidence for HI production, as there is no signal at HI^+ (Fig. 11) and the TOF spectra of $CH^{81}Br^+$ and $CH_2^{81}Br^+$ shown in Figs. 12 and 6 are indistinguishable.

D. Possibility of a Tiny Fraction of $CH_2BrI \xrightarrow{248\ nm} CH_2 + IBr$

The TOF spectrum of m/e=206, 208, IBr^+, is shown in Fig. 13. The signal is so low even at such small center-of-mass velocities when the molecular beam TOF technique is particularly sensitive that one cannot discount the possibility this signal is due to dimers. We searched for evidence of the monomer concerted reaction two other ways. Because the momentum matched CH_2 is so much lighter than IBr, its recoil velocity would be quite fast and might be observable. Fast signal was observed in the CH^+ TOF, Fig. 14, but it was not correctly related to the IBr^+ signal by momentum conservation (this signal is assigned to CH_2 from the secondary dissociation of CH_2Br and CH_2I in Section's I.F and I.G). One can predict where the CH_2 should appear in the CH^+ TOF via conservation of momentum with the observed IBr^+ signal, this is shown by the fastest broad hump between 100 to 200 μsec in the CH^+ spectrum. There is no signficant signal there. In addition, there is no evidence for IBr in the fragment ion mass I^+ TOF spectra; at 10° (Fig. 6) the peak would arrive at ~500 μsec, between the I product signal from C-I bond fission and the hump from dimer contamination. Thus the signal at IBr^+ is probably due to clusters in the beam.

Note that if any IBr were formed with a total translational energy release of less than ~4.4 kcal/mole it would not recoil away from the molecular beam with a large enough velocity to be detected. The CH_2 product from $CH_2BrI \rightarrow CH_2 + IBr$ could however be detected at 20° with as little as 0.04 kcal/mole release to translation, but might be difficult to pick out in the congested CH^+ spectrum.

E. Identification of Signal from Dissociation of Dimer Contamination in the Molecular Beam.

Although the fraction of CH_2BrI associated as dimers in the molecular beam is probably very small (the reservoir of CH_2BrI was held at 18°C and the nozzle was heated to 135°C), some contamination of the TOF spectra from dissociation of clusters can be observed at small angles. Fragments from clusters usually recoil with small c.m. velocities and thus appear in a small laboratory angular range about the molecular beam, so although their signal is not observed at large angles we are particularly sensitive to their signal at 10°.

The TOF spectra of m/e=81 and 127 at 10° and m/e=94 at 20° obtained with reduced polymer contribution to the molecular beam are shown in Fig. 15. Under the new beam conditions all the signal is substantially reduced, but the ratio of monomer molecules to clusters in the molecular beam is significantly increased. Thus any signal from cluster parent molecules will be reduced in intensity with respect to signal from dissociation of monomers. Comparing the m/e=127 TOF at 10° here in Fig. 15 with that in Fig. 6, one sees that the feature near 650 μsec flight time is clearly due to dissociation of clusters. Likewise, comparison of Fig. 12 and Fig. 15 shows that the 20° spectrum of m/e=94 in Fig. 12 contains signal from dimers around 650 μsec. The m/e=81 spectrum shows no change, however. The slow signal in this spectrum is assigned to the Br from secondary dissociation of CH_2Br product below.

F. Secondary Dissociation of CH_2Br Product, $CH_2Br \xrightarrow{248\ nm} CH_2 + Br$ (5)

The TOF at m/e=81, $^{81}Br^+$ (Fig. 9), shows broad signal at faster and at slower times than the CH_2Br product arrival time (which is toward the fast side of the Br signal from C-Br bond fission indicated in solid line). Such a broad underlying signal is characteristic of secondary dissociation of a product. After primary C-I bond fission which requires 55 kcal/mole, the CH_2Br product formed cannot be left with enough internal energy to undergo unimolecular dissociation to CH_2 + Br. Its secondary dissociation must occur via absorption of another photon. In a previous experiment in this laboratory on the photodissociation of CF_2Br_2 at 248 nm,[13] the CF_2Br product from C-Br fission absorbed another photon and dissociated to CF_2 + Br, thus it is not surprising that CH_2Br radicals also absorb at 248 nm and dissociate. When the laser power was reduced by a factor of 5.6 the relative intensity of the broad signal with respect to the primary signal decreased as shown in the low and high power TOF spectra of Br^+ at 20° in Fig. 16, thus confirming our explanation that the signal is Br product from some CH_2Br absorbing a photon and dissociating. The figure also shows that the secondary absorption is strongly saturated as it was for CF_2Br radicals.

Modeling a secondary dissociation such as this involves calculating the laboratory velocity flux distribution of the CH_2Br parent product molecules from primary C-I fission, then inputting a guessed $P(E_T)$ for dissociation to CH_2 + Br to account for the recoil of CH_2

and Br from each other. The final Br laboratory velocity is the vector sum of the molecular beam velocity, c.m. recoil velocity of CH_2Br from I and the c.m. recoil velocity of Br from CH_2. This calculation is performed for the secondary dissociation of CH_2I below, but was not attempted for CH_2Br because of the large range of laboratory velocities of the CH_2Br product. However, the similarity between the secondary dissociation signal of Br from CH_2Br, which peaks at faster and slower arrival times than the CH_2Br parent, and the secondary dissociation signal observed by Krajnovich, et al.[13] in the CF_2Br_2 TOF data is marked and expected.

A simple calculation was made to assure that the assignment of the underlying signal in the Br^+ TOF spectrum to reaction (5) is consistent with conservation of energy and momentum. If one asks how much energy would have to go into translation in the dissociation of $CH_2Br \rightarrow CH_2 +$ Br for the Br to reach the shortest observed arrival time at 10° of 180 μsec, one calculates 52 kcal/mole for the Br originating from CH_2Br in the peak of the CH_2Br + I translational energy distribution.[14] Whether the primary and secondary photons absorbed can provide all the necessary energy is easily calculated:

$$\text{Required energy} = E_{T_{I+CH_2Br}} + D_{o_{I-CH_2Br}} + E_{T_{CH_2+Br}} + D_{o_{Br-CH_2}}$$

$$= 19 + 55 + 52 + (75) \approx 201 \text{ kcal/mole}$$

$$2E_{h\nu} = 230 \text{ kcal/mole} > 201 \text{ kcal/mole.}$$

One also calculates that the CH_2 product from the secondary dissociation of CH_2Br which releases 52 kcal/mole to translation would have a total flight time (flight time to ionizer + ion flight time) of 67 μsec. This corresponds to within a few μsec to the fast side of the previously unassigned sharp spike in the CH^+ TOF of Fig. 14. Thus CH^+ signal is observed which is momentum matched with the fastest Br^+ signal observed, as required for reaction 5, and the observed product velocities are accessible with the available energy.

G. Secondary Photodissociation of CH_2I Product, $CH_2I \xrightarrow{248\ nm} CH_2 + I$ (6).

The TOF spectrum of m/e=127, I^+, contains a broad underlying signal which is mainly due to the secondary photodissociation of CH_2I product from C-Br bond fission. As was the case for CH_2Br secondary dissociation, the CH_2I product cannot have enough internal energy after the C-Br bond fission to dissociate spontaneously. It must dissociate via absorption of another photon.

The shape of the secondary dissociation TOF signal was calculated from a possible $P(E_T)$ for rxn. 6 as follows. We assumed first that all the CH_2I product from C-Br bond fission had equal probability of absorbing another photon and dissociating to $CH_2 + I$. This assumption is unlikely to be strictly true, but unless, for instance, the CH_2I product in the fast side of the distribution has a much higher likelihood of undergoing secondary photodissociation than the CH_2I in the slow side, the effect of a varying dissociation probability across

the CH_2I primary product distribution would not affect the secondary TOF calculation significantly. No obvious depletion of one part of the CH_2I TOF is evident when one compares the shape of the momentum matched Br spike in the Br^+ TOF spectra (Fig. 9) with the shape predicted (solid line) from the velocities of the observed CH_2I product, so the assumption is leant credibility. Second, one calculates the laboratory velocity flux of the CH_2I product from which the CH_2 + I fragments will originate. This is a simple extension of our usual fitting procedure with one exception. The scattered CH_2I product is constrained by symmetry to have an isotropic c.m. angular distribution with respect to θ, the angle in the plane perpendicular to the unpolarized laser beam. However, the c.m. angular distribution with respect to the out of plane angle ϕ is sensitive to any anisotropy of the primary dissociation event. To simplify the calculation we set this anisotropy to zero for the purpose of the calculation of the secondary dissociation signal, although the anisotropy parameter is shown to be 0.6 ± 0.1 in Section I.H. Because there is significant energy released to translation in the secondary dissociation event, the effect of an anisotropic primary step will be small. This is empirically verified for this case by noting in Section I.H that the shape of the TOF of the secondary signal does not change significantly when the laser is polarized. Finally, the recoil of the CH_2 from I in the secondary dissociation (6) is accounted for from each CH_2I parent molecule; we also assumed this to be isotropic. A $P(E_T)$ is guessed for the dissociation and a TOF at I^+ is calculated, then the $P(E_T)$ is refined until

the fit is good. The $P(E_T)$ shown in Fig. 17 for rxn. 6 gave the acceptable fit to the underlying signal shown in Fig. 6. Because there are other contributions to these spectra, uncertainty in what signal should be fit is evident. It is, however, certain that the secondary dissociation signal should extend underneath the primary I signal or the relative heights of the two components would not be well fit by the $P(E_T)$ derived for rxns. 1a and 1b from the CH_2Br^+ spectra.

H. Anisotropy of the C-I and C-Br Bond Dissociation Channels With Respect to the Direction of the Electric Vector of the Laser

The dependence of the I^+ signal on the direction of the electric vector of the laser, at a molecular beam to detector angle of 20°, from primary C-I bond fission producing $I(^2P_{1/2})$ and $I(^2P_{3/2})$ products is shown in Figure 18a. A polarization angle of 0° corresponds to the $\vec{E}$ vector pointing from the interaction region of the laser and molecular beam to the centerline of the detector. The electric vector is rotated in the opposite direction as the source so a polarization angle of 20° corresponds to an angle of 40° with respect to the molecular beam direction. The Newton diagram in the corner of Figure 18a shows that the peak of the I^+ signal intensity vs. polarization angle occurs when the $\vec{E}$ vector is parallel to the peak center-of-mass velocity of the I atom fragments.

Zare[15] has derived an expression for the center-of-mass (c.m.) angular distribution of the fragments formed when a molecule absorbs

light via an electric dipole transition. The expression he derived for the probability, $\omega(\theta)$, of a fragment recoiling in a direction θ from the electric vector of the laser is:

$$\omega(\theta) = {}^{1}/_{4\pi}(1 + \beta P_2(\cos\theta)) \qquad (7)$$

The anisotropy parameter β can range from 2, corresponding to a parallel ($\cos^2\theta$) angular distribution, to -1, corresponding to a perpendicular ($\sin^2\theta$) angular distribution. More exact quantum mechanical expressions have followed[16,17]; in the limit of high relative translational energies of fragments (or zero angular momenta of fragments) Zare's formula is recovered, so we obtained the anisotropy parameter β by fitting the data in Figure 18a with relation (7). If the molecule rotates during dissociation or if bending vibrations change the dissociation direction after absorption of the light, a purely parallel or perpendicular absorption will not result in anisotropies of 2 or -1; the β will be closer to zero.

The anisotropy parameter was derived from fitting of the data as follows. The $P(E_T)$ for each of the C-I bond fission channels is derived from the unpolarized light TOF data which is constrained by symmetry to be independent of anisotropy. Only the relative heights of the $I(^2P_{1/2})$ and $I(^2P_{3/2})$ signals can be affected. This $P(E_T)$, the measured molecular beam speed distribution, the ion flight time, and the molecular beam to detector angle determine the c.m. scattering angle corresponding to each signal arrival time in the TOF spectra. A

c.m. to lab transformation with β as the only variable parameter is used to calculate the variation in signal intensity integrated over a specific range of arrival times as a function of the direction of the electric vector. This is compared to experimental data integrated over the same range of arrival times. For I^+, we integrated the signal between arrival times of 304.5 to 427.5 μsec and approximately subtracted the underlying secondary signal by averaging the secondary signal between 571.5 and 628.5 μsec.

The best fit to the total primary I atom product signal intensity versus polarization direction gives $\beta = 1.0 \pm 0.1$ (the calculated curves are shown in solid line in Fig. 18a). It is easily determined that the production of both $I(^2P_{1/2})$ and of $I(^2P_{3/2})$ each independently has an anisotropy of $\beta = 1.0$. The I^+ TOF data taken with the laser light polarized at 0° and 100° are shown in Figs. 18b and c respectively with fits calculated assuming that each channel has an anisotropy of 1.0. Beside them are shown fits assuming the anisotropy of the dissociation product $I(^2P_{1/2})$ is 2.0 and the product $I(^2P_{3/2})$ is 0.5. (The probability of each channel would then have to be 1.13:1.06 instead of 0.75:1 in order to fit the unpolarized light data.) Clearly then, as shown in the fits, the $I(^2P_{1/2})$ channel with the more parallel angular distribution would be enhanced at a polarization angle of 0° and diminished at a polarization angle of 100° with respect to the less parallel $I(^2P_{3/2})$ channel, although the total intensity versus polarization angle dependence would still approximately fit Fig. 18a. Thus, the relative intensities of the $I(^2P_{1/2})$

and $I(^2P_{3/2})$ signal in the polarized light data clearly show that both channels have the same polarization dependence and indicate that they both result from excitation to an electronic state with the transition moment roughly parallel to the C-I bond.

The polarization dependence of the CH_2I^+ signal, at a molecular beam to detector angle of 20° is shown in Fig. 19a. The experimental signal was derived from the data by averaging the data between 6 and 150 μsec arrival times to obtain the background and subtracting it from the total signal intensity between 330 and 406 μsec to obtain the signal from CH_2I with the corresponding range of laboratory velocities. The expected signal from CH_2I as a function of the direction of the electric vector was then calculated as for the I^+ data and compared to the experimental data, with β again as the only variable parameter. The best fit was obtained with $\beta = 0.6 \pm 0.1$. As shown explicitly for the the I^+ polarized light data in Figures 18b and c, the good fit to the CH_2I^+ data using a uniform anisotropy of 0.6 over the entire distribution indicates that signal at the fast side and at the slow side of the distribution, which might contain various amounts of $Br(^2P_{1/2})$ and $Br(^2P_{3/2})$ product channels, have the same angular distribution. It will be evident in the discussion section that for C-Br bond fission this indicates that primarily $Br(^2P_{1/2})$ is formed in the C-Br dissociation events at 248 nm.

I. Branching Ratio Between C-I and C-Br bond fission at 248 nm

A lower bound to the relative number of molecules undergoing primary C-I bond fission to the number undergoing primary C-Br bond fission at 248 nm can be estimated from the data as follows. Careful comparision of the relative signal intensities in the spikes in the I^+ and $^{81}Br^+$ spectra assigned to I and Br atoms from primary dissociation events will give a lower limit to the C-I:C-Br bond fission probability ratio. This is a lower limit because Br^+ signal from CH_2Br would fall at arrival times in the fast part of the signal which is assumed to be only due to Br atoms. (The CH_2I product signal arrives at slower times than the sharp spikes in the I^+ spectra, so it introduces no error.)

The comparison of signal intensities proceeds in the manner described in detail by Krajnovich[18] with two additions. The signal at $^{81}Br^+$ is multiplied by two as the quadrupole was precisely tuned to only allow the 50 percent abundant $^{81}Br^+$ species to be counted and not the 50 percent $^{79}Br^+$ species. The signal intensities are also corrected for our extra sensitivity to fragments recoiling with a more parallel angular distribution with respect to the electric vector of the dissociating light. Assuming the angular divergence of the beam and finite angular acceptance of the detector are negligible, one is more sensitive to products with higher anisotropy parameters by a factor of $1 + \beta/4$. Thus product signal from C-I bond fission is divided by $1 + 1.0/4$ and product signal from C-Br fission is divided by $1 + 0.6/4$.

To obtain the lower limit for the branching ratio, the above factors are taken into account and the usual correction made for ionization cross sections of the products (calculated to be 53.1 and 44.9 for I and Br respectively with the semi-empirical method detailed in ref. 18) and velocity distribution of dissociation products. A lower limit of 1.2:1 for C-I:C-Br bond fission is obtained from the appropriate parts of the I^+ and Br^+ signal intensities at 20°. At this excitation wavelength, which may contain contributions from both the n(I) → σ*(C-I) and the n(Br) → σ*(C-Br) transitions, both C-I and C-Br fission occur to a significant extent, with C-I fission being the dominant channel.

II. Photodissociation of CH_2BrI at 193 nm

A. Thermodynamic Constraint on Stability of Dissociation Products

Identification of all the primary dissociation channels of CH_2BrI excited via absorption of a 193 nm photon is complicated by the fact that the photon energy of 147.9 kcal/mol is greater than the endoergicity of $CH_2BrI \rightarrow CH_2 + I + Br$ (see Fig. 1.). Thus it is possible that some of the CH_2I, CH_2Br, or IBr products formed will spontaneously undergo secondary dissociation as they may be internally excited above their dissociation limits. A simultaneous three-body dissociation, in which only the sum of the momenta of all three products are constrained to sum to zero, is also energetically allowed. For some systems, the complications caused by secondary dissociation of products can be

avoided by observing the momentum matched Br, I, and CH_2 respectively. For CH_2BrI at 193 nm, those spectra are so congested that analysis is difficult. One advantage does come about from this situation; any CH_2I or CH_2Br product observed at small recoil energies must necessarily come from dissociation events producing spin-orbit excited partner halogen atom fragments. This expectation is made more quantitative below and in the analysis of each dissociation channel observed. In addition, we are not sensitive to the heavy products from C-H fission or H_2 elimination; it is unlikely that these processes occur to any extent at these excitation wavelengths because, firstly, the $\sigma \rightarrow \sigma^*$ transition on the C-H bond is only accessed in the vacuum ultraviolet and secondly, both these channels will have endothermicities near 100 kcal/mole so would not be predicted by a statistical argument (if internal conversion from the initially excited state took place, one might attempt to predict the reaction channels' probabilities with statistical theories).

The secondary dissociation of CH_2I, CH_2Br, or IBr primary products will occur if the internal energies of those products is greater than their dissociation energy. Their internal energy can be derived from knowledge of the translational energy and internal energy channeled to the partner fragment (Br, I, and CH_2 respectively) in each primary dissociation. The routes for net formation of $CH_2 + I + Br$ are:

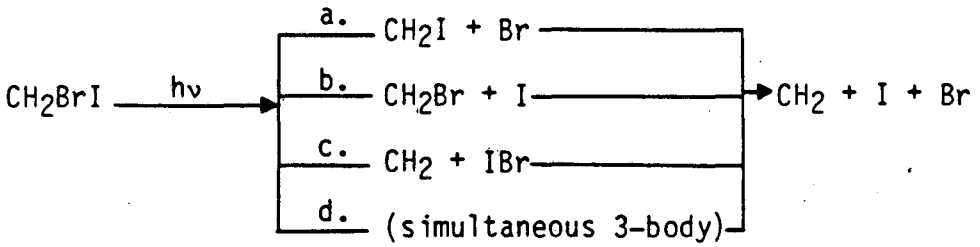

(8)

Assuming there is no barrier to dissociation beyond the endothermicity, the energy required for reaction 8 is 130.4 kcal/mol.[1] If the internal energy of the CH_2BrI parent molecule has been relaxed to less than one kcal/mol or so in the supersonic expansion and is thus negligible (see III.A), one can find a condition on what fragments will survive secondary dissociation as follows. The CH_2Br, CH_2I, or IBr fragments will necessarily be formed with total internal energies below their dissociation limits and will be observed if the energy released to translation plus the spin-orbit excitation of the partner I or Br fragment or the internal energy of the CH_2 fragment for each respective primary dissociation event is greater than $E(h\nu) - \Delta H(rxn\ 8) = 147.9 - 130.4 = 17.5$ kcal/mol. In special cases, CH_2Br, CH_2I, or IBr formed with internal energies above their dissociation limits may still survive secondary dissociation during the transit time to the detector. The fragment may be stable if, for instance, there is a rotational barrier to dissociation imposed by conservation of angular momentum (this barrier will be small for CH_2I and CH_2Br because the moment of inertia increases rapidly as the C-X bond stretches) or if an electronically excited fragment fluoresces prior to dissociation, leaving it energetically stable. The contributing factors to the stability of the individual CH_2Br, CH_2I, and IBr fragments observed at 193 nm will be outlined in each section below.

B. $CH_2BrI \xrightarrow{193\ nm} CH_2I + Br$ (9)

The TOF spectrum of m/e = 141, CH_2I^+, is shown in Fig 20. The spectrum consists of a fast narrow signal peaking at a 370 μsec flight time corresponding to CH_2I product from C-Br bond fission that has not undergone secondary dissociation to CH_2 + I, and a small broad signal peaking near 600 μsec attributed to dissociation fragments of a small fraction of dimer contamination in the beam. The c.m. product translational energy distribution derived from forward convolution fitting of the CH_2I signal is shown in Fig. 21. The fit is shown in solid line in Fig. 20. (There is necessarily uncertainty in this $P(E_T)$ below 6 kcal/mol in translation due to the contamination of the slower portion of the CH_2I TOF from dissociation of dimers.) The $P(E_T)$ shows the distribution of translational energies released in C-Br fission for the dissociation events that formed stable CH_2I radical product.

The energetic analysis in Section II.A. concluded that, if all Br atoms produced are in the ground state, the CH_2I from C-Br dissociation events that released more than 17.5 kcal/mol to translation would be left with a low enough internal energy to be stable with respect to secondary dissociation to CH_2 + I. This corresponds to only about 20 percent of the C-Br bond fissions that could have produced stable CH_2I, as trivially calculated from the area under the $P(E_T)$ (Fig. 21) above and below E_T = 17.5 kcal/mol. The C-Br bond fissions releasing less than 17.5 kcal/mol to translation would produce energetically unstable CH_2I unless the partner Br atom were spin-orbit excited. CH_2I produced

with even a kcal/mol of energy above its dissociation limit would be expected to dissociate in much less than the > 350 μsec flight time to the detector as it is a small molecule with few degrees of freedom and a large Arrhenius preexponential factor (logA~16) for dissociation to CH_2 + I. The fact that the CH_2I produced in the primary dissociation is expected to be rotationally hot due to the bent configuration of the parent I-C-Br bond (see Appendix 2 of ref. 19) suggests the possibility of a rotational barrier beyond the endoergcity of the secondary dissociation. Such a barrier would allow CH_2I to survive with internal energies above the quoted dissociation limit, but this barrier is easily shown to be small. Thus all the CH_2I observed from C-Br bond fissions releasing less than 17.5 kcal/mol to translation must necessarily produce spin-orbit excited Br atoms. Most of the $P(E_T)$ of Fig. 21 must correspond to the process:

$$CH_2BrI \xrightarrow{193\ nm} CH_2I + Br\ (^2P_{1/2}) \qquad (10)$$

One would expect, in addition, that if an appreciable fraction of C-Br bond fissions produced ground state Br atoms one would see a break in the $P(E_T)$ derived from the CH_2I^+ TOF near 17.5 kcal/mol, because the CH_2I from the ground state channel would be lost below that translational energy to secondary dissociation. It shold be noted that the division point of the $P(E_T)$ at 17.5 kcal/mol in translation below which the CH_2I observed must be from reaction 10 relies on the accuracy of the endothermicity for $CH_2BrI \rightarrow CH_2$ + I + Br of 130.4 kcal/mol. This endothermicity may be underestimated by 1-2 kcal/mol as there is

evidence for stable CH_2I product at translational energies of 5-6 kcal/mol; $E(h\nu) - E(Br(^2P_{1/2})) - E_T$ (5 kcal/mol) = 132.4 kcal/mol. Normally one could compare the distribution of c.m. velocities of CH_2I and Br atom products to determine whether any CH_2I were being lost to secondary dissociation as the two fragment velocities are related by momentum conservation. In this system, the Br^+ spectrum is too congested with signal from other dissociation pathways and prohibits the comparison.

C. $CH_2BrI \xrightarrow{193\ nm} CH_2Br + I$ (11)

The TOF spectrum of m/e = 95, $CH_2^{81}Br^+$, is shown in Fig. 22a. The spectrum shows a fast signal peaking near 300 μsec attributed to stable CH_2Br product from C-I bond fission, a slower small peak at 400 μsec and a broad slow peak at 650 μsec. The peaks at ~ 650 μsec and at 400 μsec were explicitly determined to be from dissociation of clusters in the beam by repeating the TOF measurement at reduced dimer molecular beam conditions as in I.E (compare Fig.'s 22a and 22b). The cluster dissociation signal is large in relation to the primary C-I dissociation channel signal because the fraction of C-I bond fission at 193 nm is so much smaller than at 248 nm (compare Fig. 6 and Fig. 22 and see the branching ratio determination in Section II.G).

An approximate $P(E_T)$ for C-I bond fissions that produced stable CH_2Br product was derived from forward convolution fitting of the CH_2Br^+ TOF. The $P(E_T)$ in Fig. 23 gave the fit shown in solid line in Fig. 22; the shape of the $P(E_T)$ below 10 kcal/mol is particularly

approximate due to dimer contamination of the signal. By the same argument started in Section II.A and applied in detail to the C-Br fission $P(E_T)$ in Section II.B, more than two thirds of the dissociation events that produced this stable CH_2Br product must have produced I atom in the $^2P_{1/2}$ state:

$$CH_2BrI \xrightarrow{193\ nm} CH_2Br + I(^2P_{1/2}) \qquad (12)$$

Because the spin-orbit splitting of I is so large, 21.7 kcal/mol, all the CH_2Br produced via reaction 12 would be energetically stable and could be detected in the CH_2Br^+ spectrum, independent of the translational energy of the products. C-I bond fissions producing ground state I atoms would not produce stable CH_2Br product unless more than 17.5 kcal/mol were released to translational energy of the products. As in C-Br bond fission, most of the fast peak in the $CH_2{}^{81}Br^+$ spectrum must correspond to formation of spin-orbit excited $I(^2P_{1/2})$ product (reaction 12).

As for Br^+, the I^+ spectrum in this system is too congested with signal from other dissociation pathways to determine if any of the CH_2Br signal momentum matched with the I atom product is being lost to secondary dissociation. It is clear, however, that if more than a small fraction of C-I bond fissions produced ground state I atoms one would see a break in the $P(E_T)$ derived from the CH_2Br TOF near 17.5 kcal/mol, because the CH_2Br from the ground state channel would be lost below that translational energy to secondary dissociation. The same argument applies to the C-Br bond fission channel.

D. $CH_2BrI \xrightarrow{193\ nm} CH_2 + IBr$ (13)

The TOF spectra of m/e = 206,208, IBr^+, at source to detector angles of 10° and 20° are shown in Fig. 24. The signal is easily assigned to the IBr product from the primary three-center elimination of IBr from CH_2BrI. It was explicitly determined that the signal was not due to dissociation of dimer contamination in the molecular beam as follows. First the total time of arrival of IBr product that fragmented to I^+ or Br^+ in the ionizer was obtained by correcting the IBr signal at IBr^+ for the smaller ion flight time of m/e = 127 and 81 through the ion optics and quadrupole (a correction of -10 and -17 μsec respectively). The expected time of arrival of I^+ and Br^+ from IBr elimination events that produced stable IBr product was then superimposed on the I^+ and Br^+ TOF data. The 20° data is shown in Fig. 25 a and b with the expected time of arrival of signal from IBr shown in solid line. The signal from IBr is evident in both the I^+ and Br^+ TOF's. The molecular beam conditions were then changed as described in the experimental section to reduce further the ratio of dimer to monomer in the beam and the I^+ and Br^+ TOF data were retaken. The reduced dimer molecular beam data is shown in Fig. 25 c and d for comparison. Any signal from dissociation of dimers in the beam should decrease by at least a factor of two with respect to monomer signal, as measured under the same two molecular beam conditions at 248 nm (see Section I.E.). The signal attributed to IBr did not decrease in intensity relative to the monomer dissociation signal at shorter arrival times. The

IBr product observed in the IBr^+, I^+, and Br^+ spectra must therefore be from the concerted elimination of IBr from CH_2BrI excited at 193 nm.

The $P(E_T)$ shown in Fig. 26 is derived from fitting the IBr^+ TOF shown in Fig. 24. Neglecting the small fraction of IBr that might be formed in an excited electronic state which fluoresces on a time scale faster than predissociation, the stable IBr product must have been formed in dissociation events that channelled 17.5 kcal/mol of energy to translation and the internal excitation of the CH_2 partner fragment. At lower and lower translational energies, the partner CH_2 to the IBr product must be more and more internally excited for the IBr product to be stable. Thus one would expect the $P(E_T)$ for formation of all IBr product including those which subsequently dissociate favors dissociation at a lower average translational energy than the $P(E_T)$ derived from the stable IBr product in Fig. 26. The IBr that undergoes secondary dissociation to I + Br would contribute to the signal peaking at ~ 600 and ~ 500 μsec in the I^+ and Br^+ TOF's respectively, as discussed in Section II.E.3.

The $P(E_T)$ for production of stable IBr product also suggests the nature of the IBr electronic state. The maximum energy released to translation is a very sharp 23.5 ± 1.0 kcal/mol. This energy corresponds very closely to the maximum available energy for translation if electronically excited IBr ($^3\Pi_1$) is formed:

$$CH_2BrI \rightarrow IBr\ (^3\Pi_1) + CH_2 \qquad \Delta E = 88.46 + 35.12^{21} = 123.58 \qquad (14)$$

$$E_{avail} = 147.9 - 123.58 = 24.3 \text{ kcal/mol}$$

Because the CH_2 has so few degrees of freedom one would expect that some of the fragments would recoil with very close to the total available energy. Apparently the I atom Rydberg state formed by exciting CH_2BrI at 193 nm is predissociated by a state that correlates specifically to electronically excited IBr product and ground state $CH_2(^3B_1)$. The fact that no obvious discontinuity appears in the IBr^+ spectrum at 24.3 - 9.05 = 15.3 kcal/mol, where the channel producing $IBr(^3\Pi_1)$ + $CH_2(^1A_1)$ becomes energetically allowed, suggests that primarily triplet CH_2 is produced.

E. Anisotropy of Primary Processes and Secondary Dissociation of Fragments

Two sets of TOF spectra of m/e = 127, I^+, and m/e = 81, Br^+, are shown in Figures 27 and 28 respectively. The TOF spectra in the first column are taken with the photolyzing laser being unpolarized and having a pulse energy of ~ 200 mJ/pulse. The TOF data in the second column in each figure are taken with the photolyzing laser light linearly polarized in the direction of the detector but the power reduced by a factor of ~7. The molecular beam conditions were the same for both sets of data; thus a comparison of the corresponding TOF data under each laser condition is sensitive to the polarization dependence and the power dependence of the signal.

E-1. Polarization Dependence of Signal: Anisotropy of Scattering of Fragments from the Primary Dissociation Channels

The polarization dependence of the primary dissociation channels can be qualitatively derived from the TOF spectra of I^+ and Br^+ at source to detector angles of 10°[22] shown in Figures 27a and d and 28a and d. The TOF spectra at 10° are very nearly superimposable independent of the polarization of the laser. The signal from IBr elimination to form stable IBr product rising near 500 μsec in both sets of 10° TOF data spans a wide range of c.m. angles. The Newton diagram in Figure 29 shows the angle between the electric vector of the light and the c.m. recoil direction of the observed IBr product ranges from 26° to beyond 90°. The c.m. angular distribution with respect to the molecular beam - detector plane is necessarily isotropic for the data taken with unpolarized light as the direction of the electric vector is isotropic in that plane. The fact that the shape of the TOF signal from IBr product does not change when the light is polarized even though the fastest IBr observed recoils at an angle of ~26° with respect to the electric vector of the light and the slowest recoils at angle of 90° and larger shows that the c.m. angular distribution of the stable IBr product is nearly isotropic. The same argument can be applied to the broad underlying signal attributed to the dissociation to CH_2 + I + Br extending from 400 μsec to 900 μsec in the 10° TOF data in Figures 27 and 28. (see Section II.E.3) One can also see from this data that the overlapping fast signal from CH_2Br, CH_2I, I, and Br also show no

strong polarization dependence. In fact, the TOF data shown in Fig.'s 27d-e and 28d-e are fit with all components assumed to have an isotropic angular distribution. It is evident from the Newton diagram in Figure 29 that the range of c.m. angles of these fast products detected at 10° and the electric vector of the polarized light is small, between 5 and 15°. In this case one does not expect such a large difference in the shape of the TOF spectra of the fast products, because the c.m. scattering angle does not change much across the spectra, but one does expect a large change in the relative intensity of any anisotropic fast signal relative to signal that is isotropic. If the c.m. angular distribution of the recoil of I or Br resulting from C-I or C-Br bond fissions were perpendicular, for instance, signal from I or Br in the polarized light data should disappear almost entirely in the polarized light TOF data relative to the slow isotropic IBr signal. Thus all the primary processes observed at 193 nm have close to an isotropic c.m. angular ditribution with respect to the direction of polarization of the dissociating light.

E-2. Laser Power Dependence of Signal: Identification of Secondary Dissociation of Fragments via Absorption of an Additional Photon

If the absorption transition of a fragment for a 193 nm photon is not saturated, then signal from "fragments of fragments" should decrease at least linearly with respect to the primary product signal when the laser power is decreased. There are a few obvious features in the high

power I^+ and Br^+ TOF spectra of Figures 27 and 28 a-c that substantially decrease in intensity relative to the primary fragment signal when the laser power is decreased. These secondary product peaks are most noticeable in the high S/N data at 20° for I^+ and Br^+ (Figures 27b and 28b) and in the I^+ 30° TOF data (Figure 27c). The very fast peaks in the I^+ and Br^+ TOF spectra arriving at 200 and 140 μsec respectively in the 20° TOF spectra are easily assigned to some IBr product absorbing a photon and dissociating to I + Br. If one calculates the c.m. recoil velocity corresponding to I atom product arriving at 200 μsec assuming the parent IBr was approximately travelling at the molecular beam velocity one predicts the laboratory flight time of momontum matched Br product to be 143 μsec. The corresponding c.m. translational energy released in the dissociation is calculated to be 101 kcal/mol. At this wavelength some $Br(^2P_{1/2})$ would be expected to be formed from the secondary dissociation. The two states of Br product and the initial spread in IBr parent laboratory velocities and internal energy would result in the spread in the I and Br secondary product arrival times.

The obvious broad hump in the I^+ spectrum at 20° (Fig. 27b) rising near 240 μsec and extending underneath the primary dissociation signal is assigned to the I from $CH_2I \xrightarrow{193} CH_2 + I$. The Br product from the secondary dissociation of CH_2Br is noticeable just to the fast side of the primary Br atom peak at 20° (Figure 28b) at ~ 200 μsec and clearly extends through the primary signal, as evidenced by the difference between the two 30° Br^+ TOF spectra in Figures 28 c and f

(the underlying secondary signal becomes more important at wider angles in the laboratory frame of reference). The corresponding low power TOF data show the expected substantial decrease in the secondary dissociation signal. The CH_2 fragment in the secondary dissociation of CH_2I and CH_2Br would partially overlap the CH_2 product from primary IBr elimination. This signal is apparent in the CH^+ TOF spectrum shown in Fig. 30.

E-3. Spontaneous Secondary Dissociation of Internally Excited Fragments:

$$IBr_{(\text{internally hot product})} \longrightarrow I + Br \qquad (15)$$

This section will proceed under the assumption that the net chemical reaction $CH_2BrI \xrightarrow{193\ nm} CH_2 + I + Br$ occurs via a two step process through an electronically excited IBr chemical intermediate that is formed above the dissociation limit to I + Br. It is quite possible that this net chemical reaction is more accurately viewed as a one-step three-body dissociation where only the net linear momenta of the three products must sum to zero. Certainly the $^3\Pi_1$ state of IBr may not serve as a metastable intermediate as it correlates to ground spin-orbit state products. The energetically allowed $^3\Pi_{0+}$ state could serve as an intermediate, however, as it correlates to $I + Br(^2P_{1/2})$. In the absence of coincidence measurements of all three fragments, however, the system is not uniquely defined. For the purpose of attempting a unique analysis, the two-step process will be assumed; if it is indeed a three-body dissociation, only the velocity distributions of Br and I from the triple dissociations (no $P(E_T)$) may be derived from this data.

The deconvolution of the I^+ and Br^+ spectra of Fig.'s 27 and 28 into their contributing components is somewhat flexible, particularly where the primary product signal from C-I and C-Br bond fission overlap the signal assumed here to be from spontaneous secondary dissociation of IBr, but the process still yields valuable information. The shape of the TOF signal from the stable IBr product at I^+ and Br^+ is determined by the shape of the IBr^+ spectrum and the precalibrated ion flight time through the mass spectrometer. For the C-I and C-Br bond dissociation channels, the shape of the signals from I and CH_2I product in the I^+ spectra and the shape of the signal from Br and CH_2Br in the Br^+ spectra are obtained from the isolated spectra of CH_2I and CH_2Br shown in Figures 20 and 22 as each pair of fragments must have c.m. velocities related by momentum conservation. The assumption is made here that no significant fraction of CH_2Br or CH_2I underwent secondary unimolecular dissociation, so that the CH_2Br^+ and CH_2I^+ signal represent all the primary dissociation events. The evidence that supports this assumption is that there is no discontinuity in the shape of the $P(E_T)$'s derived from the CH_2Br^+ and CH_2I^+ TOF spectra at 17.5 kcal/mol. The large broad signal indicated in long dashed (—— ——) line between 400 and 900 μsec arrival times in the I^+ and Br^+ spectra in Fig.'s 27 and 28 is most likely to be from the spontaneous secondary dissociation of internally excited IBr or from three-body dissociation (rxn. 8d). Thus three of the four curves used to fit the I^+ and Br^+ spectra are uniquely determined from other data. The relative intensity of the three curves were varied to produce the best fit to the

data while constraining the remaining broad I^+ and Br^+ signal, assumed for the analysis to be from secondary dissociation of IBr, to be smooth. The additional constraint that the signal attributed to the proposed secondary I and Br production from IBr be related by momentum conservation if they originated from IBr parent with approximately the molecular beam velocity was also imposed. Clearly the relative weighting of each dissociation channel must also be the same for each. The shape of the secondary dissociation signal obtained in this way is shown in short dashed line in Figures 27 and 28 d-f. There is clearly uncertainty in the fast portion of this signal.

An approximate $P(E_T)$ for the spontaneous secondary dissociation of IBr product can be obtained by fitting the signal attributed to secondary dissociation in the I^+ and Br^+ spectra. Because the recoil velocity of the IBr product is so small in the c.m. frame, it was assumed for the calculation that the parent IBr was travelling with the molecular beam velocity. The $P(E_T)$ shown in Figure 31 reproduced the shape of the I^+ and Br^+ signal ascribed to secondary dissociation of IBr product. The shape of the $P(E_T)$ is not certain below ~ 2 kcal/mol as here the assumption that the IBr parent c.m. velocity is neglible is not strictly true. It is also not as reliable above 8 kcal/mol; how quickly or slowly the distribution tails off to zero probability is dependent on the relative scaling of the fast peaks from C-I and C-Br fission in the TOF spectra. The mean energy released to translation of 2.9 kcal/mol in the secondary dissociation of IBr product is affected little by these uncertainties, however. One may also obtain from this

$P(E_T)$ the mean internal energy of IBr formed above its dissociation limit in the primary three center elimination of IBr from CH_2IBr. This is simply 2.9 + 41.92 ≈ 45 kcal/mol.

F. Absence of Occurrence of $CH_2BrI \xrightarrow{193\ nm} CHI + HBr$ and $CH_2BrI \xrightarrow{193\ nm} CHBr + HI$.

These dissociation channels were excluded with exactly the same method as described for the photolysis at 248 nm in Section I.C. The HI^+ and HBr^+ spectra at 193 nm are shown in Figure 32. The tiny signal at HI is likely due to fragmentation of dimers. The spectra of $CH^{81}Br^+$ and CHI^+ shown in Figure 33 are identical to that of $CH_2^{81}Br^+$ and CH_2I, further establishing that no HI or HBr elimination occurs.

G. Branching Ratio Between C-I and C-Br Bond Fission

A branching ratio between the two bond fission dissociation channels at 193 nm can be obtained with no approximations for the fragment ionization cross section by considering the spectra of Figures 27 and 28. Since secondary dissociation of IBr produces one of each halogen atom fragment, the signal from the secondary dissociation channel can be used to calibrate the detector sensitivity for Br and I atoms from C-Br and C-I bond fissions. With the deconvolution of the spectra as shown in Figures 27 and 28 and described in Section II.E.3 and the anisotropy for each channel taken to be zero (it has been shown to be close to isotropic, see Section II.E.1) a C-Br to C-I branching ratio

of 3.5:1 is obtained. The effects of the c.m. to lab transformation and number density sensitivity of the ionization process were accounted for here, as in the rest of the analysis.

III. Photodissociation of CH_2BrI at 210 nm

A. Thermodynamic Constraint on Stability of Dissociation Products

As at the 193 nm excitation wavelength, the energy of a 210 nm photon is greater than the energy required to promote the net chemical reaction $CH_2BrI \rightarrow CH_2 + I + Br$ (rxn. 8). As noted, this net chemical reaction may be arrived at via a true three-body dissociation (8d) in which all three fragments separate simultaneously, so only the sum of all three linear momenta in the c.m. must sum to zero, or it may proceed via a two step process in which CH_2I (8a), CH_2Br (8b), or IBr (8c) is formed with internal energy above its dissociation limit and subsequently dissociates. At 210 nm, however, primarily the lowest electronically excited state of IBr is energetically allowed and it correlates to ground state halogen atom products, so it may not serve as a metastable intermediate.

As described in detail in Section II.A, the energetic constraints on which products may undergo secondary dissociation is easily derived. Here, however, the photon energy of 136 kcal/mol is only slightly above the endothermicity of the net reaction (8) of 130.4 kcal/mol, so any initial internal energy of the CH_2BrI parent molecule could have a noticeable influence on the energetic constraints. If one assumes the

rotation of the parent molecule is completely relaxed in the supersonic expansion, but no vibrations relax, the internal energy distribution of the CH_2BrI parent molecules is easily estimated from the nozzle temperature of 140°C and the frequencies of the vibrational modes given in Kudchadker and Kudchadker.[1] The average internal energy of the CH_2BrI parent is found to be 1.5 kcal/mol. Thus, on the average, there is only 136 - 130.4 + 1.5 = 7.1 kcal/mol of energy for the relative translational and internal energies of the final CH_2 + I + Br products of reaction (8).

Several conditions on the stability of dissociation products and the internal energies of the final products are immediately apparent: 1) the CH_2I or CH_2Br products from dissociation events forming spin-orbit excited Br or I atoms will not undergo secondary dissociation, 2) CH_2I, CH_2Br, or IBr from dissociation events channelling greater than 7.1 kcal/mol to translation in the primary dissociation event (± ~1.5 kcal/mol due to the distribution of internal energies of the parent) will not undergo secondary dissociation, and 3) any possible three-body dissociation (rxn. 8d) may not produce spin-orbit excited halogen product and may not channel more than about 7.1 kcal/mol to the relative translation of the products (CH_2BrI parent with greater than the mean internal energy will raise the 7.1 kcal/mol limit correspondingly). The energetic constraints derived here are again dependent on the endoergicity of rxn. (8) of 130.4 kcal/mol.

The laser light is modelled as unpolarized for all the fitting of the TOF spectra in this and the following sections (excluding Section

G). The horizontal component of the electric vector is in reality favored slightly by the dispersing optic for the Raman frequencies.

B. $CH_2BrI \xrightarrow{210\ nm} CH_2I + Br$ (16)

The TOF spectrum of m/e = 141, CH_2I^+, at a 20° source to detector angle is shown in Fig. 34. The spectrum consists of a sharp spike which tails off slowly at longer arrival times and a small broad signal around 650 μsec attributed to dimer dissociation. The TOF spectrum of Br^+ at a 20° source to detector angle is shown in Fig. 35. The sharp spike in that spectrum corresponds to Br product that is momentum matched with the signal from CH_2I at CH_2I^+. The $P(E_T)$ for C-Br bond fission at 210 nm which gave the fit in solid line to the CH_2I^+ signal is shown in Fig. 36. This $P(E_T)$ was used to predict the time of arrival of Br atoms from C-Br bond fission. That fit is shown in Fig. 35. The dissociation events releasing less than 5.6 kcal/mol to translation must have produced spin-orbit excited Br atoms or the CH_2I product would not have been stable. One would not expect to resolve the Br spin-orbit states in the TOF spectrum given the large range of internal energies of the CH_2I product, so some of the dissociation events may also produce ground state Br atoms. However the polarization study shown in III.G indicates the whole distribution has the same anisotropy; because transition at the curve crossing (see discussion) is less likely in C-Br dissociation, the anisotropy suggests that all $Br(^2P_{1/2})$ atoms are formed here.

The CH_2I product also fragments to I^+ in the ionizer. This I^+ signal must have exactly the same shape in time as the CH_2I^+ TOF (neglecting any effect of change in fragmentation pattern with internal energy - indicated to be small in the 248 nm data) with a precalibrated 2μsec shift in the arrival times due to the smaller ion flight time of I^+ through the extraction fields and the quadrupole mass spectrometer. This signal is pointed out in the following section. The cracking of CH_2I to I^+ was also apparent in the 193 nm dissociation, where there was dominant C-Br fission producing CH_2I over C-I fission producing I.

C. Absence of $CH_2BrI \xrightarrow{210\ nm} CH_2Br + I$ (17)

The TOF spectra of m/e = 95, $CH_2^{81}Br^+$, and m/e = 127, I^+, at source to detector angles of 20° and both 10° and 20° respectively are shown in Fig.'s 37 and 38. Both TOF spectra show there is no primary C-I fission to produce $CH_2Br + I$; the analysis proceeds as follows. The low signal spectrum of $CH_2^{81}Br^+$ was explicitly determined to be from dissociation of clusters in the beam. First the ratio of the signals at $CH_2^{81}Br^+$ (signal suspected to be from dissociation of clusters) to that at I^+ (signal from monomers) was determined under the molecular beam conditions used for most of the data accumulation. Then the ratio was measured under molecular beam conditions which were shown in the 248 nm photolysis to reduce the ratio of clusters to monomers in the beam by a factor of ~2. The partial pressure of CH_2BrI in the beam is lowered by a factor of 4 but the seeding ratio is already so small that the beam velocity does not change by more than a couple

percent. Thus, we remain sensitive to slowly recoiling products. Under the reduced cluster beam conditions the $CH_2^{81}Br^+$:I^+ sigal ratio was remeasured and found to decrease by about a factor of 2. The raw signal intensities are shown in Table 1. Thus when one lowers the fraction of dimers relative to monomers in the beam the signal at $CH_2^{81}Br^+$ is lowered with respect to the I^+ signal. The shape of the CH_2Br^+ data did not change (see Fig. 37b), as well, indicating that all the signal is from dissociation of clusters in the beam.

A more initially obvious way to look for evidence of C-I fission is to look for signal at I^+ which is not due to CH_2I or other dissociation channels other than C-I fission. Because primary C-I fission occurs along a repulsive surface releasing a similar large fraction of the total available energy to translation as C-Br fission[23] and because I is lighter than CH_2I, the I atom product from C-I bond fission is expected to have larger c.m. recoil velocities than CH_2I from C-Br fission. This expectation is confirmed experimentally at both of the other excitation wavelengths. Thus one looks for I atom product from primary C-I fission at slightly faster arrival times than the CH_2I product from C-Br fission. The shape of the signal from CH_2I product from C-Br fission which fragments to I^+ in the ionizer is obtained from the CH_2I^+ spectrum shifted by 2 μsec for the precalibrated ion flight time. When this shape is superimposed on the I^+ spectrum (Fig. 39, see bottom frame) one obtains a perfect fit to the fast side and peak of the fast signal. There is no signal in the I^+ spectrum shown in Fig. 38 faster than that from CH_2I which can be attributed

to I atoms from primary C-I fission. As at 193 nm, the slow signal in the I^+ spectrum is from the net chemical reaction (8) and from fragmentation of IBr in the ionizer.

It is clear that the absence of any signal at CH_2Br^+ from the photodissociation of CH_2BrI monomer and the absence of any fast signal in the I^+ spectrum which does not precisely match the velocity of the CH_2I product from C-Br fission shows that CH_2BrI does not undergo primary C-I fission at an excitation wavelength of 210 nm.

D. $CH_2BrI \xrightarrow{210\ nm} CH_2 + IBr$ (18)

The TOF of m/e = 208, $I^{81}Br^+$, at a source to detector angle of 10° is shown in Fig. 39. The corresponding product velocities in the c.m. are too small for the IBr to recoil to 20° and appear in the 20° I^+ and Br^+ spectra, but the I^+ spectrum at 10° shown in Fig. 38a shows I^+ signal from IBr fragmenting in the ionizer. The signal at CH^+ was too small to be observable at the low laser fluences of the Raman shifted frequency but a $P(E_T)$ for the concerted elimination giving CH_2 + IBr (rxn. 18) is easily derived from the IBr^+ data. The $P(E_T)$ is shown in Fig. 40; the corresponding fit is shown in solid line in Fig. 39. The shape of the $P(E_T)$ below ~4 kcal/mol in translation is not sensitive to fitting the IBr^+ data because the slower IBr product will not recoil out to 10°. The sharp cutoff of the $P(E_T)$ near 13 kcal/mol is sensitive to the data; the cutoff again occurs near the total available energy corresponding to formation of all electronically

excited IBr (see Section II.D) product, no ground state IBr, in the concerted elimination.

E. Absence of Occurrence of $CH_2BrI \xrightarrow{210\ nm} CHI + HBr$ and $CH_2BrI \xrightarrow{210\ nm} CHBr + HI$

The TOF spectra of m/e = 128, HI^+, and m/e = 82, $H^{81}Br^+$, at source to detector angles of 20° are shown in Fig. 41. They show no signal from HI or HBr elimination. The I^+ and Br^+ spectra also indicate no evidence for HI or HBr elimination; the slow signal in these spectra are discussed in the next section and are assigned, as was the analogous signal at 193 nm, to the net formation of $CH_2 + I + Br$. The fast signal was easily determined to be from C-Br fission products, so no signal at I^+ or Br^+ is found that should be assigned to HI or HBr production.

F. $CH_2BrI \xrightarrow{210\ nm} CH_2 + I + Br$ (see rxn. 8)

The net reaction to form $CH_2 + I + Br$ is energetically allowed at both 193 and 210 nm and results in the broad slow signal in the I^+ and Br^+ spectra which is not from stable IBr product. It is not reasonable at 210 nm to attempt to analyze the slow signal at Br^+ in terms of a two step process in which electronically excited IBr is formed and subsequently dissociates to I + Br. The $^3\Pi_1$ state of IBr correlates to ground state I and Br atoms so no metastable IBr can be formed in that state. The energy in the system is not sufficient to

produce much IBr in the $^3\Pi_{0+}$ state, predicted to have its zero point vibrational level about 1500 cm^{-1} above the dissociation limit to ground state I and Br.[30] Thus, because 1) there is no obvious metastable IBr state which can serve as an intermediate in a two step process, 2) there is no CH_2Br product formed which can undergo secondary dissociation and give the slow signal detected at Br^+, and 3) secondary dissociation of CH_2I would not give signal peaking as close to the c.m. as that observed in the I^+ spectra, we are obliged to attribute the slow signal in the I^+ and Br^+ spectra to simultaneous three body dissociation to CH_2 + I + Br. The possibility of metastable electronically excited CH_2I or CH_2Br intermediates which all subsequently dissociate cannot be positively excluded, but because the electronic states of these radicals are not known we will not speculate further.

The distribution of translational energies imparted to the I atom and to the Br atom product respectively in the three body dissociation events is derived from fitting of the slow signal in the I^+ and Br^+ TOF spectra in Fig.'s 38 and 35. The range of translational energies of the Br atom product from the triple dissociation is shown in Fig. 42b and for the I atom product is shown in Fig. 42a. A total translational energy distribution for the three body process cannot be arrived at without coincidence measurements of the velocities of the products. The fastest I atom velocities in the slow signal may only originate from dissociation of CH_2BrI with ~2 kcal/mol of internal energy (unless the endothermicity of reaction 8 is overestimated).

G. Polarization Dependences of Dissociation Processes at 210 nm

1. Polarization Dependence of the Br^+ and I^+ Signals from Three-Body Dissociation to CH_2 + I + Br

The TOF spectra of m/e = $^{81}Br^+$, and m/e = 127, I^+, at a source to detector angle of 20° and the laser electric vector parallel to and perpendicular to the line from the interaction region to the detector are shown in Figures 43a-d. A parallel angular distribution of photofragments shows enhancement of the product signal which recoils in the c.m. in the direction of the electric vector of the light and lowering of the signal which recoils at a perpendicular direction to the electric vector in the c.m. Inspection of the slow signal in each spectrum assigned to Br or I atoms from three-body dissociations reveals the products have a parallel angular distribution. In the horizontal electric vector TOF spectra (Fig.'s 43a and c) the slower broad signal is decreased at 600 μsec where the products must recoil at 110° (90° + 20°) with respect to the electric vector. The decrease is obvious upon comparison with the unpolarized light TOF spectra in Figures 35 and 38 where anisotropy does not affect the shape of the TOF spectra. The distributions of translational energies imparted to the atomic fragments derived from the unpolarized data were used to fit the polarized light data; only the anisotropy parameter β was varied to abtain a best fit. The fit shown to the slow Br^+ signal in Fig 43a and b was obtained with an anisotropy parameter of $\beta = 0.65$. The fit shown to the slow I^+ signal from three-body dissociation was obtained with $\beta = 1.0$.

2. Polarization Dependence of $CH_2BrI \xrightarrow{210} CH_2I + Br$ (16)

The TOF spectra of m/e = 141, CH_2I^+, with horizontally and vertically polarized light are shown in Fig. 44. Most of the product recoils with such large c.m. velocities which are detected in such a small range of c.m. angles at this source to detector angle that the shape of the TOF at 20° is not very sensitive to the anisotropy. A polarization dependence can be obtained, however, by inspection of the Br atom signal intensity relative to the slow broad three-body Br atom signal analyzed above. The signal intensity as well as the shape depends on the anisotropy of the angular distribution so a β may be derived from fitting the relative intensities as a function of polarization of the fast Br^+ signal with unknown β and the slow Br^+ signal with β derived from the change in shape of the TOF. The fits shown to the fast peak in the Br+ spectra of Fig. 43 were obtained with a β of 0.6 for C-Br fission. The fits to the CH_2I^+ TOF spectra of Fig. 44 were calculated from the $P(E_T)$ for C-Br fission of Fig. 36 and the $\beta = 0.6$ thus derived.

3. Polarization Dependence of $CH_2BrI \xrightarrow{210} CH_2 + IBr$ (19)

The IBr^+ TOF spectrum at 10° taken with horizontally polarized light is shown in Fig. 45. The velocities of IBr in the c.m. are so small that, when they are summed with the range of parent velocities in the beam, an arrival time in the TOF spectra corresponds to a widened range of c.m. recoil angles. Thus the shape of the TOF is only weakly

dependent on any anisotropy in the dissociation. The dashed and chain-dashed curves fit to the IBr^+ spectra in Fig. 45 are curves obtained from limits on the anisotropy parameter for IBr elimination. The anisotropy for IBr elimination is thus shown to lie in the range $0.8 > \beta \geq -1.0$.

DISCUSSION

I. Summary of Primary Experimental Results

Although several chemically distinct dissociation reactions, including C-Br and C-I bond fission and IBr, HBr, and HI elimination, are energetically allowed via excitation of CH_2BrI at all three wavelengths,[1] the dissociation channels that result are few and specific to the excitation wavelength. At 248 nm, only C-I and C-Br bond fission occur, with C-I bond fission dominant by a ratio of more than 1.2 to 1. The C-I bond fissions produce both spin-orbit states cf iodine with the same polarization dependence in a ratio of $^2P_{3/2}:^2P_{1/2}=1.0:0.75$. The anisotropy of the recoil of the I and Br atoms are each from a parallel transition with β equal to 1.0 and 0.6 respectively. The results at 248 nm are interpreted in terms of the excitation being in a region where the $n\rightarrow\sigma^*$ transitions of I and Br respectively overlap. At 193 nm, three dissociation channels occur, C-Br bond fission, C-I bond fission and IBr elimination. The bond fissions resulting from excitation at 193 nm produce halogen atoms primarily (perhaps exclusively) in

the spin-orbit excited $^2P_{1/2}$ state. The C-Br bond fissions dominate C-I bond fission by a ratio of 3.5:1. The concerted reaction also apparently produces exclusively electronically excited IBr in the $^3\Pi_1$ and perhaps higher electronic states. The recoil of all the primary fragments are isotropic with respect to the electric vector of the light, suggesting they all result from excitation to an I atom Rydberg level which is predissociated on a time scale which is long with respect to the rotational period of CH_2BrI. Excitation at 210 nm, which is assigned to a n(Br) $\rightarrow$ σ^*(C-Br) transition, results in primary C-Br fission but no primary C-I bond fission. IBr elimination to produce probably exclusively electronically excited IBr also occurs. Dissociation to CH_2 + I + Br is energetically allowed and occurs at the two shorter wavelengths; whether this occurs as a very fast two step process or as a three body dissociation is not certain. The experimental results are summarized in Table 2.

II. Bond Selective Excitation and Evolution to Bond Selective Fission of the C-Br Bond over the Weaker C-I Bond in CH_2BrI

The possibility of inducing specific dissociation or isomerization pathways in a molecule by varying the nature of the initial excitation has been of interest of many workers in the field of photochemical and unimolecular reaction dynamics. For the dissociation of vibrationally excited molecules in the ground electronic state, theories[24] in which the energy in vibrations and active rotations of the molecule is assumed

to be distributed statistically throughout the molecule are extremely successful in modelling experimental results. Elegant selective excitation studies of unimolecular reaction dynamics in which vibrational energy is deposited into a particular local C-H stretch in the molecule[25] have shown that, at the low energies studied, vibrational energy redistribution occurs on a time scale fast with respect to isomerization or dissociation rates, so overall rates and branching ratios between dissociation pathways are successfully predicted with statistical theories. Dissociation pathways following electronic excitation of a molecule, however, are shown in this work to be critically sensitive to the electronic nature of the initial excitation and not just the energy of the exciting photon.

If one deposits energy in CH_2BrI by, for instance, heating it slowly, the weakest bond in the molecule, the C-I bond, will break preferentially. Branching ratios at a particular excitation energy E are determined from the ratio of the dissociation rate constants, approximately $k=A\cdot\exp(-E_a/E)$. The preexponential factor A for simple bond fission reactions are similar so the activation energies, E_a, which are roughly in this case the C-X bond energies, would determine the branching ratio between C-I and C-Br bond fission. C-I bond fission would dominate at low excitation energies. At extremely large excitation energies the relative amounts of C-Br to C-I fission would reach at most roughly 1:1. Photochemistry texts have generalized the results of previous experiments on the primary photodissociation pathways of polyhaloalkanes at excitation wavelengths $\geq$2000 Å as "the dominant split in the photolysis ruptures the weakest C-halogen bond",[2]

implying that the results might be similar to thermal decomposition. However, excitation in this region is to $n \rightarrow \sigma^*$ states which are purely repulsive in the respective C-halogen bond. Dissociation lifetimes have been estimated from the anisotropy of product angular distributions to be much less than a picosecond. The concept of statistical distribution of energy in the molecule on such a short time scale is not reasonable. Thus, contrary to a statistical description, the experimental results show excitation of CH_2BrI at 210 nm of a transition assigned to $n(Br) \rightarrow \sigma^*(C-Br)$ results in C-Br fission but no primary C-I fission to form $CH_2Br + I$.

The previous photolysis experiments which led to the conclusion that the weakest C-halogen bond ruptures preferentially are easily reinterpreted on the basis of selective fission of the C-X bond corresponding to the particular $n(X) \rightarrow \sigma^*(C-X)$ transition excited. The absorption band corresponding to these transitions for X=Cl or F do not peak until the vacuum ultraviolet region. The twelve[26] molecules studied have C-Br and C-Cl bonds, C-F and C-Br bonds, and C-F and C-I bonds in the same molecule; however no system was studied in which C-Br and C-I bonds were both present. At wavelengths $\geq$2000 Å the $n(Cl) \rightarrow \sigma^*(C-Cl)$ transition is expected to be at least an order of magnitude weaker than the corresponding C-Br or C-I transition. The weakest bond broke in these molecules because the $n \rightarrow \sigma^*$ transition for that bond was the one with oscillator strength at wavelengths >2000 Å. This picture is consistent with the interpretation given by Bersohn of his recent experimental results on CH_2BrI[3] irradiated primarily in the

$n(I)\rightarrow\sigma^*(C-I)$ absorption band. Here he attributes his small fraction of C-Br fission to the photolysis bandwidth partially overlapping the $n(Br)\rightarrow\sigma^*(C-Br)$ transition.

Still, the picture is oversimplified, as is evident from the results of the photodissociation experiment of 1,2-C_2F_4BrI by Krajnovich et al.[4] and the occurrence of the IBr elimination channel in addition to the C-Br bond fission channel in CH_2BrI excited at 210 nm. One might begin to think about these differences as follows. The similarity in the positions and shapes of the absorption bands, despite the dissimilarity in intensities, of CH_2BrI (or C_2F_4BrI) to the corresponding features in the spectrum of CH_3I (or C_2F_5I) and CH_3Br (or C_2F_5Br) give plausibility to the assignment of the transition as still being local. The spectra do not show the broadening and splitting found in the spectra of CH_2I_2 and CH_2Br_2 when the unperturbed σ^* orbitals of the C-X bonding lie at the same energies so mix and split. Given the truth of the resulting assumption that one is exciting essentially a $n(Br)\rightarrow\sigma^*(C-Br)$ transition in CH_2BrI at 210 nm and in 1,2-C_2F_4BrI at 193 nm, any processes other than C-Br fission must be the result of intramolecular energy transfer that is fast enough to compete with the rapid C-Br bond dissociation. The formation of IBr from CH_2BrI might result from the predissociation of the $n(Br)\rightarrow\sigma^*(C-Br)$ state by one that correlates to excited state IBr (see Discussion Section D below). It probably is not the result of internal conversion to the ground state because dissociation of vibrationally excited ground state CH_2BrI should give an overwhelmingly high fraction of C-I fission relative to

IBr elimination. That the n(Br)→σ*(C-Br) state of 1,2-C_2F_4BrI is not also predissociated to form some IBr follows easily from the geometric separation of the I and Br atoms in that molecule. However, the other difference in the dissociation pathways of the two bromo-iodo compounds is not so simply explained. The observation of an effect described as fast intramolecular electronic energy transfer occurring in 1,2-C_2F_4BrI at 193 nm, leading to a 1.7:1 ratio of C-I:C-Br fission, but not occurring in CH_2BrI at 210 nm warrants more careful inspection.

The mechanism for the fast intramolecular electronic energy transfer in 1,2-C_2F_4BrI from the initial n→σ* excitation on the C-Br bond to one on the C-I bond is not certain, but several clues can be inferred from the experimental results. The anisotropy of the products is parallel, β=1.8, so assuming the initial excitation is correctly assigned as a n(Br)→σ*(C-Br) local excitation (as indicated by the absorption spectrum's similarity in that region to C_2F_5Br) we know the initial transition moment is parallel to the C-Br bond. The translational energy distribution of the I atom product following the intramolecular energy transfer is fast and narrow, indicating the C-I bond stretches on an electronic surface that is repulsive in the C-I bond. In addition, the present results on CH_2BrI have indicated that the fraction of the total available energy (corrected by subtracting off any energy in spin-orbit excitation of I or Br product) partitioned to translation is the same for C-I fission as it is for C-Br fission at each wavelength (~0.3 at 248 nm for C-I or C-Br fission and 0.2 at 193 nm for C-I or C-Br fission). This result indicates that the I atoms and the Br atoms

from 1,2-C_2F_4BrI at 193 nm are probably both spin-orbit excited, as only then is the partitioning to translation the same in both fissions, f=0.37 (see Table 3 of Ref. 4). A repulsive surface that could correlate to $I(^2P_{1/2})$ products is the $^3Q_0$ surface on the C-I bond. Thus we have a fast intramolecular electronic energy transfer from the repulsive $^3Q_0$ n(Br)→σ*(C-Br) surface to a repulsive surface on the C-I bond, possibly the $^3Q_0$ (C-I) surface. The energy transfer must be fast enough to compete with the dissociation of the C-Br bond.

An obvious model for such an energy transfer was suggested in Ref. 4 and will be clarified here. It was stated that as the C-Br bond stretches along the repulsive electronic surface, some of the electronic energy will be converted into kinetic energy of nuclear motion associated with C-Br separation. At some C-Br separation, the electronic energy still remaining localized on the C-Br bond will become equal to the energy required to excite the n→σ* transition on the C-I bond and a near resonant electronic energy transfer could occur. The new state would roughly consist of a locally electronically excited C-I bond and a vibrationally excited C-Br bond. The question of what interaction would lead to such an energy transfer immediately comes to mind. Two interactions which have been extensively studied in terms of electronic energy exchange between molecules or atoms are an electron exchange interaction and a dipole-dipole interaction.[27] The C-I and C-Br bonds are spatially separated in 1,2-C_2F_4BrI, so the short range electron exchange interaction is probably not indicated, but a dipole-dipole interaction is a strong possibility. The requirement that both transitions, the σ*(C-Br)→n(Br) and the n(I)→σ*(C-I) transition, are dipole

allowed is met. The transition moments are roughly parallel in 1,2-C_2F_4BrI (if the transfer is to the $^3Q_0$(C-I) state as discussed); this parallel orientation particularly favors the dipole-dipole transition. Dipole-dipole electronic energy exchange is known to be extremely efficient in some cases with cross sections on the order of 1000 $Å^2$.[27] Whether such a dipole-dipole electronic energy exchange could be fast enough to compete with C-Br dissociation is discussed below.

A crude calculation was made to assess the time required for a dipole-dipole transition from the σ^*(C-Br) surface to σ^*(C-I) surface to occur. We look at the interaction, V, between the electrons in the dipole transitions as:[27]

$$V = \frac{\mu_1\mu_2}{r^3}\underbrace{[-2\cos\theta_1\cos\theta_2 + \sin\theta_1\sin\theta_2(\cos\theta_2 - \cos\theta_1)]}_{K} \qquad (20)$$

Because the C-I and C-Br bonds are fixed at a certain distance in the molecule, analogy was made to Forster energy transfer and V was assumed to be constant over the time for which the electronic energy left over in the stretching C-Br bond was equal to the energy region to excite the $n\rightarrow\sigma^*$(C-I) transition (a gross approximation). The golden rule formula can then be used[27]

$$k_{if} = 2\pi\hbar^{-1}\left|V_{if}\right|^2\rho$$

where k_{if} is the transfer probability per unit time and ρ is a measure of the overlap of the emission frequencies of the C-Br deexcitation to

the absorption frequencies of the C-I excitation. Taking r as 4.6 Å, the distance between the halogens in C_2F_4BrI, calculating μ_1 and μ_2 from the integrated absorption cross sections of each of the transitions in the molecule at the equilibrium geometry, calculating the angular factor to be K=2 as the transition moments are roughly parallel, and taking the overlap ρ as equal to the $(FWHM)^{-1}$ of the $n(I)\rightarrow\sigma^*(C-I)$ absorption band of $(\frac{10,000}{2}\ cm^{-1})^{-1}$ we obtained a transfer rate of $k_{if} = 1.5x10^{11}$ transitions/sec. Thus if the C-Br bond takes on the order of a picosecond to stretch through the region where the electronic energy in the C-Br excitation is equal to the energy required to excite to the repulsive C-I surface, the energy transfer can take place and C-I fission can result from an initially local C-Br excitation.

This model is encouraging in terms of the strength of the dipole-dipole interaction of two separate bonds, but it is difficult to extend it to the case of CH_2BrI to explain why the intramolecular electronic energy transfer does not occur in this system, thus allowing us to selectively dissociate the C-Br bond over the C-I bond. The angular factor in the dipole-dipole interaction would strongly inhibit the transfer in CH_2BrI as the angle between the C-Br and C-I bonds (to which the respective transition moments with the largest magnitude are parallel) is strongly bent in CH_2BrI and would get close to 90° as the Br recoiled from C. However, the distance between the I and Br is much closer; if one attempted to use the $1/r^3$ approximation to obtain V, the closer distance would completely overwhelm the angular factor in

favor of transfer in CH_2BrI. In fact, it is not clear that the interaction in CH_2BrI is at all well described by eqn. 20 as the $1/r^3$ dependence relies on the assumption that the distance between the two transition dipoles is large. We are left with no clear indication of why the electronic energy transfer does not occur in CH_2BrI but does occur in $1,2\text{-}C_2F_4BrI$.

III. Transitions at the Curve Crossing Between Two Electronic States Repulsive in the C-I Bond

This section will first review how a measurement of the $I(^2P_{3/2}):I(^2P_{1/2})$ product branching ratio provides a measurement of the probability of transition between two repulsive curves in CH_2BrI. Then it will briefly examine several models for this transition probability as they have been proposed to explain the results on curve crossing in a number of iodo and perfluoro-iodo-alkanes.

In a simple molecular orbital description based on comparison of the CH_2BrI spectrum with CH_3I and CH_3Br, excitation of CH_2BrI at 248 nm may either promote a nonbonding electron on the I atom to an antibonding orbital on the C-I bond or, presumably in a smaller fraction of the molecules, promote a nonbonding electron on the Br atom to an antibonding orbital on the C-Br bond. Both the Br atom signal and the I atom signal show a parallel angular distribution with respect to the polarization vector of the dissociating light, indicating that the dipole moment of the transition resulting in C-Br fission is roughly parallel to the C-Br bond and the dipole moment of the transition resulting in

C-I fission is roughly parallel to the C-I bond. It is postulated that the decrease in anisotropy from a perfect value of $\beta = 2$ results from I-C-Br bending and CH_2BrI rotation during dissociation. With this assumption, one can use the parallel anisotropy to identify the particular repulsive states to which the molecule is excited. Because of the apparent additivity of the absorption spectra, one feels confident in making an analogy to the respective transitions in CH_3Br and CH_3I. Mulliken first discussed the $n \rightarrow \sigma^*$ transition in halomethanes in detail.[28] Under strong spin-orbit interaction the $n \rightarrow \sigma^*$ transition is split into five components (see Figure 46) of which transitions to three are dipole allowed from the ground state. These three states were denoted $^1Q_1$, $^3Q_0$, and $^3Q_1$ by Mulliken. Excitation to the $^1Q_1$ or $^3Q_1$ surfaces are via a dipole transition moment perpendicular to the C-halogen bond ($\Delta\Omega = 1$) and excitation to the $^3Q_0$ state is via a dipole transition moment parallel to the C-halogen bond ($\Delta\Omega = 0$). Mulliken shows that the $^1Q_1$ and $^3Q_1$ states should correlate to $R + X(^2P_{3/2})$ and the $^3Q_0$ state should correlate to $R + X(^2P_{1/2})$. Because the $^1Q_1$ state is expected to be higher in energy than the $^3Q_0$ state at the initial R-X bond distance following a Franck Condon excitation and is shown to correlate to lower energy products than the $^3Q_0$ state, the diabatic $^3Q_0$ and $^1Q_1$ curves must cross[29] (in this quasidiatomic model). Possible transition at the curve crossing promoted by spin-orbit coupling will result in some ground state products when only the $^3Q_0$ component is initially excited.

For C-I bond fission at 248 nm, both the $I(^2P_{1/2})$ and $I(^2P_{3/2})$ products are determined to have exactly equal (±0.1) and parallel (β = 1.0) angular distributions, leading one to the inference that both channels result from initial excitation solely to the $^3Q_0$ state. This assumption is supported by the fact that if the reduced value of the anisotropy from $\beta = 2$ were due to initial excitation of some parallel and some perpendicular transition, and not merely smearing of a purely parallel absorption via bending vibrations and rotations of the parent molecule, one would expect the ground state I atom channel to have a more perpendicular angular distribution than the spin-orbit excited I atom channel. Given then that the initial excitation is to the $^3Q_0$ state, the C-I bond stretches from the repulsive force on the $^3Q_0$ potential energy surface until the crossing point of the $^3Q_0$ and $^1Q_1$ curves is reached. Some of the molecules undergo a crossing to the $^1Q_1$ surface and give $CH_2Br + I(^2P_{3/2})$ while some proceed along the $^3Q_0$ surface and give $I(^2P_{1/2})$. Thus a measure of the $I(^2P_{3/2})$ to $I(^2P_{1/2})$ product branching ratio provides an exact measurement of the probability of transition between the two repulsive electronic states at the curve crossing. An analogous picture was originally used to discuss branching ratios between different halogen product spin-orbit states in the photodissociation of heteronuclear diatomic halogen molecules.[30]

Measurement of the $I(^2P_{3/2})$ to $I(^2P_{1/2})$ product branching ratios in the ultraviolet photodissociation of alkyl and perfluoroalkyl iodides are numerous, but many techniques are plagued by quenching of the spin-

orbit I atom excitation by collisions with other molecules. Two very different techniques have yielded particularly reliable branching ratios which agree with each other to within a few percent, the laser-induced fluorescence technique of Bersohn[31] and the crossed laser-molecular beam technique for systems in which the $I(^2P_{1/2})$ and $I(^2P_{3/2})$ peaks are at least partially resolved in the TOF spectra (see Ref. 8-10). The results of several of these studies are shown in Table 3. A variety of qualitative and semiquantitative models have been used to explain $I(^2P_{1/2})$ to $I(^2P_{3/2})$ branching ratios. These may be critically examined in relation to the tabulated experimental results.

The Landáu-Zener formula for the transition probability between states in a diatomic molecule has been used by Van Veen[32] to rationalize the differences in probability of transition at the curve crossing between the $^3Q_0$ and $^1Q_1$ states in CH_3I compared to CH_3Br. While the probability of the $^3Q_0 \rightarrow {}^1Q_1$ transition is 0.3 for CH_3I, they found that no transition at the curve crossing occurs for CH_3Br excited at 193 or 222 nm. The CH_3Br molecules that absorbed via a parallel transition (to the $^3Q_0$ surface) produced exclusively $Br(^2P_{1/2})$ and those that absorbed via a perpendicular transition (to the $^1Q_1$ surface) produced exclusively $Br(^2P_{3/2})$. The probability of an adiabatic crossing between two curves a and b, or equivalently the probability of a transition from a diabatic curve 1 to a diabatic curve 2 at the curve crossing is derived by Zener[32,33] as:

$$P = 1 - \exp\left(\frac{-2\pi H_{12}}{h\nu(F_2-F_1)}\right)$$

where H_{12} is the coupling matrix element between the two diabatic curves, F_x is the slope of the diabatic potential curve x, and v is the relative velocity of the two atoms in this diatomic model at the C-I distance corresponding to the point at which the potential curves cross. Van Veen obtains a numerical ratio for the transition probability in CH_3Br versus CH_3I by letting the ratio of H_{12}'s for the two systems be equal to the ratio of the spin-orbit splitting of the isolated halogen atoms and letting the ratios of the relative velocities v at the curve crossing be the same as the ratio of the final asymptotic relative velocity of CH_3 and Br or I derived from the TOF spectra. (They assume F_2-F_1 to be equal for both systems.) In this way they derive a transition probability of 0.06 for CH_3Br from a probability of 0.30 for CH_3I.

Although Van Veen's approximate application of the Landau-Zener formula to rationalize the difference in transition probability for CH_3Br versus CH_3I gives a reasonable result, one immediately sees that if one applies his method to CD_3I versus CH_3I you would predict an opposite trend in the I:I* branching ratio than what is observed. Under the quasidiatomic modelling of Van Veen, H_{12} and F_2-F_1 must necessarily be the same for CH_3I and CD_3I, only v would differ. If one uses the final relative velocities of CH_3 and CD_3 and I as Van Veen did to estimate the relative velocity at the curve crossing, one would predict that the probability of curve crossing is greater for CD_3I than for CH_3I when in fact it is considerably smaller, 0.19 versus 0.30. Clearly a quasidiatomic picture is not at all the whole story.

Donohue and Wiesenfeld[34] correlated the I*:I branching ratio trend with the ionization potential of the alkyl group of the RI molecule. They observed that the higher the ionization potential of R, the higher the yield of $I(^2P_{1/2})$ in their flashlamp photolysis studies of alkyl and perfluoroalkyl iodides. They propose a model in which the $^3Q_0$ (A_1* in their C_{3v} notation for CH_3I) mixes with another state in the triplet manifold, A_2, which is inaccessible via electric dipole transition from the ground state. Because A_2 correlates to ground state products, the mixing results in a lower yield of $I(^2P_{1/2})$ products. They point out that the A_1* and A_2 states are degenerate in the absence of spin-orbit coupling, so the smaller the spin-orbit interaction the <u>more</u> the mixing and the lower the I* yield. They then suggest that if the R group has a low ionization potential there will be some R^+I^- character to the states and that since the $I^-(^1S_0)$ configuration contributes no spin-orbit interaction to the wavefunction the spin-orbit splitting between the A_1* and A_2 states will be reduced and the mixing greater. Although this model allowed them to roughly rationalize their experimental data, it is clear that the spin-orbit splitting between the A_1* and A_2 states in CH_3Br must be less than that in CH_3I, yet the yield of $Br(^2P_{1/2})$ atoms from the $^3Q_0$ (A_1*) portion of the excitation is ~100%[86], so Weisenfeld's presumption that less spin-orbit splitting in the ^3Q (^3E) manifold results in a lower $^2P_{1/2}$ halogen atom yield is erroneous. The state which provides the path to $I(^2P_{3/2})$ must not be in the same ^3E manifold as the initially excited $^3Q_0$ state; the $^1Q_1$ state previously suggested is the obvious candidate.

It remains now to be understood why the fluorinated alkyl iodides, where R has a higher ionization potential, have a larger yield of $I(^2P_{1/2})$ when the $^3Q_0$ component is excited and thus a less strongly coupled crossing between the $^3Q_0$ and $^1Q_1$ staes. The results for CH_3Br vs CH_3I[8b] show the greater the spin-orbit interaction (as in RI over RBr) the greater the mixing of the two states correlating respectively to $R + I(Br)(^2P_{1/2})$ and $R + I(Br)(^2P_{3/2})$ will mix and the lower the yield of $I(^2P_{1/2})$ from an initial $^3Q_0$ excitation. This would lead one to presume that the low yield of $I(^2P_{1/2})$ from RI molecules with low R group ionization potential results from a greater effective spin-orbit interaction, not a lower effective spin-orbit interaction postulated by Weisenfeld. The change in the effective spin-orbit interaction with ionization potential of R in RI has been previously discussed by Leone,[5] but the discussion seems to ignore one crucial point. Leone postulates that in the $n\rightarrow\sigma^*$ transition, the spin-orbit interaction induced by the unpaired n electron remaining on the halogen atom is modified by the extent to which the excited σ^* electron is localized near the I end of the C-I bond. They conclude that the electron donating groups, such as ethyl, localize the σ^* orbital toward I and "neutralize" the unpaired spin density on the I atom, reducing the spin-orbit interaction with concomitant reduction in the quantum yield of $I(^2P_{1/2})$. They omit the fact that in the case of excitation to a triplet surface, localization of the σ^* electron, which now has the same spin as the unpaired n electron, toward the I end of the C-I bond

would not neutralize the unpaired spin density on the I atom, it would augment it. One should thus conclude the reverse of Leone and Weisenfeld; the lower the ionization potential of R, the greater the effective spin-orbit interaction is and the lower the quantum yield of $I(^2P_{1/2})$. The greater the spin-orbit interaction the more the terms in the ^3Q manifold would split and the more the $^3Q_0$ surface would be coupled to the $^1Q_1$ surface which correlates to ground state product. An additional potentially relevant contribution to curve crossing probabilities was suggested by Child and Bernstein in their study of transition probabilities in heteronuclear diatomic halogen molecules in which they proposed that the coupling matrix element is reduced by "the effective quenching of the spin-orbit coupling by the electrostatic field of the second atom".[30]

Bersohn[31] points out that a large difference in the upper electronic states of C_2H_5I, $n\text{-}C_3H_7I$, and C_4H_9I is unlikely but that the branching ratio does decline from .68 to .60 to .53. He proposes that this may be explained if the high frequency C-H stretching is an effective acceptor mode. The trend may also clearly be predicted with the Landau-Zener formula. The iodine recoils more slowly from the radical as the size of the radical increases, so the branching ratio would be correctly predicted to decrease down the series assuming the velocity at the crossing point decreases as the asymptotic R and I velocities do.

Still the difference between the I*:I ratio in CH_3I vs CD_3I has not been rationalized. Because the CH_3 (CD_3) umbrella mode is excited as the I atom begins to recoil from the C atom,[8a,b] the trend might be

rationalized by the assertion that the overlap of the ν_2 bending states is better for CH_3I than for CD_3I. Because of the closer vibrational spacings of the CD_3 bands, Franck Condon factors may not favor the transitions between the surfaces in CD_3I because overlap of states of higher vibrational quantum number of the CD_3 mode is smaller than in the lower vibrational quantum number states of CH_3. This explanation is loosely related to Bersohn's general proposal[31] that the number and nature of the vibrational modes could affect the transition rate between the two repulsive surfaces.

Using a combination of 1) the Landau-Zener theory, where H_{12} is dependent on the spin-orbit splitting of the halogen atom and the quenching of the spin-orbit coupling by the higher ionization potential of the R groups and when the transition probability is dependent on the relative velocity of R and I at the curve crossing and 2) the requirement of Franck Condon overlap on the alkyl group, one can roughly rationalize the experimental data summarized in Table 3. In addition, because in CH_2BrI the fragments separate with such a large orbital angular momentum in the half collision (see Ref. 19 Appendix 2) that angular momentum may also help to couple the Ω=0 and Ω=1 states via orbit rotation coupling,[35] resulting in that molecule's very large probability for transition at the curve crossing. Such qualitative explanations where there are competing effects of uncertain magnitude are not wholly satisfactory, however. A rigorous treatment of the curve crossing probability in the RI molecules, with the availability of a variety of reliable data on related but different systems as test cases, awaits theoretical attention.

IV. Concerted Elimination of Electronically Excited IBr from CH_2BrI at 210 and 193 nm

The product translational energy distributions for the formation of IBr + CH_2 at both 210 and 193 nm cut off sharply at energies corresponding to the total available energy if only electronically excited, not ground state, IBr were formed in the concerted reaction. In addition, no concerted reaction occurred following excitation at 248 nm. Formation of ground state IBr + CH_2 is energetically allowed at 248 nm, but formation of electronically excited IBr($^3\Pi_1$) is not. These two experimental results lead us to the conclusion that the electronic states of CH_2BrI resulting from excitation that is assigned as promotion of a nonbonding p electron on the I atom to a higher s Ryberg level and from excitation assigned as promotion of a nonbonding p electron on the Br atom to an antibonding orbital on the C-Br bond are not predissociated by a state which correlates to ground state IBr, they are predissociated by a state which correlates specifically to electronically excited IBr (hereafter referred to as IBr*).

The result that only IBr*, not IBr, is formed from electronic excitation of CH_2BrI may shed light on previous experimental results on CF_2Br_2 and CH_2I_2. Although Krajnovich et al.[13] found that no concerted elimination of Br_2 occurred from CH_2Br_2 following excitation at 248 nm, an older experiment by Simons and Yarwood[36] indicated that Br_2 was formed when CF_2Br_2 was irradiated with light extending down to wavelengths of 2000 Å. Leone and coworkers[5] and Style and Ward [37]

detected fluorescence of I_2 after photolyzing CH_2I_2 at 193 nm. Broad-band photolysis experiments reviewed briefly in ref. 2a report concerted elimination of Br_2, FBr and Cl_2 from a variety of polyhalomethanes at short wavelengths, but the electronic states of the diatomic fragment is not identified. It appears that concerted elimination of X_2(X_2=Br_2, I_2 or IBr) from the substituted methanes following photoexcitation in the UV may produce exclusively electronically excited X_2, and cannot occur when the photon energy is too small to produce electronically excited X_2.

The experimental result that exclusively electronically excited IBr($^3\Pi$) is produced in the concerted reaction is consistent with a simple LCAO-MO description of the dissociation in which the reaction proceeds along a least motion path and spin is conserved. The evolution of the reaction under this model is shown in Fig. 47. Following the excitation, the C-Br coordinate is repulsive and the C-Br bond will stretch; the CH_2I portion of the molecule will rotate to reduce the Br-C-I angle as the C recoils from Br, better aligning the orbitals labelled as p_z on the halogen atoms which will combine to form σ and σ^* orbitals of IBr. One immediately sees there are three electrons in the two p_z orbitals; when the IBr product is formed one of these electrons will be forced to the σ^*(IBr) orbital. Thus no ground state IBr may be formed along this least motion path. Only electronically excited IBr may be formed, consistent with our experimental results. The model is readily applied to the photodissociation of CH_2I_2 and CH_2Br_2. This would explain why Br_2 elimination was not observed at

248 nm[4] but was observed at shorter excitation wavelengths[36] and it suggests that the I_2 fluorescence observed by Leone[5] and by Style and Ward is representative of all the I_2 formed in the reaction. The first group[5] suggested study of the $I_2(B)$ and $I_2(X)$ channels; this model shows the $I_2(X)$ channel probably does not occur.

The model suggests an interesting possibility. If the electron spin is conserved after the excitation during the evolution of the reaction, then only a ^1Q excitation can correlate to $CH_3(^3B_1)$ + $IBr(^3\Pi_1)$. The $^3Q_0$ excitation may only correlate to one triplet and one singlet product. One might postulate then that excitation to the ^1Q surface results in IBr elimination and excitation to the ^3Q surface results in C-Br fission (the lowest energy elimination path not being spin allowed). This hypothesis is consistent with the parallel angular distribution of the Br atom from C-Br bond fission because excitation to the $^3Q_0$ surface is via a transition moment parallel to the C-Br bond. In this case the branching ratio between C-Br fission and IBr elimination might be controlled by tuning the excitation wavelength through the $n(Br)\rightarrow\sigma^*(C\text{-}Br)$ absorption band where the oscillator strengths of the $^1Q_1$ and $^3Q_0$ transitions would vary. One would also expect that all the Br atoms would be formed in the $^2P_{1/2}$ spin-orbit excited state.

V. Product Energy Partitioning in the Simple Bond Fission Channels

The simple bond fission reactions resulting from the UV excitation of CH_2BrI in this work occur via electronically excited surfaces which are repulsive in the respective C-X bond. Even the excitation at 193 nm is to a Rydberg state which is predissociated by repulsive electronic surfaces (see Ref. 8b). Breaking of a C-X bond on such a repulsive surface is amenable to modelling with very simple classical impulsive force expressions.[39] Particularly at the higher energy excitation wavelengths where the repulsive potential is very steep, one would expect an impulsive force approximation to be good. The partitioning of the total available energy, with any electronic energy in the products subtracted from it, to translational, rotational, and vibrational energy may be predicted under one of two very simple impulsive force models originally suggested by Wilson.[39] Derivations of the expressions for energy partitioning in the soft radical and hard radical impulsive models are outlined in Appendix 1; it was found that the expression for partitioning between vibration and rotation given by Wilson is dependent on there being no geometry changes in the radical formed. A more general expression is derived in this work. Appendix 2 presents the specific calculations for CH_2BrI. The soft radical impulsive model predicts that 20.3% of the available energy is channeled to translation in C-I fission and 20.4% is channeled to translation in C-Br fission. The experimental results shown in Table 2 show that the soft radical model correctly predicted the average fraction of the energy

partitioned to translation in C-X fission at the 193 nm excitation wavelength. At the lower excitation energies the portion of the repulsive potential reached is not so steep and the heavy X atom recoils away not just from the light carbon atom, but from the whole radical, resulting in a larger fraction of the energy being partitioned to translation.

The calculations presented in Appendix 2 also suggest that the rotational excitation of the CH_2I or CH_2Br fragments is quite large, ~54% of the total available energy in the soft radical approximation. Unlike many previously studied haloalkanes such as CH_3I, CF_3I, C_2F_5I, or CH_3Br, bond fission in CH_2BrI occurs with the fragments leaving each other at a large impact parameter, resulting in the radical having rotational energies predicted to be as great as 37 kcal/mole for CH_2I from the C-Br fission observed at 193 nm. Whether the orbital motion of the separating collision partners can couple effectively with the molecule's spin and orbital angular momenta and affect the dissociation pathway is an interesting question and was briefly mentioned in Section III of the discussion in reference to the production of ground or spin-orbit excited I atom product at 248 nm.

Finally, consideration of the constraint on the exit impact parameter imposed by conservation of energy and angular momentum provides a partial explanation for our observation of such reduced values of the anisotropy β for C-I and C-Br fission at 248 nm following presumed purely parallel excitations. In a classical picture, when two fragments depart with exit impact parameter b and relative translational energy E_T, conservation of angular momentum requires that

$$E_{rot} = \frac{1}{2} I\vec{\omega}^2 = \frac{1}{2} \frac{|\vec{L}|^2}{I} = \frac{1}{2} \frac{\mu^2 \vec{v}_{rel}^{\,2} b^2}{I} = E_T \frac{\mu b^2}{I}$$

where μ is the reduced mass of the two fragments and I is the moment of inertia of the radical R formed in dissociation to R + atom X. Since the sum of the rotational and translational energies must be less than or equal to the total available energy one easily derives that

$$b \leq \frac{I}{\mu} \left(\frac{E_{avail}}{E_T} - 1 \right)^{1/2}$$

For C-I bond fission in CH_2BrI at 248 nm where 12.5 kcal/mole is released to translation, near $\overline{E}_T$, and $I(^2P_{1/2})$ is formed, the exit impact parameter must be $\leq$ 1.26 Å (I for CH_2Br is taken as 45.53 $Å^2$ g/mol). The equality is only realized if $E_{vib} = 0$. If the molecule dissociated from its equilibrium configuration with a repulsive force along the C-I bond the exit impact parameter would be much greater, ~1.5 Å. Thus, to undergo C-I fission to $CH_2Br + I(^2P_{1/2})$ with 12.5 kcal mol in translation the molecule must distort significantly during dissociation, resulting in a reduced anisotropy in the angular distribution of the scattered product following an absorption parallel to the C-I bond.

APPENDIX 1.

Impulsive Force Models for Dissociation Dynamics.

A. Recoil of X from a Rigid Radical R.

For completeness, a very simple derivation of the classical formula for energy partitioning in the fragmentation of polyatomic molecules under the rigid radical impulsive model is given here. The formula resulting has been stated previously by Wilson, but no explicit derivation was given.

If an atom X recoils from a rigid radical R, conservation of energy dictates:

$$E_{avail} = E_{rot} + E_{vib} + E_{trans}$$

The assumption of a rigid fragment => $E_{vib} = 0$ so

$$E_{avail} = 1/2\ I\ \vec{\omega}^2 + 1/2\ \mu\ \vec{v}_{rel}^{\,2} \qquad (1)$$

where:

$\vec{\omega}$ is the angular velocity of the rotating R fragment,

I is the moment of inertia about the axis the R fragment is rotating, and

$\vec{v}_{rel}$ is the final relative velocity of X and the c.m. of R.

If the initial RX molecule is not rotating and electrcnic angular momentum is neglected, the initial angular momentum of the system is zero. The final angular momentum, the sum of the orbital angular

momentum of X leaving the c.m. of R with impact parameter b and the rotational angular momentum of the R fragment, must be zero:

$$0 = \mu \vec{v}_{rel} b + I \vec{\omega} \tag{2}$$

With the fact that the dissociation occurs with an impulsive force between X and the atom it is bonded to in R and with the assumption the excitation obeys the Franck Condon principle, one can determine the direction of v_{rel} as along the bond connecting X to R and, thus, the magnitude of b from the ground state equilibrium geometry of RX. With $(I\omega)^2 = (\mu v_{rel} b)^2$ from 2, one can rewrite (1) trivially as:

$$E_{avail} = \frac{1}{2} \frac{(\mu \vec{v}_{rel} b)^2}{I} + \frac{1}{2} \mu \vec{v}_{rel}^{\,2}$$

$$E_{avail} = \frac{1}{2} \mu \vec{v}_{rel}^{\,2} \left(1 + \frac{\mu b^2}{I}\right)$$

$$\frac{E_T}{E_{avail}} = \frac{1}{1 + \frac{\mu b^2}{I_R}} \tag{3}$$

and $$\frac{E_{rot}}{E_{avail}} = 1 - \frac{E_T}{E_{avail}} = \left[1 + \frac{I}{\mu b^2}\right]^{-1} \tag{4}$$

which is the same expression given by Wilson.

B. Recoil of X from a Soft Radical R.

The formula stated by Wilson for energy partitioning in the case of an atom X recoiling a "soft" radical R (see description of model by

Wilson, Ref. 39) should be restricted to the case in which the geometry of the radical does not change from the molecule to the free radical. The partitioning to translation was correctly given by Wilson and is trivially derived from

a) conservation of initial linear momentum between X and the atom in the radical R to which it is bonded, say C

$$m_x \vec{v}_{x(initial)} = - m_c \vec{v}_{c(initial)}$$

b) conservation of energy

$$E_{avail} = E_{rot} + E_{vib} + E_T$$
$$\text{where } E_T = 1/2\ \mu_{RX} \vec{v}^2_{rel,RX}$$

c) conservation of energy within the radical R after the impulsive force has imparted a velocity to C:

$$1/2\ m_c \vec{v}^2_{c(initial)} = E_{vib,R} + E_{rot,R} + 1/2\ m_R \vec{v}^2_R$$

One may obtain then the same expression given by Wilson for partitioning to translation

$$\frac{E_T}{E_{avail}} = \frac{\mu_{C-X}}{\mu_{R-X}} \qquad (5)$$

The partitioning for total internal energy to the radical R is also necessarily correctly given by Wilson as

$$\frac{E_{int}}{E_{avail}} = 1 - \frac{\mu_{C-X}}{\mu_{R-X}}$$

However, the division of the internal energy of R into rotation and vibration given by Wilson is not a general one:

$$E_{rot,R} = \left(1 - \frac{\mu_{C-X}}{\mu_{R-X}}\right) E_{avail} \sin^2 X$$

(where X is the angle between X, C, and the c.m. of R)

The expression is only valid when the geometry of R in RX is the same as when the radical is free. The dissociation only determines the angular momentum imparted to the rotation of R, $|\vec{L}| = I\,|\vec{\omega}|$. Since $E_{rot} = 1/2\ I\vec{\omega}^2 = 1/2\ \vec{L}^2/I$ the rotational <u>energy</u> of the radical will change as it is allowed to distort from the shape it was in when the impulsive force occurred. Wilson's formula for $E_{rot,R}$ (above) and $E_{vib,R}$ are only correct if the geometry of R is the same whether X is bonded to it or not, but the assumption of a soft radical R allows for distortion of R after the impulsive force is over. A more general expression is derived here. The rotational angular momentum $\vec{L}_{rot}$ is necessarily conserved, so if one knows the moment of inertia of R one can calculate the partitioning to rotation and vibration as follows:

$$|\vec{L}_{rot}| = |I\,\vec{\omega}| = |\mu_{RX}\vec{v}_{rel,RX}b|$$

$$E_{rot} = \frac{1}{2}\,\frac{(\mu_{RX}\,\vec{v}_{rel,RX}b)^2}{I} = \frac{E_T\,b^2\,\mu_{RX}}{I} \qquad (6)$$

$$\frac{E_{ROT}}{E_{avail}} = \frac{b^2\mu_{C-X}}{I} \qquad (7)$$

The partitioning of energy to vibration is:

$$\frac{E_{vib}}{E_{avail}} = 1 - \frac{E_{ROT}}{E_{avail}} - \frac{E_T}{E_{avail}} = 1 - \frac{b^2 \mu_{C-X}}{I} - \frac{\mu_{C-X}}{\mu_{RX}}$$

As in the rigid radical impulsive model, the molecule is assumed not to distort on the time scale that momentum is being imparted to, in this case, the C and X atoms, and b is calculated from the ground state equilibrium geometry of RI.

APPENDIX 2: Prediction of Energy Partitioning in the Bond Fission Dissociation Channels of CH_2BrI with Impulsive Force Models.

The fraction of the available energy which goes into the relative translation of the products in the two bond dissociation channels observed for CH_2BrI can be calculated under the assumption of the rigid radical impulsive force model and the soft radical impulsive force model.

The geometry of the molecule at the time the I and C atoms are separated by an impulsive force (in the case of a rigid radical, the rest of the radical fragment is necessarily driven by the force as well) is taken to be the equilibrium geometry of CH_2BrI estimated by Kudchadker and Kudchadker (KK) (see Ref. 1) with the exception that the C-I bond distance is 2.13 Å; the value of 1.76 Å given by KK is presumably a misprint. Using this geometry follows from modelling the dissociation as being initiated by a Franck Condon excitation to a repulsive state. The geometry estimated by KK is given in Table 4. Because the molecule is symmetric with respect to the ICBr plane in which the relative translation and rotation will occur for these models, the molecule was reduced to a planar geometry for calculation of impact parameters and moments of inertia about the axis perpendicular to that plane. Thus the hydrogens were taken as an atom of mass 2 at the center of the line between them in CH_2BrI. Taking the ICBr plane as the yz plane and the C-I bond direction as the +y axis, coordinates for all the atoms (H_2

taken as one unit) were calculated and are given in Table 4. These coordinates and the masses 127, 80, 12 and 2 were used for I, $^{79,81}Br$, C, and H_2 respectively for all the calculations below.

A. Partitioning to Translational and Rotational Energy in the Rigid Radical Model.

The fraction of the available energy that has become relative translational energy in C-I and C-Br dissociations respectively in CH_2BrI is trivially calculated from equation (3) and (4) in Appendix 1A.

For $CH_2BrI \rightarrow CH_2Br + I$ one calculates:

$$\frac{E_T}{E_{avail}} = \frac{1}{1 + \dfrac{\dfrac{(127+94)}{(127+94)}\ \text{g/mole}\ (1.50\ \text{Å}^2)}{45.53\ \text{Å}^2 \cdot \text{g/mole}}} = 0.272$$

The b of 1.50 Å, the perpendicular distance from the center-of-mass of the rigid CH_2Br fragment to the velocity vector of the I atom (which is taken to be along the C-I bond in this model), is calculated from the coordinates of the atoms given in Table 4. The moment of inertia I of the CH_2Br rigid radical about an axis perpendicular to the ICBr plane and through the center of mass of the CH_2Br product is also calculated from the coordinates given in Table 4. Thus, if CH_2BrI dissociates to $I + CH_2Br$, modelling the dissociation as I leaving a rigid CH_2Br radical from the geometry given gives the prediction that 27 percent of the

available energy becomes relative translational energy of the fragments. The rotational energy partitioning is necessarily:

$$\frac{E_{rot}(CH_2Br)}{E_{avail}} = 1 - 0.272 = 0.728$$

For $CH_2BrI \rightarrow CH_2I + Br$ the impact parameter for Br leaving the c.m. of CH_2I is calculated from the geometry of Table 4 to be 1.76 Å. The moment of inertia of CH_2I is calculated to be 60.08 g/mole·Å^2. Thus the partitioning to translation for C-Br bond fission under the rigid radical impulsive force model is (from eq. 3 in Appendix 1 part A).

$$\frac{E_T}{E_{avail}} = \frac{1}{1 + \frac{(80)(141)\text{g/mole}}{80 + 141} \frac{(1.76\ \text{Å})^2}{60.08}} = 0.276$$

and $$\frac{E_{rot}}{E_{avail}} = 1 - 0.276 = 0.724.$$

B. Partitioning to Translation, Vibration, and Rotation in the Soft Radical Model

The partitioning to translational energy in the soft radical impulsive force model is independent of any assumptions of the geometry of the molecule at the moment the impulsive force acts. It is calculated by the formula given by Wilson shown in Appendix 1.B.

For C-I bond fission:

$$\frac{E_T}{E_{avail}} = \frac{\frac{(12)(127)}{12 + 12}}{\frac{(94)(127)}{(127 + 94)}} = 0.203$$

For C-Br bond fission:

$$\frac{E_T}{E_{avail}} = \frac{\frac{(12)(80)}{12 + 80}}{\frac{(141)(80)}{141 + 80}} = 0.204$$

Partitioning of the leftover 80 percent of the energy between rotation and vibration is dependent of the following two assumptions. First, one assumes that the impulsive force between C and Br or I acts when the molecule is in the same geometry as the ground state equilibrium geometry of CH_2BrI (in accordance with a Franck Condon excitation to a repulsive electronic surface, so not necessarily applicable to the excitation at 193 nm, see Discussion). Second, since the geometry of the CH_2Br and CH_2I radicals is not known, we will approximate the bond distance and angles as the same as in CH_2BrI. Although certainly the ICH_2 bond angle will change in the radical, this will not have a big effect on the moment of inertia about the axis perpendicular to that plane. Thus the approximation is good unless the C-I (or C-Br in the CH_2Br radical) bond distance changes significantly in the molecule versus the radical. One then can calculate b and I for each channel from the appropriate coordinates in Table 4. The partitioning of energy to rotation is calculated from equation 7 in Appendix 1B with these assumptions to be:

for C-I fission:

$$\frac{E_{rot}}{E_{avail}} = \frac{(1.50\ \text{Å})^2\ (\frac{(12)(127)}{12 + 127}\ \text{g/mole})}{45.53\ \text{Å}^2\ .\ \text{g/mole}} = 0.544$$

for C-Br fission:

$$\frac{E_{rot}}{E_{avail}} = \frac{(1.76\ \text{Å})^2\ (\frac{(80)(12)}{(80 + 12)}\ \text{g/mole})}{60.08\ \text{Å}^2\ .\ \text{g/mole}} = 0.536$$

The left over energy for vibrational excitation of the CH_2Br or CH_2I radicals are respectively:

for C-I fission

$$\frac{E_{vib}(CH_2Br)}{E_{avail}} = 1 - 0.203 - 0.544 = 0.253$$

$$\frac{E_{vib}(CH_2I)}{E_{avail}} = 1 - 0.204 - 0.536 = 0.260$$

REFERENCES

1. The heats of formation of a variety of chemical species used to calculate the enthalpies shown in Fig. 1 were obtained from: H. M. Rosenstock, K. Draxl, B. W. Steiner, and J. T. Herron, J. Phys. Chem. Ref. Data 6, Suppl. 1, I-774 (1977). The heat of formation of CH_2BrI, 17.338 kcal/mole at OK, is calculated in S. A. Kudchadker and A. P. Kudchadker, J. Phys. Chem. Ref. Data 7, 1285 (1978). In addition, the C-I and C-Br bond fission energies in CH_2BrI were assumed to be the same as in CH_3I and CH_3Br respectively. Calculation of the HI and HBr elimination channels' endoergicities also required the assumption that the energy required to remove H from CH_2Br or CH_2I is the same as required to remove it from CH_3. C-H bond fission and H_2 elimination are not included as we are not sensitive to these channels in our experiment.

2. a) J. G. Calvert and J. N. Pitts, Jr., Photochemistry (John Wiley and Sons, Inc., New York, 1966), Chap. 5, p. 522-528.; b) R. P. Wayne, Photochemistry (American Elsevier Publishing Co., Inc., New York, 1970) Chap. 3, p. 66-67.

3. S. J. Lee and R. Bersohn, J. Phys. Chem. 86, 728 (1982).

4. D. Krajnovich, L. J. Butler, and Y. T. Lee, J. Chem. Phys. 81, 3031 (1984).

5. W. H. Pence, S. L. Baughcum, and S. R. Leone, J. Phys. Chem. 85, 3844 (1981).

6. ONR/NRL Workshop on Energetic Materials Initiation Fundamentals, 30 October-1 November 1984.

7. This is a result of both sets of products recoiling down a similar repulsive energy surface except for the difference in final product energies. The complete or partial resolution in TOF spectra of products from carbon-halogen bond fission producing two spin-orbit states of halogen atom product has been previously observed for CH_3I,[8a-e] CF_3I,[8b,9] CH_3Br,[8b] CF_3Br,[9] CD_3I,[8b] and $1,2\text{-}C_2H_4ClI$.[10]

8. a) R. K. Sparks, K. Shobatake, L. R. Carlson, and Y. T. Lee, J. Chem. Phys. 75, 3838 (1981); b) G. N. A. van Veen, "Excited Species from Photofragmentation," Ph.D. Thesis, Amsterdam (1984); c) M. D. Barry and P. A. Gorry, Mol. Phys. 52, 461 (1984); d) S. J. Riley and K. R. Wilson, Disc. Faraday Soc. 53, 132 (1972); e) M. Dzvonik, S. Yang, and R. Bersohn, J. Chem. Phys. 61, 4408 (1974).

9. Unpublished data of authors.

10. T. K. Minton, P. Felder, R. J. Brudzynski, and Y. T. Lee, J. Chem. Phys. 81, 1759 (1984).

11. This product channel branching ratio assumes both dissociation channels have the same anisotropy with respect to the direction of the laser electric vector. Even though the light is unpolarized, detection is of products in the plane perpendicular into the direction of travel of the light so we are typically twice as sensitive to products from a transition with dipole moment parallel to the bond that breaks as from one that is perpendicular. The angular distribution measurements of I from CH_2BrI at 248 nm described in Section I.H prove that the anisotropy of both C-I bond fission channels is the same, thus the branching ratio stated is correct.

12. An alternative way is to set the resolution so high that any leakage is effectively stopped, but then a lack of signal is ambiguous since the transmission of the quadrupole is reduced as the resolution is raised.

13. D. Krajnovich, Z. Zhang, L. Butler, and Y. T. Lee, J. Phys. Chem. 88, 4561 (1984).

14. It was explicitly checked with a simple classical calculation that the C-I bond fission imparted enough rotation to the CH_2Br fragment that the recoil angle of the Br when CH_2Br absorbed another photon and dissociated would not be constrained to be at a specific angle from the recoil direction of the CH_2Br from I. The sum of the orbital angular momentum of the departing CH_2Br and I fragments will determine the rotational angular momentum imparted to the CH_2Br by angular momentum conservation. Assuming the fragments leave the c.m. at an impact parameter estimated from the geometry of the molecule with velocities derived from the peak of the TOF spectra, the CH_2Br will be made to rotate with a period of 5.6×10^{-11} sec/revolution. At our dissociating pulse energies/cm^2 the CH_2Br fragment could rotate hundreds of times before absorbing a photon (assuming a cross section of $\sim 10^{-18}$ cm^2).

15. R. N. Zare, Mol. Photochem. 4, 1 (1972).

16. Y. B. Band, K. F. Freed, D. J. Kouri, Chem. Phys. Lett. 79, 233 (1981).

17. Y. B. Band and K. F. Freed, Chem. Phys. Lett. 79, 238 (1981).

18. D. J. Krajnovich, Ph.D. thesis, University of California, Berkeley, California, Appendix B, 1983.

19. Appendices 1 and 2 at end of Chap. 1 of L. J. Butler, Ph.D. thesis, University of California, Berkeley, California, 1985.

20. The stipulation "remaining" is added because a 193 nm photon contains 148 kcal/mole of energy, enough to form CH_2I and CH_2Br products from some dissociations with enough internal energy to unimolecularly dissociate to CH_2 + X. See text.

21. V_{00} = 12255 cm^{-1} for the $A^3\Pi_1$, state of IBr is obtained from K. P. Huber and G. Herzberg, Molecular Spectra and Molecular Structure IV: Constants of Diatomic Molecules (Van Nostrand Reinhold Co., New York, 1979).

22. The 10° data will favor detection of primary products over fast secondary products from two photon events.

23. Quickly recoiling products from C-I fission following n(Br)→σ*(C-Br) excitation in 1,2-C_2F_4BrI were observed in Ref. 4.

24. a) P. J. Robinson and K. A. Holbrook, Unimolecular Reactions, (Wiley-Interscience, New York, 1972), b) I. W. M. Smith, Kinetics and Dynamics of Elementary Gas Reactions (Butterworth, London/Boston, 1980).

25. F. F. Crim, Ann. Rev. Phys. Chem. 35, 657 (1984).

26. See Calvert and Pitts of Ref. 2, Chap. 5, p. 526.

27. J. T. Yardley, Introduction to Molecular Energy Transfer (Academic Press, New York, 1980).

28. Electronic levels in iodoalkanes are derived with analogy to HI, see R. S. Mulliken, Phys. Rev. 51, 310 (1936), related papers, and ibid. 47, 413 (1935) as well as review given in Ref. 4.

29. When one talks of the diabatic $^3Q_0$ and $^1Q_1$ curves crossing, the coupling interaction which causes transitions between the two states is not included. An alternate formalism for looking at the problem is to consider "hopping" between two adiabatic curves (which would correspond to no transition between diabatic curves). For clarification, see L. D. Landau and E. M. Lifshitz, Quantum Mechanics 3 (Pergamon Press, Ltd., New York, 1977) p. 347.

30. M. S. Child and R. B. Bernstein, J. Chem. Phys. 59, 5916 (1973).

31. P. Brewer, P. Das, G. Ondrey, and R. Bersohn, J. Chem. Phys. 79, 720 (1983).

32. See Ref. 8b, p. 115-116.

33. See Ref. 8b or C. Zener, Proc. R. Soc., Ser. A, 137, 696 (1932) or Ref. 29.

34. T. Donohue and J. R. Weisenfeld, J. Chem. Phys. 63, 3130 (1975).

35. Private communication, Millard Alexander.

36. J. P. Simons and A. J. Yarwood, Nature 192, 943 (1961).

37. D. W. G. Style and J. C. Ward, J. Chem. Soc., 2125 (1952).

38. This assumes there would not be significant coupling between the diabatic $^3Q_0$ and $^1Q_1$ curves for C-Br fission in CH_2BrI as there was not for C-Br fission in CH_3Br[8b].

39. G. E. Busch and K. R. Wilson, J. Chem. Phys. 56, 3626 (1972).

Table 1: CH_2Br^+:I^+ signal ratios at high and low cluster molecular beam conditions.

Ion Fragment	Molecular Beam Conditions	No. of Laser Shots	Background (per 4 μsec channel gate) (average in channels 2-40)	Signal (Sum of in channels 80-210 at 4 μsec/chan)	$\frac{CH_2Br^+}{I^+}$
CH_2Br^+	High Dimers	200,000	422	2311	
					.0913
I^+	High Dimers	200,000	390	25326	
CH_2Br^+	Low Dimers	300,000	419	969	
					.0496
I^+	Low Dimers	300,000	378	19551	

Table 2: Summary of primary experimental results.

Reaction	Wavelength	$\bar{E}_T$ (kcal/mol)	FWHM (kcal/mol)	$E_T(max)$[a] (kcal/mol)	β	E_{avail}[b] (kcal/mol)	$f_T = \frac{\bar{E}_T}{E_{avail}}$
$CH_2BrI \rightarrow CH_2Br + I(^2P_{3/2})$	248.5	18.6	4.3	--	1.0 ± 0.1	60.0	.31
$\rightarrow CH_2Br + I(^2P_{1/2})$	248.5	12.4	4.5	--	1.0 ± 0.1	38.3	.32
$\rightarrow CH_2I + Br(^2P_{3/2}, \underline{^2P_{1/2}})$[c]	248.5	11.1	8.2	--	0.6 ± 0.1	(47.4, <u>36.8</u>)[c]	(.23, <u>.30</u>)[c]
$CH_2BrI \rightarrow CH_2I + Br(^2P_{3/2}, \underline{^2P_{1/2}})$[c]	210	15.0	9.2	--	(∥)[d]	(68.5, <u>57.9</u>)[c]	(.22, <u>.26</u>)[e]
$\rightarrow CH_2 + IBr(^3\Pi_1)$[e]	210	5.5	7.1	13.6	--	12.5[e,f]	.44[e]
$CH_2BrI \rightarrow CH_2Br + I(^2P_{1/2})$	193.3	14.1	8.5	--	~0	71.1	.20
$\rightarrow CH_2I + Br(^2P_{1/2})$	193.3	14.1	10.0	--	~0	69.7	.20
$\rightarrow CH_2 + IBr(^3\Pi_1)$[e]	193.3	11.7	19.0	23.7	~0	24.3[e]	.48[e]

a) $E_T(max)$ is the maximum energy in translation for those processes in which a sharp cutoff is observed.

b) E_{avail} for this table = $E_{h\nu} - \Delta E_{rxn} - E_{elec}$; e.g. for C-Br fission to form spin-orbit excited Br $\Delta E_{rxn} = D_0(C\text{-}Br)$ and E_{elec} = 10.54 kcal/mol, the spin-orbit splitting of Br. The initial internal energy of the parent is not included here but is discussed in the text.

c) The more likely spin-orbit state of the Br product is underlined, see text.

d) (∥) signifies a parallel angular distribution, here $\beta = 0.6 \pm 0.3$.

e) The electronic state of the IBr product is assumed to be solely $^3\Pi_1$ for this table. The experiment only determined that some of the IBr is formed in the $^3\Pi_1$ state and none is formed in the ground state. Some fraction of the IBr may be formed in the $^3\Pi_0$ state if energetically allowed.

f) Note the $E_T(max)$ is greater than E_{avail} because the internal energy of the CH_2BrI parent of ~1.5 kcal/mol was not included in the E_{avail}.

Table 3: Experimental data for the probability of the $^3Q_0 \dashrightarrow {}^1Q_1$ transition at the curve crossing in the photolysis of RI.

Molecule	Component[a] Excited	λ (nm)	Fraction of $I(^2P_{3/2})$	Fraction of $I(^2P_{1/2})$	I.P. of R (eV)	Final v_{rel}[d] ($\times 10^4$ cm/sec)
C_2F_5I[4]	$^3Q_0$	248	0.0	1.0	9.98[b]	16.9
1,2-C_2F_4BrI[4]	$^3Q_0$	248	~0.0	~1.0	-----	14.8
1,2-C_2F_4BrI[4]	$^3Q_0$	266	~0.0	~1.0	-----	14.1
CF_3I[8b,9]	($^3Q_0$)	248	0.08 ± 0.01	0.92 ± 0.01	10.10[b], (9.5[c])	21.6[e]
CD_3I[8b]	($^3Q_0$)	248	.19	.81	9.831 ± 0.007[c]	43.1[e]
1,2-C_2H_4ClI[10]	$^3Q_0$	266	~0.25	~0.75	-----	17.9[e]
CH_3I[8b,c]	$^3Q_0$	248	0.30	0.70	9.837 ± 0.005[c]	47.4[e]
CH_3I[8a]	$^3Q_0$	266	0.30	0.70	9.837 ± 0.005[c]	42.4[e]
C_2H_5I[31]	($^3Q_0$)	248	0.32 ± 0.02	0.68 ± 0.02	8.25[b]	(slower than CH_3I[8d])
n-C_3H_7I[31]	($^3Q_0$)	248	0.40 ± 0.02	0.60 ± 0.02	8.15[b]	(slower than C_2H_5I[8d])
CH_2BrI	($^3Q_0$)	248	0.57	0.43	-----	13.9[e]

a. When no parenthesis appears, excitation of only the parallel transition to the $^3Q_0$ surface has been confirmed through the observation of a $\beta \geq 1.8$ for all I atom products.

b. From Table I in Ref. 34.

c. Values from National Bureau of Standards, Ionization Potential and Appearance Potential Measurements, 1971-1981, NSRDS-NBS 71.

d. v_{rel} is the asymptotic final relative velocity of the R and I fragments. The value quoted here is an average value calculated from the $\bar{E}_T$ of the measured product translational energy distribution.

e. For the channel producing R + $I(^2P_{1/2})$.

Table 4: Geometry of CH_2BrI (calculated from values in Ref. 1).

Geometric Parameters[a]		Derived Cartesian Coordinates of Atoms[b]	
Bond	Bond Length (Å) or Angle (degrees)	Atom	(x, y, z) (Å)
C-H	1.09	I	(0, 2.13, 0)
C-Br	1.93	Br[c]	(0, -.7615, 1.7734)
C-I	2.13	H_2[b]	(0, -.327, -.271)
<H-C-H	111.35°	C	(0, 0, 0)
<H-C-I	107.95°		
<Br-C-I	113.24°		

a. Estimated in Kudchadker and Kudchadker, Ref. 1.

b. The hydrogens are taken as mass 2 at the center of their positions as all the relevant forces are in the I-C-Br plane.

c. Taken as mass 80 for calculations; there is equal isotopic abundance of mass 79 and mass 81.

FIGURE CAPTIONS

Fig. 1. Energetically allowed dissociation channels of CH_2BrI excited at 193 and 248 nm. The C-I and C-Br bond dissociation enthalpies are assumed to be the same as that in CH_3I and CH_3Br calculated from heats of formation given in ref. 1. The HI and HBr elimination channel endothermicities were calculated from the C-I and C-Br energies estimated above, the H, I and Br heats of formation from ref. 1 and the assumption that the enthalpy of $CH_2X \rightarrow CHX + H$ (X=I,Br) are the same as that for $CH_3 \rightarrow CH_2 + H$ calculated from ref. 1. The enthalpy for $CH_2BrI \rightarrow CH_2 + I + Br$ was calculated using $\Delta H_{f,o}$ from Rosenstock et al. (see Ref. 1) for the products and the enthalpy of formation of CH_2BrI at OK calculated by Kudchaker and Kudchaker (see Ref. 1). The IBr elimination channel enthalpy is calculated from the above value and the enthalpy of $I + Br \rightarrow IBr$ from Rosenstock et al. The energetically allowed C-H bond fission and H_2 elimination channels are not shown. An asterisk indicates the atom is formed in the $^2P_{1/2}$ spin-orbit excited state.

Fig. 2. UV absorption spectra of gaseous CH_2BrI (Cary spectrometer).

Fig. 3. Optical arrangement for production of 210 nm polarized or unpolarized light. 1) 50 cm f.1 quartz lens. 2) Raman cell with 300 psig H_2 gas, room temperature. 3) Pellin-Broca dispersing prism, quartz for unpolarized light, MgF_2 for polarized light. 4) Suprasil right angle turning prism.

5) 240 mm f.1 MgF_2 lens. 6) Aperture to pass only desired wavelength and polarization. View is from top.

Fig. 4. a) TOP, view from side of optical arrangement for production of horizontally polarized 193 nm light. 1) coated mirror; 2) MgF_2 birefringent prism; 3) horizontally polarized component beam; 4) vertically polarized component, dumped; 5) 240 mm f.1. MgF_2 lens.

b) BOTTOM, top view of optical arrangement for production of horizontally polarized 248 nm light and subsequent rotation of electric vector. 1) MgF_2 Pellin-Broca; 2) Suprasil right angle turning prism; 3) horizontally polarized component; 4) vertically polarized component; 5) Karl Lambrecht first-order retarder, rotates $\vec{E}$ vector; 6) 240 mm f.1. MgF_2 lens.

Fig. 5. 248 nm: Product TOF spectra taken at m/e=95, $CH_2{}^{81}Br^+$, at a source to detector angle of 20°. o Experimental points, ———— best fit to the data, obtained by adding the two components ——— — ——— of CH_2Br product from reactions 1a and 1b, calculated from the two component $P(E_T)$ shown in Fig. 7, an anisotropy of β=1.0 for each channel, and a branching ratio of rxn 1b:1a of 0.75:1.

Fig. 6. 248 nm: Product TOF spectra taken at m/e=127, I^+, at three source to detector angles of 10°, 20°, and 30°. o Experimental data. ———— fit calculated as the sum of the individual contributions of $I(^2P_{3/2})$ (——— — ———,

shorter arrival time), $I(^2P_{1/2})$ (——— – ———, longer arrival time) (rxns. 1a and 1b) and I product of CH_2I secondary dissociation (— — —). The contributions from rxns. 1a and 1b are calculated from the two component $P(E_T)$ shown in Fig. 7 which was derived from the CH_2Br TOF spectrum (Fig. 5). The secondary dissociation contribution was calculated from the $P(E_T)$ shown in Fig. 17, see Section I.G. The two 20° TOF's shown differ only in that signal was accumulated during 2 μsec time intervals for one and 3 μsec time intervals for the other.

Fig. 7. Center-of-mass product translational energy distribution for $CH_2BrI \xrightarrow{248\ nm} CH_2Br + I$. The two component $P(E_T)$'s shown as ——— show the shape of each component channel (see text) producing I $(^2P_{1/2})$ (lower translational energies) and I $(^2P_{3/2})$ (higher translational energies). This $P(E_T)$ was derived from forward convolution fitting of the CH_2Br^+ TOF shown in Fig. 5 and was used to fit the I contribution from primary dissociation in the I^+ TOF spectra of Fig. 6. The branching ratio for formation of $I(^2P_{1/2}):I(^2P_{3/2})$ is obtained to be 0.75:1 from the relative areas under each $P(E_T)$ given the measurement of the same anisotropy for each channel of β = 1.0.

Fig. 8. 248 nm: Product TOF spectra taken at m/e=141, CH_2I^+, at a source to detector angle of 20°. o Experimental points. ——— fit to the data calculated for CH_2I product from rxn. 2 from the $P(E_T)$ shown in Fig. 10.

Fig. 9. 248 nm: Product TOF spectra taken at m/e=81, $^{81}Br^+$, at three source to detector angles of 10°, 20°, and 30°. o Experimental points. ——— shape of Br product contribution from C-Br primary bond fission (rxn. 2) calculated from the $P(E_T)$ shown in Fig. 10 derived from the CH_2I TOF of Fig. 8.

Fig. 10. Center-of-mass product translational energy distribution for $CH_2BrI \xrightarrow{248\ nm} CH_2I + Br$. Derived from forward convolution fitting of the CH_2I product TOF of Fig. 8.

Fig. 11. 248 nm: Product TOF spectra taken at m/e=82, $H^{81}Br^+$, top, and m/e=128, HI^+, bottom, at a source to detector angle of 20°. Baseline was calculated from averaging counts in time range between 2 and 100 μsec after the dissociating laser pulse. o Experimental points.

Fig. 12. 248 nm: Product TOF spectra taken at m/e=140, CHI^+, top, and m/e=94, $CH^{81}Br^+$, bottom, at a source to detector angle of 20°. o Experimental points.

Fig. 13. 248 nm: Product TOF spectra taken at m/e=206, 208, $I^{79,81}Br^+$ at a source to detector angle of 10°. The assumed shape of the signal shown in (— — —) was used to calculate the shape of the signal that would be observed at CH^+ (see Fig. 14) if the IBr^+ signal is due to concerted elimination of IBr (rxn. 5). o Experimental points. Signal is proposed to be from fragmentation of dimers. See text.

Fig. 14. 248 nm: Product TOF spectra taken at m/e=13, CH^+, at a source to detector angle of 20°. o Experimental points. ——— total fit, sum of contributions from CH_2I (— — —) and CH_2Br (—— – ——). The $P(E_T)$'s shown in Figs. 7 and 10 which are derived from other TOF spectra were used to calculate where signal would be observed from CH_2I and CH_2Br respectively in this TOF. The hump at short arrival times (—— – – – ——) shows where one would expect CH_2 from rxn. 5 if the signal observed in Fig. 13 were IBr product. The fast data shown without a fit is attributed to CH_2 from the secondary photodissociation of CH_2Br and CH_2I products (see Section I.F and I.G).

Fig. 15. 248 nm: Product TOF spectra taken with special molecular beam conditions to reduce clusters in the beam. Top, taken at m/e=127, I^+ at a source to detector angle of 10°. Middle, taken at m/e=81, $^{81}Br^+$ at a source to detector angle of 10°. Bottom, taken at m/e=94, $CH^{81}Br^+$, at a source to detector angle of 20°. o Experimental points.

Fig. 16. 248 nm: Product TOF spectra taken at m/e=81, $^{81}Br^+$, at two different laser pulse energies ~200 mJ/pulse and ~35 mJ/pulse at a source to detector angle of 20°. (Laser focused to 1 mm x 3 mm, 17 nsec pulse width.)

Fig. 17. Center-of-mass product translational energy distribution used to fit the I signal in the I^+ TOF (Fig. 6) from the secondary photodissociation of CH_2I rxn. 6. See Section I.G for discussion of assumptions in fitting the secondary dissociation signal.

Fig. 18. 248 nm: a) (top) Polarization Dependence of I atom signal from C-I bond fission. o Experimental points. ———— best fit calculated using the $P(E_T)$ for C-I fission of Fig. 7 and an anisotropy of β=1.0 in expression (7). Fits showing confidence in the value of β are — — — β=1.1 and —— – —— β=0.9. (Data and all fits normalized to highest point = 1.0). Bottom left corner shows velocity vector diagram that indicates that the I signal intensity peaks when the electric vector is aligned parallel to the c.m. recoil direction of the fragment. Error in angle is ±2°.

b,c) (left frames) Fits to m/e=127, I^+, TOF spectra taken at a source to detector angle of 20° with the polarization vector of the light at 0° and at 100° (see Fig. 8a for diagram). o Experimental points. ———— total fit to the data assuming each channel (—— – ——), rxn's 1a and b, independently has an anisotropy of 1.0 and using the $P(E_T)$ derived from the unpolarized TOF data.

d,e) (right frames) Fits to the same I^+ data as in b,c) assuming the channel producing $I(^2P_{1/2})$ has a β of 2.0 and that producing $I(^2P_{3/2})$ has a β of 0.5. The weighting of

the two channels is chosen so the unpolarized light data (Fig. 6) and the total I atom signal intensity vs polarization (Fig. 8a) would still be fit. The poor fits obtained show the two channels do not have different anisotropies.

Fig. 19. 248 nm: a) (top) Polarization Dependence of CH_2I fragment signal from C-Br fission. o Experimental points. ———— best fit calculated using the $P(E_T)$ for C-Br fission of Fig. 10 and an anisotropy of β=0.6 in expression (7). Fits showing confidence in the value of β are — — — β=0.7 and —— – —— β=0.5 (data and all fits normalized to highest point = 1.0). Fits assume that the same anisotropy is representative of the whole $P(E_T)$. Newton diagram shown in bottom left.
b,c) Fits to the m/e=141, CH_2I^+, TOF spectra taken at a source to detector angle of 20° with the polarization vector of the light at 0° (middle) and at 100° (bottom). o Experimental points. ———— fit to the data assuming the whole $P(E_T)$ is for dissociation events with an anisotropy of β=0.6.

Fig. 20. 193 nm: Product TOF spectrum taken at m/e=141, CH_2I^+, at a source to detector angle of 20°. o Experimental points. ———— fit to the remaining[20] CH_2I signal calculated from the $P(E_T)$ shown in Fig. 21.

Fig. 21. Center-of-mass translational energy distribution for $CH_2BrI \xrightarrow{193\ nm} CH_2I + Br$, for which the CH_2I is left with little enough internal energy to be stable. The $P(E_T)$ was derived from fitting the CH_2I signal in Fig. 20. The $P(E_T)$ probably corresponds to formation of all $Br(^2P_{1/2})$. See text.

Fig. 22. 193 nm: Product TOF spectra taken at m/e=95, $CH_2{}^{81}Br^+$.
a) Top, o Experimental points. ———— fit to the signal from stable[20] CH_2Br product from C-I bond fission of the monomer CH_2BrI. Fit was calculated from the $P(E_T)$ in Fig. 23.
b) Bottom, o Experimental points obtained under molecular beam conditions which reduce the ratios of clusters to monomer CH_2BrI in the beam.

Fig. 23. Center-of-mass product translational energy distribution for $CH_2BrI \xrightarrow{193\ nm} CH_2Br + I$ for which CH_2Br is left with little enough internal energy to be stable. The $P(E_T)$ was derived from fitting of the signal from dissociation of CH_2BrI monomer giving CH_2Br product in Fig. 22. The $P(E_T)$ probably corresponds to formation of all $I(^2P_{1/2})$. See text.

Fig. 24. 193 nm: Product TOF spectra taken at m/e=206,208, IBr^+, at source to detector angles of 10° (top) and 20° (bottom). o Experimental points. ———— fit calculated from the $P(E_T)$ shown in Fig. 26.

Fig. 25. 193 nm: a) Top left, product TOF spectrum taken at m/e=127, I^+ at a source to detector angle of 20°. o Experimental points. ———— shape of signal from IBr product fragmenting to I^+ in the ionizer obtained from the IBr^+ TOF spectrum of Fig. 24 and the precalibrated ion flight time. Shading shows hump in data where the signal from IBr is evident.

b) Bottom left, product TOF spectrum of m/e=81, Br^+, at a source to detector angle of 20°. o Experimental points. ———— shape of signal from IBr products fragmenting to Br^+ in the ionizer obtained from the IBr^+ TOF spectrum and ion flight time difference. Shading shows hump in data where the signal from IBr is evident.

c,d) Product TOF spectra of m/e=127, I^+ (top right) and m/e=81, $^{81}Br^+$ (bottom right) at a source to detector angle of 20° under molecular beam conditions where the ratio of clusters to monomers in the beam is reduced. Note features in these spectra corresponding to IBr product are just as intense relative to their signal in 25 a and b. o Experimental points.

Fig. 26. Center-of-mass product translational energy distribution for $CH_2BrI \xrightarrow{193\ nm} CH_2 + IBr$, for which the IBr survived secondary dissociation to I + Br. IBr may be lost via predissociation if it has enough internal energy or via absorption of a 193 nm photon. The shape of the $P(E_T)$ below ~4 kcal/mol (shown as — — —) is not sensitive to the data as then the c.m. recoil velocity of the IBr is too small for detection at 10°.

Fig. 27. 193 nm: Product TOF spectra of m/e=127, I^+, at source to detector angles of 10, 20, and 30°.

a,b,c) Left top, middle, and bottom, taken with the laser unpolarized and high power ~200 mJ/pulse. o Experimental points.

d,e,f) Right top, middle, bottom, taken with laser polarized at 0° and the laser power reduced by a factor of 6 to 8. o Experimental points. ———— total fit to the data, sum of contributions from CH_2I from C-Br fission (short dashed, — — —) I from C-I fission (—— – ——), IBr from the concerted elimination (—— – – – ——), and I atoms from $CH_2BrI \longrightarrow CH_2 + Br + I$ (long dashed, —— ——). The first 3 contributions were obtained from other TOF spectra, see text. Each component fit is calculated from the corresponding $P(E_T)$ (Figures 21, 23, 26, and 31 respectively) and an anisotropy of $\beta=0$.

Fig. 28. 193 nm: Product TOF spectra of m/e=81, $^{81}Br^+$, at source to detector angles of 10, 20, and 30°.

a,b,c) Left top, middle, bottom taken with the laser unpolarized and high power ~200 mJ/pulse. o Experimental points.

d,e,f) Right top, middle, bottom taken with laser polarized at 0° and the laser power reduced by a factor of 6 to 8. o Experimental points. ———— total fit to the data, sum of contributions from Br from C-Br fission (short dashed, — — —), CH_2Br from C-I fission (—— – ——), IBr from concerted elimination (—— – – – ——) and Br atoms from $CH_2BrI \longrightarrow CH_2 + Br + I$ (long dashed, —— ——). The first three contributions were obtained from other TOF spectra, see text. Each component fit is calculated from the corresponding $P(E_T)$ (Figures 21, 23, 26 and 31 respectively) and an anisotropy of $\beta=0$.

Fig. 29. 193 nm: Velocity vector diagram showing the range of c.m. recoil angles of the IBr, CH_2I, and Br fragments detected at a source to detector angle of 10°.

Fig. 30. 193 nm: Product TOF spectra of m/e=13, CH^+ at a source to detector angle of 20°. o Experimental points. — — — expected time-of-arrival of CH_2I product at CH^+, —— – —— expected time-of-arrival of CH_2Br product at CH^+, —— – – – —— expected time-of-arrival of CH_2 product momentum-matched with IBr product; scaling is arbitrary. Leftover signal is due to secondary photodissociation of mostly CH_2I and some CH_2Br product and the triple dissociation (rxn 8) $CH_2BrI \longrightarrow CH_2 + I + Br$.

Fig. 31. 193 nm: Center-of-mass product translational energy distribution for IBr (product) (predissociation) → I + Br assuming the slow signal in the I^+ (Fig. 27) and Br^+ (Fig. 28) TOF spectra can be described by a two step process (see text). The energy partitioned to translation for I atoms or Br atoms respectively (for comparison with Fig. 38) are $\frac{80}{207}$ and $\frac{127}{207}$ times the energies shown.

Fig. 32. 193 nm: Product TOF spectra of m/e=82, $H^{81}Br^+$ (top), and m/e=128, HI^+ (bottom), at a source to detector angle of 20°. Baseline was calculated from averaging signal between 2 and 100 μsec after the dissociating laser pulse. o Experimental points.

Fig. 33. 193 nm: Product TOF spectra of m/e=140, CHI^+ (top), and m/e=94, $CH^{81}Br^+$ (bottom), at a source to detector angle of 20°. o Experimental points.

Fig. 34. 210 nm: Product TOF spectrum of m/e=141, CH_2I^+, at a source to detector angle of 20°. o Experimental points. ———— fit to the data calculated from the $P(E_T)$ shown in Fig. 36.

Fig. 35. 210 nm: Product TOF spectrum of m/e=81, $^{81}Br^+$, at a source to detector angle of 20°. o Experimental points, ———— total calculated fit to the data, sum of contributions of Br atoms from C-Br fission (— — —) and Br atoms from the triple dissociation $CH_2BrI \longrightarrow CH_2 + Br + I$ (—— - - - ——). The former is calculated from the $P(E_T)$ shown in Fig. 36 derived from the TOF spectrum of the CH_2I product (Fig. 34) and the latter is the fit calculated from a distribution of translation energies (Fig. 42b) imparted to the Br fragment in the triple dissociation.

Fig. 36. 210 nm: Center-of-mass product translational energy distribution for $CH_2BrI \xrightarrow{210\ nm} CH_2I + Br$. This $P(E_T)$ was derived from fitting of the CH_2I product TOF signal at CH_2I^+ shown in Fig. 34 and was used to fit the Br atom signal from primary C-Br fission shown in Fig. 35.

Fig. 37. 210 nm: Product TOF spectra of m/e=95, $CH_2{}^{81}Br^+$ taken at source to detector angles of 20° under two different molecular beam conditions. a) Top, data taken with usual molecular beam conditions; b) Bottom, data taken with reduced cluster formation molecular beam conditions. o Experimental points.

Fig. 38. 210 nm: Product TOF spectra of m/e=127, I^+, at source to detector angles of 10 and 20°. o Experimental points. ———— total fit to the data, the sum of contributions from CH_2I product of C-Br fission (— — —) and I atoms from the triple dissociation $CH_2BrI \rightarrow CH_2 + Br + I$ (—— – – – ——) (some of the slow signal may be I atoms from spontaneous dissociation of CH_2I product). The former is calculated from the $P(E_T)$ shown in Fig. 36 (or from shifting the CH_2I spectrum at CH_2I^+ by the small difference in ion flight times) and the latter is the fit calculated from a distribution of translational energies (Fig. 42a) imparted to the I fragment in the triple dissociation. (The 10° data also contains a contribution from slow IBr elimination product (long dashed, —— ——) calculated from the $P(E_T)$ shown in Fig. 40.) Each contribution is scaled for best total fit.

Fig. 39. 210 nm: Product TOF spectrum of m/e=208, $I^{81}Br^+$, at a source to detector angle of 10°. o Experimental points. ———— fit calculated from the $P(E_T)$ shown in Fig. 40.

Fig. 40. 210 nm: Center-of-mass product translational energy distribution from $CH_2BrI \xrightarrow{210} CH_2 + IBr$. The shape of the $P(E_T)$ below ~4 kcal/mol (shown as — — —) is not sensitive to the data as at those energies the c.m. recoil velocity of the IBr product is too small for it to be detected at 10°.

Fig. 41. 210 nm: Product TOF spectra of m/e=128, HI^+ (top) and m/e=94, $CH^{81}Br^+$ (bottom) at source to detector angles of 20°. Baseline was calculated from averaging signal between 2 and 100 μsec after the dissociating pulse. o Experimental points.

Fig. 42. 210 nm: Energies imparted to translation for two of the fragments from the triple dissociation $CH_2BrI \xrightarrow{210} CH_2 + Br + I$.

a) Left. Distribution of translational energies (c.m.) released to the I atom fragment; it is derived from fitting the slow signal in the I^+ 20° TOF spectrum (Fig. 38) assuming none of that signal is from spontaneous secondary dissociation of CH_2I product from C-Br fission (true if all $Br(^2P_{1/2})$ is formed).

Note: The highest energies correspond to dissociation events for which the CH_2BrI parent must have contained some internal energy that was released to translation in the final fragments.

b) Right. Distribution of translational energies (c.m.) released to the Br atom fragment; it is derived from fitting the slow signal in the Br^+ TOF spectrum (Fig. 35).

Fig. 43. 210 nm: Product TOF spectra of m/e=81, $^{81}Br^+$, (a+b, top) and m/e=127, I^+ (c+d, bottom) at a source to detector angle of 20° with the laser polarized at 0° (left two frames) and 90° (right two frames). o Experimental points.

a,b) (top) ———— total fit to the data, the sum of contributions from Br atoms from primary C-Br fission (— — —)

and Br atoms from the triple dissociation $CH_2BrI \xrightarrow{210} CH_2 + I + Br$ (— — — — —). Note: The relative probability for each channel (as a function of the anisotropies) and translational energy distributions are previously obtained from the unpolarized light data, the anisotropy parameters which gave the fits shown to the changing shapes (for the slow signal) and relative intensities of the slow vs the fast signal in this polarized light data are $\beta = 0.6$ for Br atoms from C-Br fission and $\beta = 0.65$ for Br atoms from the triple dissociation. There is considerable uncertainties in these values; both distributions definitely do, however, have a parallel polarization dependence.

c,d) (bottom) ———— total fit to the data, the sum of contributions from CH_2I from primary C-Br fission (— — —) and I atoms from the triple dissociation $CH_2BrI \xrightarrow{210} CH_2 + I + Br$ (— — — — —). See note in a,b) above. Anisotropies for c+d were constrained to be $\beta = 0.6$ for the CH_2I signal at I^+ (as obtained for C-Br fission from fitting of the Br^+ signal) and found to be $\beta = 1.0$ for the fit to the I^+ signal from triple dissociation. Again these values are uncertain; both distributions do, however, have parallel polarization dependences.

Fig. 44. 210 nm: Product TOF spectra of m/e=141, CH_2I^+, at a source to detector angle of 20° with the laser polarized at 0° (top) and 90° (bottom). The fit shown is calculated from the $P(E_T)$ (Fig. 36) derived from the unpolarized light TOF data and an anisotropy parameter of $\beta = 0.6$ obtained from fitting the partner Br fragment signal in Fig. 43.

Fig. 45. 210 nm: Product TOF spectra of m/e=208, $I^{81}Br^+$, at a source to detector angle of 20° with the laser polarized at 0°. The fits shown are calculated from the $P(E_T)$ (Fig. 40) derived from the unpolarized light data and anisotropies of $\beta = 0.8$ (— — —) and $\beta = -1.0$ (—— – ——).

Fig. 46. Schematic diagram of the quasidiatomic $n(I) \rightarrow \sigma^*(C\text{-}I)$ diabatic repulsive potentials in a molecule RI and their correlation to R + I ($^2P_{1/2}$ or $^2P_{3/2}$) products. ∥ denotes an electric dipole allowed transition where the dipole moment vector is parallel to the C-I bond and ⊥ denotes an electric dipole allowed transition where the dipole moment vector is perpendicular to the C-I bond. The notation Q originated with Mulliken and is analogous to a Π state in HI.

Fig. 47. Schematic diagram of the LCAO-MO least motion path model for the concerted elimination of IBr from CH_2IBr. The path shown is one following a singlet excitation by the photon in which the CH_2 product is constrained to be triplet. A $^3\Pi$ IBr product is necessarily produced; no ground state IBr is formed in this model.

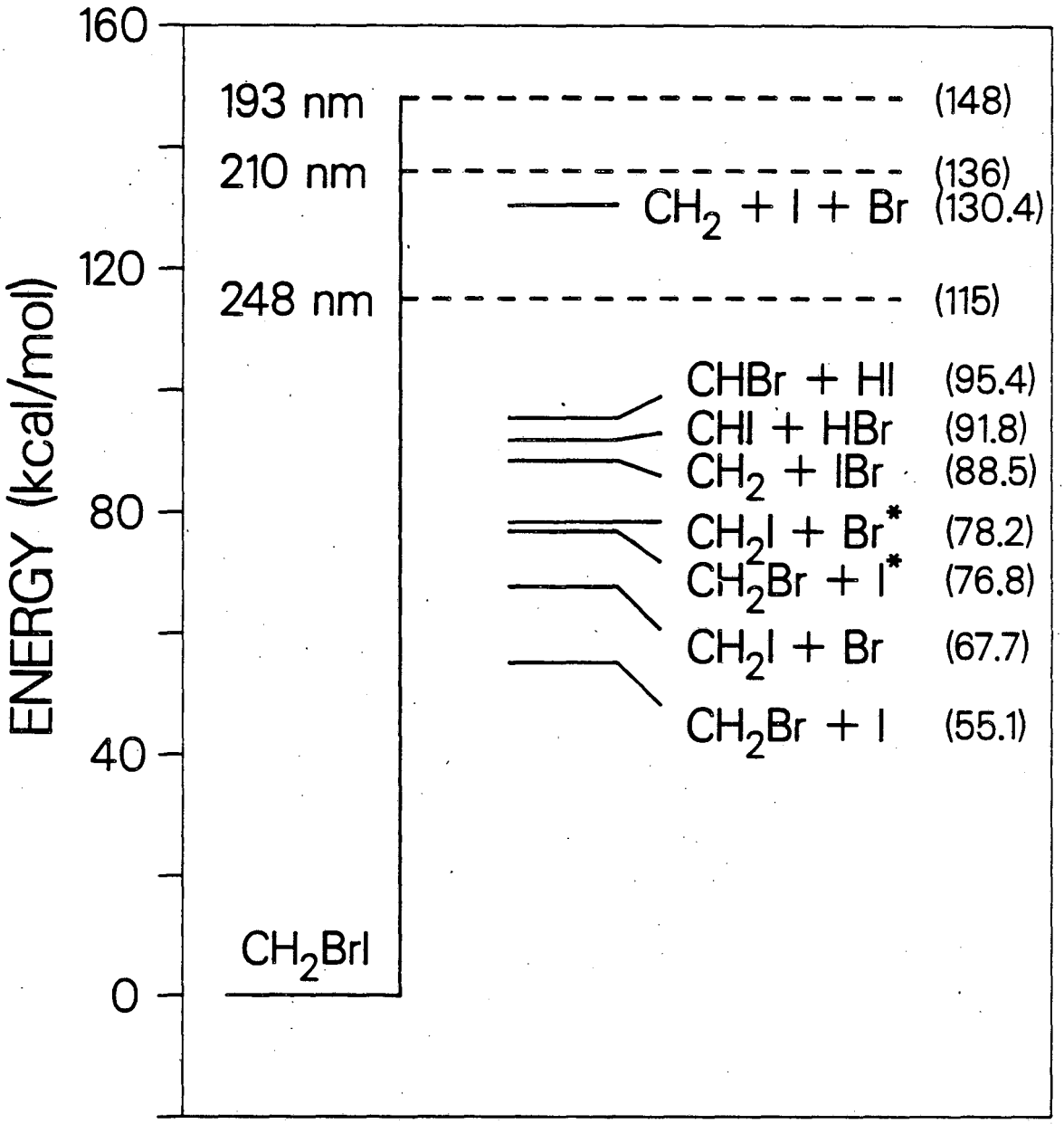

XBL 859 3871

Fig. 1

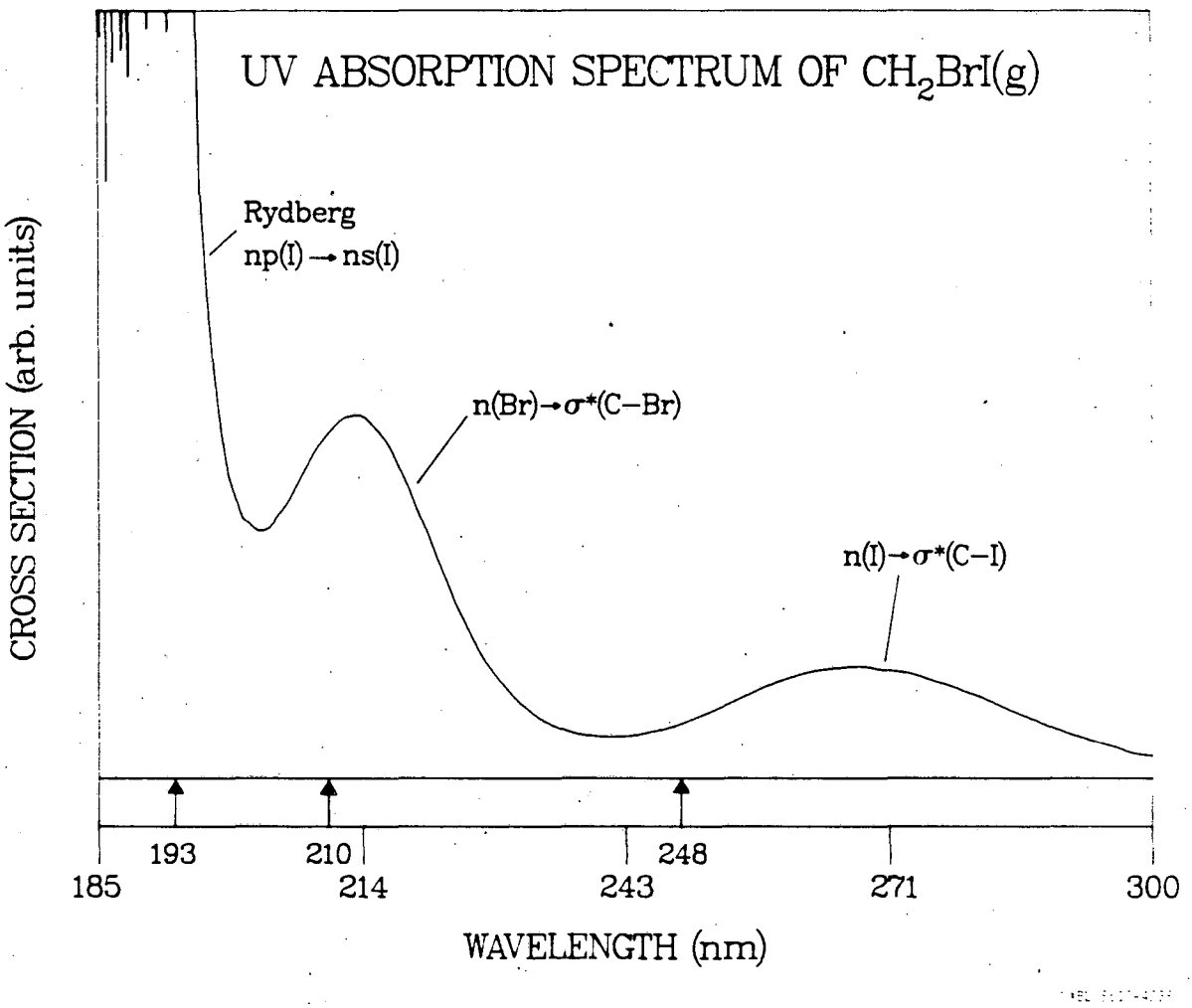
UV ABSORPTION SPECTRUM OF $CH_2BrI(g)$
Rydberg
np(I) → ns(I)
n(Br)→σ*(C–Br)
n(I)→σ*(C–I)
CROSS SECTION (arb. units)
193
210
248
185
214
243
271
300
WAVELENGTH (nm)

Fig. 2

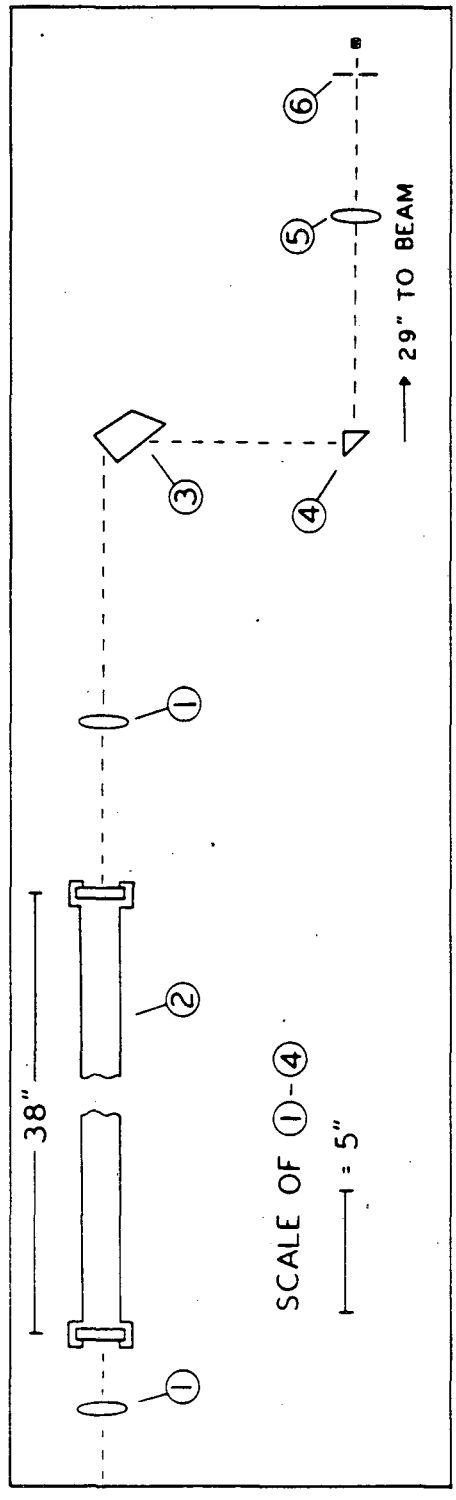

XBL 859-4075

Fig. 3

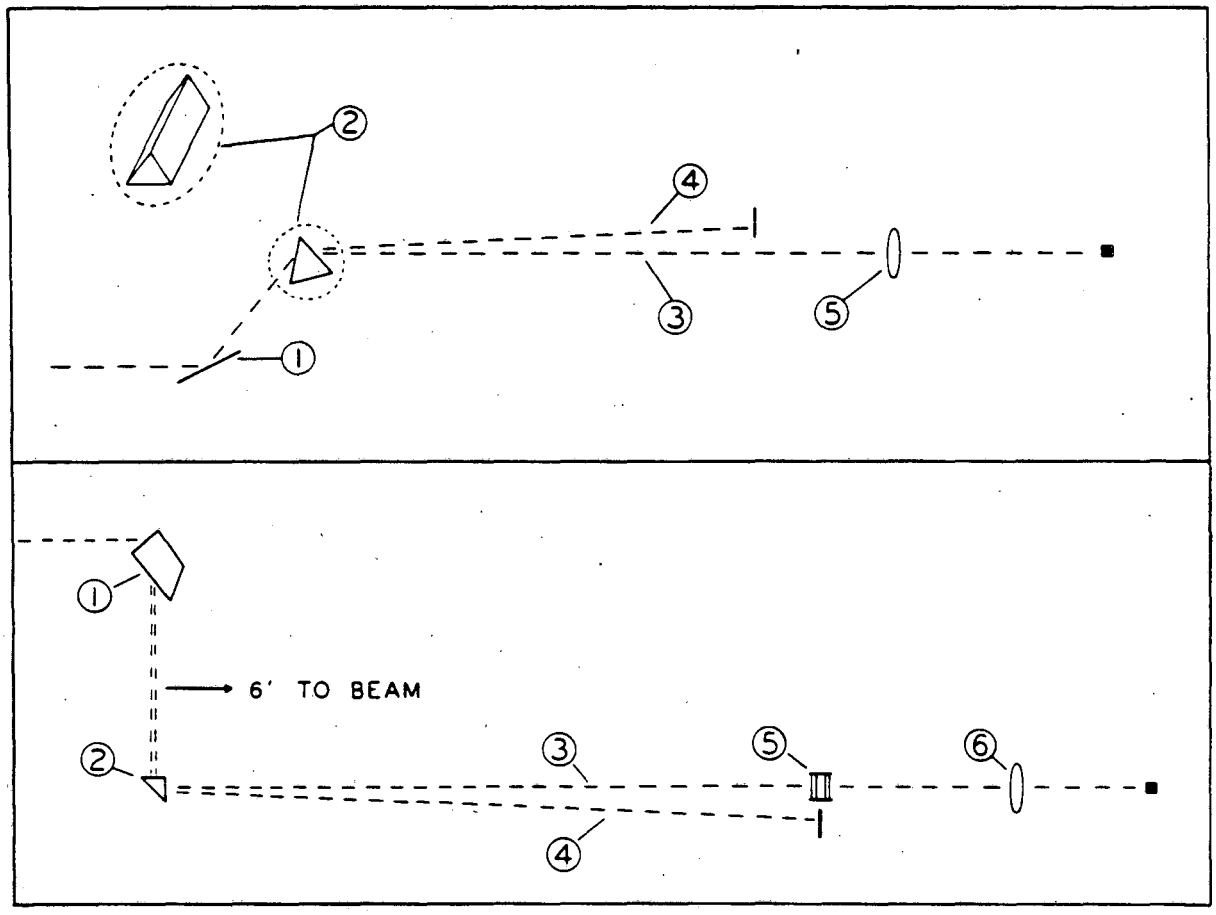

XBL 859-4074

Fig. 4

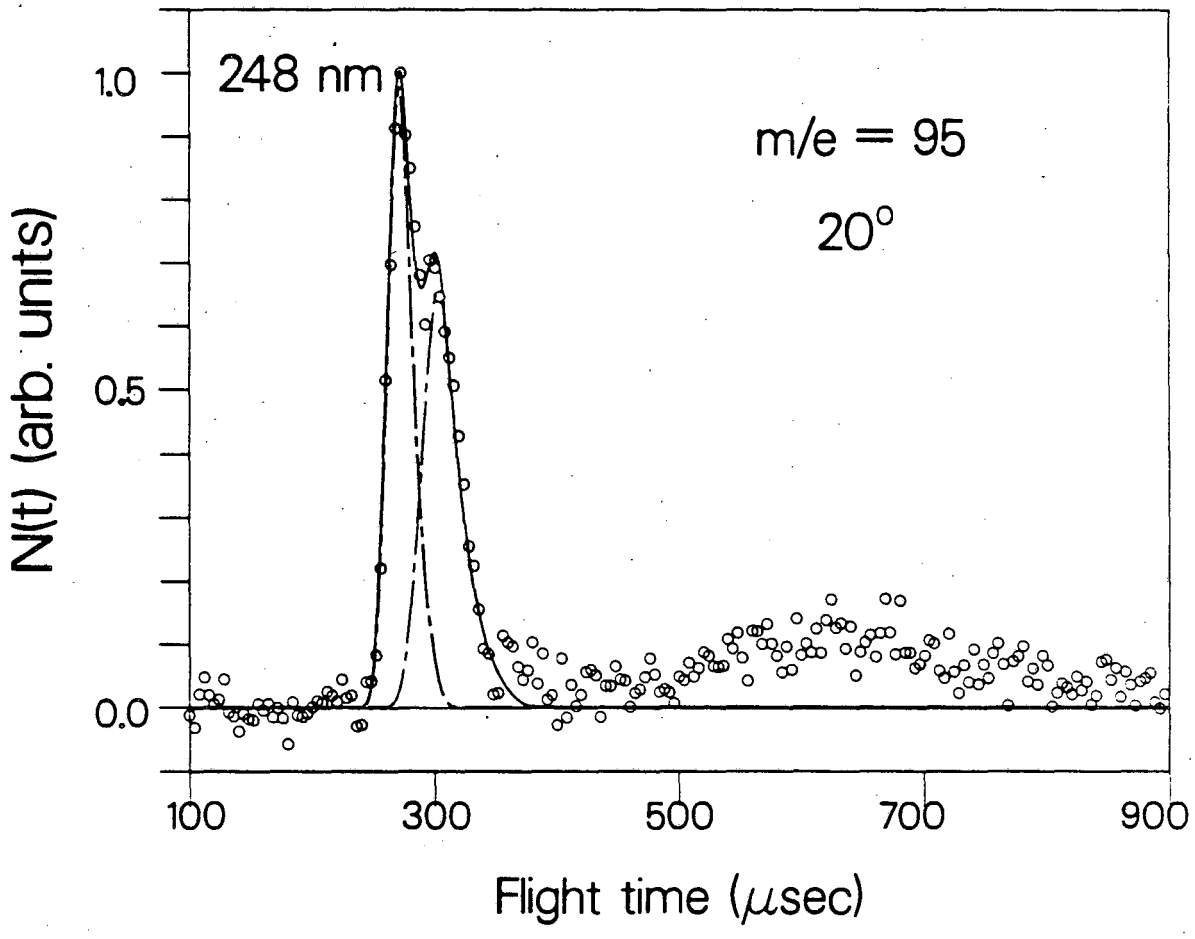

XBL 858 3721

Fig. 5

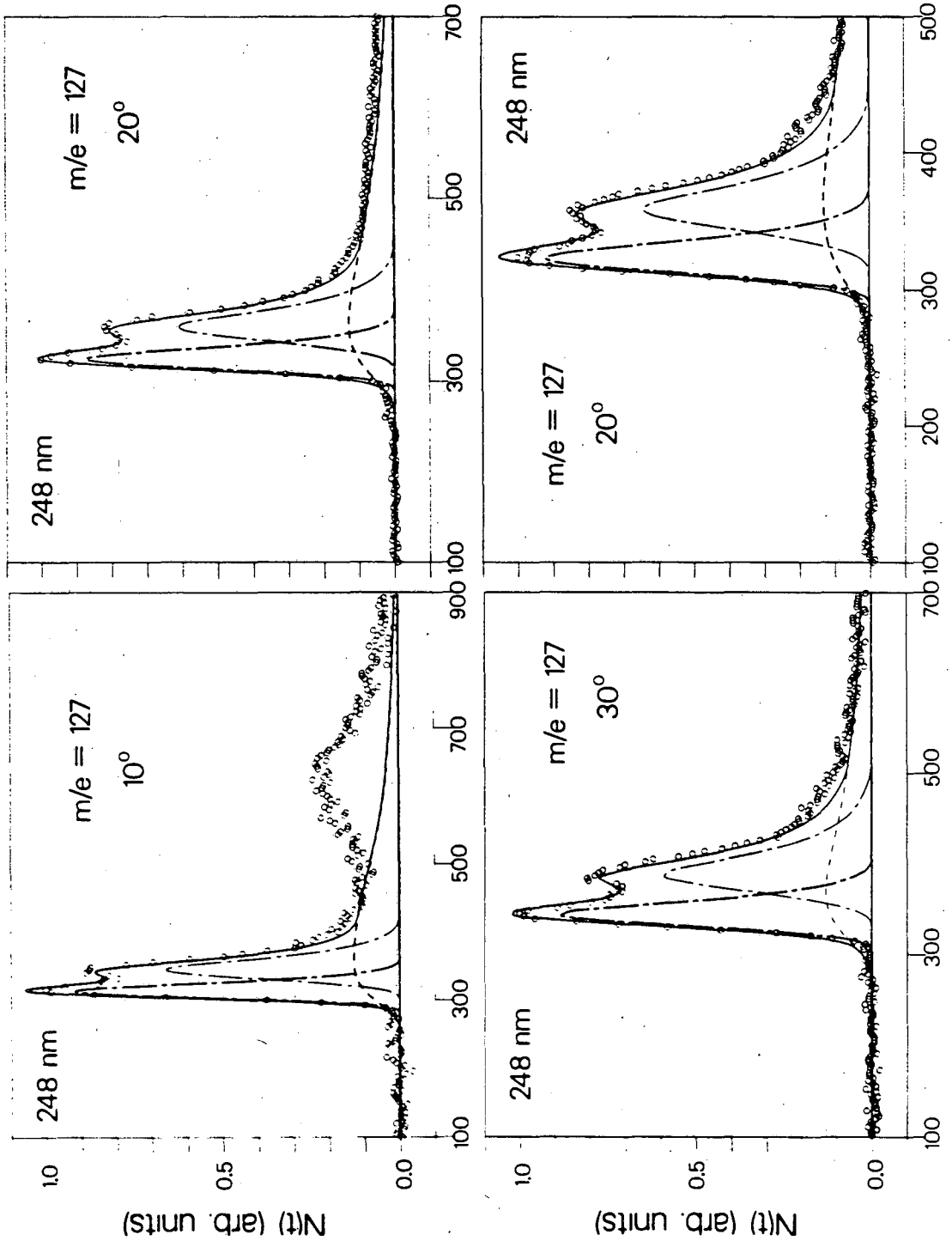

XBL 858 3728

Fig. 6

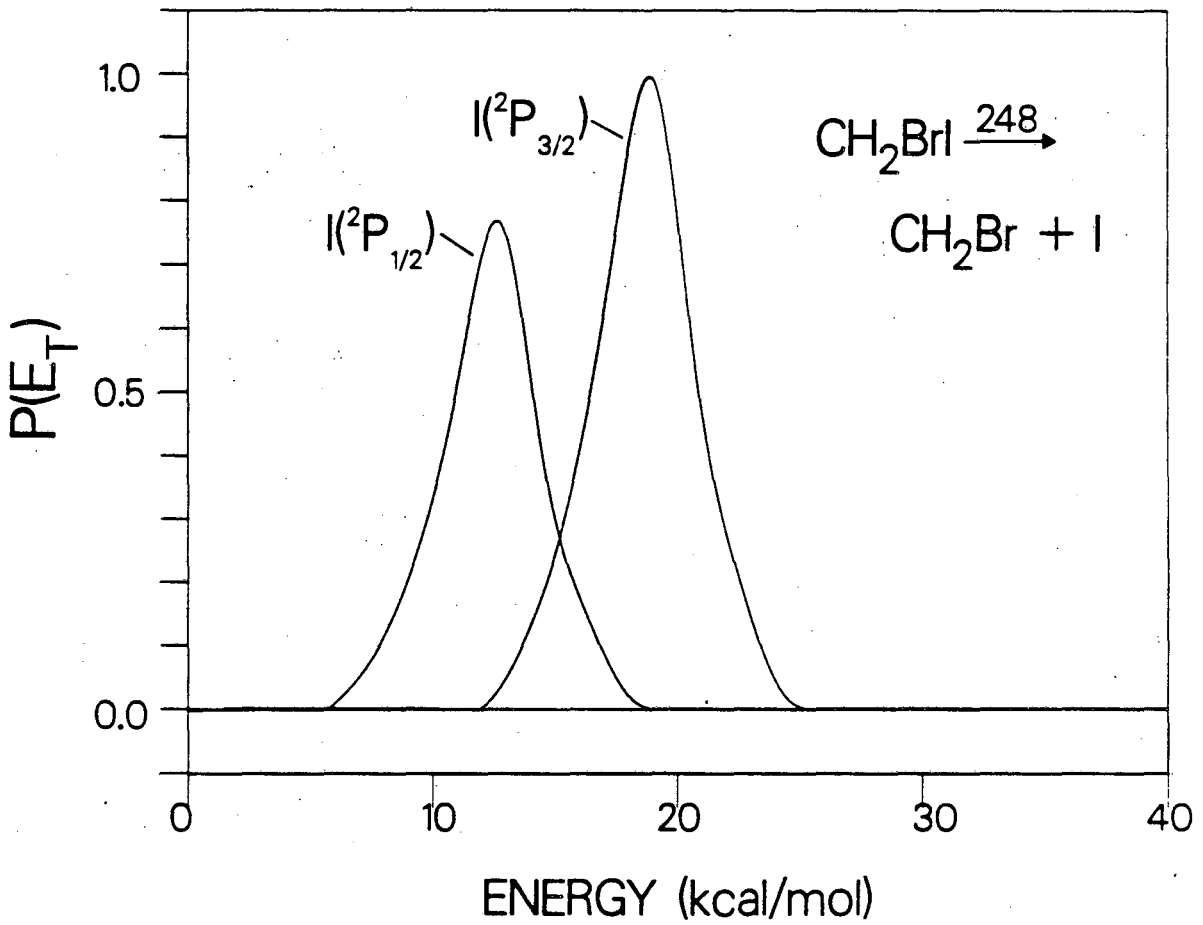

XBL 858 3722

Fig. 7

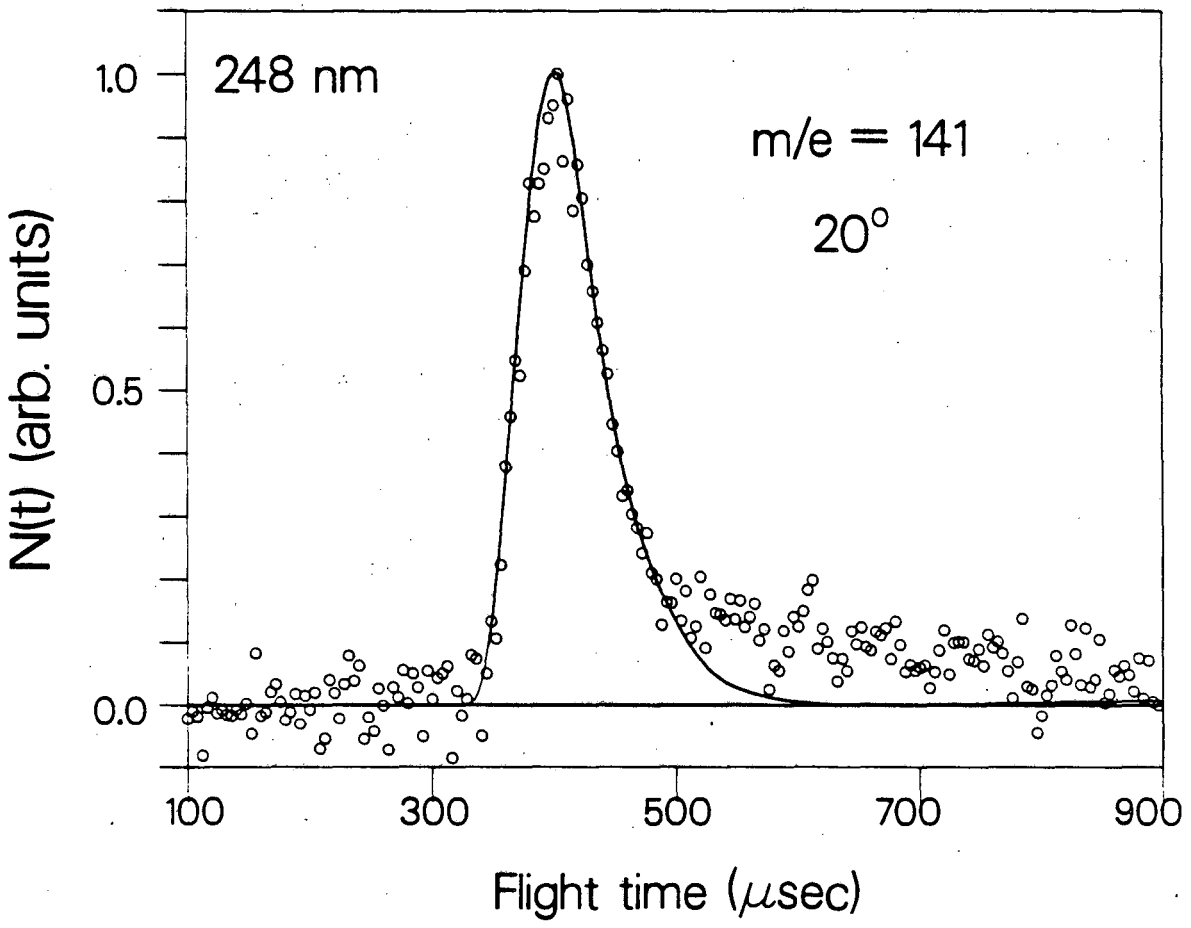

XBL 858 3727

Fig. 8

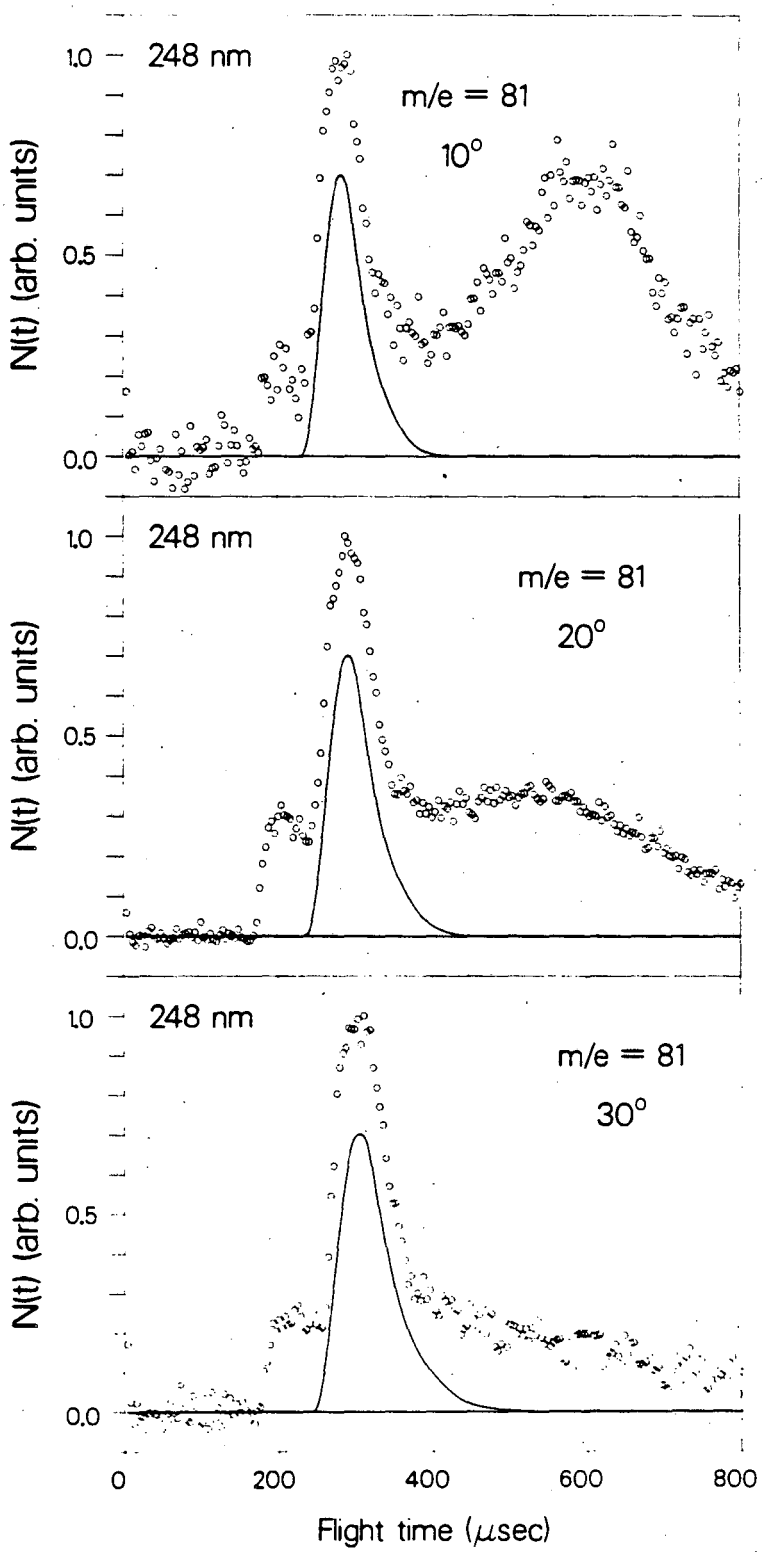

XBL859 3799

Fig. 9

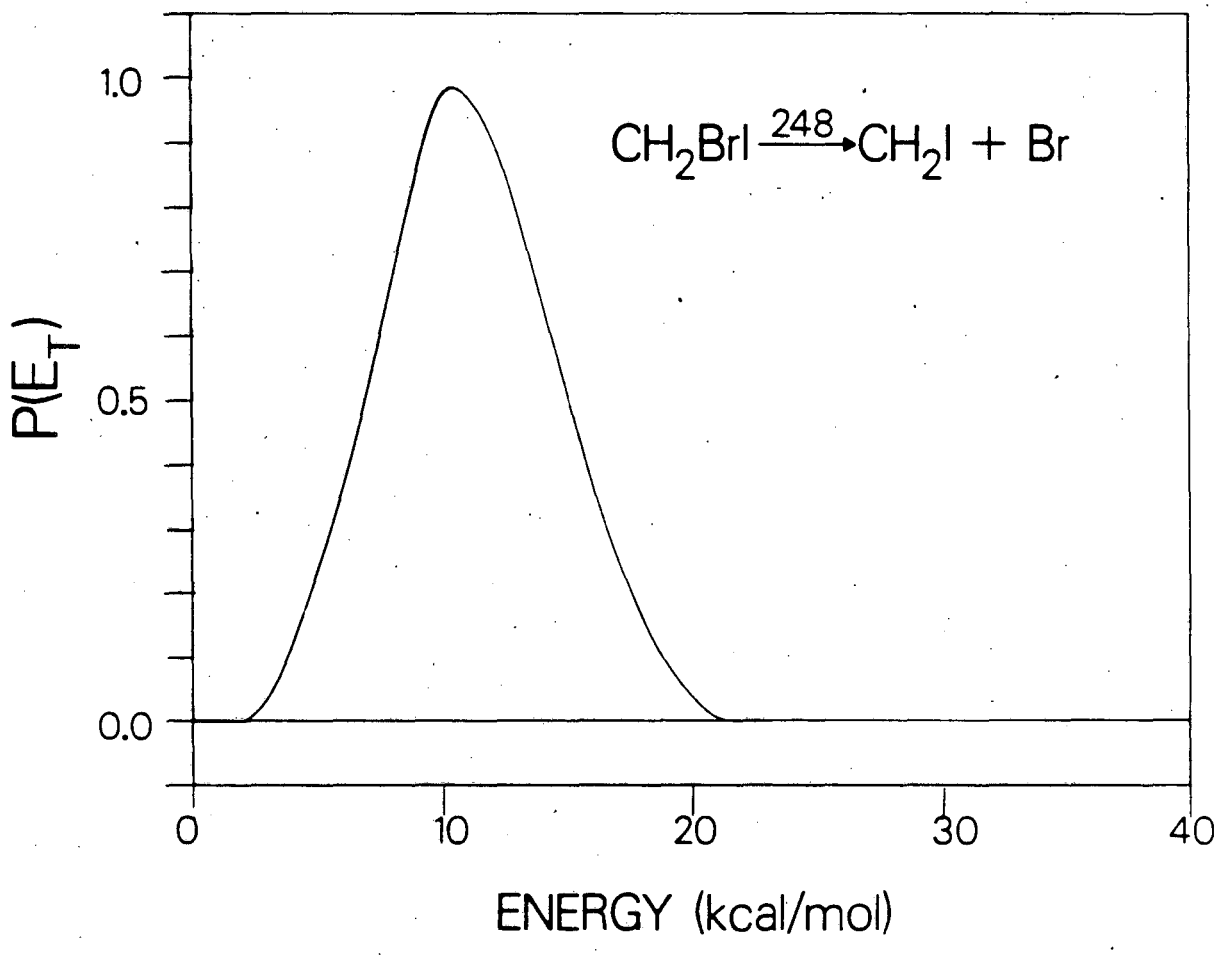

XBL 858 3731

Fig. 10

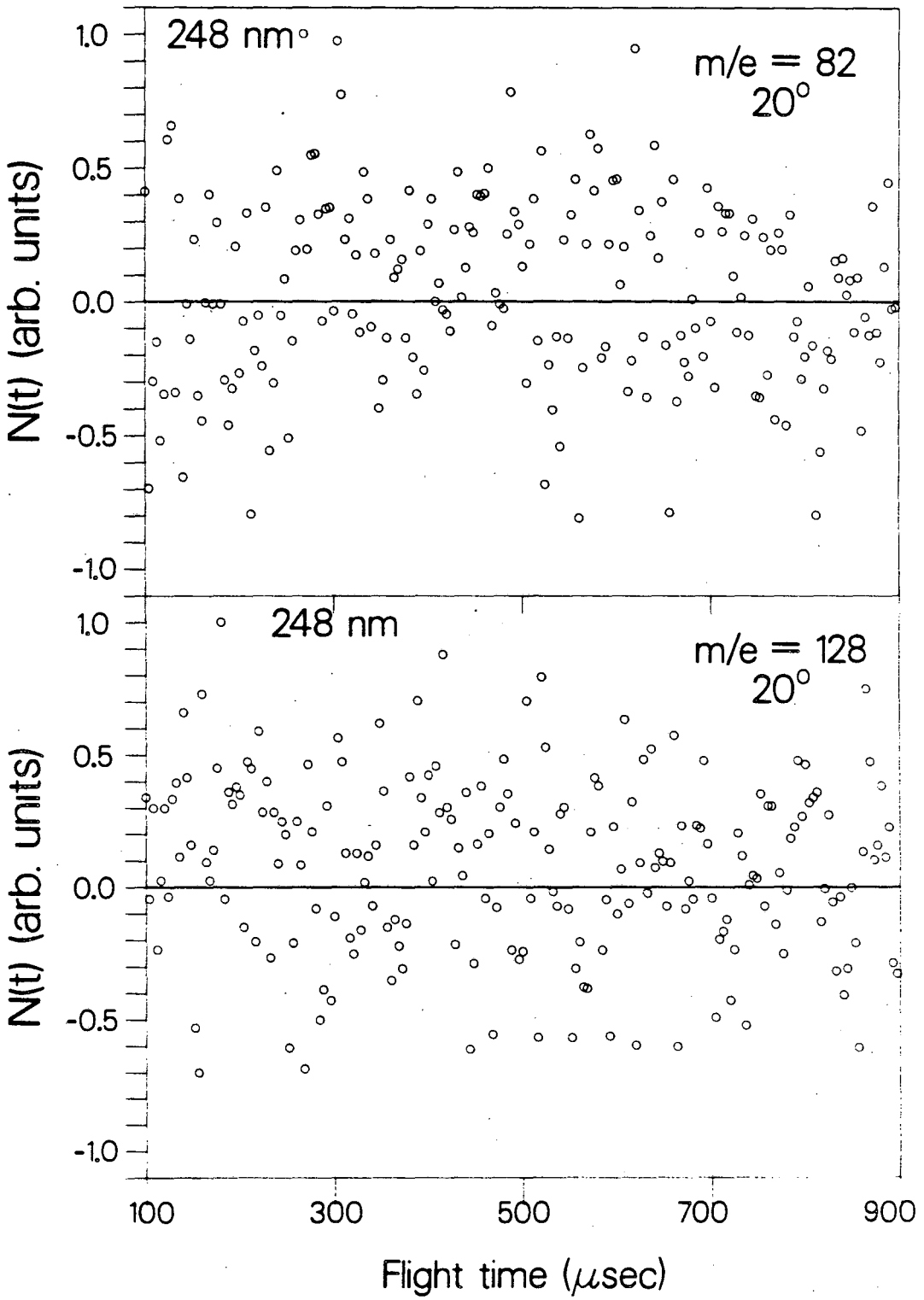

XBL 858 3732

Fig. 11

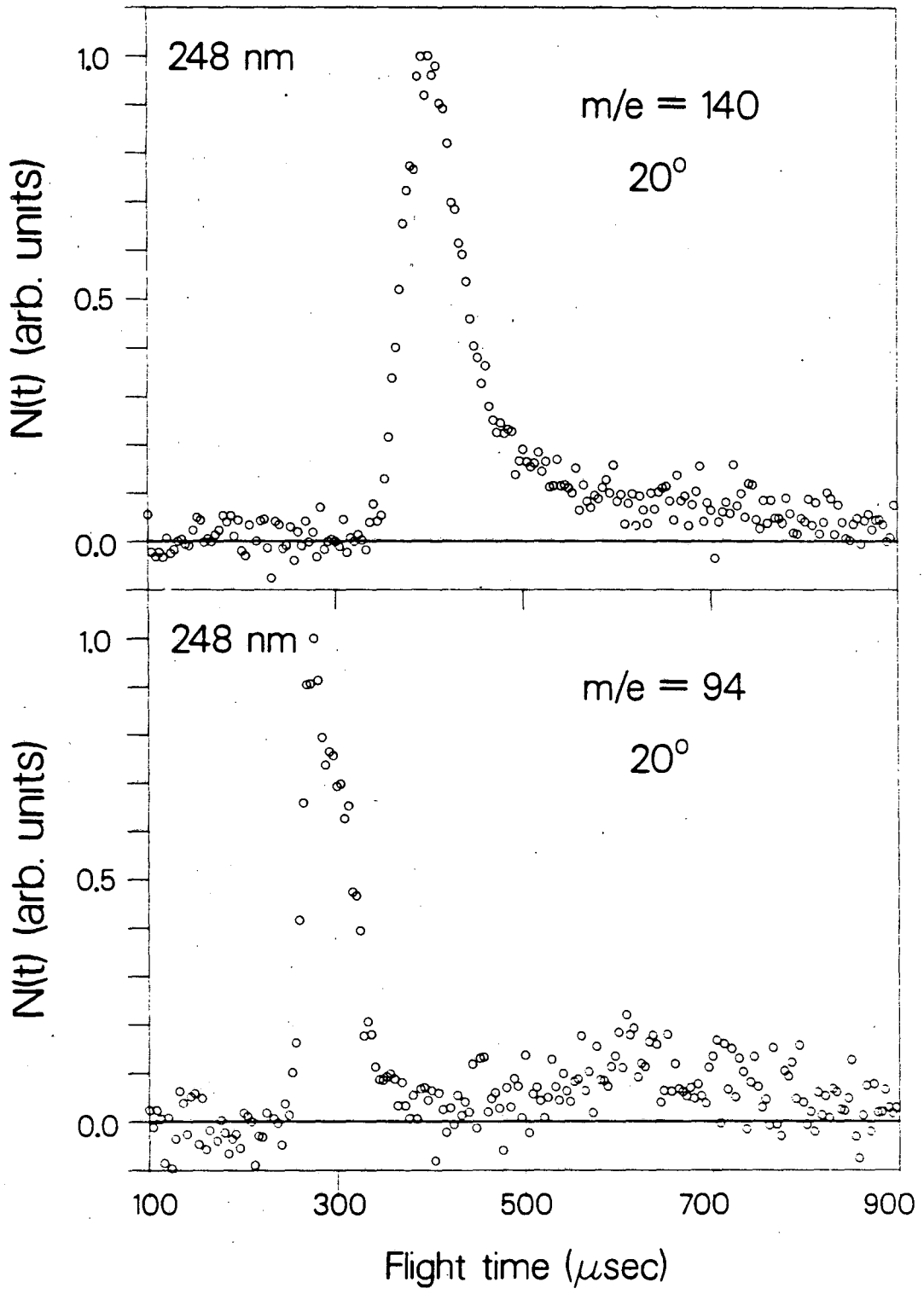

XBL 858 3729

Fig. 12

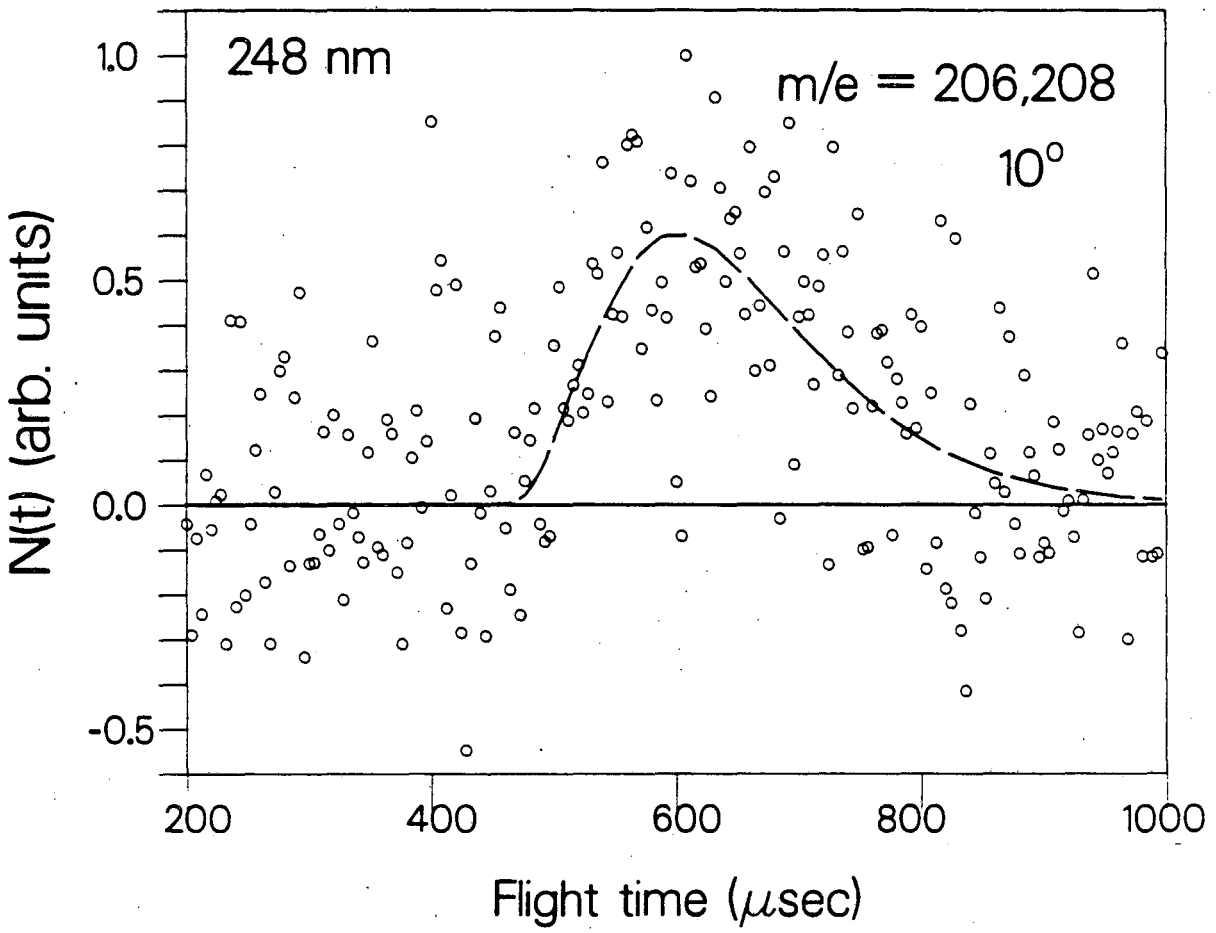

XBL 858 3724

Fig. 13

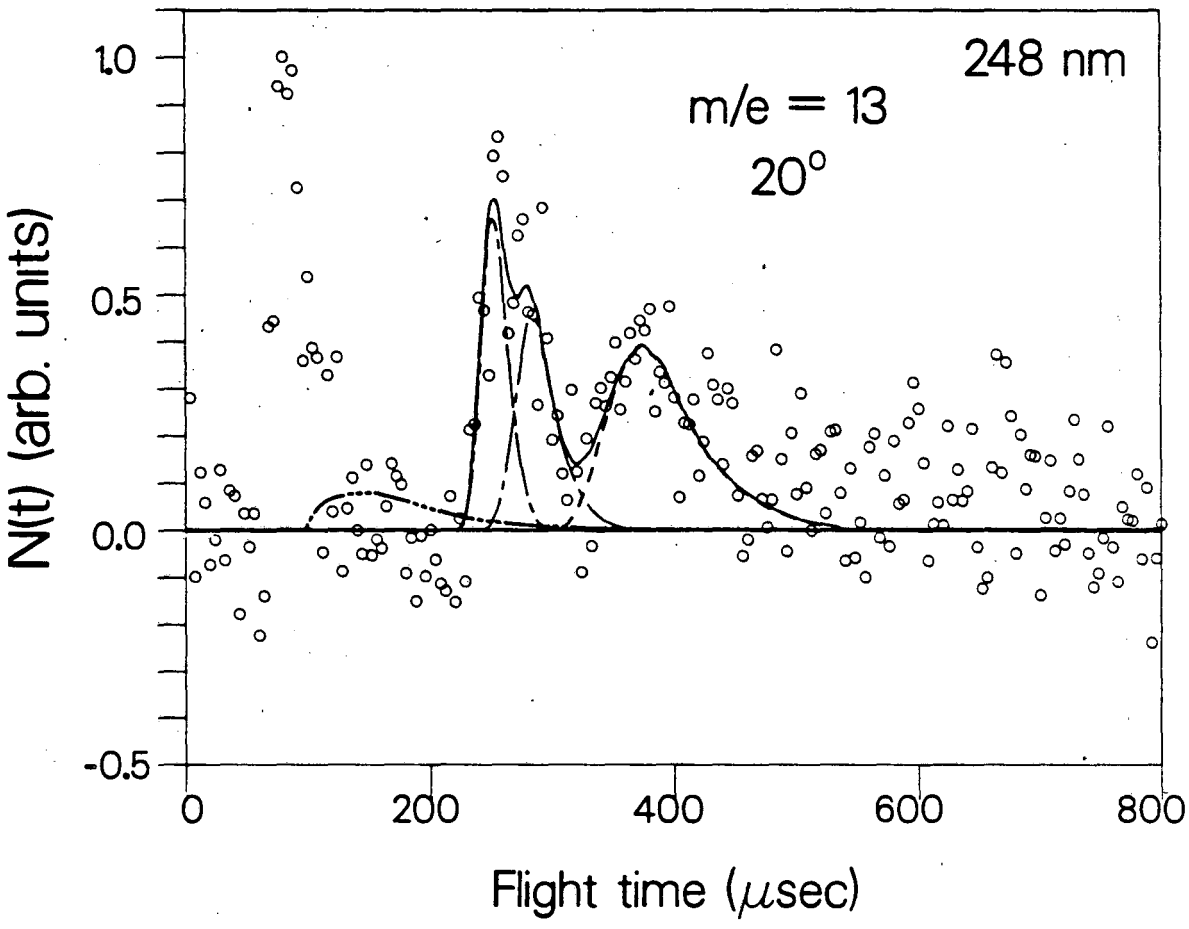

XBL 858 3723

Fig. 14

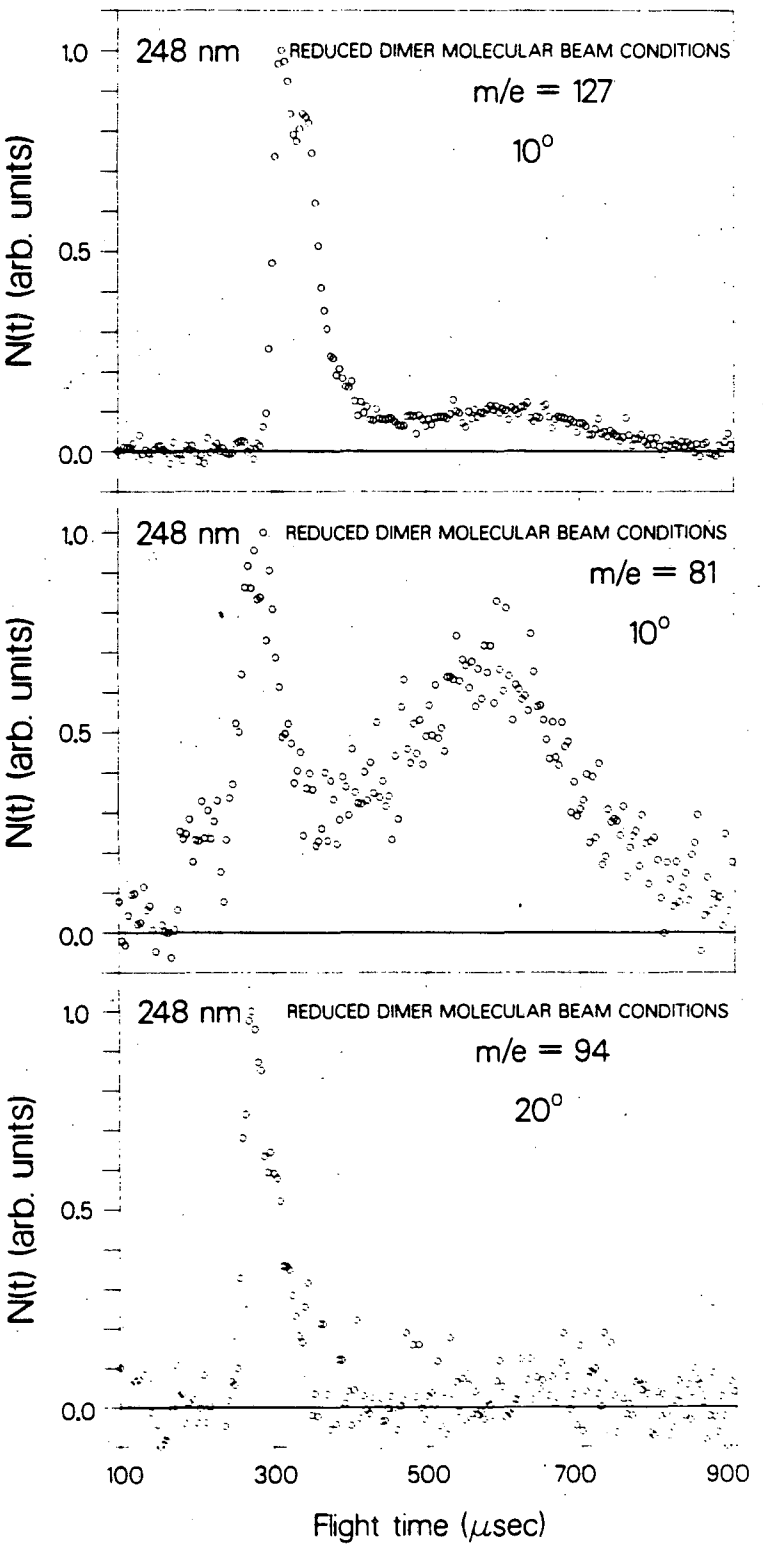

XBL 859 3800

Fig. 15

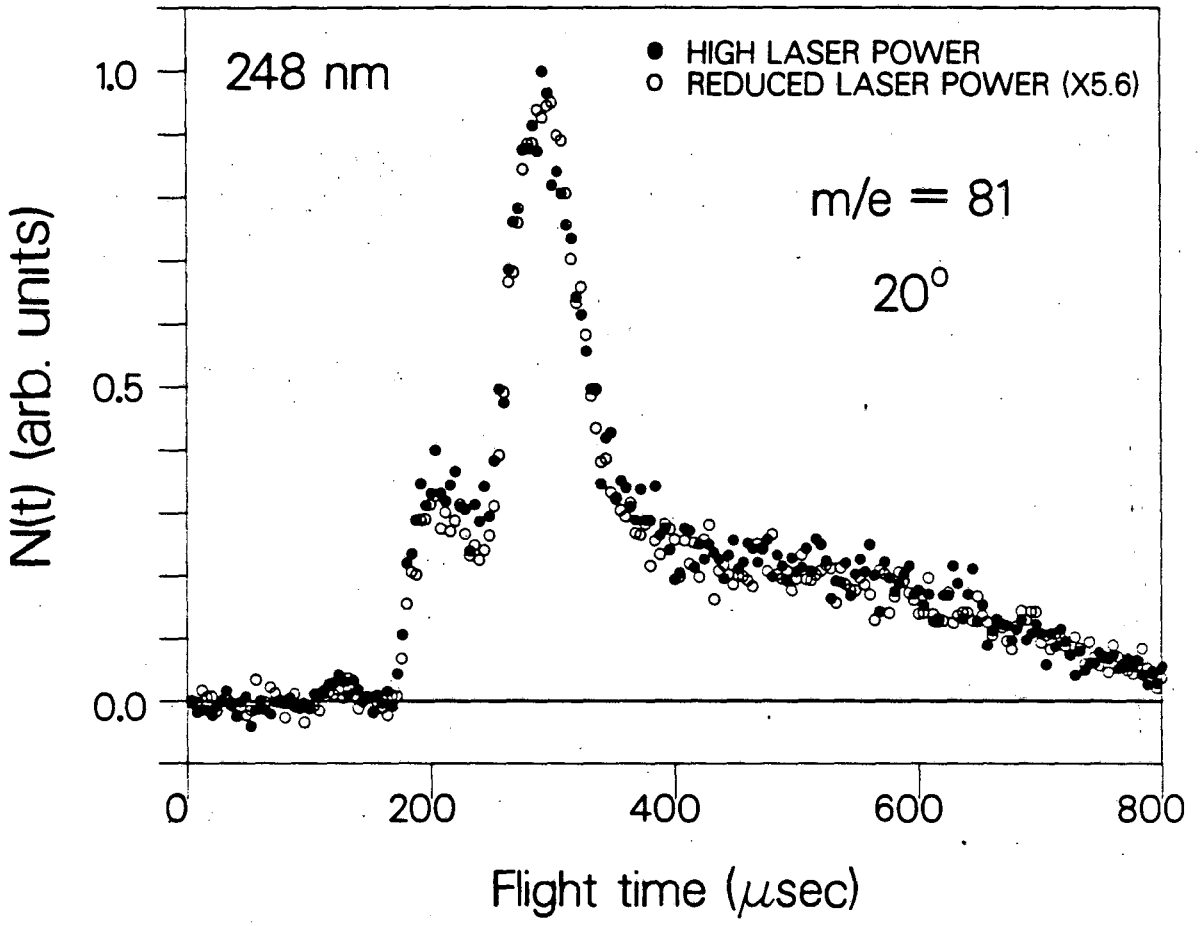

XBL 859 3795

Fig. 16

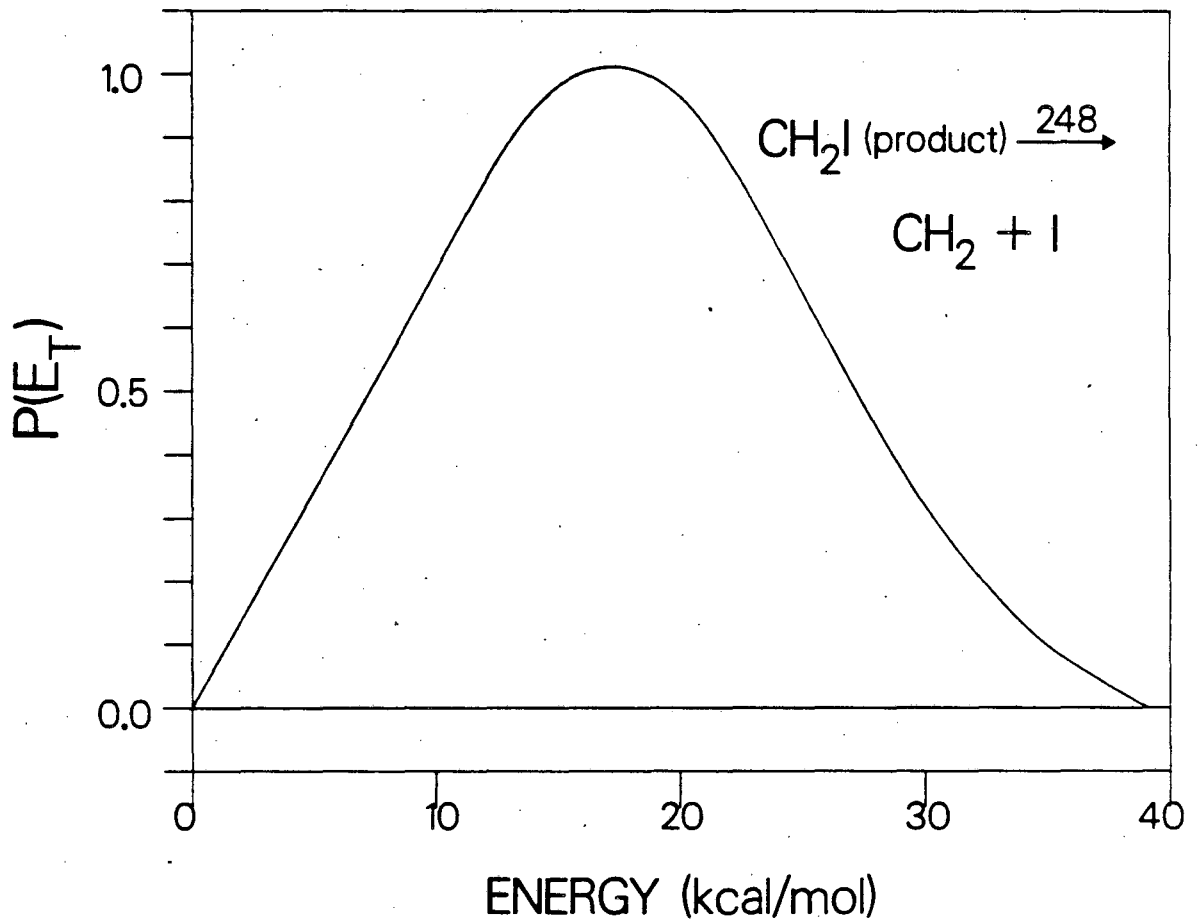

XBL 858 3720

Fig. 17

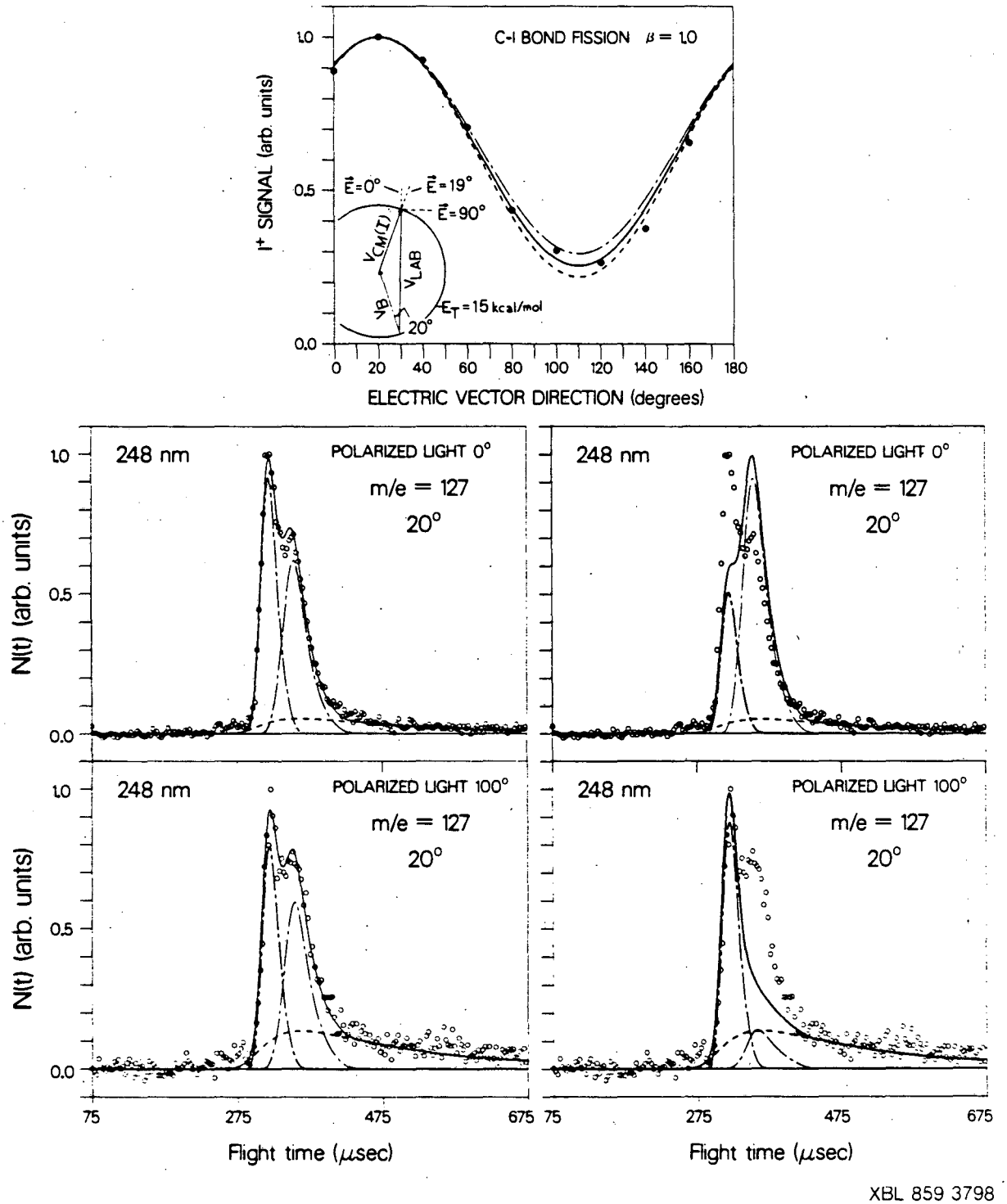
C-I BOND FISSION β = 1.0
I+ SIGNAL (arb. units)
1.0
0.5
0.0
0 20 40 60 80 100 120 140 160 180
ELECTRIC VECTOR DIRECTION (degrees)
E=0°
E=19°
E=90°
V(M/I)
VLAB
VR
ET = 15 kcal/mol
20°
248 nm
POLARIZED LIGHT 0°
m/e = 127
20°
248 nm
POLARIZED LIGHT 0°
m/e = 127
20°
248 nm
POLARIZED LIGHT 100°
m/e = 127
20°
248 nm
POLARIZED LIGHT 100°
m/e = 127
20°
N(t) (arb. units)
N(t) (arb. units)
1.0
0.5
0.0
75 275 475 675
Flight time (μsec)
75 275 475 675
Flight time (μsec)
XBL 859 3798

Fig. 18

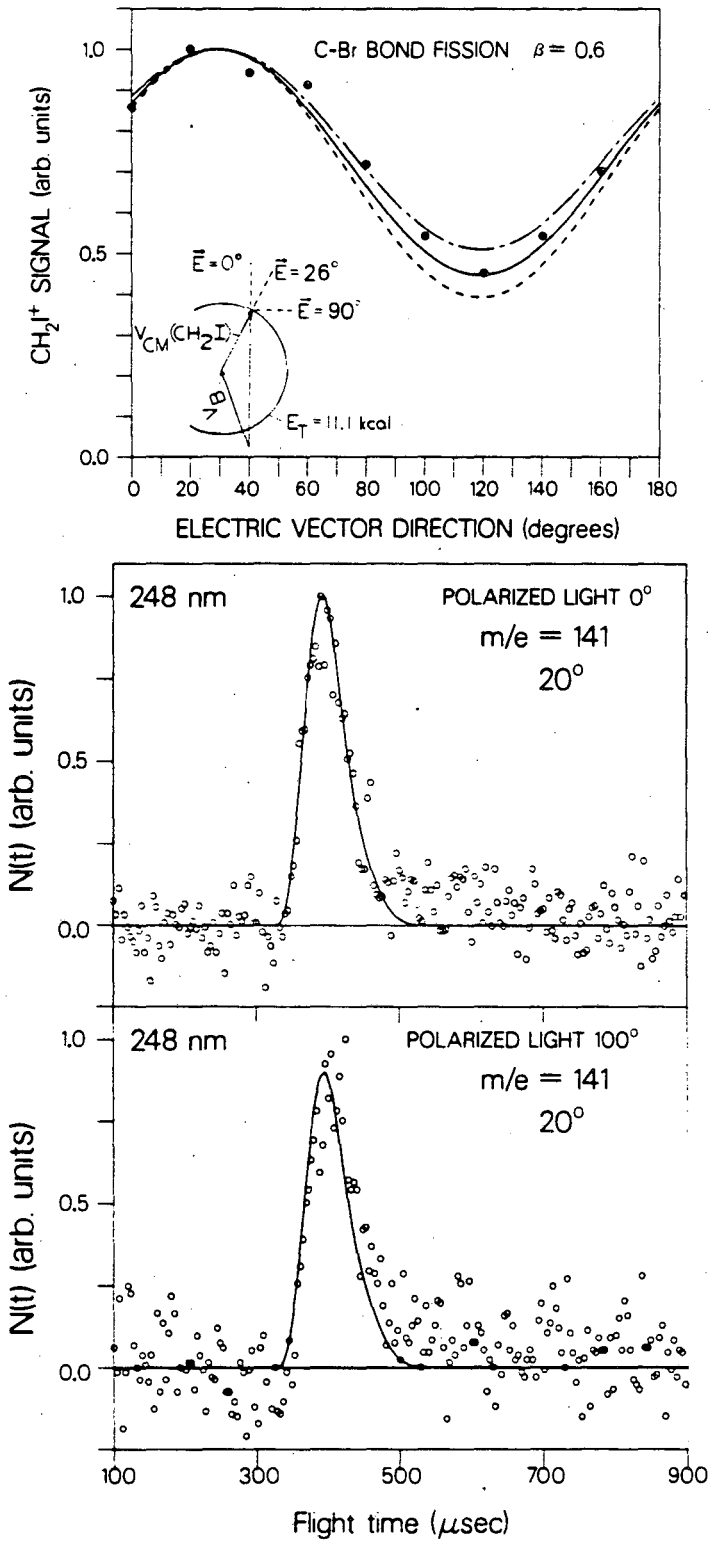

XBL 859 3971

Fig. 19

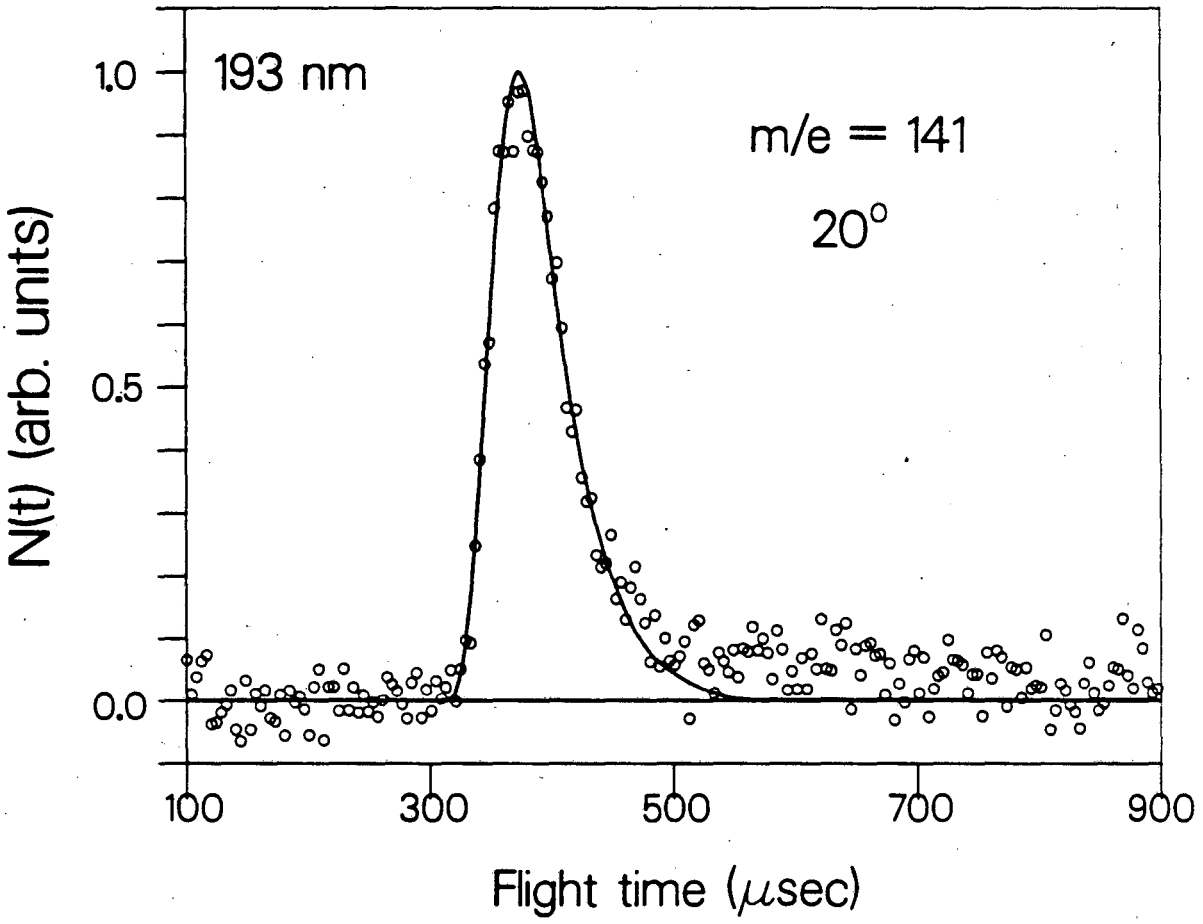

XBL 858 3725

Fig. 20

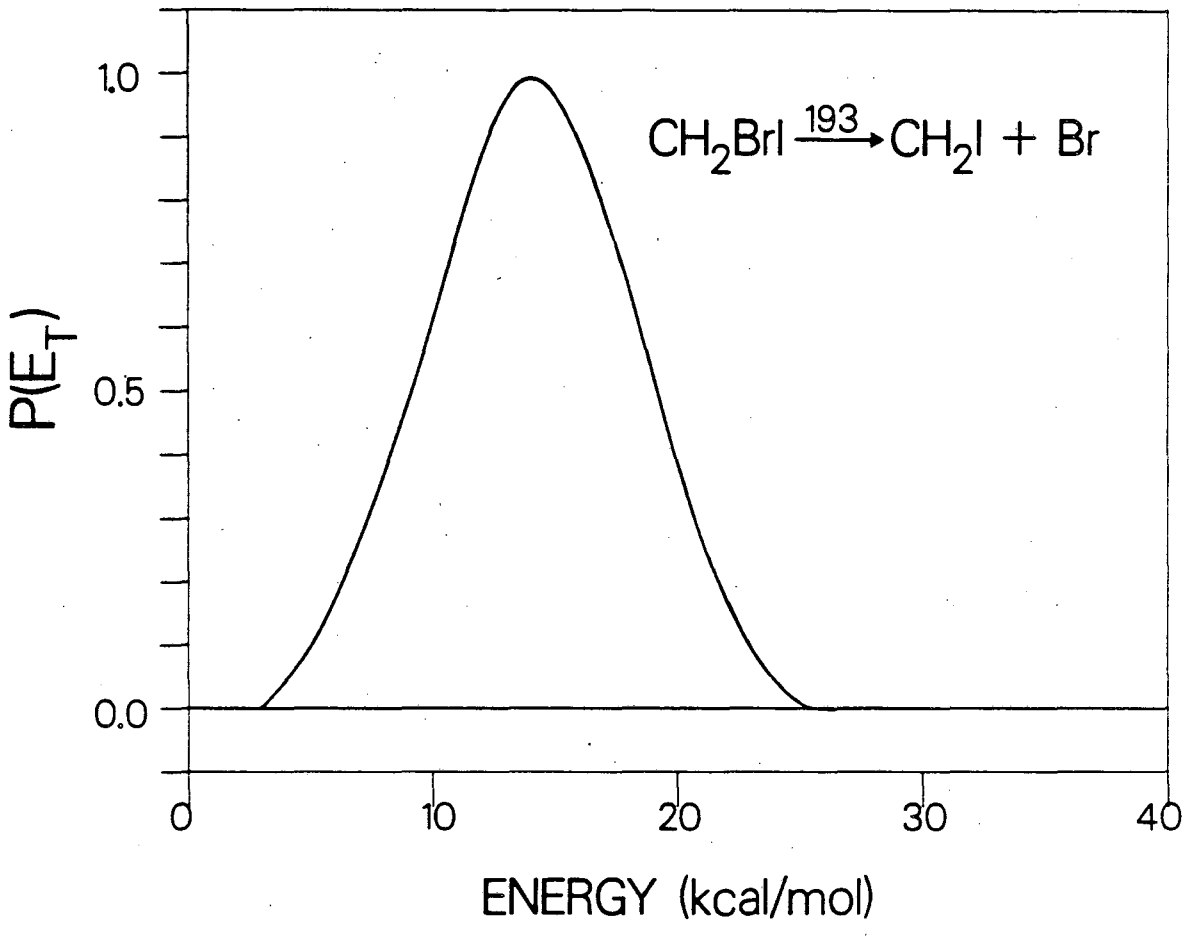

XBL 858 3730

Fig. 21

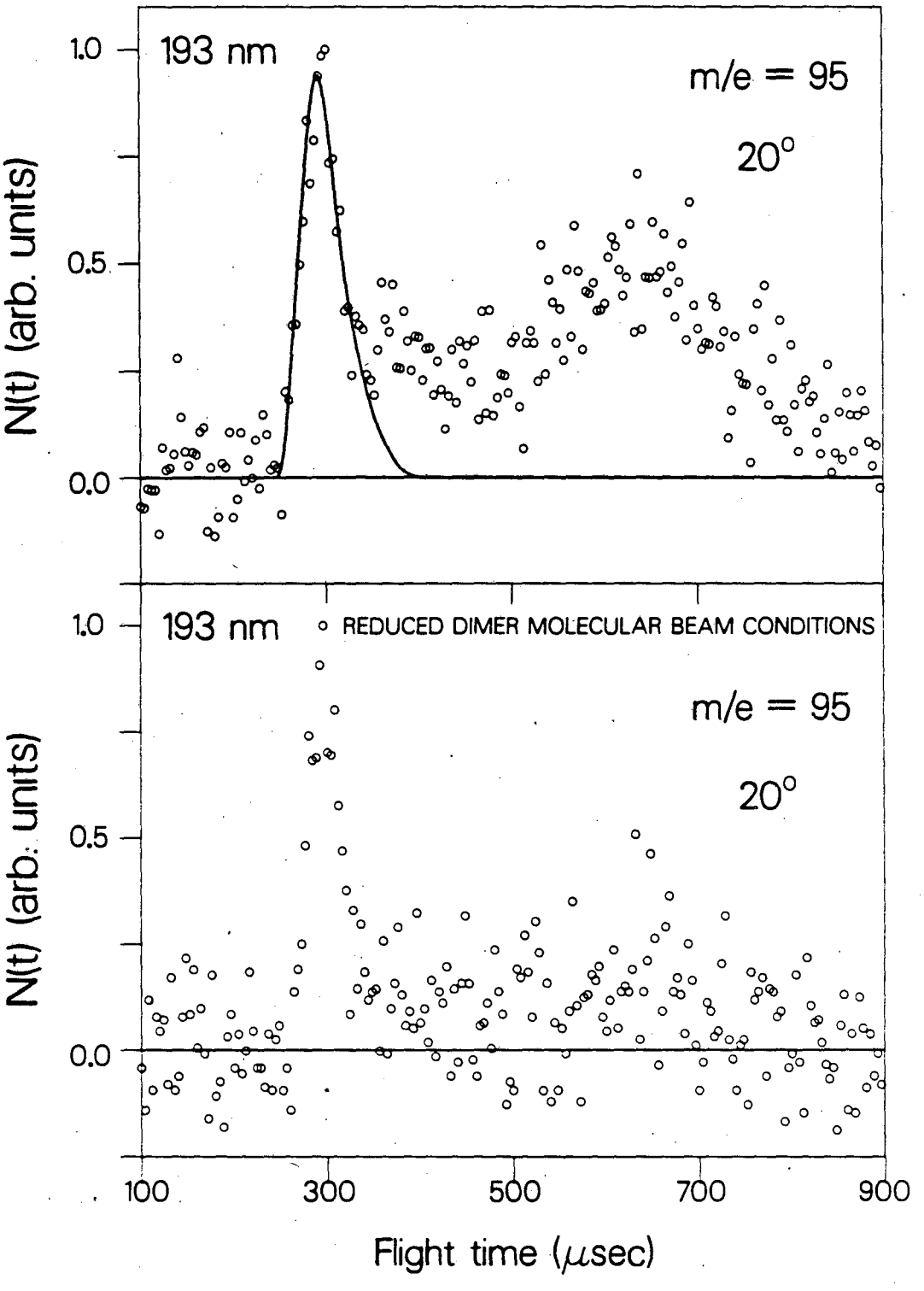

XBL 859 3797

Fig. 22

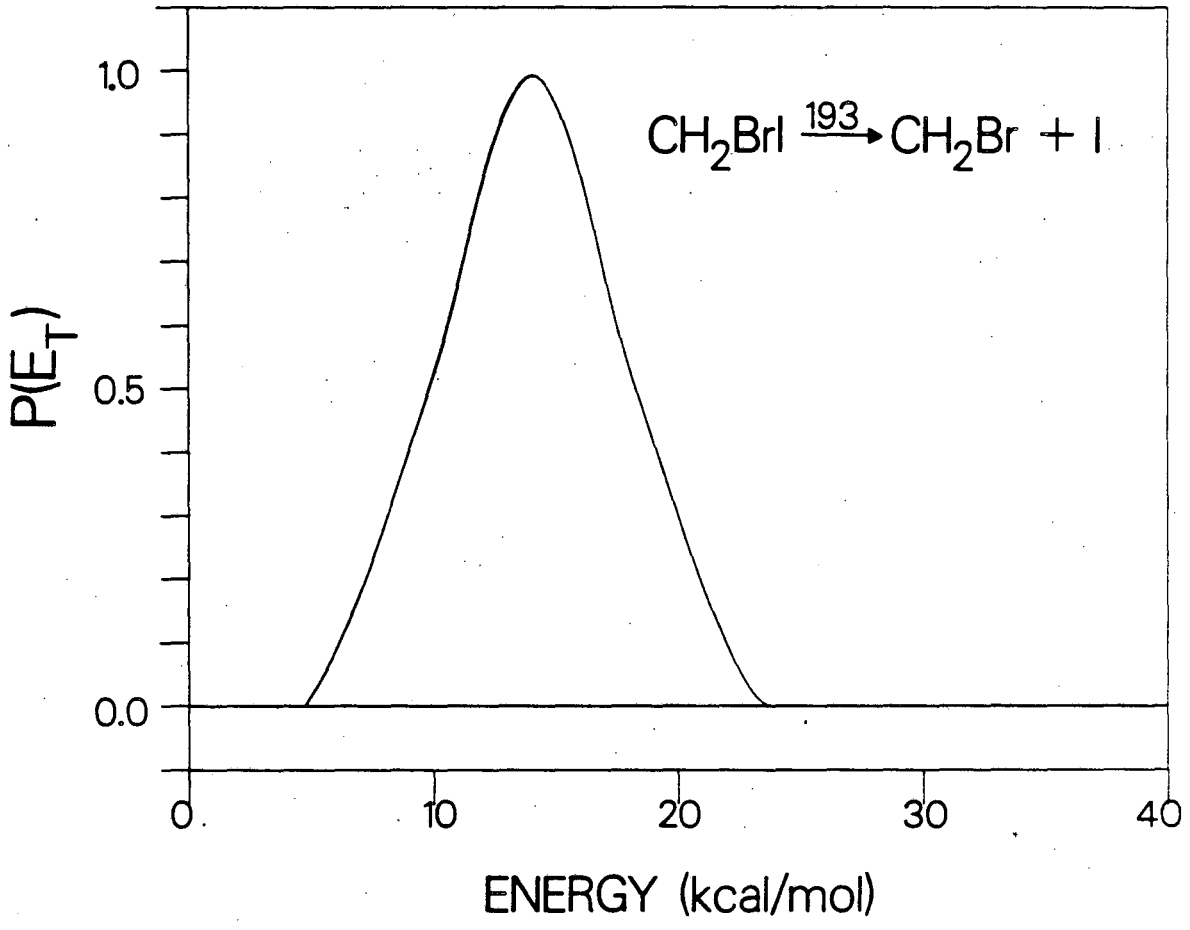

XBL 858 3726

Fig. 23

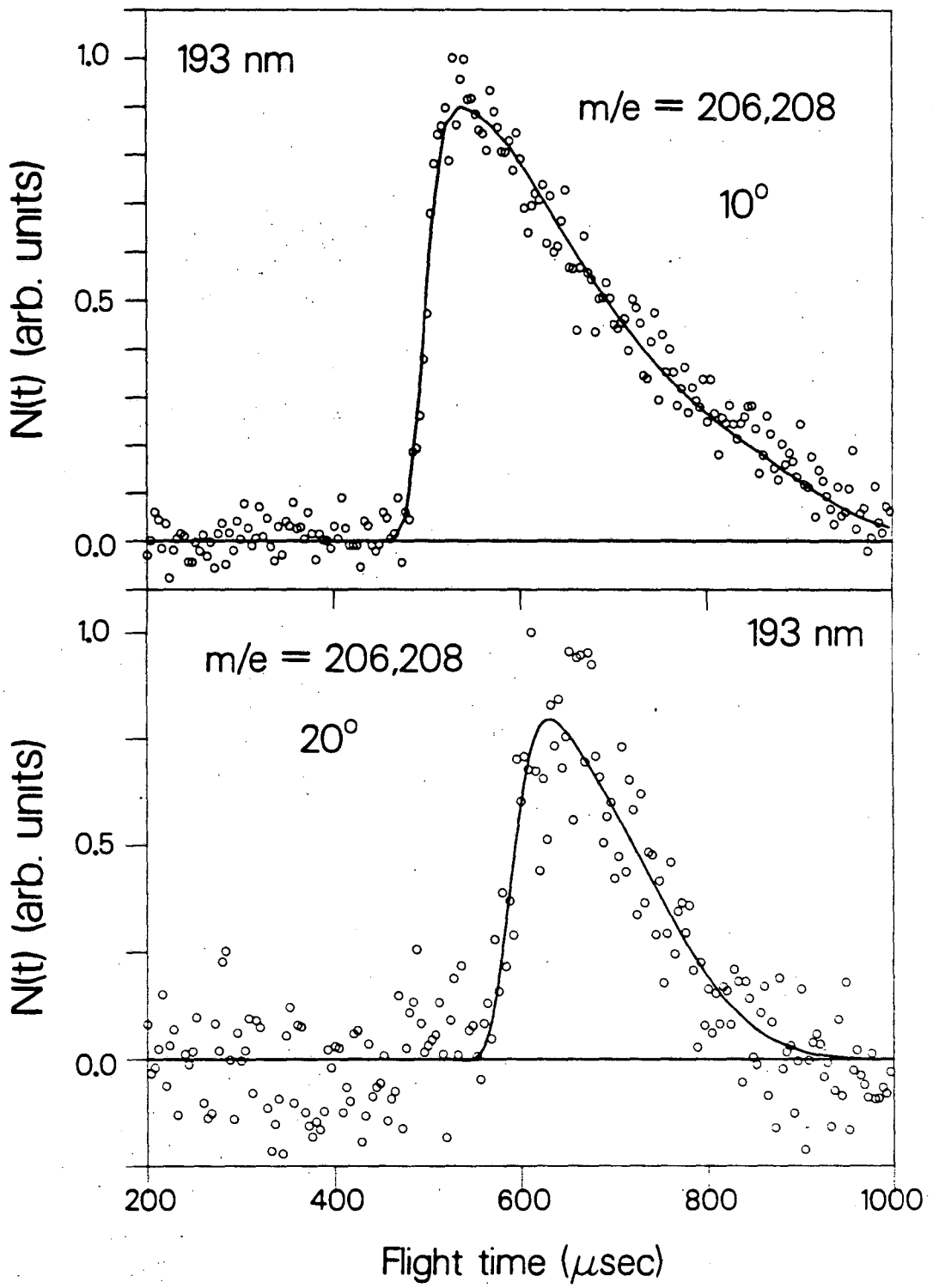

XBL 859 3796

Fig. 24

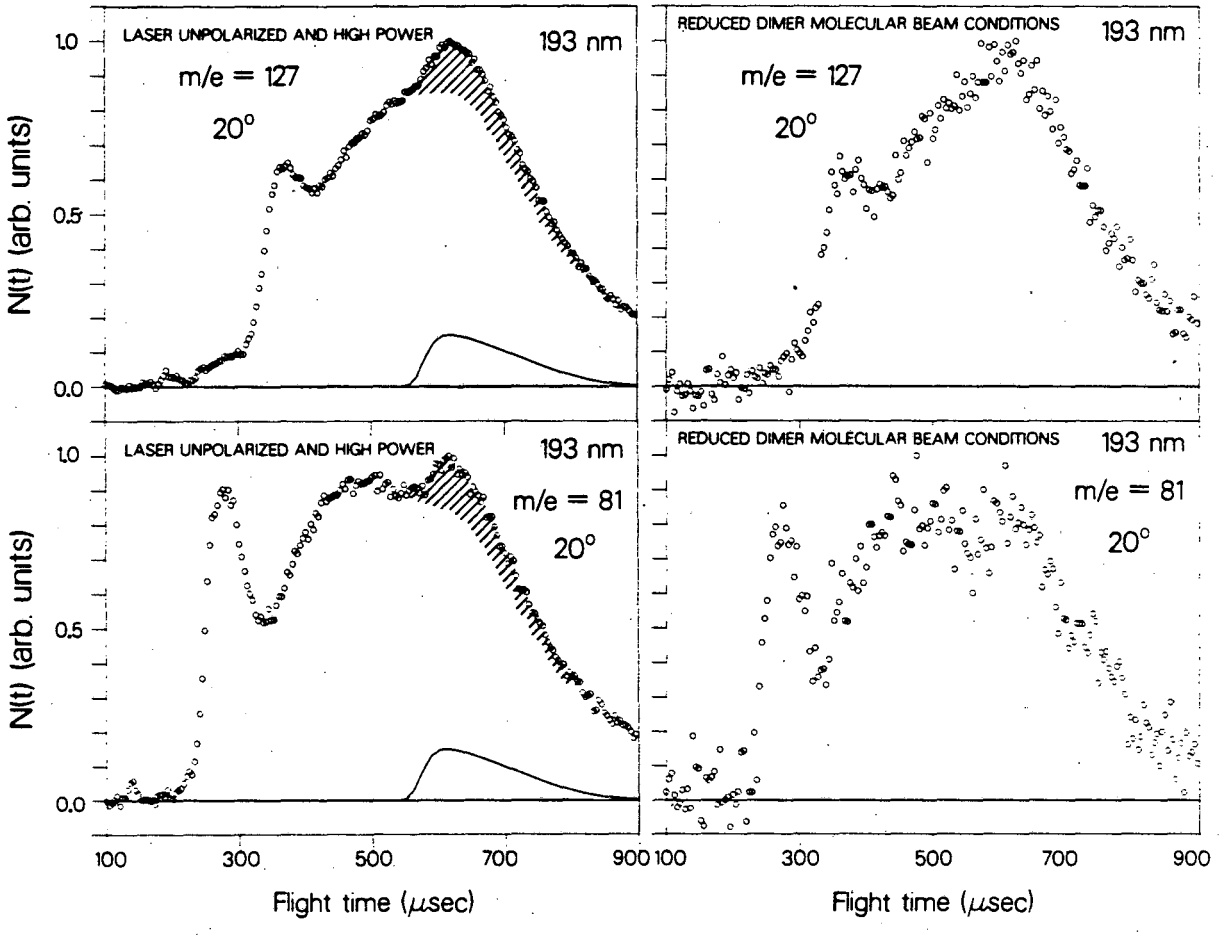

XBL 859 3802

Fig. 25

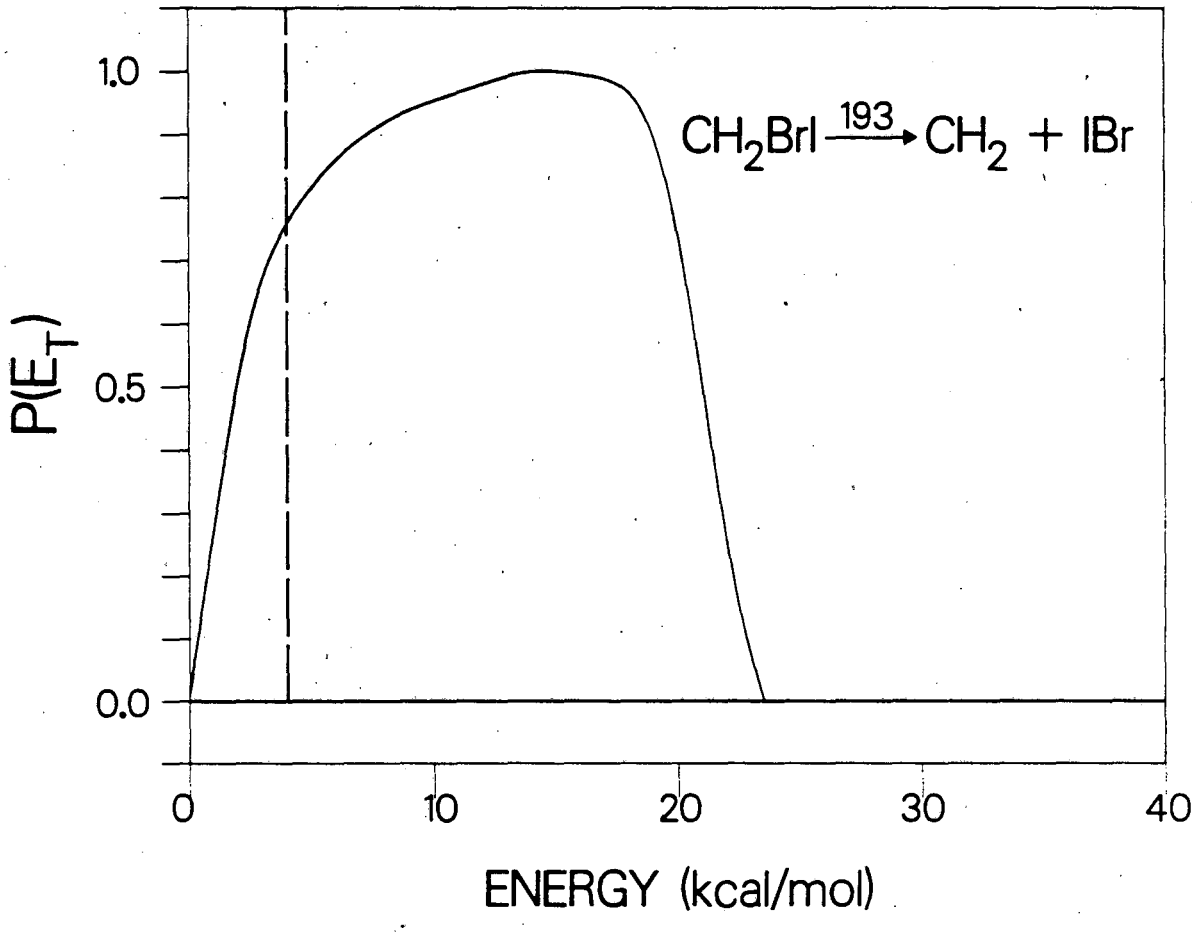

XBL 859 3794

Fig. 26

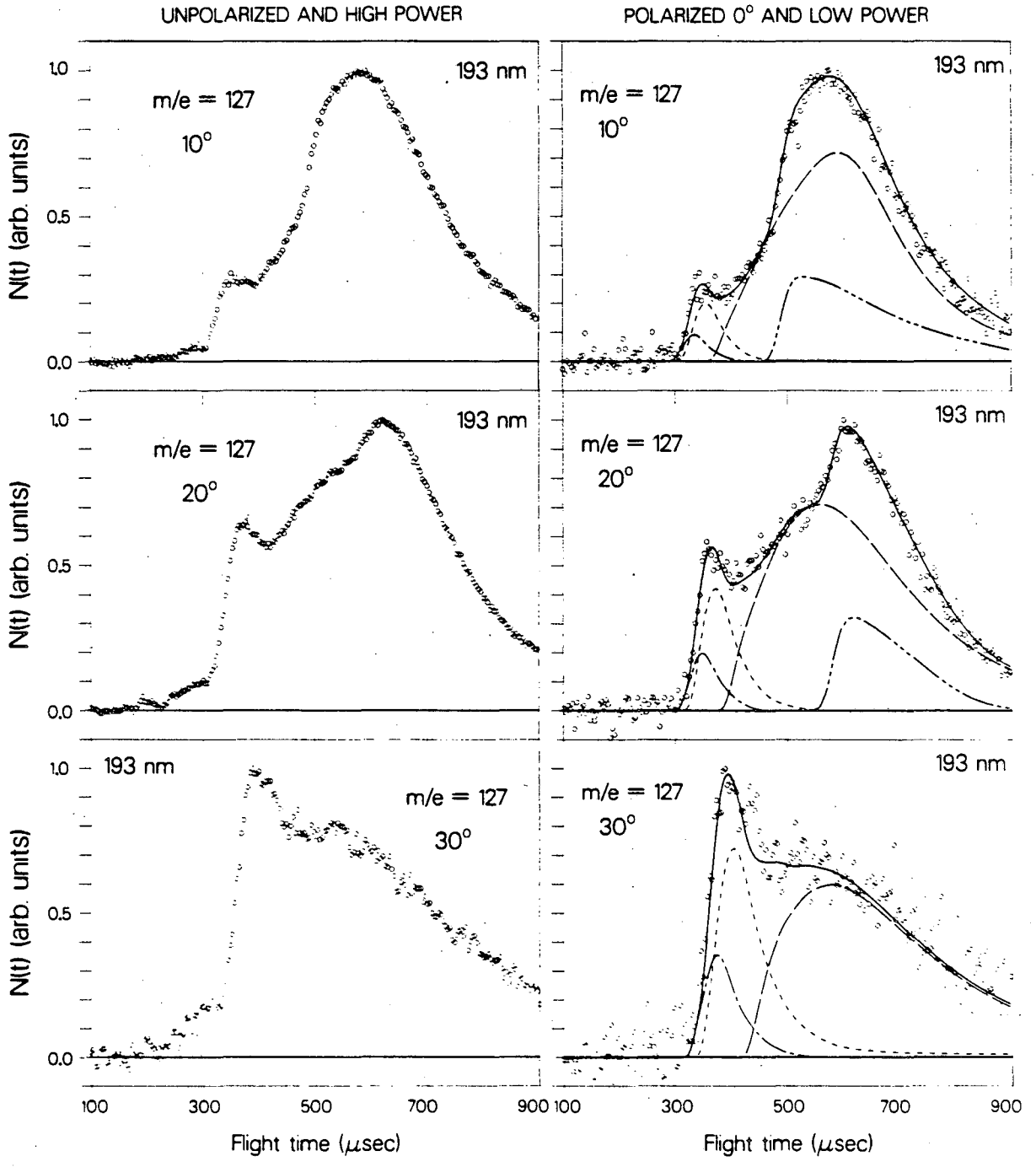

XBL 859 3801

Fig. 27

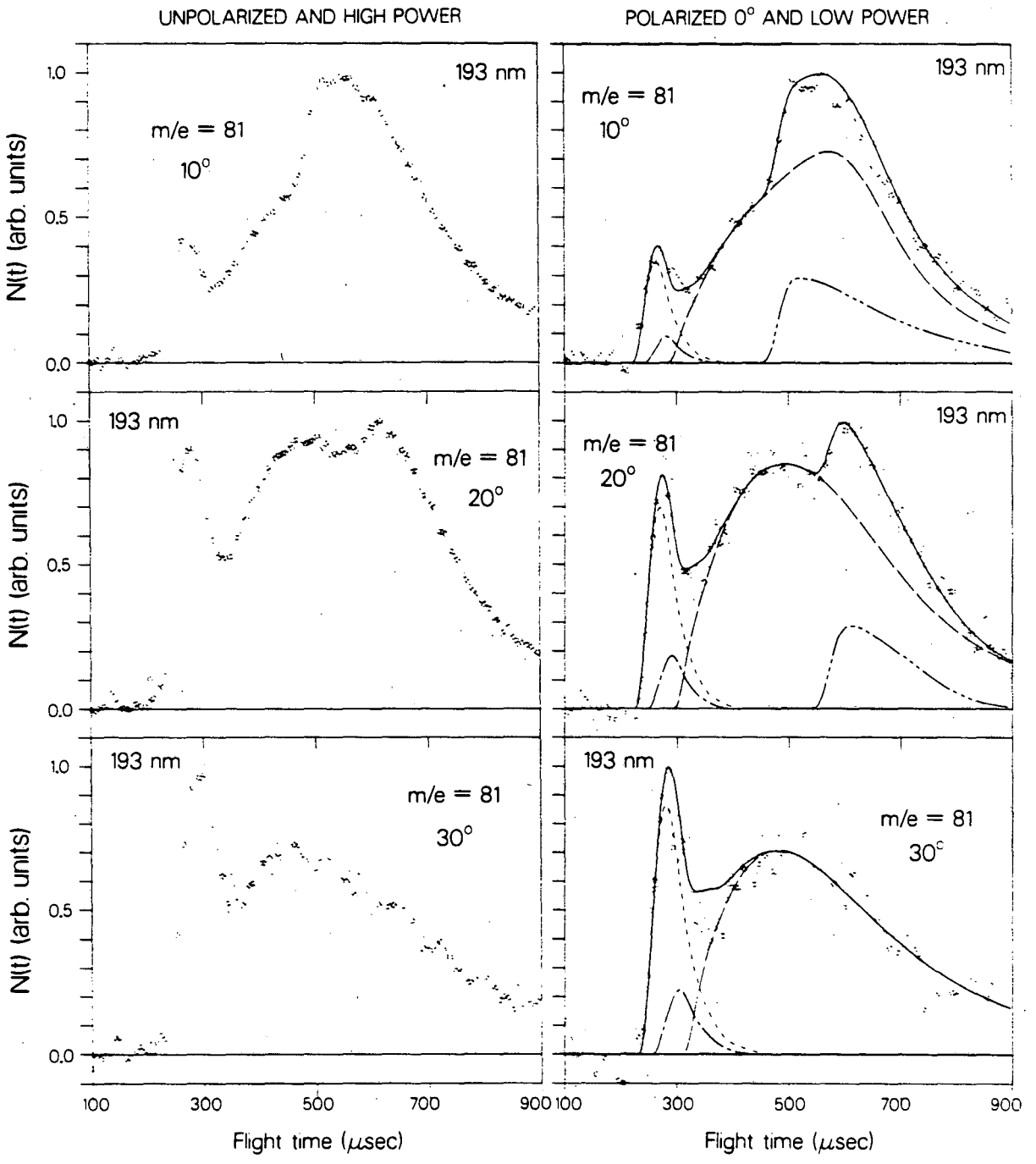

XBL 859 3824

Fig. 28

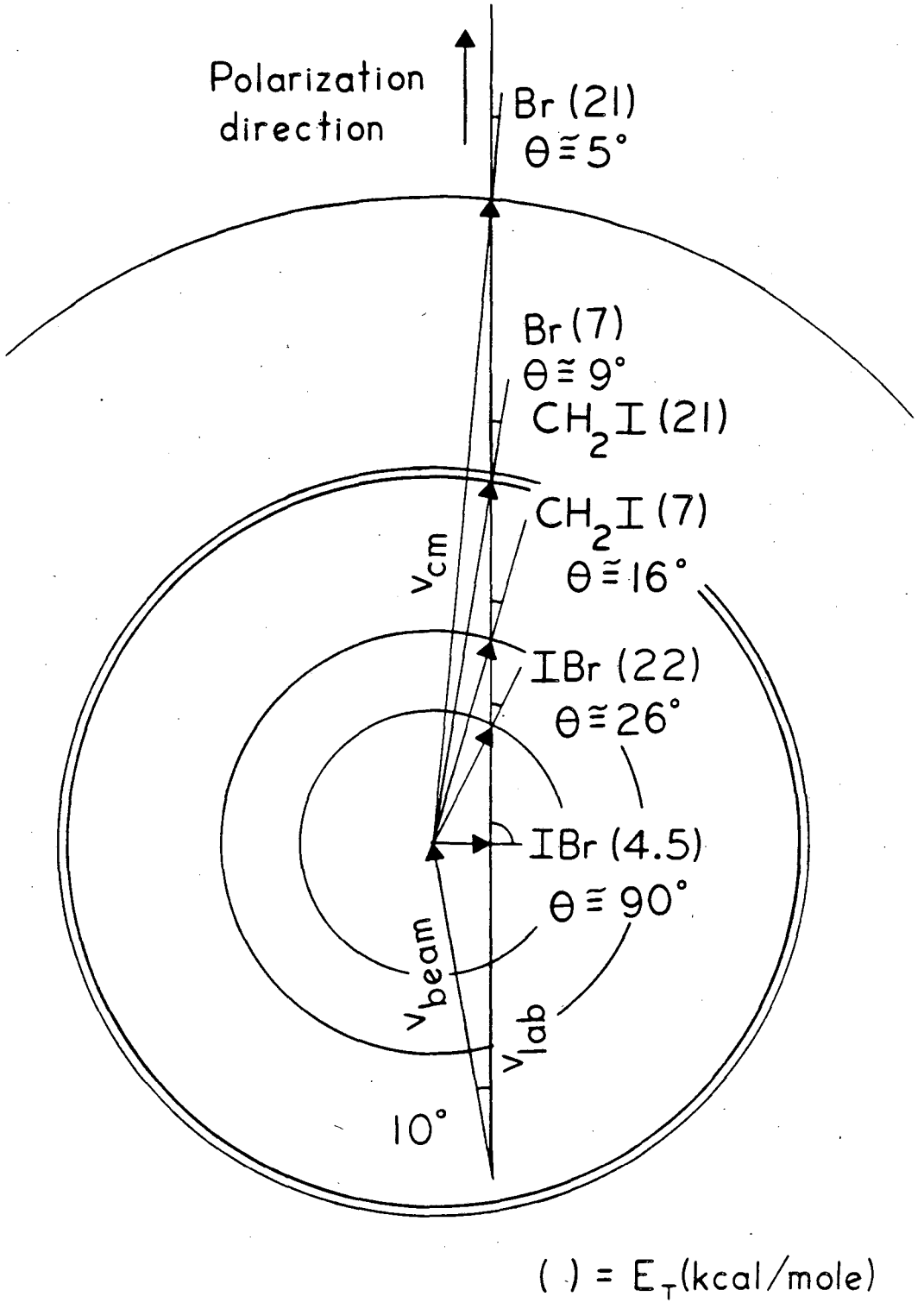

XBL 859-4101

Fig. 29

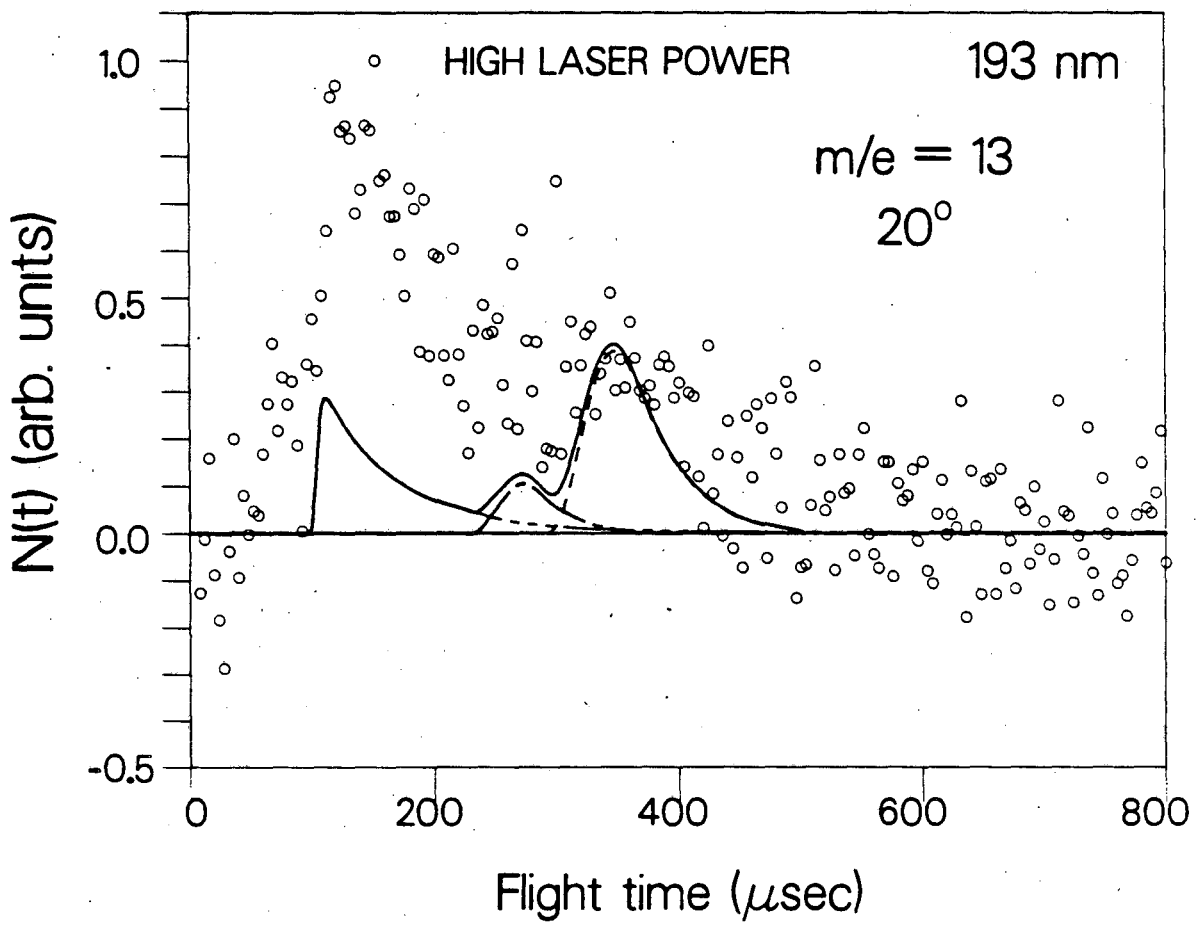

XBL 859 3826

Fig. 30

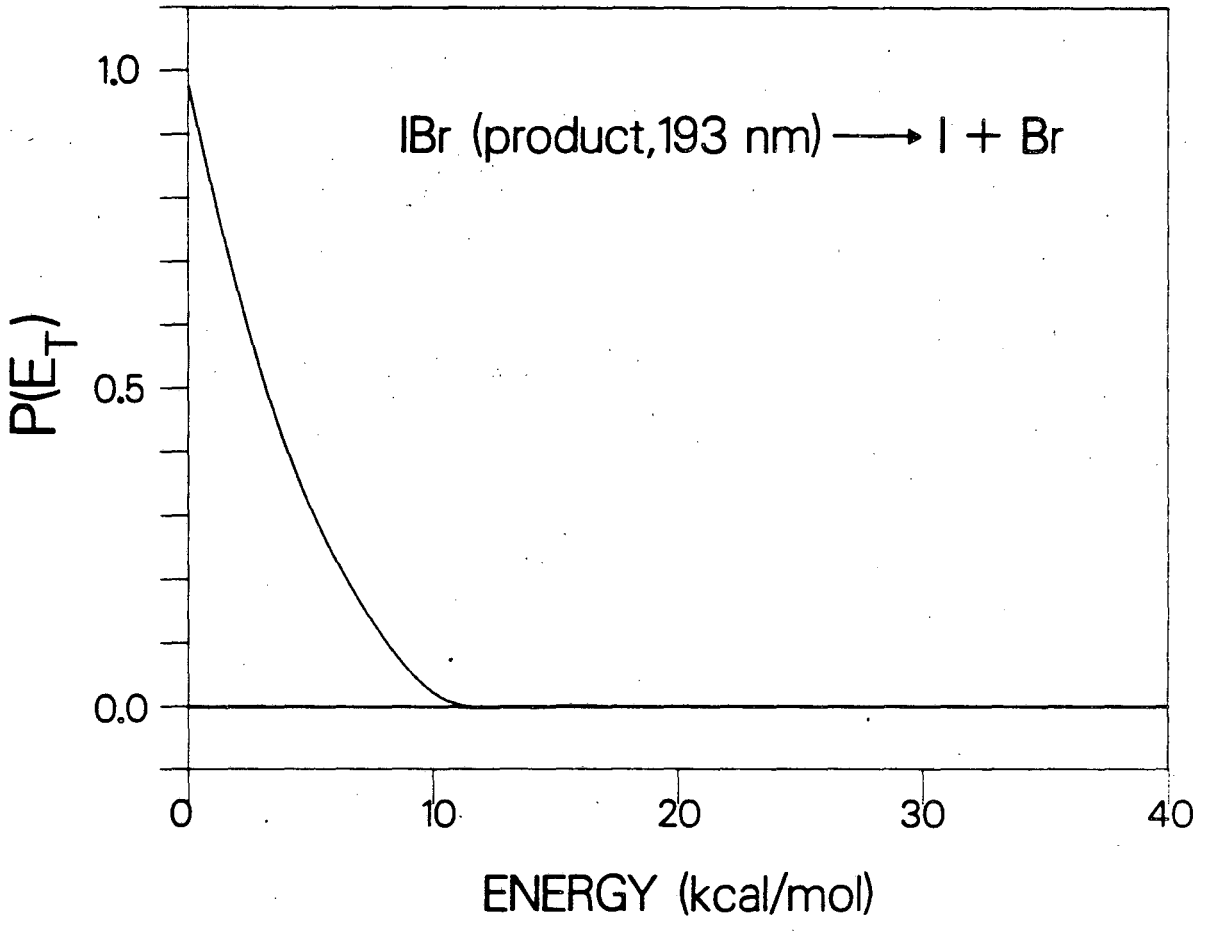

XBL 859 3828

Fig. 31

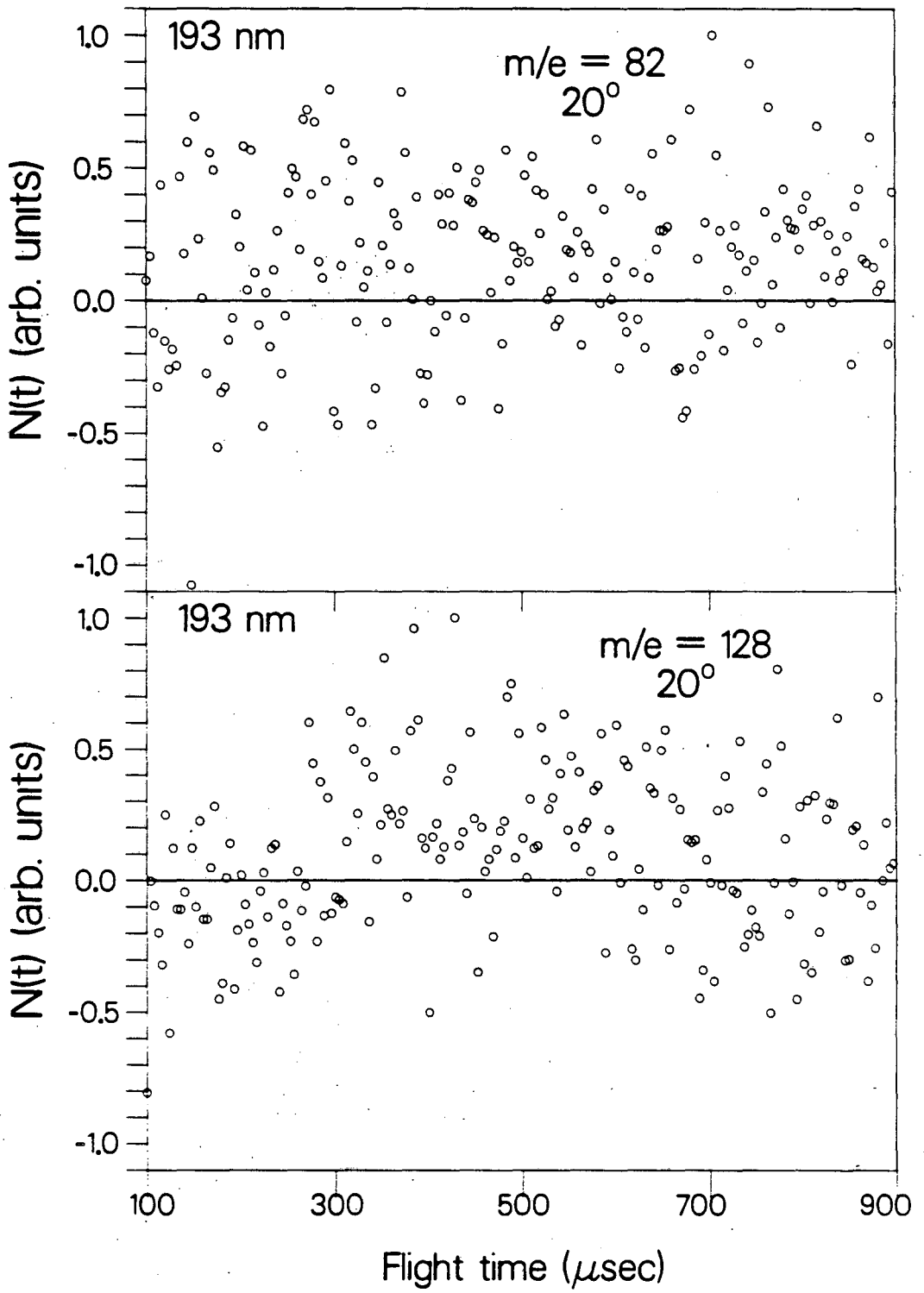

XBL 859 3825

Fig. 32

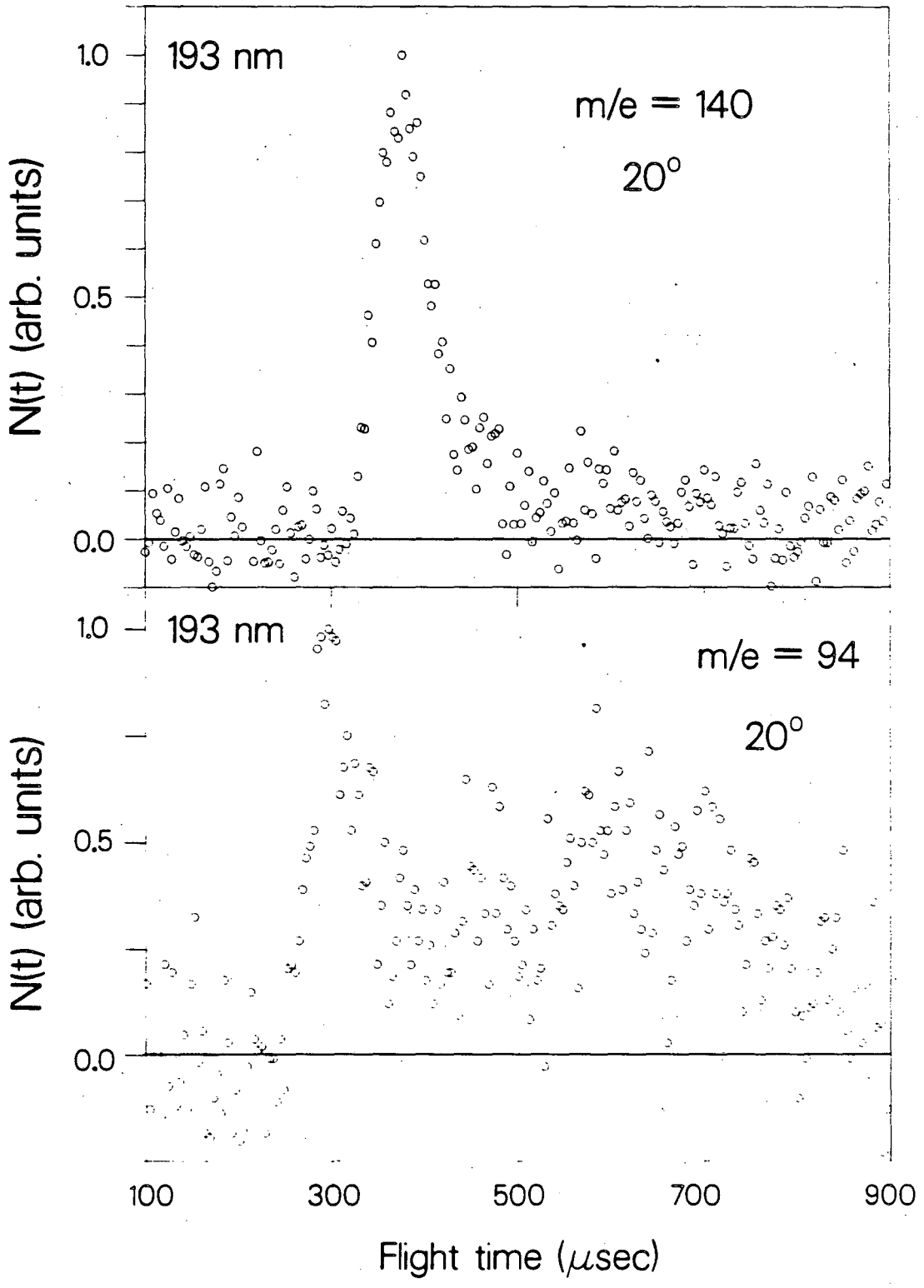

Fig. 33

XBL 859 3866

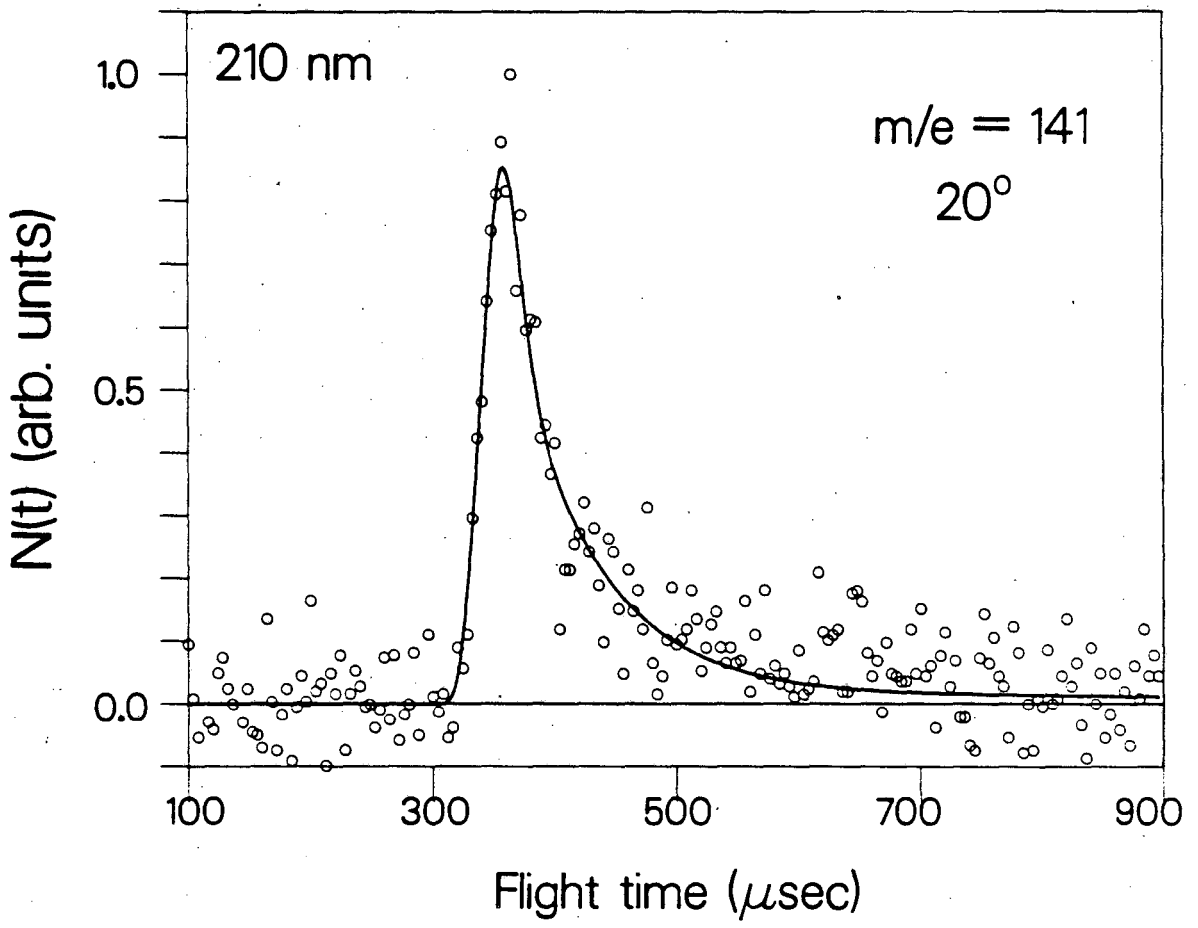

XBL 859 3827

Fig. 34

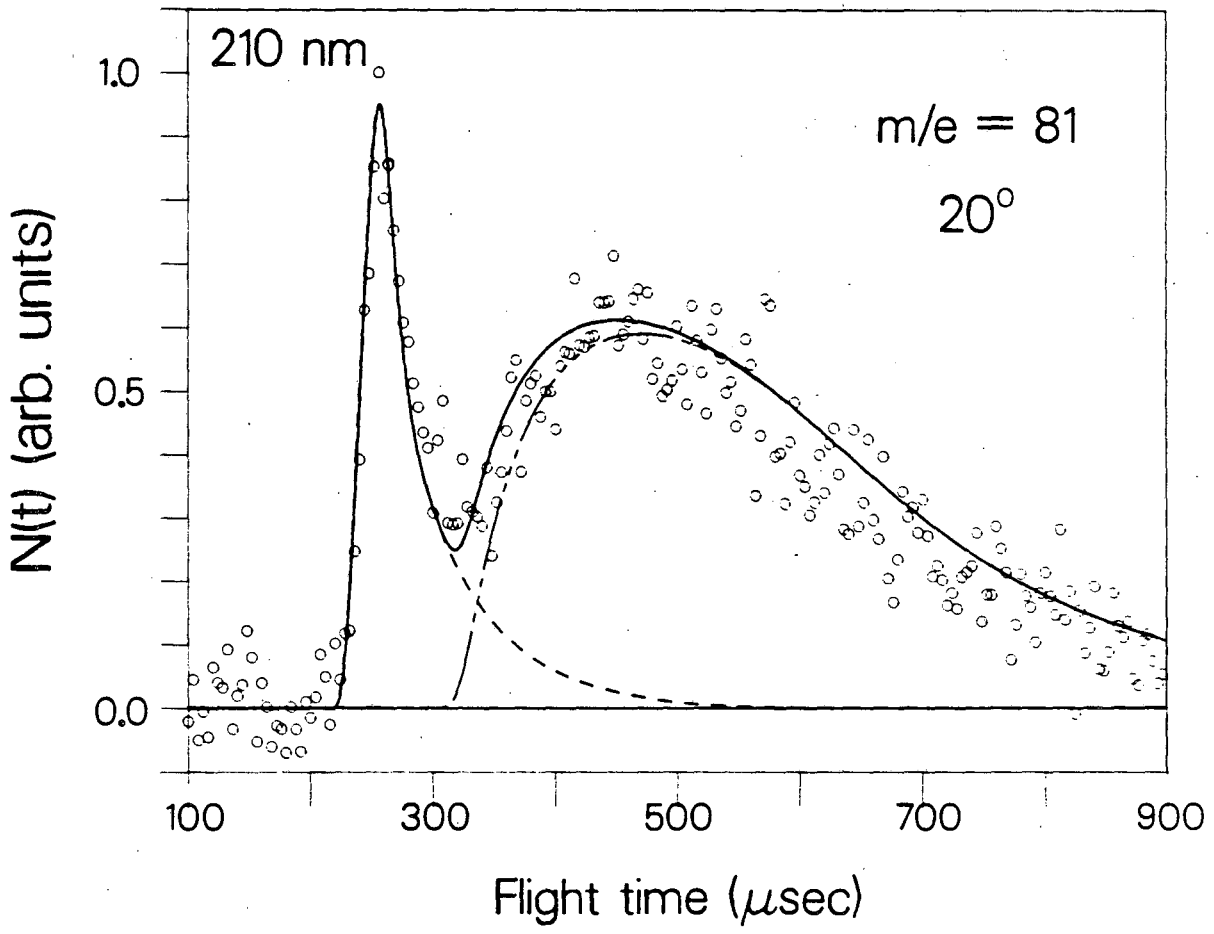

XBL859 3869

Fig. 35

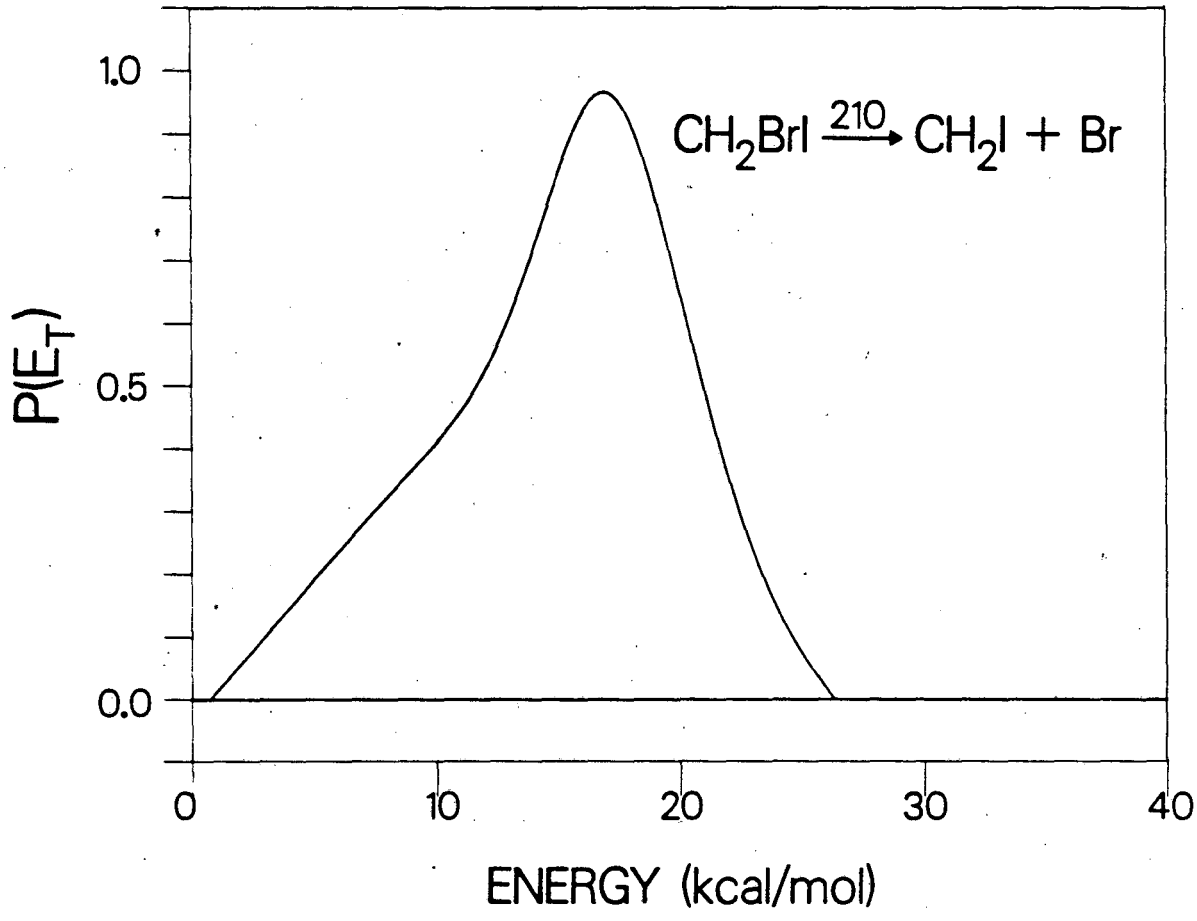

XBL 859 3829

Fig. 36

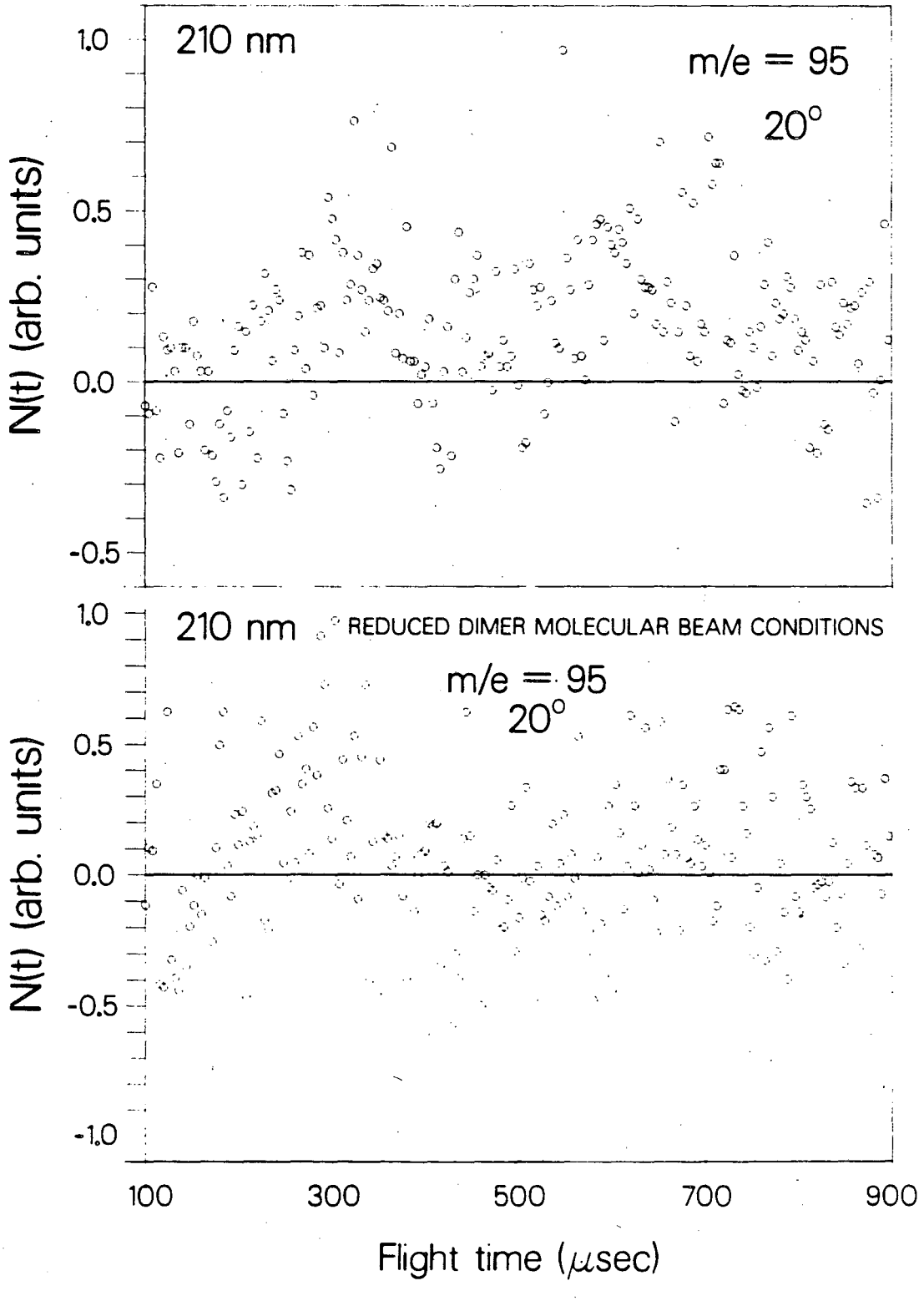

Fig. 37

XBL 859 3864

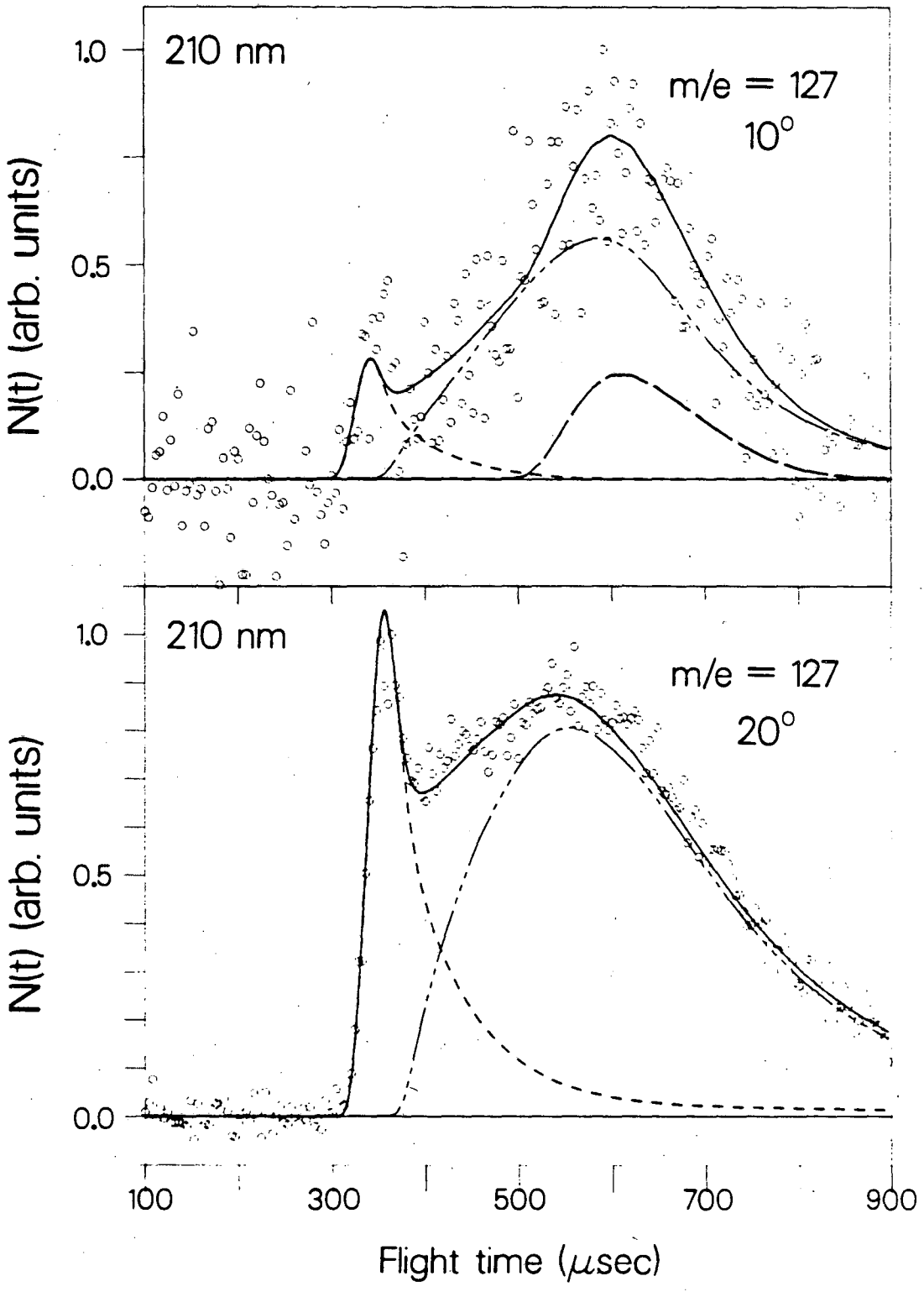

Fig. 38

XBL 859 3865

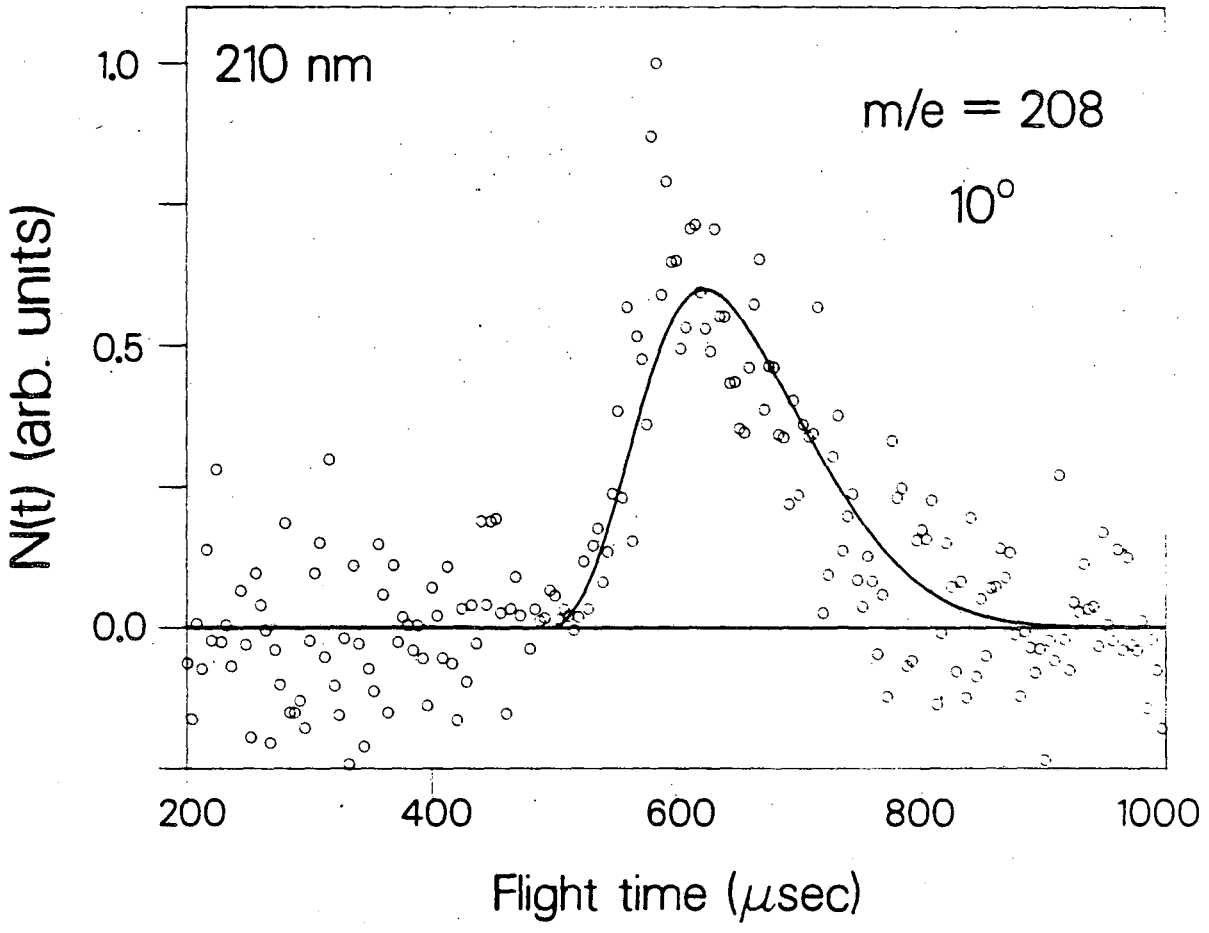

XBL 859 3868

Fig. 39

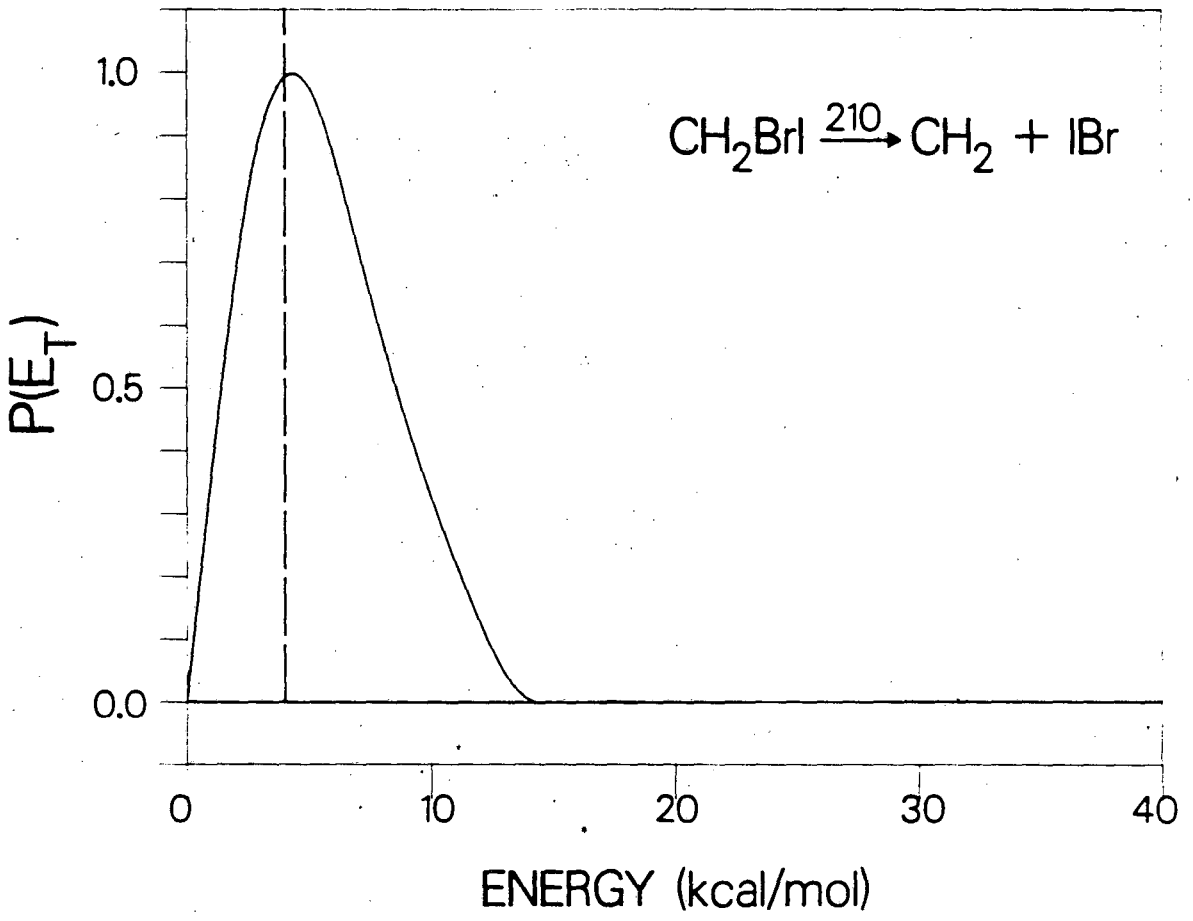

XBL 859 3872

Fig. 40

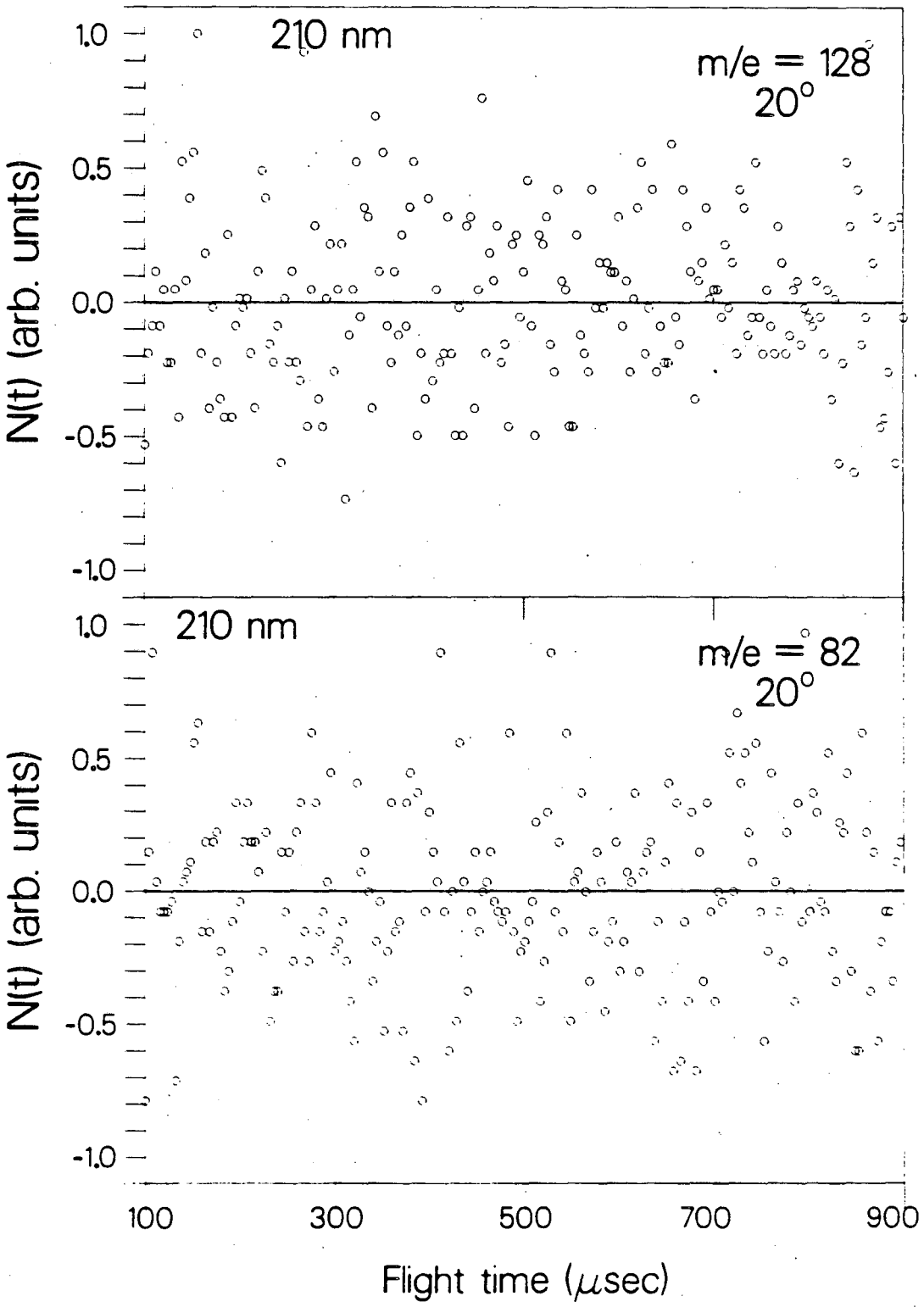

Fig. 41

XBL 859 3863

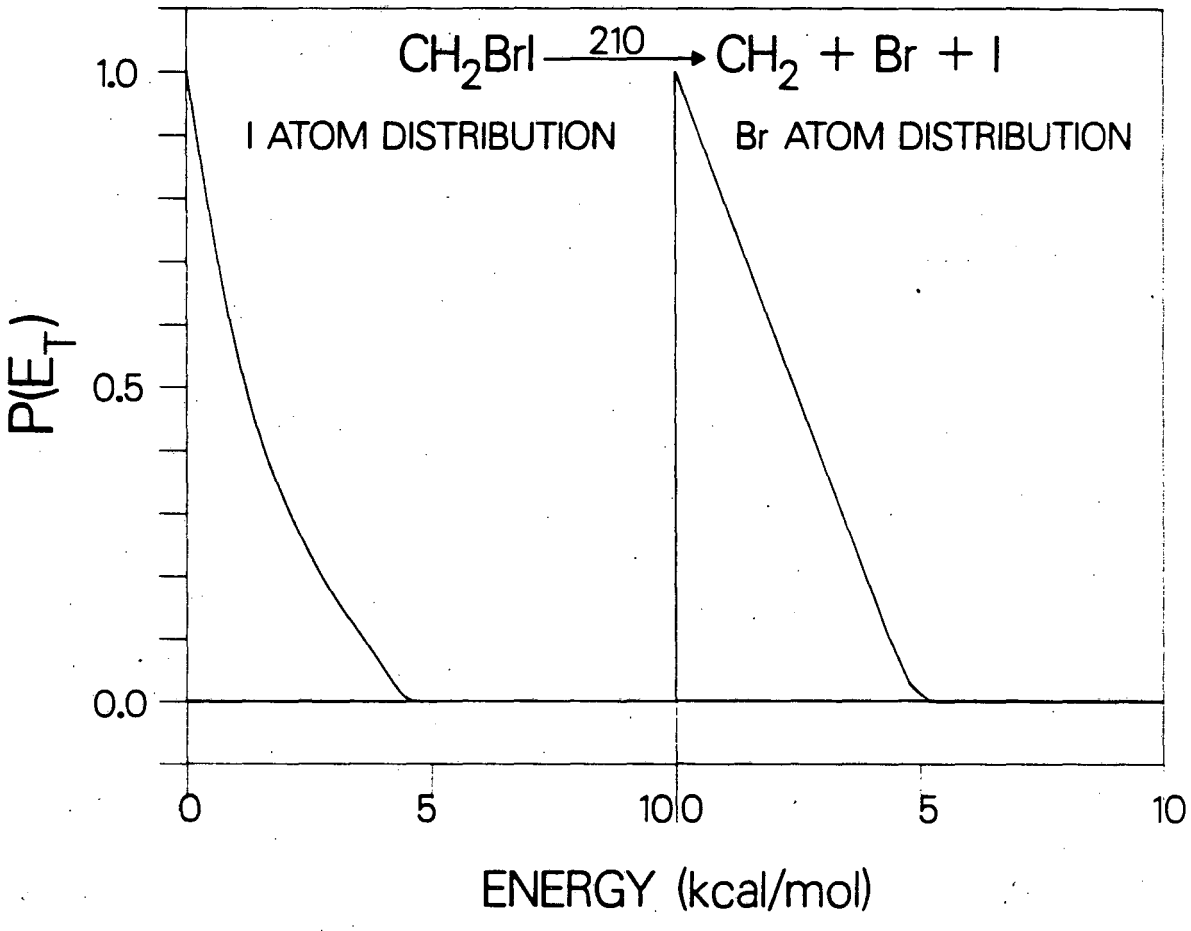

XBL 859 3867

Fig. 42

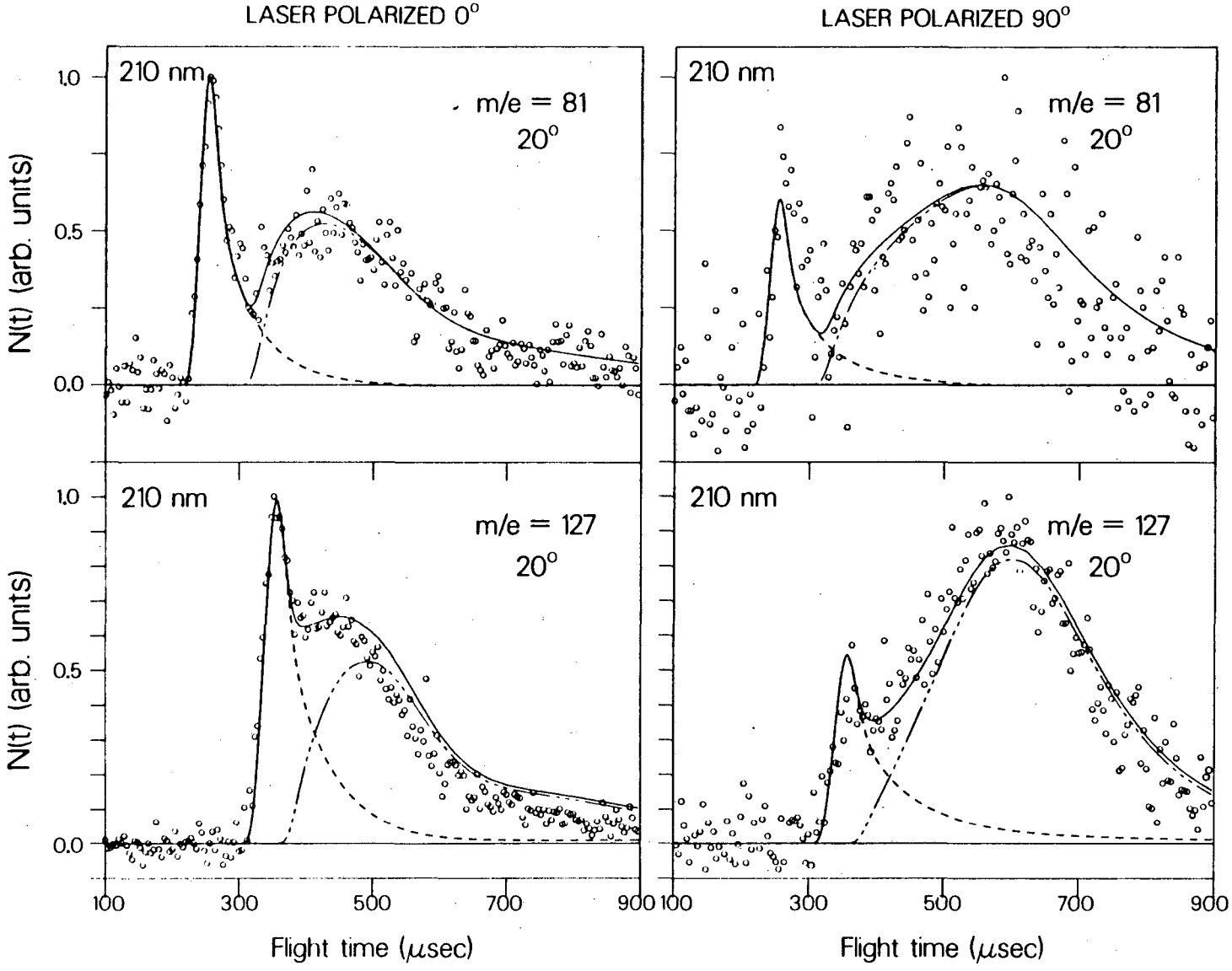

Fig. 43

XBL 859 3861

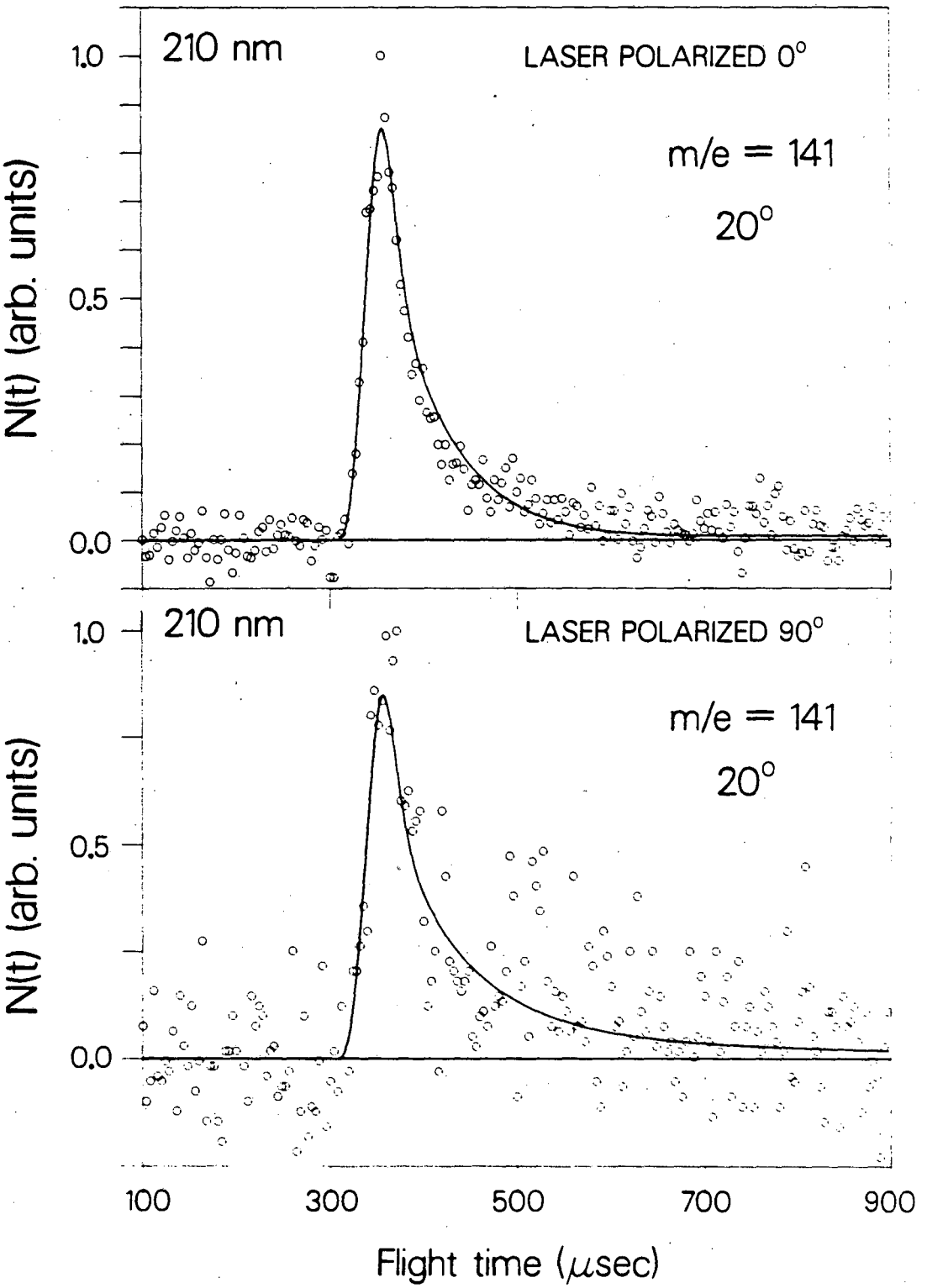

XBL 859 3862

Fig. 44

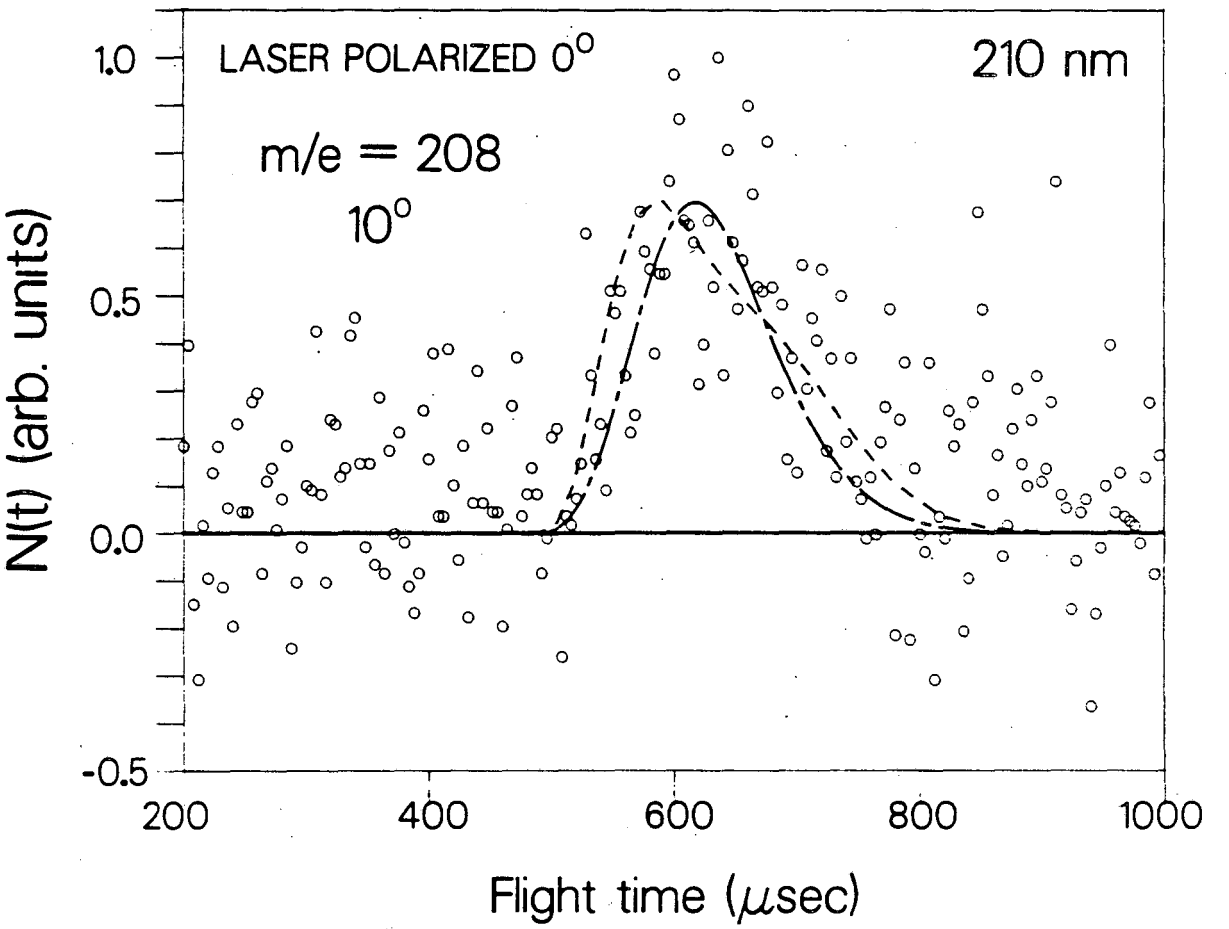

Fig. 45

XBL 859 3870

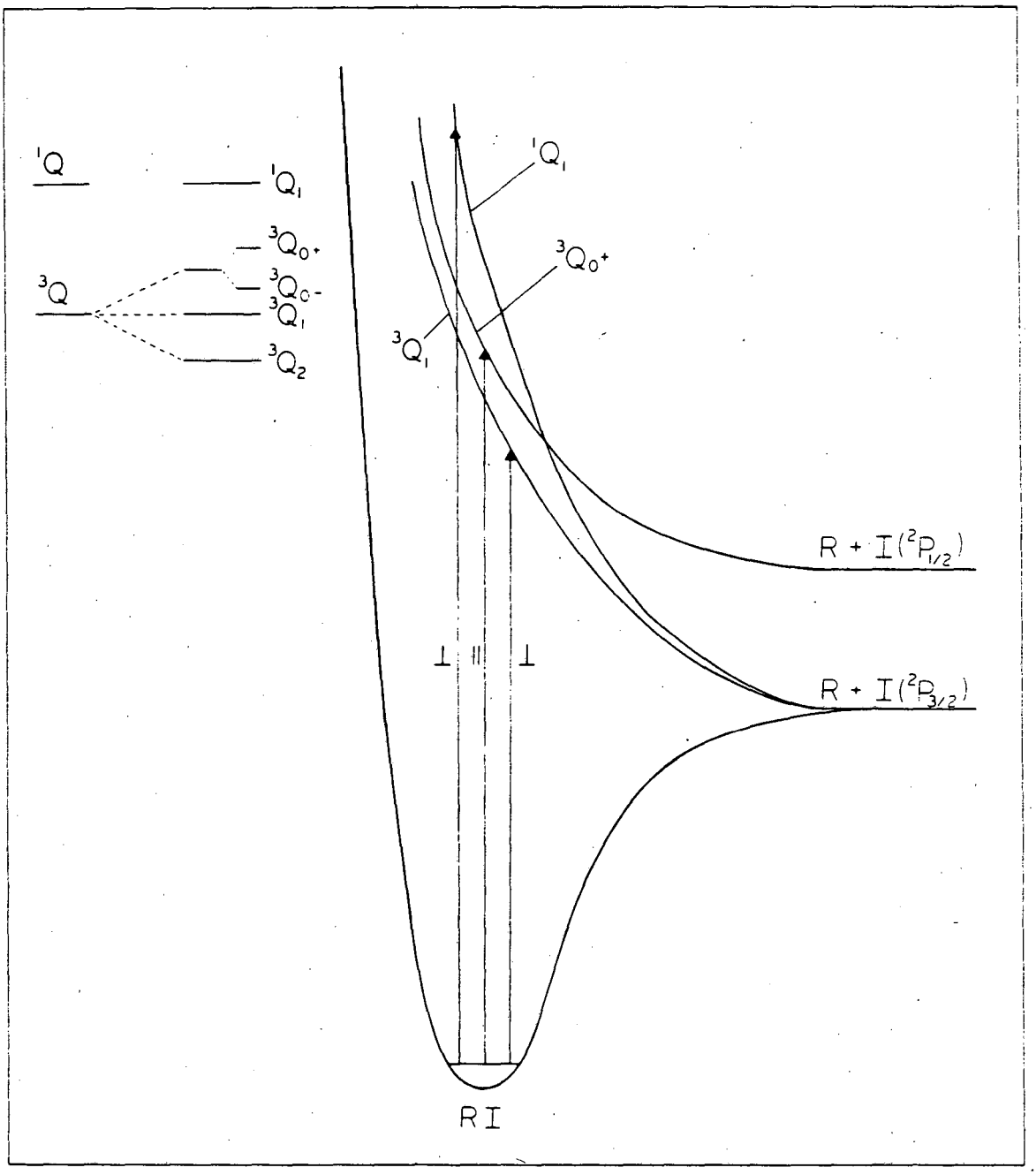

XBL 859-4076

Fig. 46

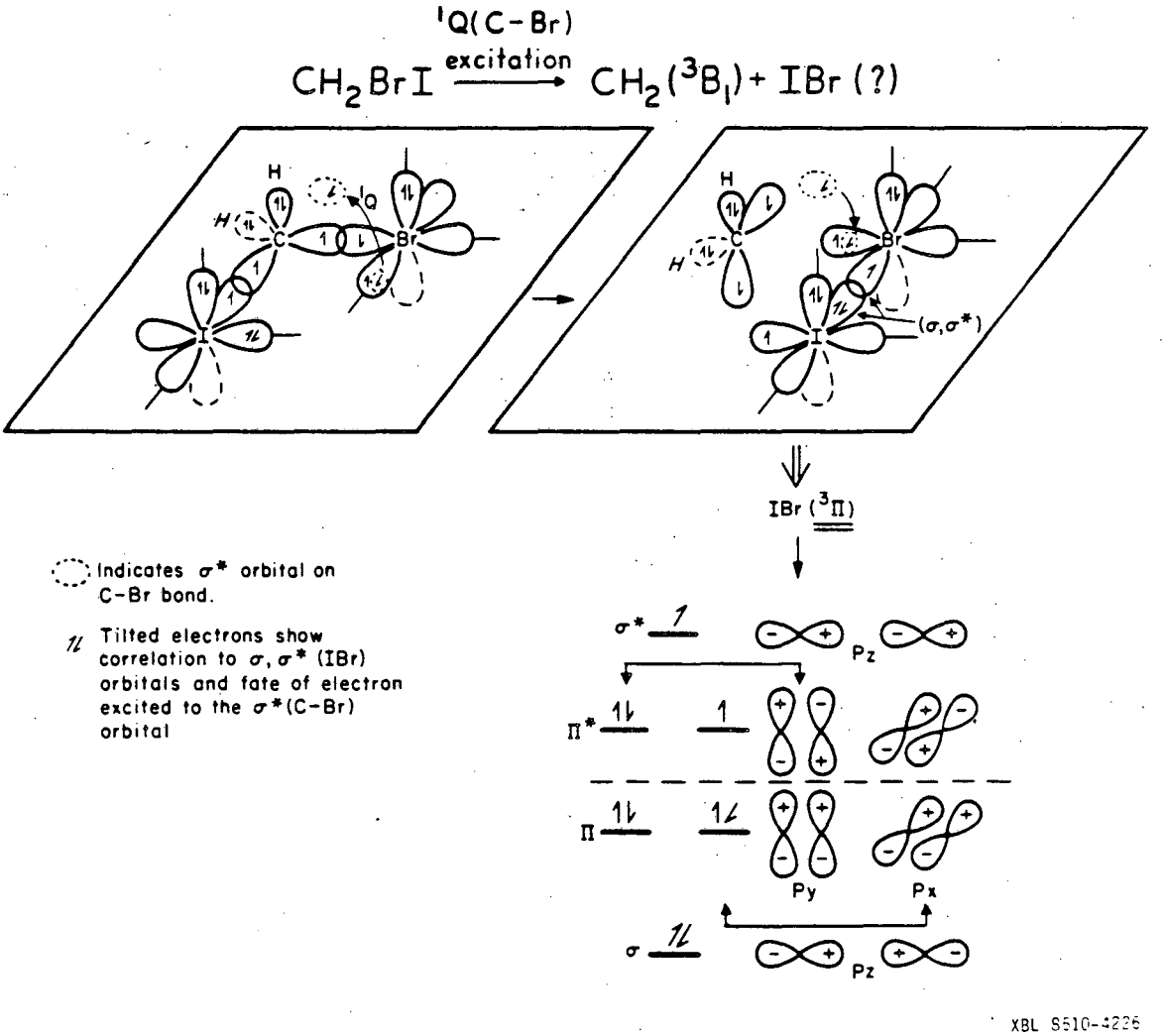
$^1Q(C-Br)$
$CH_2BrI \xrightarrow{\text{excitation}} CH_2(^3B_1) + IBr\ (?)$
H
C
Br
I
(σ,σ^*)
$IBr\ (^3\Pi)$
Indicates σ^* orbital on C–Br bond.
Tilted electrons show correlation to σ, σ^* (IBr) orbitals and fate of electron excited to the σ^*(C–Br) orbital
σ^*
Π^*
Π
σ
Pz
Py
Px
XBL 8510-4226

Fig. 47

CHAPTER TWO

THE PHOTODISSOCIATION OF NITROMETHANE AT 193 nm*

ABSTRACT

The dissociation of nitromethane following the excitation of the $\pi^* \leftarrow \pi$ transition at 193 nm has been investigated by two independent and complementary techniques, product emission spectroscopy and molecular beam photofragment translational energy spectroscopy. The primary dissociation process is shown to be cleavage of the C–N bond to yield CH_3 and NO_2 radicals. The translational energy distribution for this chemical process indicates that there are two distinct mechanisms by which CH_3 and NO_2 radicals are produced. The dominant mechanism releasing a relatively large fraction of the total available energy to translation probably gives NO_2 radicals in a vibrationally excited $^2B_2$ state. When dissociated, other nitroalkanes exhibit the same emission spectrum as CH_3NO_2, suggesting little transfer of energy from the excited NO_2 group to the alkyl group during dissociation for the dominant mechanism. This conclusion is supported by the apparent loss of the slow NO_2 product in the molecular beam studies to unimolecular dissociation to NO + O, which will occur for NO_2 with 72 kcal/mole or more internal energy. Evidence is presented which suggests that the NO_2 produced via the minor mechanism, which releases a smaller

---

*Published in The Journal of Chemical Physics 79, 1708 (1983).

fraction of the available energy to translation, has a large cross section for absorbing an additional photon via a parallel transition and dissociating to NO + O.

INTRODUCTION

The optical absorption spectrum of nitromethane[1,2] is a broad continuum extending down from 370 nm to the VUV having maxima at 198 nm (ϵ = 4000 M^{-1} cm^{-1}) and 270 nm (ϵ = 10 M^{-1}). Nagakura[2] assigned the strong and weak bands to $\pi^* \leftarrow \pi$ and $\pi^* \leftarrow n$ transitions, respectively, where both transitions are localized on the NO_2 moiety. Photoelectron and electron energy loss spectroscopic studies[3-5] are for the most part consistent with these assignments although Rabelais[3] believes the strong transition to be a promotion of a C-N σ bonding electron to the antibonding π^* orbital of the NO_2 and Flicker et al.[5] suggest that this $\pi^* \leftarrow \sigma$ transition occurs in the same region as the $\pi^* \leftarrow n$ transition and accounts for almost all of the 270 nm peak in the optical spectrum.

The energetically allowed photodissociation channels involving simple bond rupture, and two other channels involving the migration of H or O atoms, are shown in Fig. 1. A short review of previous studies of the ultraviolet photolysis of nitromethane has been presented by Schoen et al.[6] Gas phase photochemical studies to date have been limited to excitation of the $\pi^* \leftarrow n$ transition (perhaps better assigned as a $\pi^* \leftarrow \sigma$ transition by Flicker et al.). Flash photolysis studies[7,8]

indicate that formation of CH_3 and NO_2 radicals is the major process for this region, though Honda et al.[7] show evidence of other minor channels.

Three recent gas phase photodissociation studies in the region of the 270 nm transition(s) have relied on direct detection of the photodissociation products[9,10,6] by laser induced fluorescence (LIF) or electron bombardment ionization methods. Spears and Brugge[9] dissociated CH_3NO_2 at 252.6 nm and probed the vibrational population of the ground electronic state NO_2 formed. By filtering the LIF signal they concluded that the NO_2 is highly excited in all vibrational modes. Kwok et al.[10] studied the photodissociation of nitromethane at 266 nm in a collision-free crossed laser-molecular beam experiment with mass spectrometric detection. Although the vibrational predissociation of small clusters of nitromethane molecules was detected, dissociation products from the monomer were not observed. They estimated from their detection sensitivity and the absorption cross section at 266 nm that the quantum yield for dissociation of the monomer is less than 3 percent for several possible products that would fragment to give CH_3^+, NO_2^+, NO^+, HNO^+, or CH_3NO^+ in the ionizer. Schoen et al.[6] used a 5 ps photolyzing pulse at 264 nm and monitored the subsequent evolution of the NO_2 fragment by LIF with a 5 ps 527 nm pulse. They estimated a 1 percent quantum yield of NO_2 product. They found that the dissociation occurred in <5 ps and that some of the NO_2 product was formed in an excited fluorescing state.

In the present paper, two complementary techniques have been used to study the primary processes occurring when nitromethane is excited

at 193 nm near the maximum of the $\pi^* \leftarrow \pi$ transition. The method of photofragment translational energy spectroscopy in a crossed laser-molecular beam apparatus identifies the primary photochemical process as cleavage of the C-N bond and shows that there are two distinct mechanisms which produce CH_3 and NO_2 products. Product translational energy distributions for the dissociation pathways are measured and a comparison of the product velocity distributions suggest that for the dominant process the NO_2 radical retains much of the internal energy. The method of fluorescence emission spectroscopy identifies the excited electronic state of the NO_2 radical for the dominant process and the emission spectra of a series of nitroalkanes provides independent evidence that little energy has transferred from the NO_2 group to the CH_3 during dissociation. The emission spectra suggest and the molecular beam studies confirm that the hottest $NO_2(^2B_2)$ is formed with sufficient internal energy to spontaneously decompose. Evidence from the molecular beam studies is also presented which suggests that the NO_2 produced in the minor primary processes undergoes efficient secondary photodissociation to NO + O via a parallel transition.

EXPERIMENTAL

The fluorescence emission studies and the laser polarization dependence measurement presented here were done at Columbia University while the complementary molecular beam study presented was done at Berkeley. The results of these independent measurements when combined

allowed many conclusions to be made about the primary photochemical processes studied here. Some product velocity distributions were measured at Columbia, but the Berkeley data is presented as it is more complete and as the Berkeley apparatus has a rotatable detector and is thus sensitive to lower product recoil energies than the fixed 90° geometry detector at Columbia.

A. Molecular Beam Experiments

Time-of-flight (TOF) and angular distributions of the photofragments were measured in a molecular beam apparatus described in detail elsewhere.[11] The molecular beam was formed by bubbling helium through nitromethane (Mallinckrodt spectrophotometric grade) maintained at 20°C and expanding the mixture through a 0.005" diameter stainless steel nozzle at a total stagnation pressure of 300 torr (11 percent CH_3NO_2/89 percent He). The nozzle was heated to 240°C to effectively eliminate contributions from molecular clusters in the beam. The velocity distribution of the nitromethane beam was determined by time-of-flight measurements. The beam had a peak velocity of 1470 m/s with the full width at half maximum (FWHM) of the distribution being 18 percent. The beam was collimated by a skimmer, and, after passing through two pressure reducing differential chambers, it was crossed by the laser beam. The molecular beam was defined to an angular divergence of ~1.6°.

The 193 nm photons were produced by a Lambda Physik EMG 101 ArF excimer laser. For most of the data taken for measurement of product

translational energy and angular distributions, the laser was run at a repetition rate of 50 Hz and the average power was maintained at 2.0 ± 0.04 W (40 mJ/pulse). The laser light was unpolarized and was focussed onto the molecular beam by a 35 cm focal length fused silica spherical lens to a final spot size of ~4 mm^2. This resulted in a (time-integrated) photon flux through the interaction region with the molecular beam on the order of ~1 x 10^{18} photons/cm^2-pulse. For the power dependence measurements, the power was adjusted by changing the high voltage for the gas discharge and running the laser with the beginning or end of a gas fill; the focus and alignment were kept constant.

The dissociation products were detected in the plane of the laser and molecular beams by a rotatable ultra-high vacuum mass spectrometer consisting of an electron bombardment ionizer, quadrupole mass filter, and particle counter. The flight path between the beam crossing point and the ionizer was 20.8 cm. Angular and TOF distributions were measured in the usual way.[12]

Signal was observed when the quadrupole mass spectrometer was set to pass the following mass to charge ratios: m/e = 46, 30, 16, 15, 14, and 13 corresponding to NO_2^+, NO^+, O^+, CH_3^+, (CH_2^+, N^+), and CH^+. Typical signal levels at a detector angle of 10° from the molecular beam were 2.8 counts/pulse for NO^+, 0.18 counts/pulse for NO_2^+, 0.85 counts/pulse for O^+, and 0.42 counts/pulse for CH_3^+. The NO_2^+ signal was much lower than the NO^+ signal from the NO_2 product presumably due to extensive fragmentation of vibrationally hot NO_2 molecules in the ionizer. No significant signal was observed at m/e = 47, 45, 44, 31 or

29 corresponding to $HONO^+$, CH_3NO^+, CH_2NO^+, (CH_3O^+, HNO^+), and (CH_3N^+, CHO^+) respectively. At all masses but m/e = 29, this signal was less than 1 percent of the NO^+ signal level. At m/e = 29 a signal on the order of 10 percent of the NO^+ signal was observed and was attributed to crosstalk from the large signal at m/e = 30 due to the finite resolution of the quadrupole.

TOF distributions were measured for CH_3^+, NO_2^+, and NO^+ at three detector angles with respect to the molecular beam: 10°, 25°, and 40°. TOF data was also taken for O^+ at 10° at the same photon flux as the above data (noted previously) and for m/e = 14 and 13 at 10° and laser pulse energies of ~ 13 mJ. The data presented for CH_3^+, NO_2^+, NO^+, and O^+ were obtained by counting for between 5×10^4 and 10^6 laser pulses at each angle. All but one of the CH_3^+ TOF spectra taken had a very slow laser correlated background arriving between 210 and 750 μsec that remained when the laser beam was pulsed but the molecular beam was flagged.[13] It did not significantly overlap the data and was discriminated against in the angular distribution measurements described below.

Angular distributions were measured for CH_3^+, NO_2^+, and NO^+ between 8° and 45° in 3° increments, although good signal to noise ratios were not obtained for NO_2^+. We gated the CH_3^+ signal from 20 - 200 μsec, so that the slow laser-correlated background was not included, and corrected for this in our calculation for the fit to the angular distribution. Each point in the CH_3^+ angular distribution is the integrated signal for 12,000 laser shots and is the normalized sum of a forward/backward angular scan. The NO^+ angular disribution is the sum of

three scans taken by reversing directions in between each; each point is the integrated signal collected for 6,000 laser pulses.

B. Laser Polarization Dependence

The dependence of the m/e = 15, CH_3^+, signal on the polarization of the laser was performed with a low photon flux on the Columbia molecular beam apparatus described elsewhere.[14] The product was detected 7.8 cm from the interaction region at right angles to the pulsed laser and an effusive molecular beam. Here the laser was focussed with a 40 cm focal length cylindrical lens and polarized with a pile of ten plates polarizer, resulting in a photon flux of ~ 1×10^{17} photons/cm^2. The electric vector of the light was rotated with a half wave plate cut for 193 nm (Optics for Research). The TOF distribution for m/e = 15 was measured at eight different polarization angles in a staggered fashion to average out experimental fluctuations in background signal and laser power. The laser power was kept constant to within 15 percent and signal was accumulated for 2160 laser shots at each angle.

C. Fluorescence Emission Experiments

Fluorescence measurements were carried out in a flowing cell. Pressures ranged from 20 to 100 mtorr and were regulated to within 2 percent. Because of the broad spectral range of the emission, several photomultipliers were used. The fluorescence from the dissociation of

nitromethane was viewed with an RCA 31035 photomultiplier tube which was cooled with dry ice/acetone. This PMT has a flat response from 400 to 800 nm, so the spectrum (Fig. 6), gives a true picture of the NO_2^* emission. For comparison with different molecules (Fig. 7) uncorrected spectra were recorded from 380 to 650 nm. The resolution of the 1/4 m monochromator (Jarrell-Ash) was ~4 nm FWHM.

RESULTS AND ANALYSIS

A. Determination of the Primary Photodissociation Processes

There is strong evidence from the molecular beam study that CH_3 is the only primary carbon containing photodissociation fragment. The TOF spectra of m/e = 15 corresponding to CH_3^+ is shown in Fig. 2. The m/e = 13, CH^+, TOF data is exactly the same as the CH_3^+ data when the usual small correction for the mass dependent ion flight time through the mass spectrometer is made. This suggests that CH^+ is a daughter ion of CH_3 and that there are no other primary products which give CH^+ in the ionizer. In addition, no significant signal (<1 percent of the NO^+ signal or signal accounted for by crosstalk from m/e = 30 due to the finite resolution of the quadrupole) was observed at the masses corresponding to $HONO^+$, CH_3NO^+, CH_2NO^+, (CH_3O^+, HNO^+), or (CH_3N^+, CHO^+). These observations also support the conclusion that the CH_3 radical is the only primary carbon containing photofragment and thus identifies the primary chemical process as:

$$CH_3NO_2 \longrightarrow CH_3 + NO_2 \,. \qquad (1)$$

The angular distribution of the m/e = 15, CH_3^+, signal is shown in Fig. 3. The angular and TOF distributions of the methyl product were fit by a trial-and-error forward convolution method using a completely flexible point form for the center-of-mass (c.m.) translational energy distribution, P(E'), and angular distribution, $\omega(\theta)$. For a single photon process in the electric dipole approximation, the c.m. angular distribution must be of the form

$$\omega(\theta) = 1/4\pi[1 + 2bP_2(\cos\theta)], \qquad (2)$$

where θ is the angle between the electric vector of the laser light and the final c.m. recoil direction of the products, and the anisotropy parameter, b, is constrained to the range $-0.5 \leq b \leq +1.0$. Therefore, the c.m. angular distribution is completely described by the single parameter b. A completely flexible point form for the P(E') was used. The fits to the CH_3^+ data in Figs. 2 and 3 were calculated using the solid-line P(E') in Fig. 4 and assuming an isotropic c.m. angular distribution (i.e., b = 0). We then attempted to fit the data with several anisotropy parameters between b = 0.0 and b = -0.5. The fit to the laboratory angular distribution can be improved if b = -0.1 is used, but it begins to degrade the best simultaneous 10°, 25°, and 40° TOF fits. With a b parameter of -0.3 it is impossible to get an acceptable fit to the TOF's or angular distribution. The result of the analysis is that if the entire primary photodissociation process is fit

with one anisotropy parameter, it must be nearly isotropic in the c.m. reference frame. The nearly isotropic distribution observed at this laser energy fluence may have been influenced by saturation effects. The photon flux in this experiment is high enough to dissociate almost all the molecules regardless of the orientation of their transition moment with respect to the polarization of the laser. For a perhaps more significant measurement of the anisotropy parameter, see Part D.

It is important to note that though the laser used in this experiment was unpolarized, the data is still sensitive to anisotropy as a consequence of the geometry of our detection. The laser light can be resolved into a component perpendicular to the plane of the laser and molecular beam, the plane of detection, and an equal component parallel to the molecular beam. The perpendicular component gives an isotropic contribution to the detection plane but the parallel component does not.

The translational energy distribution for the primary photochemical process, process (1), is shown by the solid line in Fig 4. Derived from the CH_3^+ TOF data, it has two maxima, a sharp feature peaking at 2 kcal/mole translational energy and a broad feature peaking at 8 kcal/mole and extending out to 44 kcal/mole in translation. Within the resolution of this experiment, the shape indicates that there are two distinct physical mechanisms by which the chemical products CH_3 and NO_2 are produced. A minor mechanism releases a small fraction of the total available energy to translation and peaks at 2 kcal/mole and the dominant mechanism channels a larger amount of the total available energy to translation and extends out to a translational energy of 44 kcal/mole.

B. Fluorescence Emission from NO_2^* Product

A prompt fluorescence was seen after the excimer laser was fired through a cell containing 20 mtorr of nitromethane. The fluorescence lifetime was measured to be 35 ± 5 μs (Fig. 5). In the Discussion Section it will be suggested that this is characteristic of the $^2B_2$ state of NO_2. The dispersed fluorescence is shown in Fig. 6 for nitromethane. The emission extends from the dissociation limit of NO_2 (398 nm) out to the infrared, with a complete lack of any structural features. Similar broad spectra, characteristic of NO_2, have been reported for the chemiluminescent reaction of O + NO[15] and the photodissociation of $(NO_2)_2$.[16] The presence of emission near the dissociation limit of NO_2 indicates that some of the NO_2 product may have been formed with enough internal energy to unimolecularly dissociate to NO + O, as is discussed in part C.

As shown in Fig. 7, variations in the alkyl group attached to NO_2 do not influence the emission spectrum. This result implies that the excited state NO_2 is formed in the same set of final states regardless of the alkyl group and that the dissociation time is faster than the time necessary for relaxation of the NO_2 by the alkyl groups.

Figure 8 shows the emission spectrum obtained when nitromethane was photolyzed with the laser strongly focussed. Superimposed on the NO_2^* continuum are additional features due to CN(B→X) and CH(A→X) emission which can only arise from a multiphoton process.

C. Spontaneous Unimolecular Decay of Highly Excited NO_2

The m/e = 46, NO_2^+, TOF data is shown in Fig. 9. As CH_3 and NO_2 are formed in the primary dissociation, their velocities with respect to the center of mass are related by momentum conservation. One should be able to fit the NO_2^+ TOF data using the P(E') which fit the CH_3^+ TOF data. When we attempted to do this we found that the fast NO_2 product was correctly related to the fast CH_3 product by momentum conservation, but that much of the slow NO_2 product was not detected. The good fits to the NO_2^+ data in Fig. 9 were actually calculated from the dashed-line P(E') in Fig. 4 (again assuming b = 0). Evidently, much of the NO_2 product formed in dissociation events releasing less than 16 kcal/mole to translation has disappeared. We will now consider what evidence we have concerning how this NO_2 is lost.

The NO_2^* fluorescence emission studies of part B have shown that the excess energy is concentrated in the excited NO_2 product. Because the band origin of the $^2B_2$ state is calculated to be 27.9 kcal/mole[17,18] and the total available energy is 90 kcal/mole, any NO_2 from dissociation events releasing 62 kcal/mole or less into translation could be in the $^2B_2$ state. Thus we tentatively assign the major primary dissociation process (corresponding to the broad energy distribution extending out to 44 kcal/mole) to process (3) below:

$$CH_3NO_2 \longrightarrow CH_3 + NO_2(^2B_2) \qquad (3)$$

It appears from the P(E') derived from the NO_2 TOF's that all of the surviving NO_2 results from this process. The P(E') derived from the NO_2^+ data starts to deviate from the P(E') derived from the CH_3^+ data below 16 kcal/mole. At 16 kcal/mole translational energy, the NO_2 product could have as much as 74 kcal/mole internal energy. With 72 kcal/mole or more internal energy, $NO_2(^2B_2)$ will unimolecularly dissociate to NO + O. Thus the loss of some of the $NO_2(^2B_2)$ product at translational energies less than 16 kcal/mole might reasonably be assigned to its unimolecular dissociation to NO + O (process 4 below), particularly as the $NO_2(^2B_2)$ fluorescence extends to the dissociation limit.

$$CH_3NO_2 \longrightarrow CH_3 + NO_2 \qquad (4)$$
$$\qquad\qquad\qquad\qquad\quad \vdots$$
$$\qquad\qquad\qquad\qquad\quad \hookrightarrow NO + O$$

Now notice that practically all of the NO_2 formed in the minor primary dissociation process (which gives rise to the peak in the CH_3^+ P(E') at 2 kcal/mole) has also been lost. Whether this should be ascribed to the unimolecular dissociation of this NO_2 product is much less clear. If this were so, then essentially all of this NO_2 would have had to retain 72 kcal/mole or more internal energy, since there is no hint of the 2 kcal/mole feature in the NO_2 product P(E'). Analysis of the NO^+ and O^+ data in the following subsection suggests that, for some reason, the NO_2 formed in the minor primary process undergoes very efficient secondary photodissociation to NO + O.

D. Secondary Photodissociation of NO_2

The NO^+ TOF distributions are shown in Fig. 10. They are not identical to the NO_2^+ distributions shown in Figure 9. Therefore the NO^+ signal is not due solely to cracking of NO_2 in the ionizer.[19] The most striking difference between NO^+ and NO_2^+ is the presence of a fast "shoulder" in the NO^+ TOF distributions. This shoulder becomes quite prominent at larger angles. Also, the main peak in the NO^+ distribution is slightly broader than in the NO_2^+ distribution.

Initially we thought that the shoulder and broadening in the NO^+ data might be entirely due to NO radicals produced in the spontaneous unimolecular decay of hot NO_2 (see Part C). Certainly the slight broadening of the main peak in the NO^+ TOF distribution at small angles may be attributed to this cause. However, for energy and momentum to be conserved spontaneous decay of hot NO_2 cannot account for the fast shoulder in the NO^+ TOF distributions. At 10°, the fastest product in the shoulder is travelling at 2.5×10^5 cm/s in the c.m. frame. In a sequential dissociation of CH_3NO_2 producing $CH_3 + NO + O$, the NO will attain a maximum velocity for a given amount of translational energy when the CH_3 and O are formed moving in the opposite direction of the NO with the same speed. For 18 kcal/mole available translational energy, the maximum NO velocity is calculated to be only 1.6×10^5 cm/sec. This maximum NO velocity is still much too slow to account for the fastest observed NO^+ product.

Another explanation for the fast NO^+ signal is that secondary photodissociation of the NO_2 product is occurring during the excimer

laser pulse:

$$NO_2 \xrightarrow{193\ nm} NO + O. \qquad (5)$$

To test this explanation we measured an O^+ TOF distribution at 10° (Fig. 11). The shoulder on the O^+ distribution begins at even shorter times than the shoulder on the NO^+ TOF distribution, as expected on the basis of reaction (5). (Of course, the O^+ shoulder may contain contributions from both NO and O, but the contribution from O will dominate the fastest part of the shoulder.)

While this evidence convinced us that rxn. (5) is occurring under our experimental conditions, it is clear that not all of the NO_2 undergoes secondary photodissociation. A lot of NO_2 survives. In fact, the experimental CH_3:NO_2 ratio (calculated by correcting the measured CH_3^+ and NO^+ signals for relative ionization cross sections and radical fragmentation in the ionizer) agrees with the CH_3:NO_2 ratio calculated from the CH_3 and NO_2 P(E')'s in Fig. 4 within experimental error. (The details of this calculation are given in Appendix 1). That is, the majority of the "missing" NO_2 seems to be accounted for already by the discrepancy between the CH_3 and NO_2 P(E')'s. This would seem to indicate that only a rather small fraction of the NO_2 corresponding to the NO_2 P(E') undergoes secondary photodissociation. If this is the case, the intensities of the shoulders in the NO^+ and O^+ TOF's, relative to the main peak, should decrease linearly as the laser power is decreased.[20]

Even before we measured the O^+ TOF distribution, we remeasured the NO^+ TOF distribution at a laser power ten times lower than that used in Fig. 10. (This measurement was only made at $\theta = 40^\circ$, where the shoulder is more prominent.) To our surprise, the shoulder intensity relative to the main peak was only slightly (~20 percent) lower, compared to the ~10-fold change which had been anticipated. After measuring the O^+ TOF distribution, and convincing ourselves that secondary NO_2 photodissociation had to be occurring, we repeated the NO^+ TOF measurements at three laser powers spanning a 50-fold range. The raw data is shown in Fig. 12, where all three distributions have been normalized to the same peak height. The dependence of the relative shoulder intensity on the laser power is confirmed, but the power dependence is indeed very weak.

To obtain a measure of the relative shoulder intensity, we calculated the ratio of the signal in the shoulder (channels 15-35) to the signal in the main peak (channels 36-120). The background/channel was calculated by averaging channels 2-13 and was subtracted out before integrating the TOF distributions. The dwell time per channel was 3 μs. The results for the three measurements of Fig. 12, as well as for the two earlier measurements, are collected in Table 1. As the laser pulse energy increases from 0.7 to 33 mJ/pulse, a factor of 47, the relative shoulder intensity increases by only a factor of 1.5. For reference, the <u>total</u> NO^+ signal increases by a factor of six over this same range.

We are faced with an apparent paradox. The weak power-dependence of the shoulder intensity indicates that the secondary photodissociation

signal is strongly saturated, just as the primary nitromethane photodissociation signal is strongly saturated. Yet the measured CH_3:NO_2 signal ratio indicates that most of the NO_2 primary product survives (Appendix 1). The most reasonable way out of this dilemma is to attribute the secondary photodissociation signal to NO_2 which is produced in the minor primary photodissociation process which gives rise to the "blip" in the CH_3 P(E') at low recoil energies. We should emphasize that very hot NO_2 ($^2B_2$) from the major primary photodissociation process cannot contribute to the secondary photodissociation signal, since NO_2 ($^2B_2$) levels which lie above the NO ($^2\Pi$) + O(^{3}P) limit are strongly predissociated (predissociation lifetimes on the order of picoseconds), and would not live long enough to absorb a second photon. This also implies that most of the NO_2 which is produced in the minor primary process, while presumably vibrationally hot, must be below the NO($^2\Pi$) + O(^{3}P) limit.

On the basis of the above assignment, we attempted to fit the NO^+ and O^+ data by varying the P(E') and anisotropy parameter for the secondary photodissociation reaction (5) and the ratio, ϵ, of the fraction of NO_2 which undergoes secondary photodissociation to the fraction of surviving NO_2. The details of the calculations and the final fits are given in Appendix 2 (see Figs. 14-17). Here we will only mention the main results. (1) To fit the <u>shape</u> of the shoulders in the NO^+ TOF distributions, it was necessary to use a P(E') for reaction (5) which peaked around 10 kcal/mole and tailed off smoothly to zero around 100 kcal/mole, with a mean translational energy of 31 kcal/mole. (2)

To fit the relative shoulder intensities in the NO^+ TOF's at 10°, 25° and 40°, it was necessary to use a positive anisotropy parameter (b = +0.5) for reaction (5). Evidently, the secondary photodissociation of NO_2 proceeds via a parallel transition. (3) To fit the observed ratio of the shoulder intensity to the main peak in the NO^+ and O^+ TOF's, it was necessary to assume that $\epsilon \sim 0.50$. This implies that about 1/3 of the total NO_2 (less that fraction which spontaneously decomposes) undergoes secondary photodissociation at our highest laser pulse energies. For discussion of the quantitative significance of the derived ϵ value, see Appendix 2.

To summarize, we have assumed that the NO_2 which is produced via the minor photodissociation channel of CH_3NO_2 (which gives rise to the blip in the CH_3 P(E')) undergoes very efficient secondary photodissociation to NO + O, while the NO_2 ($^2B_2$) which is produced in the major primary photodissociation process does not. On the basis of this assumption, we have been able to calculate very good fits to all of the NO^+ and O^+ data and at the same time rationalize (roughly) the observed percentage of NO_2 undergoing secondary photodissociation and the very weak power-dependence of the secondary photodissociation signal.

E. Polarization Dependence Measurement

The dependence of the CH_3^+ signal on the polarization of the laser was measured at the lower photon flux of $\sim 1 \times 10^{17}$ photons/cm^2 in the effusive molecular beam apparatus. The result was an anisotropic distribution shown in Fig. 13. Each point is the integrated fast portion

of the TOF signal. The angular distribution was fit to the equation:

$$I(\theta) = 1 + 2bP_2(\cos\theta - \theta_0) \qquad (6)$$

by a least squares method. $b = -0.3 \pm 0.1$ and $\theta_0 = 14 \pm 5^\circ$ gave the best fit. To nominally transform from the laboratory to the center of mass frame of the molecule[21] a $\theta_0 = 8^\circ$ was expected as calculated from the molecular beam velocity and the average speed of the methyl radical. This agrees roughly with the measured shift of $14 \pm 5^\circ$ in this distribution.

DISCUSSION

A. The Nature of the Excited State of Nitromethane

A simple molecular orbital picture for the π electron structure of the nitro group in nitromethane was given by Nagakura.[2] The orbitals and their symmetries (assuming C_{2v} for the nitro group) are:

$$b_2: \ \phi_0 = 0.7133\ N + 0.7009\ (O_1 + O_2)/\sqrt{2} \qquad (7)$$

$$a_2: \ \phi_1 = (O_1 - O_2)/\sqrt{2} \qquad (8)$$

$$b_1: \ \phi_2 = 0.7009\ N - 0.7133\ (O_1 + O_2)/\sqrt{2} \qquad (9)$$

The $2p\pi$ atomic orbitals for the nitrogen and two oxygen atoms are designated by N, O_1 and O_2. In the ground state, the b_2 and a_2 orbitals are filled, and the symmetry is A_1. The transfer of an electron from a_2 to b_1 is believed to be responsible for the strong peak in the

absorption spectrum, near which the ArF laser is exciting. This excited state configuration has B_2 symmetry and the transition is therefore polarized in the molecular plane perpendicular to the C-N bond. More refined calculations[22,23] agree with this assignment of the 198 nm transiton as $^1B_2 \leftarrow {}^1A_1$, though a controversial assignment of the transition to a $\pi^* \leftarrow \sigma$ ($^1B_1 \leftarrow {}^1A_1$) has been proposed by Rabelais.

Assuming the $\pi^* \leftarrow \pi$ assignment is correct, the electronic excitation is localized on the NO_2 group and the dissociation would not be expected to proceed as a direct dissociation from the excited electronic state. The $\pi^* \leftarrow \pi$ state must be predissociated by an electronic state repulsive in the C-N bond or by a lower bound electronic state above its dissociation limit. The $^1A_1$ repulsive electronic state described briefly by Harris[23] could predissociate the $^1B_2$ state in C_s and would correlate to $^2B_2$ excited state NO_2 product. This would be consistent with the emission studies as will be discussed. The predissociation is expected to be fast as indicated by the lack of structure in the absorption spectrum. The lack of strong anisotropy in the angular distribution could result from a combination of many factors: rotation of the excited molecule through a non-negligible angle between the excitation and dissociation process, the excitation of out-of-plane or antisymmetric stretching modes of the NO_2 group, or participation of another electronic state in the absorption with a parallel transition moment.

This paper has presented two different measurements of the anisotropy parameter, b. In the experiment performed on an effusive molecular beam of nitromethane with a low photon flux, $b = -0.3 \pm 0.1$ was

measured consistent with the perpendicular assignment of the transition. In the experiment performed at high photon flux with a supersonic molecular beam, the c.m. angular distribution was determined to be nearly isotropic, $b = 0 \sim -0.1$. Assuming no experimental error and admitting the uncertain statistics of the first measurement, what differences between the two experiments could have caused the discrepancy? An accepted difference between supersonic and effusive molecular experiments is that the rotation of the parent molecule in an effusive expansion is not relaxed, while it is to some degree in a supersonic expansion, so the rotation of the parent molecule after excitation but before dissociation will smooth the angular distribution of photofragments more in an effusive experiment. Here, however, the supersonic expansion gives the more smoothed angular distribution, so this cannot explain the difference between the two measurements. A possible explanation for the differing measurements may result from the difference in photon flux in the two experiments assuming that the internal rotation of the nitromethane molecule has relaxed in the supersonic expansion. Ling and Wilson[24] have shown that for linear molecules, saturation of the parallel or perpendicular transitions by high photon fluxes causes a smearing of the measured angular distribution of photofragments. They point out that the effect is particularly small for perpendicular transitions as here the dipole moment vector is anywhere in a plane perpendicular to the dissociating bond. In the case of nitromethane, however, if the internal rotation of the NO_2 with respect to the CH_3 group is relaxed, the dipole moment vector which is perpendicular to the NO_2 plane is no

longer defined by the entire plane perpendicular to the C-N bond. The overall rotation of the CH_3NO_2 molecule will not bring the dipole moment vector, $\vec{\mu}$, in perfect alignment with the electric field vector, $\vec{E}$, for a significant fraction of the molecules, yet these molecules will be dissociated with near unit probability at very high values of photon flux along with those molecules whose $\vec{\mu}$ becomes parallel with $\vec{E}$ during the molecules' rotation. The result is a more isotropic angular distribution of photofragments. This explanation may partially account for the more isotropic angular distribution measured on the supersonic molecular beam experiment at the high photon flux.

B. Dynamics of the Dissociation

Conservation of energy allows us to write an expression for the partitioning of energy.

$$E_{avail} = h\nu + E^P_{int} - D_o(R - NO_2) = E_E + E_T + E_V + E_R \qquad (10)$$

where the available energy, E_{avail}, consists of the photon energy, $h\nu$, plus the internal energy of the parent molecule, E^P_{int}, minus the energy, $D_o(R\text{-}NO_2)$, required to break the C-N bond. This energy is partitioned into the translational, rotational, vibrational, and electronic degrees of freedom of the fragments. An upper limit for the vibrational energy of the parent molecule would assume no relaxation of the vibrational modes in the supersonic expansion and may be calculated

from the known vibrational frequencies[25] of nitromethane for the 240°C nozzle temperature; this gives 2.1 kcal/mole vibrational energy. As rotational relaxation is believed to follow translational relaxation and the velocity distribution of the nitromethane indicates translation has relaxed to <30°K, we will assume no significant contribution to the available energy from the overall rotations of the molecule or the one near free rotation about the C-N bond. As the translational energy distribution has been measured, the combined vibrational, rotational, and electronic energy of the fragments can be inferred. These two studies, in addition, have given information on the electronic energy of the products and the partitioning of internal energy between the CH_3 and NO_2 fragments, as will be discussed below.

I. Fluorescence Emission Studies

Let us first consider the electronic state of the excited state NO_2 product. The spectroscopy and theory of NO_2 is reviewed in the first chapter of the spectral atlas of Hsu et al.[26] The ground state is designated as $X^2 A_1$ and the three lowest excited states are $A\ ^2B_2$, $B\ ^2B_1$ and $C\ ^2A_2$. The nearness of these states causes mixing of the vibrational levels by vibronic coupling, Jahn- and Renner-Teller and spin-orbit interactions. As a result most of the spectrum of NO_2 has yet to be analyzed. Lifetime measurements have yielded a large number of different values depending on the excitation used.[27-30] When excited at 593.3 nm two lifetimes were observed which Stevens et al.[30]

have attributed to the $^2B_2$ state (30 ± 5 μs) and the $^2B_1$ state (115 ± 10 μs). Our measurement of 35 ± 5 μs is not intended to be yet another value for the lifetime. All that can be said is that the lifetime falls within the range reported and that the excited NO_2 state that is formed is probably in the $^2B_2$ state. The fluorescence studies do not eliminate the possibility that some of the NO_2 product is formed in the ground state or the non-fluorescing $^2A_2$ state. If according to the majority of theoretical and experimental results (and consistent with our angular distribution) nitromethane is excited to the $^1B_2$ state at 193 nm, then the products $NO_2(A^2B_2)$ + CH_3 (X^2A_1'') have the same overall symmetry. It is also believed that the $^2B_2$ state of NO_2 is responsible for most of the visible emission.[31]

The emission spectrum has been studied by a number of workers. When NO_2 is directly excited by a single wavelength, a discrete structure is observed superimposed on a broad continuum. Sakurai and Broida[32] measured the ratio of discrete to continuous emission as a function of excitation energy and found that the continuum emission increased with increasing energy. In a series of studies Kaufman et al.[28,33] explained the sharpness as due to emission from levels initially populated whereas the continuum is due in part to collisional relaxation to a large number of other radiating levels and in part to an inherent property of NO_2 in the absence of collisions. The lack of any discrete features in the emission spectra of Fig. 6 implies that the NO_2 is formed very high up in the vibrational manifold of the $^2B_2$ state where the spacing between levels is smaller. That the NO_2 is

vibrationally hot is consistent with the low average translational energies found for the fragments.

II. Molecular Beam Studies

The analysis has shown that the primary process in the photodissociation of nitromethane at 193 nm is cleavage of the C-N bond to yield CH_3 and NO_2 radicals and that there are two distinct mechanisms for formation of these chemical products. The data further suggests that a significant (>10 percent) fraction of the NO_2 product formed in the dominant mechanism retains 72 kcal/mole of internal energy or more and dissociates to NO + O, as evidenced by the apparent loss of the slow NO_2 product depicted in Fig. 4. This interpretation is supported by the emission studies of the NO_2 product from the photodissociation of the series of nitroalkanes, which also indicate that much of the total available energy is retained as internal energy of the excited state NO_2. It is further supported by the observation of NO_2 fluorescence near the dissociation limit to NO + O.

The molecular beam study does not identify the electronic state of the products, but it is consistent with a large fraction of the NO_2 product being formed in the $^2B_2$ state. The total available energy for product translational + internal energy is 90 kcal/mole. As the largest amount of energy that goes into translational energy in the dissociation process is 44 kcal/mole, the major fraction of the NO_2 product contains much more internal energy than the electronic energy of the $^2B_2$ state, particularly considering the evidence that the alkyl group carries away little internal energy.

If one assigns the main feature of the product translational energy distribution shown in Fig. 4 to production of NO_2 in the excited $^2B_2$ state and subtracts the electronic energy, E_E = 27.9 kcal/mole[17,18], of the $^2B_2$ state from the total available energy, then the average fraction of the modified total available energy, $E^*_{avail} = E_{avail} - E_E$, that goes into translation is:

$$f_T = \frac{\overline{E_T}}{E^*_{avail}} = \frac{(13.4 + 16.2)}{2(90-27.9)} = 0.24 \pm 0.02 \qquad (11)$$

The major uncertainty in f_T is in the approximation of $\overline{E}_T$ for the major primary process. It is certainly lower than 16.2 kcal/mole, the $\overline{E}_T$ for the $NO_2(^2B_2)$ product distribution, because the slow $NO_2(^2B_2)$ product has undergone unimolecular decomposition, and it is larger than 13.4 $\overline{E}_T$ for the CH_3^+ distribution, as here the low translational energies from the 2 kcal/mole mechanism are included, so the true $\overline{E}_T$ for process (2) lies between these limits. Here we take the average and state the uncertainty due to these considerations. Thus, the average translational energy release, ~15 kcal/mole, is only 24 percent of the total available energy minus electronic energy, leaving a large fraction, 47 kcal/mole, for excitation of rotation and vibration of the CH_3 and NO_2 fragments.

Some characteristics of the excitation and dissociation suggest how this vibrational and rotational energy might be partitioned in the NO_2 and CH_3 fragments. First, if the symmetry of the ground state is

preserved in the excited state, little rotational angular momentum will be generated during the separation of the fragments CH_3 and NO_2. Second, the change in geometry of the CH_3 group from near tetrahedral to near planar might be expected to excite the symmetric bend of the methyl radical, but only by 2-3 quanta if analogy is made with the recent experiments on the photodissociation of CH_3I.[34,35] Thus, most of the internal excitation will be found in the NO_2 fragment. The initial absorption of a photon by the NO_2 group might be expected to excite the bend and symmetric stretch of the NO_2 group in the $^1B_2$ state as this would be the case for π electron excitation in free NO_2. The geometry of the X $^1A_1$ state of nitromethane is given by Cox and Waring[36] as $<NCH = 107.2^\circ$, $<ONO = 125.3^\circ$ and N-O = 1.224 Å; the $^1B_2$ excited state geometry has not been calculated to our knowledge. The bond angles and lengths for ground $^2A_1$ NO_2 are 134° and 1.20 Å as compared to the theoretical values of 102° and 1.26 Å for the $^2B_2$ state.[37]

Though much information on the dominant dissociation mechanism of nitromethane has been derived from these experiments, only a few facts have been learned about the minor pathway. A possible explanation for a translational energy distribution that peaks sharply at such low energies might be internal conversion and dissociation from the ground electronic state of nitromethane to ground state products. This channel would be expected to release a much smaller fraction of the total available energy to translation than the dominant process of predissociation of the $\pi \rightarrow \pi^*$ state, presumably by a surface that is repulsive in the C-N bond correlating to excited state NO_2. If this ground state NO_2

product absorbed a 193 nm photon, it could be brought to the upper $^2B_2$ state of NO_2 which is thought to correlate to NO + O(^{1}D) at 117 kcal/mole.[38] This is consistent with the angular distribution of fast NO and O photofragments which resulted from a parallel transition, and with the maximum translational energy release for the secondary dissociation being less than the total available energy of ~119 kcal/mole [148(hν) + 148(hν) -60(C-N) -117(ON-O(^{1}D))]. This explanation is not completely satisfactory for two reasons. First, dissociation from the ground state might be expected to have a translational energy distribution peaking at zero kcal/mole if there were no barrier to dissociation. Second, it is not clear to us why the proposed ground state product for the minor channel would differ in its cross section for absorption of a 193 nm photon from the $^2B_2$ NO_2 product from the major channel because these two electronic states are so strongly mixed at high internal energies. This dynamically distinct mechanism for producing CH_3 and NO_2 radicals requires further investigation.

One further question concerning the assignment of the absorption bands of CH_3NO_2 at 198 and 270 nm needs to be considered. While Schoen et al.[6] found at an excitation wavelength of 264 nm that the quantum yield of NO_2 from C-N bond fission was only about 1 percent, the quantum yield of NO_2 product at 193 nm is nearly unity.[42] Yet the $n \rightarrow \sigma^*$(C-N) absorption is assigned to the 270 nm band, in which the quantum yield for C-N fission is low. A priori one would expect a high probability of C-N fission if an electron were promoted to an antibonding orbital in that bond. These considerations suggest that the assignment of the band at 270 nm may be erroneous.

REFERENCES

1. W. D. Taylor, T. D. Allston, M. J. Moscato, G. B. Fazekas, R. Kozlowski and G. A. Takacs, Int. J. Chem. Kinet. 12, 231 (1980).
2. S. Nagakura, Mol. Phys. 3, 152 (1960).
3. J. W. Rabelais, J. Chem. Phys. 57, 960 (1972).
4. T. Fujikawa, T. Ohta and H. Kuroda, Chem. Phys. Lett. 28, 433 (1974).
5. W. M. Flicker, O. A. Musher, and A. Kuppermann, J. Chem. Phys. 72, 2788 (1980).
6. P. E. Schoen, M. J. Marrone, J. M. Schnur and L. S. Goldberg, NRL Memor. Report 4755, p.3 (1981); Chem. Phys. Lett. 90, 272 (1982).
7. K. Honda, H. Mikuni, and M. Takahasi, Bull. Chem. Soc. Japan 45, 3534 (1972).
8. I. M. Napier and R. G. W. Norrish, Proc. Roy. Soc. A 299, 317 (1967).
9. K. G. Spears and S. P. Brugge, Chem. Phys. Lett. 54, 373 (1978).
10. H. S. Kwok, G. Z. He, R. K. Sparks, and Y. T. Lee, Int. J. Chem. Kinet. 3, 1125 (1981).
11. Y. T. Lee, J. D. McDonald, P. R. LeBreton and D. R. Herschbach, Rev. Sci. Instrum. 40, 1402 (1969).
12. See, for example, Aa. S. Sudbo, P. A. Schulz, Y. R. Shen, and Y. T. Lee, J. Chem. Phys. 69, 2312 (1978).
13. This background is presumably due to scattered light from the intense laser dissociating or desorbing diffusion pump oil from

the wall behind the interaction region in the viewing region of the detector. As would be expected there, it appears at a typical hydrocarbon fragment mass.

14. M. Kawasaki, S. J. Lee and R. Bersohn, J. Chem. Phys. 66, 2647 (1977).

15. A. Fontijn, C. B. Meyer, and H. I. Schiff, J. Chem. Phys. 40, 64 (1964).

16. G. Inoue, Y. Nakata, Y. Usui, H. Akimoto, and M. Okuda, J. Chem. Phys. 70, 3689 (1979).

17. G. D. Gillispie and A. U. Khan, J. Chem. Phys. 65, 1624 (1976).

18. J. C. D. Brand, K. J. Cross, and A. R. Hoy, Can. J. Phys. 60, 1081 (1982).

19. This assumes that the cracking pattern of NO_2 is essentially the same for the range of internal energies of the NO_2 product.

20. Because the main feature here is due to the remaining NO_2 product, this is only strictly true if the fraction of NO_2 that absorbs another photon is small. If the fraction were larger, then the relative power dependence would be expected to be even stronger than linear.

21. G. E. Busch and K. R. Wilson, J. Chem. Phys. 56, 3638 (1972).

22. K. L. McEwen, J. Chem. Phys. 32, 1801 (1960).

23. L. E. Harris, J. Chem. Phys. 58, 5615 (1973).

24. J. H. Ling and K. R. Wilson, J. Chem. Phys. 65, 3 (1976).

25. G. Geisler and H. Kessler, Ber. Bunsen Physik. Chem. 68, 571 (1964).

26. D. K. Hsu, D. L Monts, and R. N. Zare, Spectral Atlas of Nitrogen Dioxide 5530 to 6480A, Academic Press, N.Y. (1978).

27. D. Neuberger and A. B. F. Duncan, J. Chem. Phys. 22, 1693 (1954).

28. V. M. Donnelly and F. Kaufman, J. Chem. Phys. 66, 4100 (1977); ibid. 69, 1456 (1978).

29. S. E. Schwartz and H. S. Johnston, J. Chem. Phys. 51, 1286 (1969).

30. C. G. Stevens, M. W. Swagel, R. Wallace, and R. N. Zare, Chem. Phys. Lett. 18, 456 (1973).

31. H. Okabe, Photochemistry of Small Molecules, Wiley-Interscience, N.Y. (1978) p. 232.

32. K. Sakurai and H. P. Broida, J. Chem. Phys. 50, 2404 (1969).

33. D. G. Keil, V. M. Donnelly, and F. Kaufman, J. Chem. Phys. 73, 1514 (1980).

34. H. W. Hermann and S. R. Leone, J. Chem. Phys. 76, 4766 (1982).

35. R. K. Sparks, K. Shobatake, L. R. Carlson and Y. T. Lee, J. Chem. Phys. 75, 3838 (1981).

36. A. P. Cox and S. Waring, J. Chem. Soc., Faraday Trans. 2, 68, 1060 (1972).

37. G. D. Gillispie, A. U. Khan, R. P. Hosteng, and M. Krauss, J. Chem. Phys. 63, 3425 (1975).

38. R. J. S. Morrison, B. H. Rockney and E. R. Grant, J. Chem. Phys. 75, 2643 (1981).

39. R. E. Center and A. Mandl, J. Chem. Phys. 57, 4104 (1972).

40. T. M. Miller and B. Bederson, Adv. At. Mol. Phys. 13, 1 (1977).

41. D. Krajnovich, F. Huisken, Z. Zhang, Y. R. Shen and Y. T. Lee, J. Chem. Phys. 77, 5977 (1982).

42. N. C. Blais, J. Chem. Phys. 79, 1723 (1983).

APPENDIX 1: Comparison of Experimental and Calculated CH_3:NO_2 Ratios

The true experimental CH_3:NO_2 ratio at laboratory angle θ is related to the observed CH_3^+:NO^+ ion signal ratio according to

$$\frac{N_{CH_3}(\theta)}{N_{NO_2}(\theta)} = \frac{N_{CH_3^+}(\theta)}{N_{NO^+}(\theta)} \cdot \frac{\sigma_{ion}(NO_2)}{\sigma_{ion}(CH_3)} \cdot \frac{f(NO^+|NO_2)}{f(CH_3^+|CH_3)} ,$$

where $\sigma_{ion}(NO_2)$ is the ionization cross section of NO_2, $f(NO^+|NO_2)$ is the fraction of those NO_2 radicals which are ionized which give NO^+, and similarly for $\sigma_{ion}(CH_3)$ and $f(CH_3^+|CH_3)$. At $\theta = 40°$, the observed CH_3^+ and NO^+ signal levels were 0.30 and 0.98 counts/pulse, respectively. (We will ignore the contribution of NO radicals from secondary NO_2 photodissociation to the NO^+ signal, since this contribution (~20 percent) is small compared to errors involved in the determination of the radical fragmentation patterns, as will be discussed below.)

The ionization cross sections were estimated using the following empirical correlation between peak ionization cross section and the polarizability[39]

$$\sigma_{ion} = 36\sqrt{\alpha} - 18,$$

where σ_{ion} and α are in units of $Å^2$ and $Å^3$, respectively. Molecular polarizabilities were approximated as the sum of the atomic polarizabilities. This is expected to be a good approximation except in the case of highly polarizable one-electron atoms such as H (or the alkalis) where the atomic polarizability tends to overestimate the contribution

to the molecular polarizability. This is illustrated by the fact that the polarizabilities of atomic and molecular hydrogen are nearly equal. Therefore, for H, we took $\alpha_H = (1/2)\alpha_{H_2} = 0.3$. The values of the other other atomic polarizabilities were taken from Ref. 40: $\alpha_C = 1.8$, $\alpha_N = 1.1$, $\alpha_O = 0.8$. Thus, $\sigma_{ion}(CH_3) = 41$, $\sigma_{ion}(NO_2) = 41$. (If α_H is used instead of $(1/2)\alpha_{H_2}$ to calculate the contribution of H to the CH_3 polarizability, $\sigma_{ion}(CH_3)$ increases to 50. This difference is negligible at the present level of comparison.)

Methyl radicals fragment mainly to give CH_3^+, CH_2^+ and CH^+ in the ionizer. We measured the following signal ratio in our experiment:

$$m/e = 15:14:13 = 100:167:43.$$

The m/e = 15 and 13 TOF distributions look identical. Therefore all of the m/e = 13 signal is due to CH^+. However, the TOF distribution at m/e = 14 clearly shows contributions from both CH_3 (as CH_2^+) and NO_2 (as N^+). Unfortunately the data quality at m/e = 14 is quite poor, due to high detector background at this mass. We estimate roughly that only 1/3 of the m/e = 14 signal is due to CH_3. (This is the weakest point in this analysis.) Then, $CH_3^+:CH_2^+:CH^+ = 100:56:43$, and $f(CH_3^+ \; CH_3) = 0.50$.

NO_2 radicals fragment mainly to NO^+, O^+ and N^+. (The NO_2^+ signal is 10–20 times lower than the NO^+ signal and may be safely ignored.) We measured

$$CH_3^+:NO^+:O^+ = 15:100:29.$$

Using this data, together with the assumption that 2/3 of the m/e = 14 signal is due to NO_2, we obtain the following NO_2 fragmentation pattern:

$$NO^+:O^+:N^+ = 100:29:16.$$

This gives $f(NO^+|NO_2) = 0.69$.

The experimental $CH_3:NO_2$ ratio at 40° is therefore

$$\frac{N_{CH_3}(40^\circ)}{N_{NO_2}(40^\circ)} = \frac{0.30}{0.98} \times \frac{41}{41} \times \frac{0.69}{0.50} = 0.42.$$

If, at the other extreme, all of the m/e = 14 signal is ascribed to CH_2^+, we get $f(CH_3^+|CH_3) = 0.32$, $f(NO^+|NO_2) = 0.78$, and

$$\frac{N_{CH_3}(40^\circ)}{N_{NO_2}(40^\circ)} = 0.75.$$

The theoretical $CH_3:NO_2$ ratio at any angle is automatically calculated by the c.m. → LAB transformation program using the P(E')'s for CH_3 and NO_2, respectively. The two P(E')'s must be normalized as shown in Fig. 4 (to properly take into account the loss of slow NO_2). The details of the general calculation are reviewed in Appendix B of Ref. 41. The result is

$$\frac{N_{CH_3}(40^\circ)}{N_{NO_2}(40^\circ)} = 0.63.$$

The experimental and calculated CH_3:NO_2 ratios agree reasonably well. (If anything, the experimental CH_3:NO_2 ratio is too small, indicating "too much" NO_2 relative to CH_3.) Therefore, we cannot assume that a large fraction of the <u>total</u> NO_2 primary product undergoes secondary photodissociation. This result forms the basis for the assumption that it must be the slow NO_2 formed in the minor primary photodissociation process [which gives rise to the blip in the CH_3 P(E')] which is responsible for the strongly saturated secondary photodissociation signal.

APPENDIX 2: Calculation of Fits to NO^+ and O^+ Data.

The contribution of NO_2 to the NO^+ and O^+ data is calculated using the NO_2 P(E') shown in dashed line in Fig. 4 and the nitromethane beam velocity distribution for the distribution of c.m. velocities. We want to fit the shoulders in the NO^+ and O^+ TOF distributions by adjusting the P(E') and anisotropy parameter for the secondary photodissociation reaction:

$$NO_2 \longrightarrow NO + O, \qquad (5)$$

and varying the contributions of NO and O relative to NO_2. Strictly speaking, when calculating the laboratory angular and TOF distributions of NO and O, we should use the laboratory number density angle-velocity distribution of the primary NO_2 product in place of the nitromethane beam velocity distribution to represent the distribution of c.m. velocities. Here we are assuming that only the slow NO_2 produced via the minor primary dissociation pathway undergoes secondary photodissociation. This NO_2 is concentrated in a fairly narrow cone about the original nitromethane beam direction. Since much more translational energy is released in the secondary reaction (5) than in the minor primary dissociation reaction, the calculated NO and O angular and TOF distributions are insensitive to the details of the energy release in the primary reaction. In the fits to be presented below, we simply approximated the parent NO_2 c.m. velocity distribution for reaction

(5) by the nitromethane beam velocity. We will not justify this approximation in detail here, but it is, in fact, a very good approximation in this case.

The relative contributions of NO_2 and NO to the NO^+ signal should be given by

$$N_{NO^+}(\theta,t) = N_{NO_2}(\theta,t) + \epsilon \cdot \frac{\sigma_{ion}(NO)}{\sigma_{ion}(NO_2)} \cdot \frac{f(NO^+|NO)}{f(NO^+|NO_2)} \cdot N_{NO}(\theta,t),$$

where $N_{NO}(\theta,t)$ is calculated from the NO_2 P(E') in dashed line in Fig. 4, using an isotropic c.m. angular distribution, and $N_{NO}(\theta,t)$ is calculated from a P(E') and anisotropy parameter describing reaction (5). ϵ is the ratio of the fraction of NO_2 which undergoes secondary photodissociation to the fraction of NO_2 which survives. (For other notation, see Appendix I.) Similarly, the relative contributions of NO_2, NO and O to the O^+ signal should be given by

$$N_{O^+}(\theta,t) = N_{NO_2}(\theta,t) + \frac{\epsilon}{\sigma_{ion}(NO_2) \cdot f(O^+|NO_2))} \cdot$$

$$[\sigma_{ion}(NO) \cdot f(O^+|NO) \cdot N_{NO}(\theta,t) + \sigma_{ion}(O) \cdot N_O(\theta,t)].$$

We began by adjusting the P(E') for reaction (5) to fit the shape of the shoulder in the NO^+ TOF at 40° (assuming b = 0). We obtained a good fit with the P(E') shown in Fig. 14, which has a mean translational energy of 31 kcal/mole. However, using this P(E') and b = 0, the NO_2:NO ratio which gave a good fit to the magnitude of the shoulder at 40° did not give a good fit to the shoulder heights at smaller

angles; the calculated shoulders were too small at 10° and 25°. To compensate for this, a positive anisotropy parameter for reaction (5) was required. The best-fits to the NO^+ TOF data shown in Fig. 15 were calculated using the P(E') in Fig. 14, b = +0.5, and the following NO_2:NO ratio:

$$N_{NO^+}(\theta,t) = N_{NO_2}(\theta,t) + 0.3\, N_{NO}(\theta,t).$$

Therefore it appears that the secondary photodissociation of NO_2 occurs via a parallel transition. From the empirically determined NO_2:NO ratio we have:

$$\varepsilon \cdot \frac{\sigma_{ion}(NO)}{\sigma_{ion}(NO_2)} \cdot \frac{f(NO^+|NO)}{f(NO^+|NO_2)} = 0.3,$$

or

$$\varepsilon \cdot f(NO^+|NO) = 0.27.$$

The corresponding fit to the measured NO^+ laboratory angular distribution is shown in Fig. 16.

To consistently fit the O^+ TOF distribution, we must use the same P(E') and anisotropy parameter for reaction (5), and an NO_2:NO:O ratio which is constrained by

$$N_{O^+}(\theta,t) = N_{NO_2}(\theta,t) + 3.84\, \varepsilon \cdot f(O^+|NO) \cdot N_{NO}(\theta,t) + 1.72\, \varepsilon \cdot N_O(\theta,t),$$

where we have used the NO_2 fragmentation pattern and ionization cross sections specified in Appendix 1.

Unfortunately, we had no way of determining the NO fragmentation pattern in this experiment. At first we assumed that $f(O^+|NO) = 1-f(NO^+|NO)$ (i.e., all NO is ionized to either NO^+ or O^+). However, using this assumption, we could not get a satisfactory fit to the O^+ shoulder for any value of ϵ (the NO contribution was always too large compared to the O contribution). Evidently, some of the NO also fragments to N^+ in the ionizer. By arbitrarily assuming that $f(O^+|NO) = 1/2[1-f(NO^+|NO)]$, we were able to obtain the fit to the O^+ data shown in Fig. 17, using the value $\epsilon = 0.50$. This ϵ value implies that 1/3 of the total NO_2 primary product (less that fraction which spontaneously decomposes) undergoes secondary photodissociation.

The area under the CH_3 P(E') in Fig. 4 is 36 percent larger than the area under the NO_2 P(E'). If all of this 36 percent difference were due to NO_2 which undergoes secondary photodissociation there would be almost perfect agreement with the ϵ value deduced above. However, part of the 36 percent difference is undoubtedly due to spontaneous unimolecular decay of hot NO_2 ($^2B_2$) produced in the major primary dissociation process. Therefore, the value $\epsilon = 0.50$ is a bit on the high side. Still, given the guesswork involved in the above analysis, we do not feel that this discrepancy is fatal. (If, on the other hand, we had deduced a value of $\epsilon \geq 1$, we would have been compelled to abandon the hypothesis that the secondary photodissociation signal is due to NO_2 produced in the minor primary dissociation process.)

The spontaneous decay of hot NO_2 from the major primary dissociation process is also reflected in the NO^+ and O^+ TOF distributions at small angles. The hottest NO_2 is formed in low recoil energy events, and, in the laboratory, should appear near the molecular beam velocity. The flight time corresponding to the nominal c.m. (CH_3NO_2) is ~150 μsec. The actual NO^+ and O^+ TOF data is smeared out in the vicinity of the c.m. velocity, due to spontaneous decay of the hottest NO_2. The smearing, however, is not too severe, suggesting that even the hottest NO_2 radicals are not too far above the $NO(^2\Pi) + O(^3P)$ dissociation limit. (Recall that the maximum possible NO_2 excess energy is 18 kcal/mole.)

Table 1. Power dependence of the relative shoulder intensity in the NO^+ TOF spectrum at $\theta = 40^\circ$.

Pulse Energy (mJ)	Photon Flux† (photons/cm^2-pulse)	Laser Intensity† (MW/cm^2)	$\frac{S(15-35)}{S(36-120)} \pm \sigma$
0.7*	1.7×10^{16}	1.3	0.045 ± 0.008
2.0	4.9×10^{16}	3.6	0.049 ± 0.005
3.3*	8.0×10^{16}	5.9	0.047 ± 0.005
20	4.9×10^{17}	36	0.062 ± 0.003
33*	8.0×10^{17}	59	0.067 ± 0.003

*These measurements correspond to the data shown in Fig. 12.
†Calculated assuming a 4 mm^2 laser spot size at the molecular beam and a 14 ns laser pulse duration.

FIGURE CAPTIONS

Fig. 1. Some energetically allowed dissociation channels of CH_3NO_2 excited at 193 nm. ΔH^o_{300} values were calculated from ΔH^o_{f300} values tabulated in S.W. Benson, Thermochemical Kinetics, 2nd ed. (John Wiley and Sons, New York, 1976), or estimated using Benson's rules. Only ground electronic state products are shown; NO may be produced in either spin-orbit state and NO_2 may be formed in the X^2A_1, A^2B_2, B^2B_1, or C^2A_2 states.

Fig. 2. TOF distributions of m/e = 15, CH_3^+, at three angles to the molecular beam. • Experimental points, ——— best fit calculated using the solid-line P(E') in Fig. 4 and b = 0.

Fig. 3. Laboratory angular distribution of the CH_3^+ signal. • Experimental points. Error bars represent plus or minus one half standard deviation of the statistical counting error; ——— calculated using the solid-line P(E') in Fig. 4 and b = 0.

Fig. 4. Center-of-mass translational energy distributions for the products of the primary photodissociation reaction $CH_3NO_2 \rightarrow CH_3^+ + NO_2$. ——— Derived from CH_3^+ angular and TOF distributions; - - - - derived from NO_2^+ TOF distributions. The uncertainty in fitting the feature at ~100 μsec in the CH_3^+ TOF distributions (Fig. 2) is represented by the shaded area near 2 kcal/mole in the solid-line P(E'). The top border of the grey area fits the 10° TOF perfectly; the lower border fits the 40° TOF well.

Fig. 5. Fluorescence decay of NO_2^* from the photolysis of nitromethane.

Fig. 6. Dispersed fluorescence due to electronically excited NO_2 from the photolysis of nitromethane at 193 nm. The dissociation limit shown is for $NO_2 \rightarrow NO + O(^3P)$.

Fig. 7. Dispersed fluorescence of NO_2^* formed by the photodissociation of $R-NO_2$. The spectra are unchanged for the four different R groups ($(CH_3)_3CNO_2$ is not shown). The $R-NO_2$ bond energies of the three compounds shown are within 2 kcal/mole of each other and the bond energy of $(CH_3)_3CNO_2$ is estimated to be 59 ± 2 kcal/mole.

Fig. 8. Dispersed fluorescence from the photolysis of nitromethane by a focused 193 nm laser.

Fig. 9. TOF distributions of m/e = 46, NO_2^+, at three angles to the molecular beam. • Experimental points; ——— best fit calculated using the dashed-line P(E') in Fig. 4, assuming b = 0.

Fig. 10. TOF distributions of m/e = 30, NO^+, measured at three angles to the molecular beam. Fits are shown in Appendix 2, Fig. 15.

Fig. 11. TOF distribution of m/e = 16, O^+, measured at 10° from the molecular beam. Fits are shown in Appendix 2, Fig. 17.

Fig. 12. NO^+ TOF distributions measured at three laser pulse energies. All three distributions were measured at $\theta = 40°$ and have been normalized to the same peak height.

Fig. 13. Angular distribution of the methyl radicals formed by the photodissociation of nitromethane at 193 nm in the effusive molecular beam apparatus. The solid curve is the best fit to the equation $I(\theta) = A[1 + 2bP_2(\cos(\theta-\theta_0))]$ using $b = -0.30$ and $\theta_0 = 14°$.

Fig. 14. Approximate form of the center-of-mass product translational energy distribution for the secondary photodissociation reaction $NO_2 \rightarrow NO + O$.

Fig. 15. TOF distributions of NO^+. • Experimental points (same as Fig. 10); ———— best fit, obtained by adding the individual contribution of NO_2 (—— - ——) and NO (- - -) to the NO^+ signal. The NO_2 contribution was calculated using the dashed-line P(E') in Fig. 4 and $b = 0$. The NO contribution was calculated using the P(E') in Fig. 14 and $b = +0.5$. Spontaneous unimolecular decay of hot NO_2 was neglected.

Fig. 16. Laboratory angular distribution of the NO^+ mass spectrometer signal. • Experimental points; ——— fit obtained by adding the individual contributions of NO_2 and NO shown in dashed lines. The relative contributions of NO_2 and NO to the total was kept the same as for the fits of the TOF distributions of NO^+ (Fig. 15). (For the experimental points, $\pm 2\sigma$ error bars are roughly the size of the dots shown.)

Fig. 17. TOF distributions of O^+. • Experimental points (same as Fig. 11); ——— best fit, obtained by adding the individual contributions of NO_2 (—— - ——), NO (- - - -) and O (—— • ——) to the O^+ signal. The NO_2 contribution was calculated using the dashed-line P(E') in Fig. 4 and b = 0. The NO and O contributions were calculated using the P(E') in Fig. 14 and b = +0.5. Spontaneous unimolecular decay of hot NO_2 was neglected.

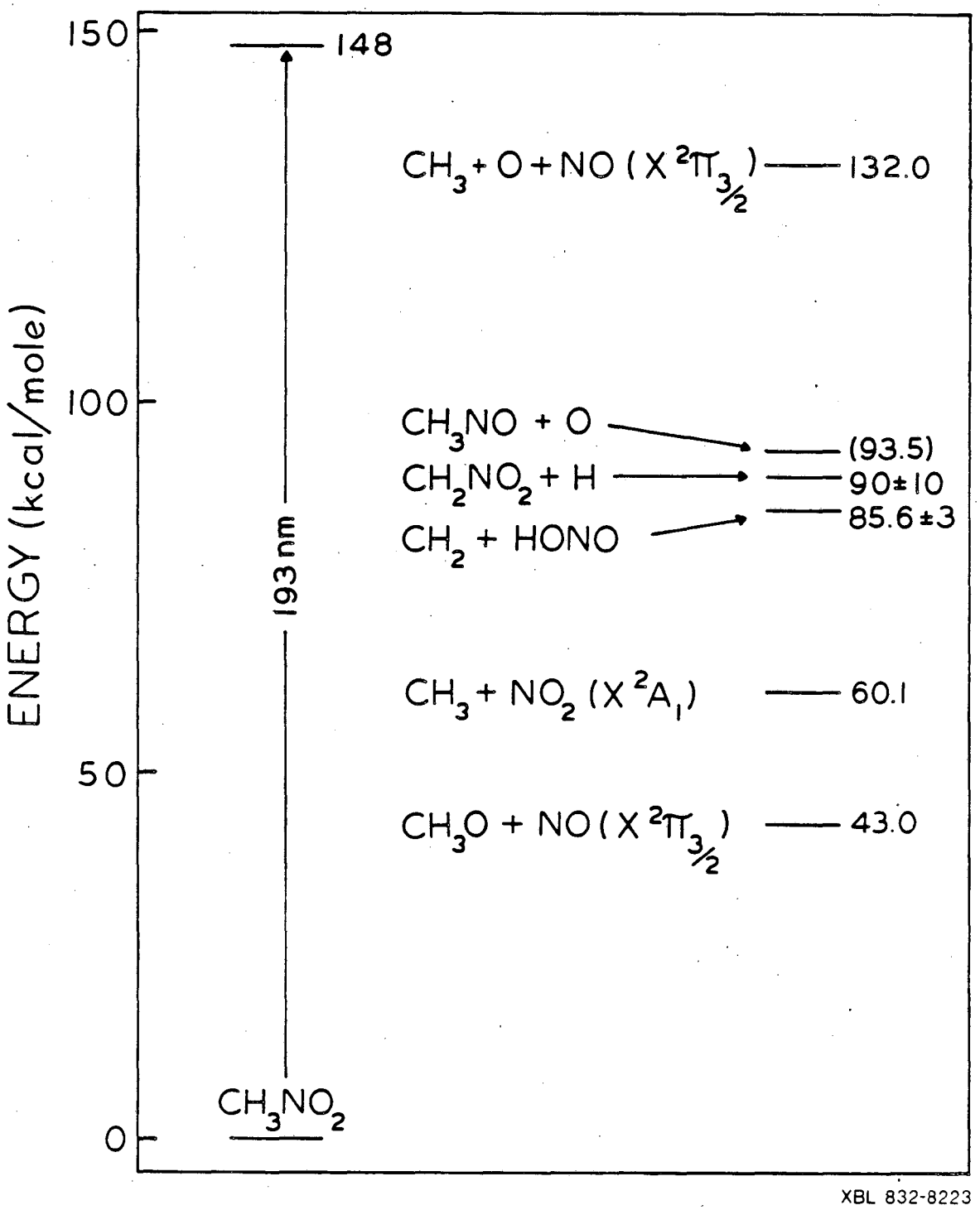
150
100
50
0
ENERGY (kcal/mole)
148
193 nm
CH_3NO_2
$CH_3 + O + NO(X\,^2\Pi_{3/2})$ — 132.0
$CH_3NO + O$ — (93.5)
$CH_2NO_2 + H$ — 90±10
$CH_2 + HONO$ — 85.6±3
$CH_3 + NO_2(X\,^2A_1)$ — 60.1
$CH_3O + NO(X\,^2\Pi_{3/2})$ — 43.0
XBL 832-8223

Fig. 1

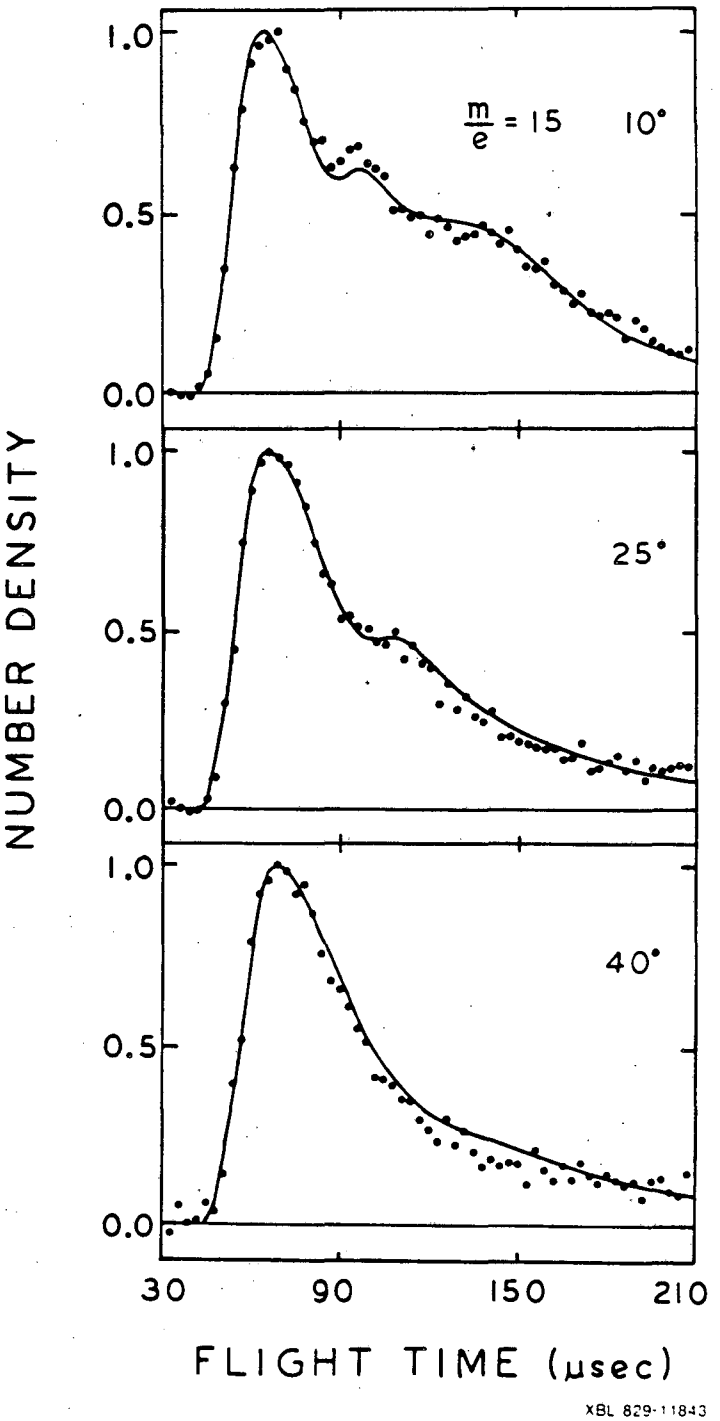
1.0
0.5
0.0
m/e = 15
10°
25°
40°
NUMBER DENSITY
30
90
150
210
FLIGHT TIME (μsec)
XBL 829-11843

Fig. 2

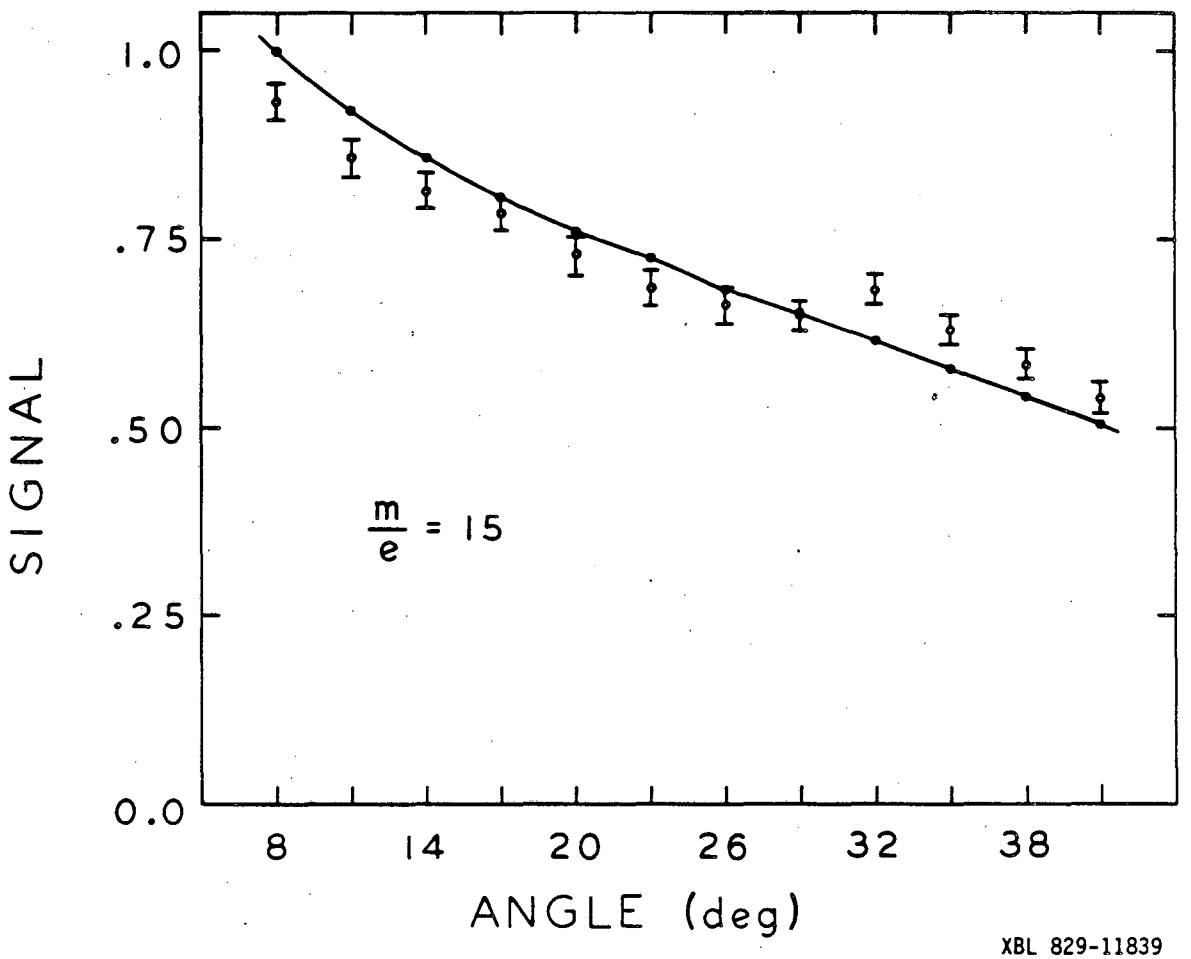
1.0
.75
.50
.25
0.0
SIGNAL
m/e = 15
8
14
20
26
32
38
ANGLE (deg)
XBL 829-11839

Fig. 3

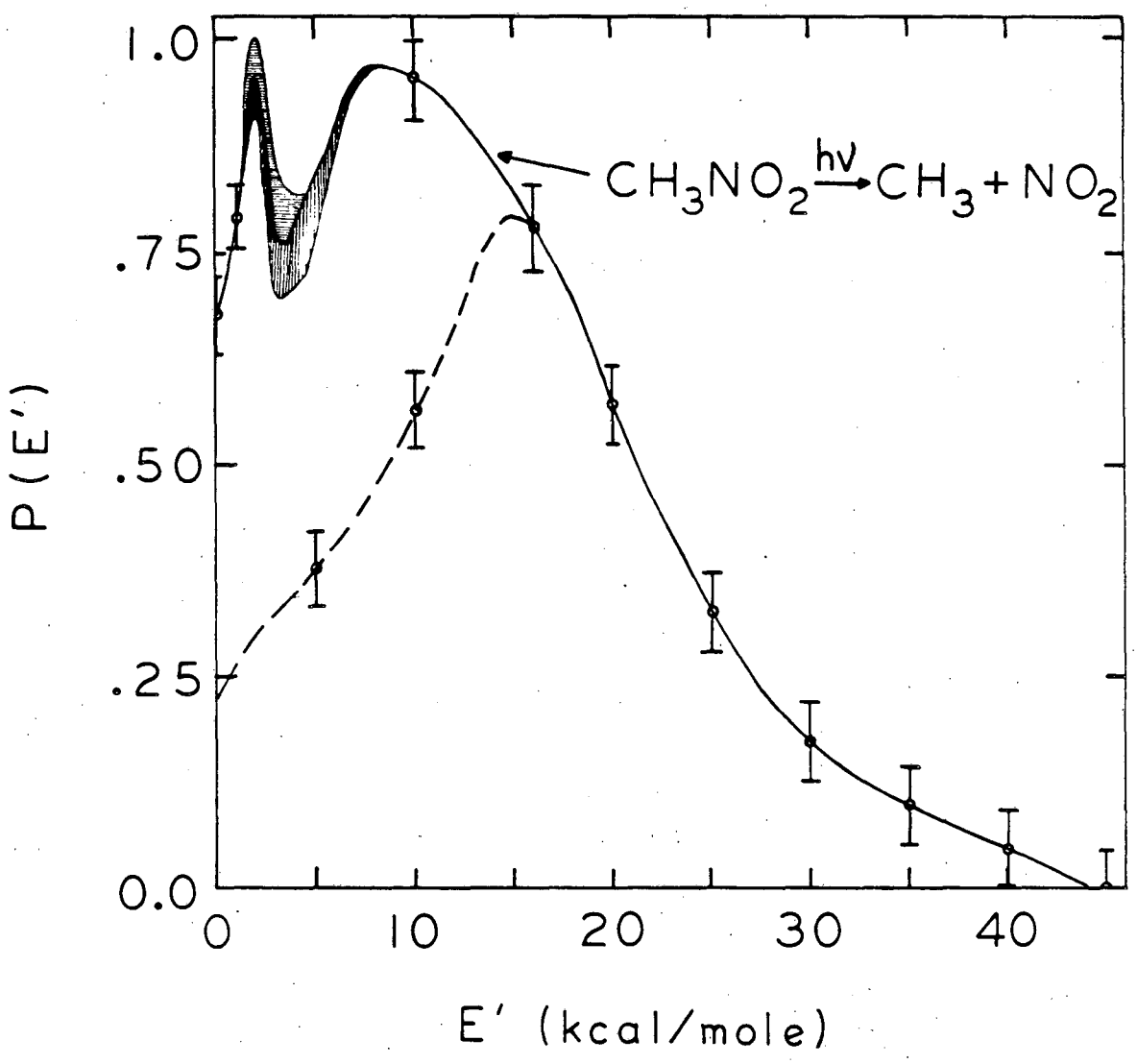

Fig. 4

829-11840

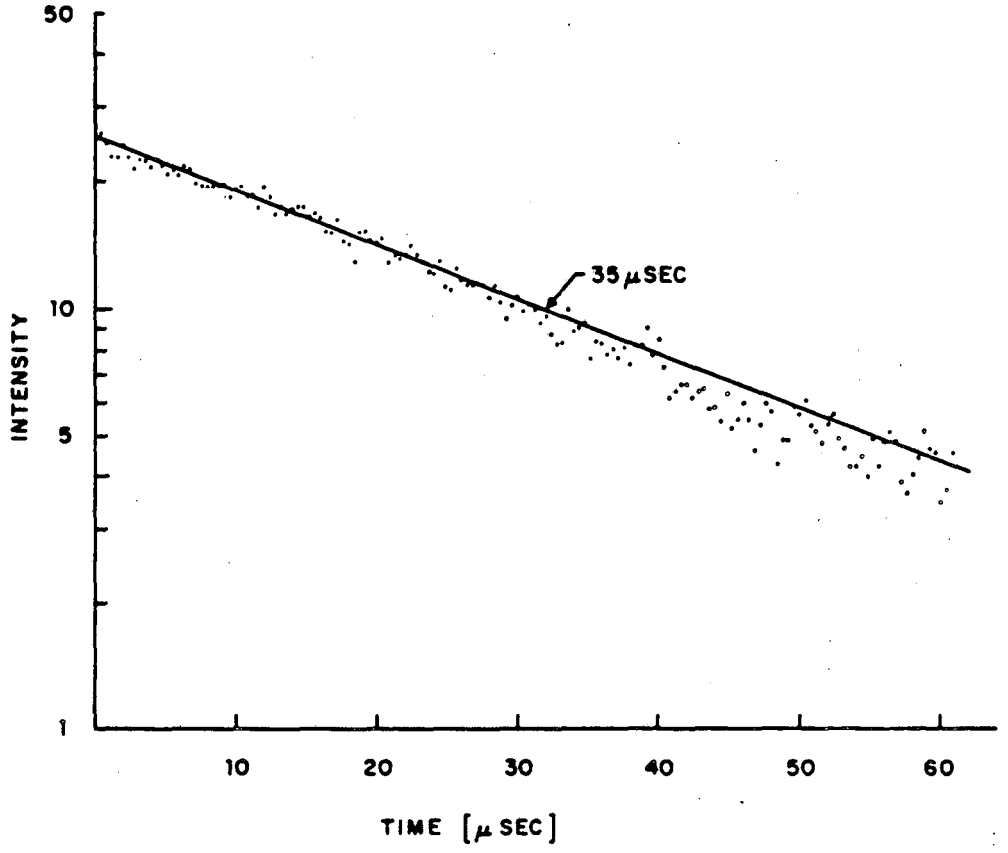

XBL 832-8190

Fig. 5

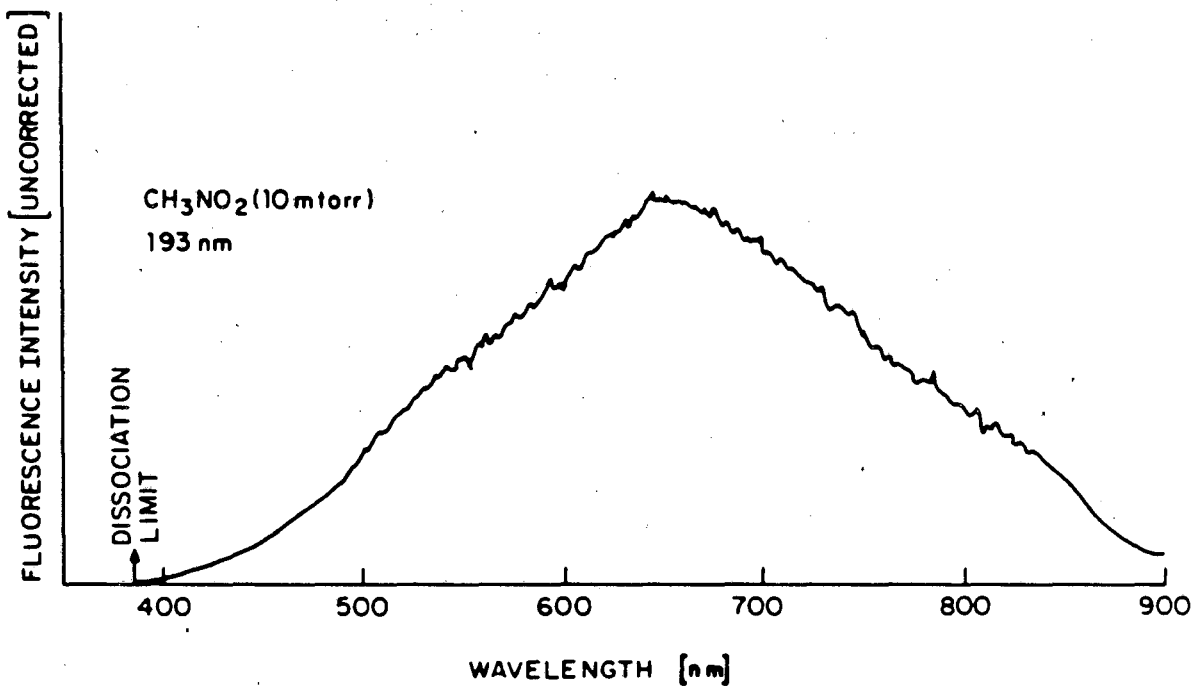

XBL 832-8189

Fig. 6

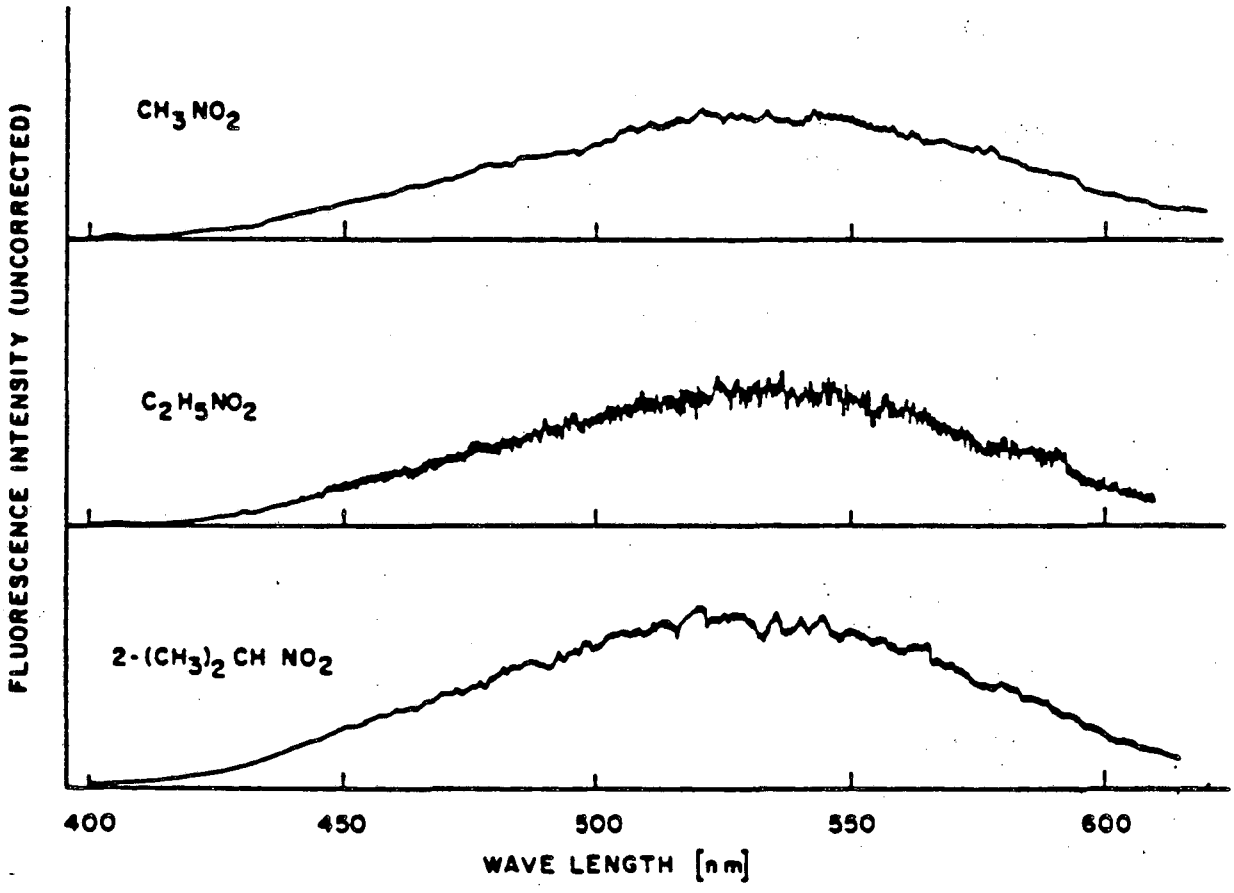

XBL 859-4108

Fig. 7

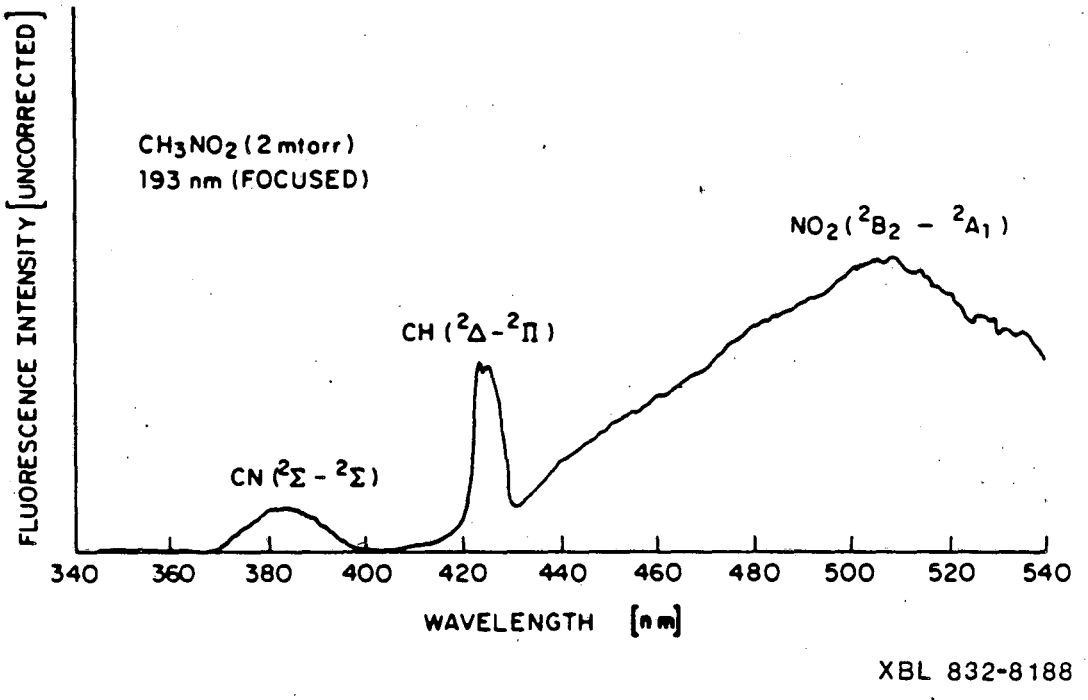
FLUORESCENCE INTENSITY [UNCORRECTED]
CH_3NO_2 (2 mtorr)
193 nm (FOCUSED)
NO_2 ($^2B_2$ – $^2A_1$)
CH ($^2\Delta$-$^2\Pi$)
CN ($^2\Sigma$ - $^2\Sigma$)
340
360
380
400
420
440
460
480
500
520
540
WAVELENGTH [nm]
XBL 832-8188

Fig. 8

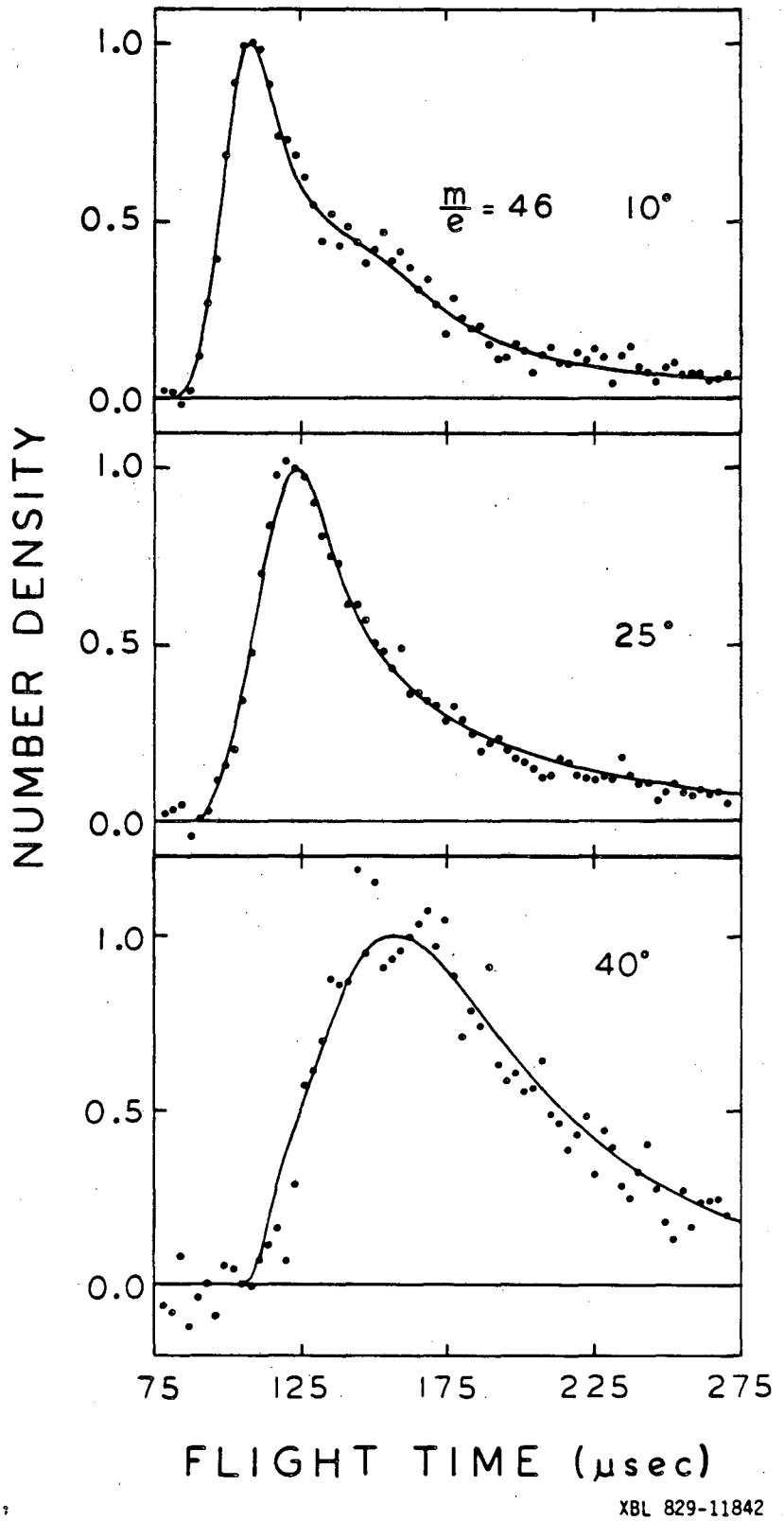
1.0
0.5
0.0
m/e = 46
10°
25°
40°
NUMBER DENSITY
75
125
175
225
275
FLIGHT TIME (μsec)
XBL 829-11842

Fig. 9

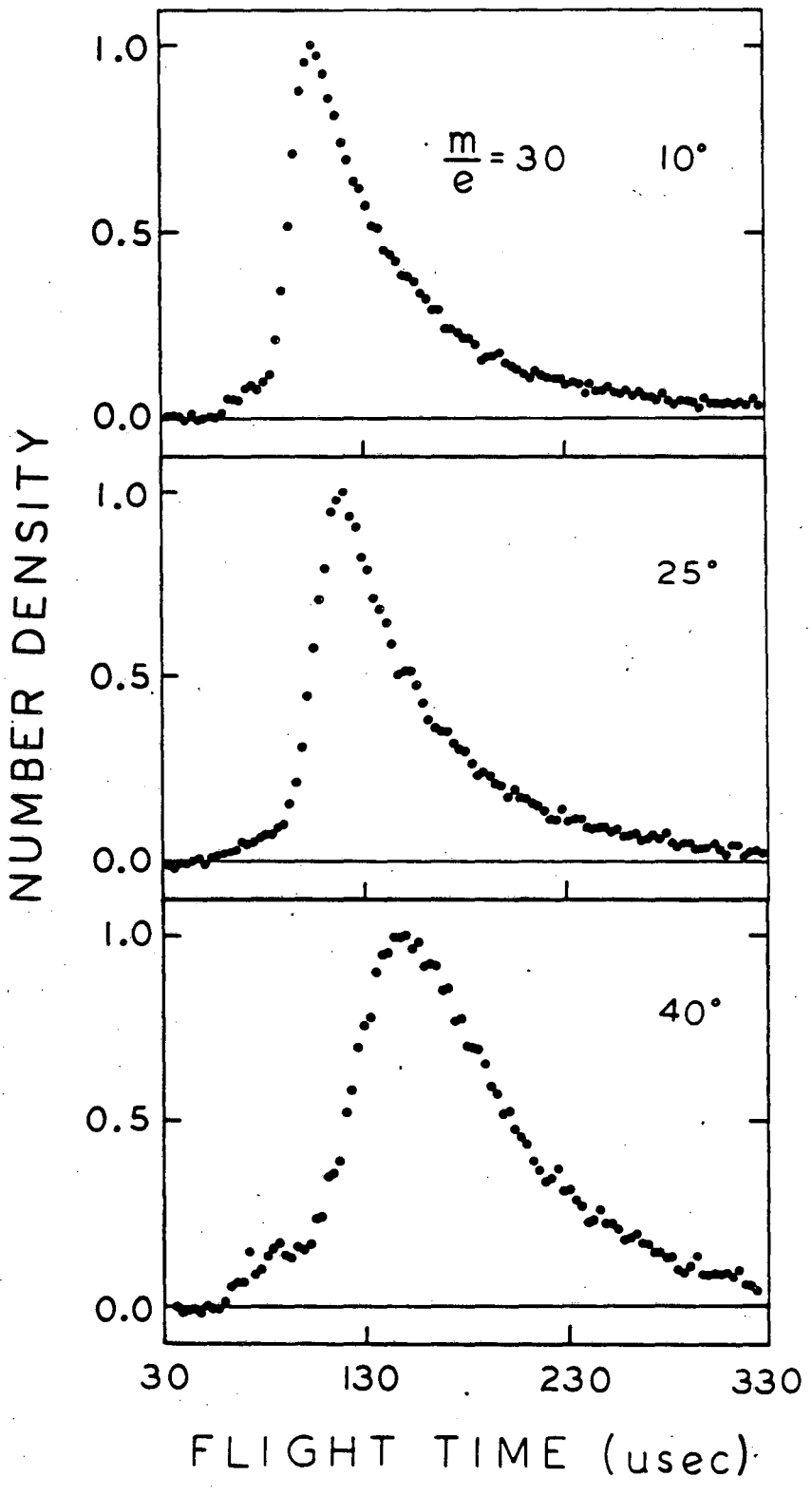

XBL 829-11841

Fig. 10

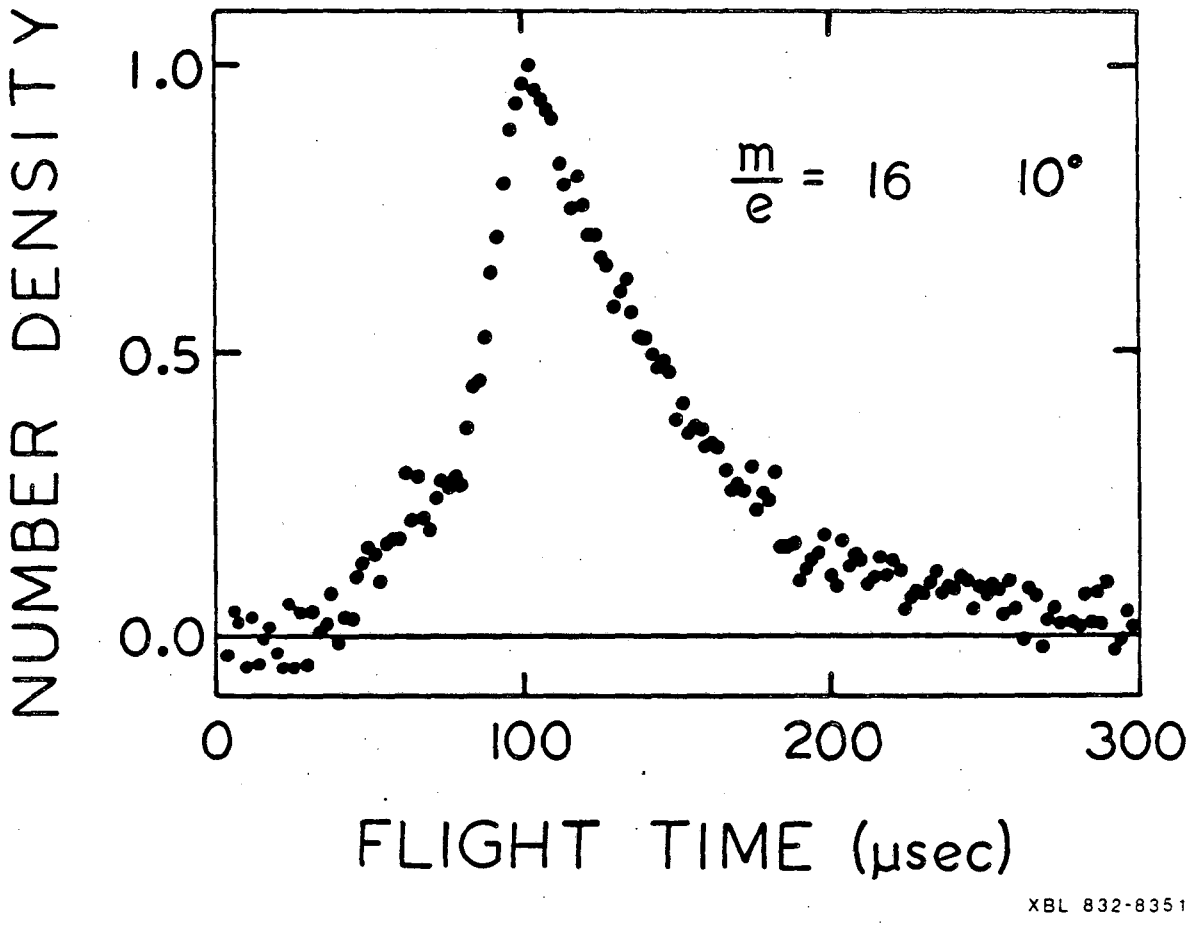
NUMBER DENSITY
1.0
0.5
0.0
m/e = 16
10°
0
100
200
300
FLIGHT TIME (μsec)
XBL 832-8351

Fig. 11

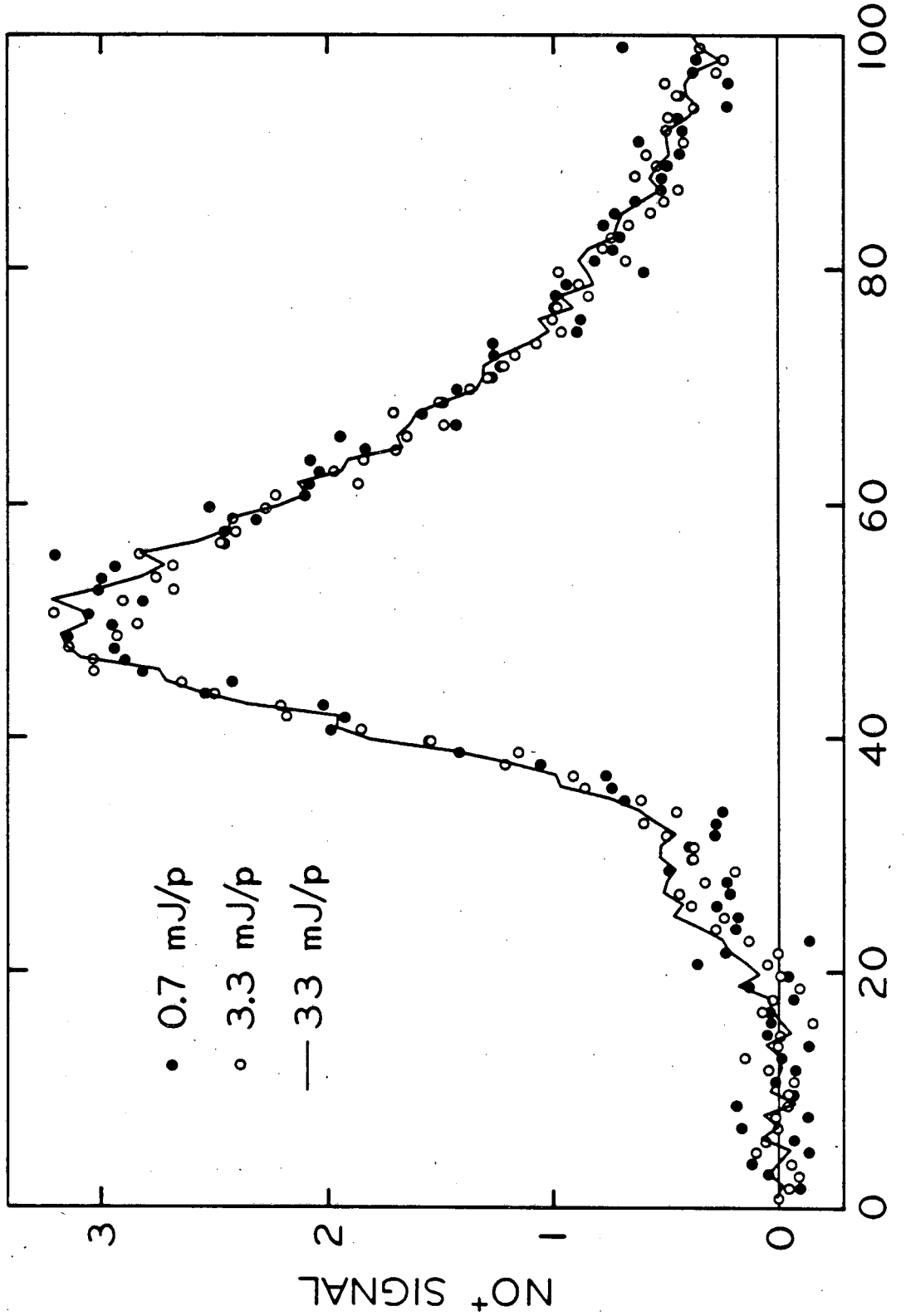

XBL 832-8291

Fig. 12

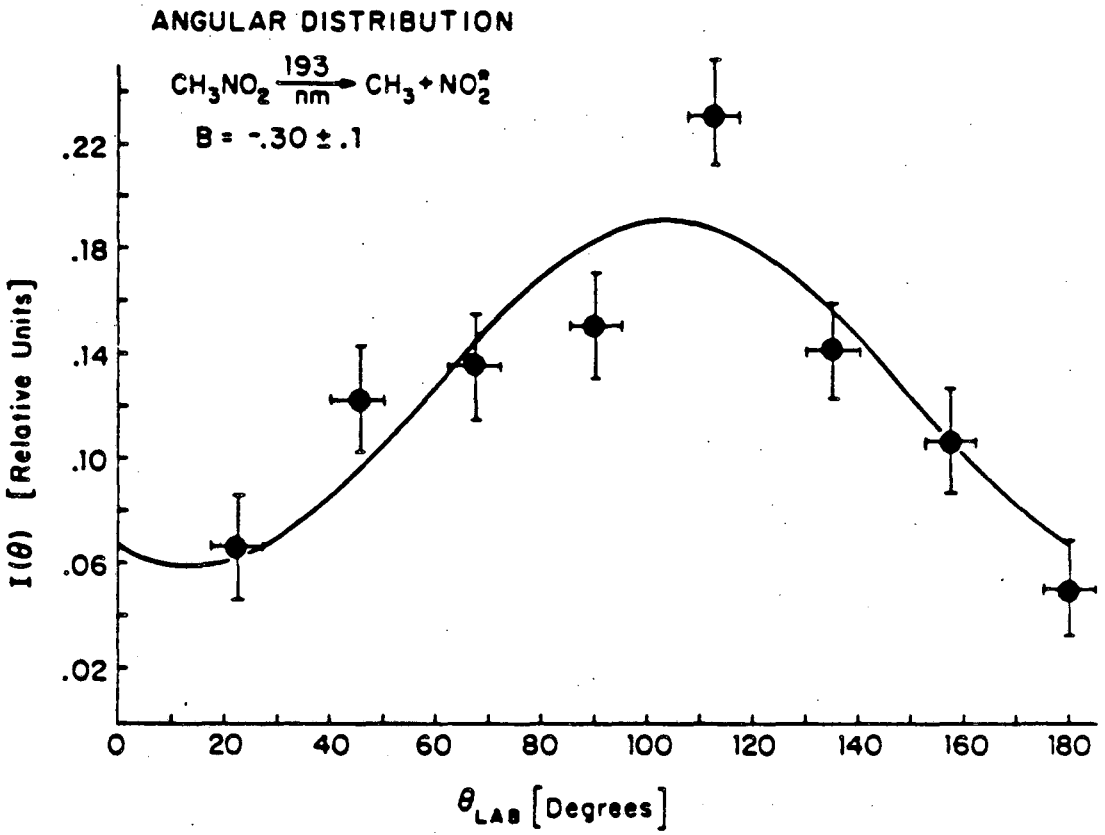

XBL 859-4109

Fig. 13

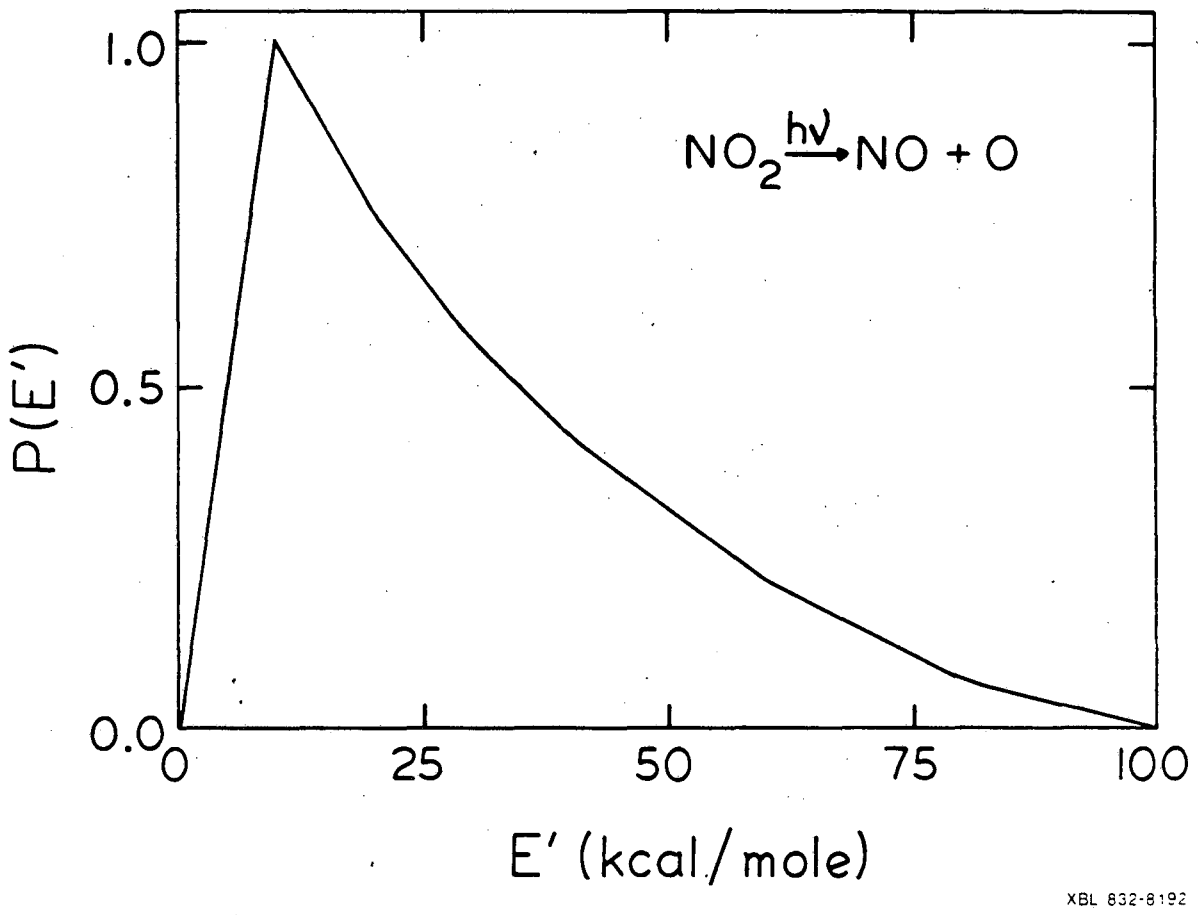
1.0
0.5
0.0
P(E')
0
25
50
75
100
E' (kcal/mole)
$NO_2 \xrightarrow{h\nu} NO + O$
XBL 832-8192

Fig. 14

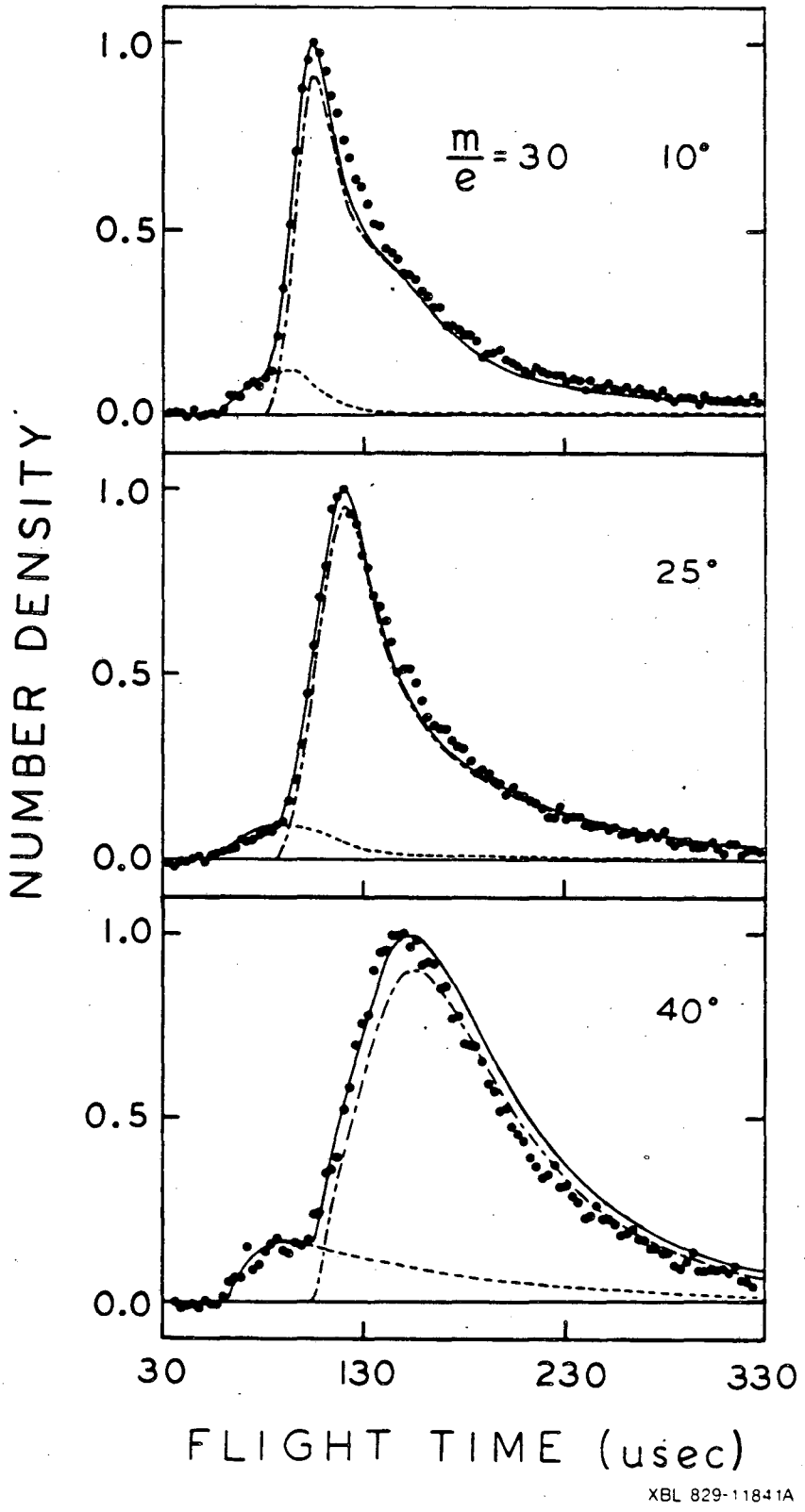
1.0
0.5
0.0
m/e = 30
10°
25°
40°
NUMBER DENSITY
30
130
230
330
FLIGHT TIME (usec)
XBL 829-11841A

Fig. 15

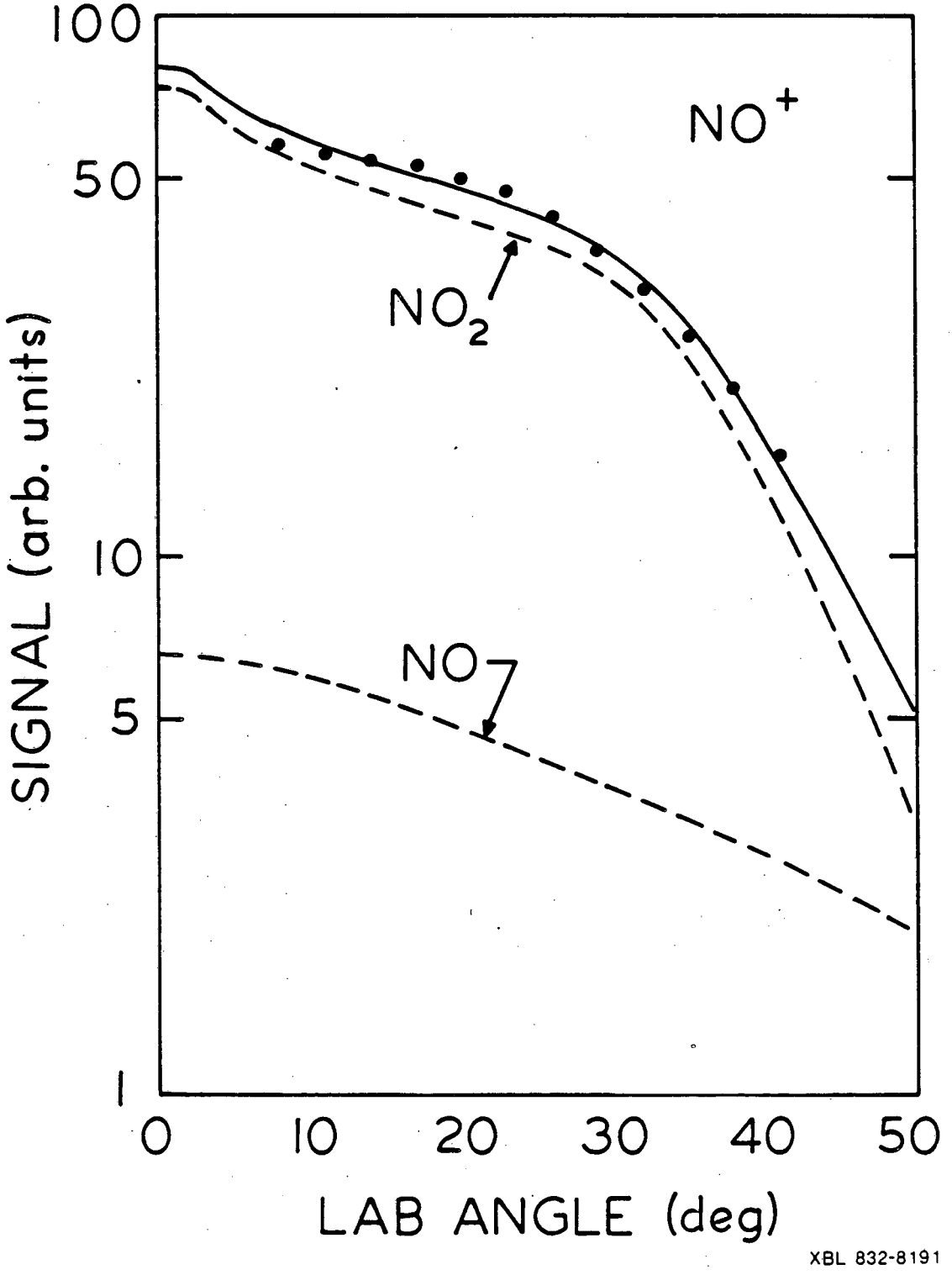
100
50
10
5
1
SIGNAL (arb. units)
NO+
NO2
NO
0
10
20
30
40
50
LAB ANGLE (deg)
XBL 832-8191

Fig. 16

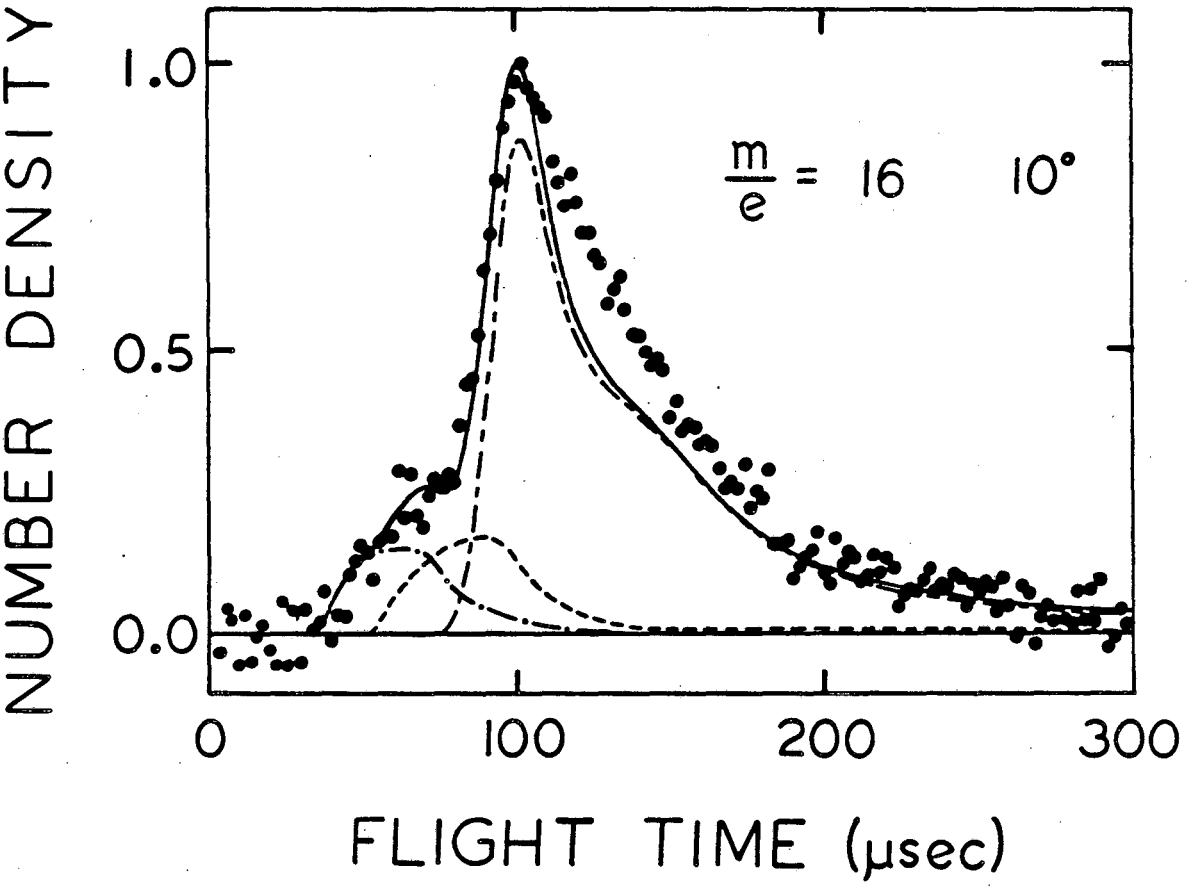

XBL 832-8222

Fig. 17

CHAPTER THREE

ENERGY PARTITIONING TO PRODUCT TRANSLATION IN THE INFRARED MULTIPHOTON DISSOCIATION OF DIETHYL ETHER*

ABSTRACT

The infrared multiphoton decomposition of diethyl ether (DEE) has been investigated by the crossed laser-molecular beam technique. The center-of-mass product translational energy distributions (P(E')) were measured for the two dissociation channels: (1) DEE → C_2H_5O + C_2H_5 and (2) DEE → C_2H_5OH + C_2H_4. The shape of the P(E') measured for the radical channel (1) is in agreement with predictions of statistical unimolecular rate theory. The translational energy released in the concerted reaction (2) peaks at 26 kcal/mole, with an average energy released to translation of 24 kcal/mole; this exceedingly high translational energy release with a relatively narrow distribution results from the recoil of the products from each other down the exit barrier. Applying statistical unimolecular rate theory, we estimate the average energy levels from which DEE dissociates to products using the measured P(E') for the radical channel (1).

---

*Published in The Journal of Physical Chemistry 87, 5106 (1983).

INTRODUCTION

Previous molecular beam investigations of unimolecular reaction dynamics have shown that potential energy barriers in the exit channel beyond the endoergicity have a large effect on the asymptotic product translational energy distributions. For almost all of the simple fission reactions studied, in which a single bond is broken without an exit barrier and no new bonds are formed, the products have statistical translational energy distributions.[1] However for all the complex fission reactions studied, in which bonds are broken and formed simultaneously, the translational energy distributions of the products reflect their recoil from each other down the substantial potential energy barrier in the exit channel.[2-4] Huisken et al.[2] studied the infrared multiphoton dissociation (IRMPD) of ethyl vinyl ether (EVE) in a crossed laser-molecular beam apparatus. They observed competition between two dissociation channels: (1) EVE $\rightarrow$ $CH_3CHO + C_2H_4$ and (2) EVE $\rightarrow$ $CH_2CHO + C_2H_5$ and found that approximately 70 percent of the 38 kcal/mole exit barrier for reaction (1) was released into product translational energy. Such a high translational energy release, ~30 kcal/mole, in the unimolecular dissociation of a polyatomic molecule in the ground electronic state was previously unsuspected. Several other similar experiments, which measured the product translational energy distributions for reactions involving three- and four-center HCl elimination from halogenated hydrocarbons[3] and a three-center Cl_2 elimination from CF_2Cl_2,[4] are reviewed in the paper of Huisken et al. In the

four-center elimination of hydrogen halides, a large fraction of the exit barrier appears as vibrational excitation of the products; the average translational energy release does not usually exceed 10 kcal/mole. Also reviewed there are some examples of infrared[5] and laser induced fluorescence[6] techniques used in bulk experiments to measure the internal energy distributions of products from complex fission reactions.

Two groups have independently studied the thermal decomposition of diethyl ether (DEE) and derived preexponential factors and activation energies for the the Arrhenius expression for the rate constants of the primary dissociation processes. Laidler and McKenney[7] and István and Péter[8] both report two competing primary channels, a simple C–O bond fission reaction with little or no exit barrier:

$$CH_3CH_2OCH_2CH_3 \longrightarrow C_2H_5O + C_2H_5 \qquad (1)$$

and a molecular elimination reaction with a large exit barrier:

$$CH_3CH_2OCH_2CH_3 \longrightarrow C_2H_5OH + C_2H_4 \qquad (2)$$

The Arrhenius parameters for the four-centered elimination (2) were reported to be log A = 18.0 and E_a = 84 kcal/mole by Laidler and McKenney and log A = 13.9 and E_a = 66.0 by István and Péter. The A-factor and activation energy for the radical channel were reported to be 14.0 and 78 kcal/mole respectively by Laidler and McKenney and 14.3 and 77.5 by István and Péter. Benson and O'Neal[9] point out that the

Laidler and McKenney A-factors are not reliable as (2) should have a larger, more positive entropy of activation than reaction (1) so it is expected that the A factor of (2) is larger than that of (1). They also point out that a fairly reliable estimate for the parameters of the radical reaction (2) can be made from the thermodynamics by assuming a recombination rate of $k_{rec} = 10^{9.7 \pm 1.0}$ l/mol.sec, from which they obtain log A = 16.3 and E_a = 81.8. The other energetically allowed decomposition channels are shown in Fig. 1 along with these two channels. The activation energies shown are those estimated by Benson and O'Neal for the radical channel (1) and reported by Istvan and Peter for the molecular elimination reaction (2).

Thus this system allowed the molecular beam study of two competing dissociation channels, one a concerted reaction with a constrained transition state resulting in a large exit barrier and the other a simple bond fission reaction with a large activation energy but no significant exit barrier. We wished to confirm the identification of these two channels, to investigate the possibility of the occurrence of the other two energetically allowed channels shown in Fig. 1 and to determine the effect of the large exit channel barrier for reaction (1) on the product translational energy distribution. As will be seen, the velocity distributions of the radical channel products allowed us to determine limits on the energy levels from which the molecules dissociated, thus providing an estimate on the average number of photons absorbed in our IRMPD experiment.

EXPERIMENT

Time-of-flight (TOF) distributions of the photofragments were measured in a molecular beam apparatus described in detail elsewhere.[10] The molecular beam was formed by bubbling helium through diethyl ether (DEE) (Mallinckrodt AR grade) maintained at 0°C and expanding the mixture through a 0.13 mm diameter stainless steel nozzle at a total stagnation pressure of 400 torr (~50 percent DEE/50 percent He). The nozzle was heated to 300°C to eliminate the formation of molecular clusters during the supersonic expansion. The velocity distribution of the DEE beam was determined by TOF measurements to have a peak velocity of 1120 m/sec and a full width at half maximum of 30 percent. The beam was collimated by a skimmer and, after passing through two pressure-reducing differential pumping chambers, it was crossed by the laser beam. The molecular beam was defined to an angular divergence of ~1.6°.

The infrared photons were produced by a Gentec DD-250 CO_2 TEA laser tuned to the P(24) line in the 001-020 vibrational band at 1043.16 cm^{-1}. The TT conformer of DEE has an absorption band at 1047 cm^{-1} and the less stable (by 1.1 kcal/mole) TG conformer absorbs at 1021 and 1067 cm^{-1}. A photon drag detector was used to measure the temporal output of the laser pulse; the intensity is strongest near the beginning of the pulse, which has a 300 nsec FWHM and a long tail extending to 600 nsec with an average intensity of ~40 percent of the peak. The laser was run at a 50 Hz repetition rate. For all the TOF data, but the m/e = 26 TOF, the total energy fluence crossing the

molecular beam in the interaction region is estimated to be ~2.4 J/cm^2. The m/e = 26 TOF was taken at an energy fluence of ~1.8 J/cm^2. The laser light was unpolarized and was focused onto the molecular beam with a 25 mm focal length spherical zinc selenide lens. For the total signal dependence on laser fluence, the lens position was kept fixed and the fluence was adjusted from 5.5 to 0.5 J/cm^2 by attenuating the laser beam by passing it through a gas cell filled with C_2H_4 at pressures from 0 to 360 torr.

The dissociation products were detected in the plane of the laser and molecular beam by a rotatable ultra-high vacuum mass spectrometer consisting of an electron bombardment ionizer, quadrupole mass filter, and particle counter. The emission current in the ionizer was 10 mA with a 240 eV electron energy. The flight path between the beam crossing point and the ionizer was 20.7 cm. TOF distributions were measured in the usual way.[12]

Signal was observed when the quadrupole mass spectrometer was set to pass the following mass to charge ratios: m/e = 14, 15, 26, 27, 28, 29, 30, 31, and 44; after very long counting times a very small signal was detected at m/e = 57. These masses correspond to CH_2^+, CH_3^+, $C_2H_2^+$, $C_2H_3^+$, (CO^+, $C_2H_4^+$), ($C_2H_5^+$, CHO^+), (CH_2O^+, $CHOH^+$), (CH_2OH^+, CH_3O^+), and $C_2H_4O^+$ and to $C_2H_4OCH^+$. No measurable signal was detected at m/e = 46, 58, or 59 corresponding to $C_2H_5OH^+$, $C_2H_4OCH_2^+$ and $C_2H_5OCH_2^+$ or their isomers after signal averaging for 300,000 laser shots for each. The data taken at m/e = 45 ($C_2H_5O^+$) were discarded when it was found that the m/e = 44 data taken that day showed evidence of poor mass tuning of

the quadrupole. Typical signal levels at a detection angle of 10° from the molecular beam and a photon fluence of ~2.4 J/cm^2 ranged from 0.14 to 0.82 counts/laser pulse for all but m/e = 57, at which the signal level was 0.003 counts/laser pulse. A good signal to noise ratio was obtained for all masses but 14, 15 and 57.

RESULTS AND ANALYSIS

A. Identification of the Molecular Elimination Channel

The m/e = 31 (CH_2OH^+, CH_3O^+) TOF measured at an angle of 10° to the molecular beam is shown in Fig. 2. Let us first focus our attention on the faster peak in this spectrum. This sharp feature, which corresponds to a narrow energy distribution at a relatively high average translational energy, can only contain contributions from the heavier molecule of each pair of products shown in Fig. 1. It is easily calculated from momentum and energy conservation that about 24 kcal/mole of the total available energy would have had to be released as translational energy of the products for the acetaldehyde, ethanol or ethoxy radical product to arrive at the detector at times corresponding to the peak of the fast distribution in the m/e = 31 TOF. The total product translational energy would have to be as much as 115 kcal/mole at the peak of the distribution if the $C_2H_5OCH_2$ product were responsible for the fast peak in the m/e = 31 TOF spectrum. Thus, it is very clear that the fast velocity product in the mass 31 TOF must be due to one of the two energetically allowed molecular elimination reactions as

only these two channels have enough energy available through the conversion of the exit potential energy barrier to give the observed product translational energies. The radical channels from simple bond rupture are not expected to have such a high average translational energy release with such a narrow energy distribution, even if an excessively large number of photons are absorbed before dissociation.

Identification of the molecular elimination channel would be easy if we had observed the same fast product velocity distribution at m/e = 46, ($C_2H_5OH^+$), but the fast product was not observed at this mass or at m/e = 44 (CH_3CHO^+, CH_2CHOH^+). This is understandable because the energies required to dissociate $C_2H_5OH^+$ or CH_3CHO^+ to their smaller ion fragments are known to be small, ~15 kcal/mole, and the ionization of highly vibrationally excited C_2H_5OH or CH_3CHO products is not expected to yield the parent ion in electron bombardment ionization. By careful examination of the masses at which daughter ions of the heavy product appear and of the masses at which daughter ions of the lighter partner (C_2H_4 for the ethanol product or C_2H_6 for the acetaldehyde product) appear, one can be reasonably certain that DEE dissociates to form ethanol and ethylene but not acetaldehyde and ethane. First, m/e = 31 is the major ion mass fragment of ethanol[13]. Second, no signal from acetaldehyde was detected at m/e = 31 in a previous IRMPD experiment on the same apparatus in which acetaldehyde was a product;[2] H atom migration must occur to get signal from acetaldehyde at m/e = 31 CH_2OH^+. Third and perhaps most important, the lighter fragment of the molecular elimination channel does not appear in the m/e = 30 or 29 TOF

spectra (see Fig. 3 and Fig. 4) but it does appear in the m/e = 28 spectra. If the C_2H_6 product were being formed one would expect it to give m/e = 30 or 29, yet there is no additional broadening of the fast peak in the m/e = 30 or 29 TOF which is expected from the lighter fragment. The lighter, faster product is not detected until the m/e is tuned to 28 ($C_2H_4^+$), as would be expected if DEE dissociates to give ethanol and ethylene. The TOF of m/e = 28 is shown in Fig. 5.

B. Identification of the Radical Channel

The TOF spectra of m/e = 44 ($C_2H_4O^+$) at 10° from the molecular beam is shown in Fig. 6. The fast partner to this velocity distribution appears in the TOF spectra taken at masses m/e = 29, 28, 27 (Fig. 7), 26 (Fig. 8), 15 and 14. Thus the radical channel, reaction (1) which forms $C_2H_5O + C_2H_5$ must be occurring since the CH_3 product in the other radical channel cannot give any contribution at the higher of the masses. The extremely small signal at m/e = 57 (0.003 counts/laser pulse) suggests that a small fraction of the DEE may dissociate by breaking a C–C bond:

$$C_2H_5OC_2H_5 \longrightarrow C_2H_5OCH_2 + CH_3 \qquad (3)$$

However this small signal may underestimate the extent of dissociation via reaction 3 as $C_2H_5OCH_2$ may not fragment to give m/e = 57, 58, or 59. The contribution of $C_2H_5OCH_2$ and CH_3 to smaller ion masses would largely be obscured by the overlapping TOF spectra of the other

dissociation products. The dissociation of DEE into two channels with vastly different translational energy distributions can also be seen easily in Fig. 8 as this TOF has contributions from both of the molecular elimination products and the lighter radical product. The momentum-matched heavier radical product and the heavier molecular product can be seen in Figs. 2 and 3 without contributions from the overlapping lighter products.

C. Product Translational Energy Distributions:

1. $C_2H_5OC_2H_5 \longrightarrow C_2H_5O + C_2H_5$

When a molecule dissociates to two fragments, the linear momentum of one fragment is equal in magnitude and opposite in direction to that of the other fragment in the center of mass coordinate system, so the measured velocity distribution of one derived from the experimental measurements will completely define the velocity distribution of the other fragment and the total center of mass translational energy distribution, P(E'), of the dissociation process. The TOF distribution of the C_2H_5O product (Fig. 6) was fit by a trial and error forward convolution method using a completely flexible point form for the P(E'). The good fit shown in Fig. 6 was calculated from the P(E') in Fig. 9. We used this P(E') to fit the slow peak in the m/e = 26 and 27 TOF spectra (Figs. 8 and 7) by varying the relative amounts of C_2H_5O and C_2H_5 product contributing to these TOF distributions. In both cases the best fit was obtained when only the C_2H_5 product's contribution was used.

During the trial and error fitting procedure of the m/e = 44 TOF, a daughter ion of the C_2H_5O product, it was immediately found that the better fits were achieved by making the P(E') peak at translational energies near 0 kcal/mole. We then tried to fit the data with a translational energy distribution derived with RRKM theory. In an IRMPD experiment the molecules dissociate from a distribution of levels above the dissociation limit determined by the experimental conditions. Thus the RRKM translational energy distribution used to fit the data should be a sum of the translational energy distributions from single energy levels weighted by the fraction of molecules that dissociate from each level. In order to estimate weighting factors for these levels, we simulated the infrared photon absorption and dissociation process for this system with a simple rate equation model described in detail elsewhere.[14] We calculated the RRKM dissociation rate constants (see Fig. 10) from published molecular vibrational frequencies and frequencies of transition states chosen to reproduce the A-factor and activation energy estimated by Benson and O'Neal for the radical channel and the reported parameters of Istvan and Peter for the molecular elimination channel (at 800°K). This procedure is known to give reasonable RRKM rate constants as a function of internal energy.[15] The spread of dissociating energy levels was found to be only weakly dependent on the parameters of the model which are not known, most importantly, the change in photon absorption and stimulated emission cross section as a function of internal energy. The simulation suggested a representative form for the relative dissociation yields from a group of neighboring

energy levels which we used to calculate the effective RRKM P(E'). With each level spaced 2.983 kcal/mole apart, corresponding to the photon energy, the contribution from neighboring energy levels to the RRKM translational energy distribution were weighted by factors of 8, 20, 38, 60, 73, 80, 73, 60, 38, 20, 8^{16}; this dissociating population distribution was used to calculate the RRKM P(E') at several median dissociation energies. The data were then fit using the resulting P(E') for each mean energy. The model calculation took into account the fact that we could only detect dissociation occurring while the excited molecule was in the viewing region of the detector. It also included the competition between the three competitive processes above the dissociation limits: dissociation to radical products, dissociation to molecular products, and change in energy level due to absorption or stimulated emission of a photon. The unknown parameters in the model, which related to the absorption and stimulated emission of photons, had a large effect on the actual median energy level from which dissociation occurred, but, as will be seen, fitting of the product velocity distribution from the radical channel helped limit the uncertainty in this energy level.

We then attempted to fit the m/e = 44 TOF with several different averaged RRKM translational energy distributions. The best fit was achieved with molecules dissociating from eleven energy levels 1.73, 4.71, 7.69, 10.68, 13.66, 16.64, 19.63, 22.61, 25.59. 28.57 and 31.56 kcal/mole above the 81.8 kcal/mole dissociation limit. The translational energy distributions, calculated from RRKM theory, from each of

these levels was weighted by the population distribution above and summed to give the P(E') used to fit the data. We will call this the "averaged 16.64 kcal/mole P(E')." This is the P(E') shown in Fig. 9. It is slightly broader than the usual single level RRKM translational energy distribution calculated assuming all the molecules dissociate from the level 16.64 kcal/mole above the dissociation limit. Acceptable fits to the TOF data could also be obtained with an "averaged" 22.61 kcal/mole P(E') and an averaged 10.68 kcal/mole P(E'), but not with P(E')'s calculated assuming the molecules dissociated from levels peaked at higher or lower energies than these. Thus the measured C_2H_5O TOF suggests that most of the detected radical products were formed from DEE dissociating from energy levels between 5 and 28 kcal/mole above the 81.8 kcal/mole dissociation limit (including energy levels in the population distribution weighted by a factor of 60 or greater). It should be noted that since the excited diethyl ether molecule is traveling ~1120 m/sec through a small region (~3 mm long) viewed by the detector, we are only sensitive to molecules with dissociation times less than a few microseconds. Using the calculated RRKM dissociation rate constant of 0.5641×10^4 sec^{-1}, only about 1 percent of the DEE that dissociates to radical products at 16.64 kcal/mole above the dissociation limit will dissociate within the detector viewing volume and have a chance to be detected.

2. $C_2H_5OC_2H_5 \longrightarrow C_2H_5OH + C_2H_4$

The fast peak in the m/e = 31 TOF (Fig. 2) was fit with a completely flexible point form for the P(E'). The dotted curve fit to the

TOF spectrum shown in Fig. 2 was calculated from the P(E') shown in Fig. 11. This P(E') peaks near 26 kcal/mole and extends out to beyond 45 kcal/mole, with an average energy released of ~24 kcal/mole. The curves fit to the fast peaks in the m/e = 26 and 27 TOF's (Figs. 8 and 7) were calculated from this P(E') using the relative contribution of the C_2H_5OH and C_2H_4 to these masses as the only variable parameter.

Assuming (1) the A-factor and activation energy of Istvan and Peter for this channel are correct and (2) the conclusions about the energy levels those molecules which dissociated to radicals had reached are also correct, we can estimate the energy levels from which the molecules dissociated to ethanol and ethylene. Since the RRKM rate constants for the molecular elimination channel are higher than those for the radical channel for internal energies up to ~125 kcal/mole (see Fig. 10), the molecular eliminations will occur on the average from slightly lower energy levels. How much lower will depend on the mean energy level from which the radical dissociations occur and the fraction of molecules that dissociate during the laser pulse. A good estimate based on our approximate modeling is that the molecules that dissociate via reaction (2) and are detected do so from energy levels that are 1-9 kcal/mole below the energy levels from which the radical products are formed. We thus estimate that the DEE dissociates to give molecular products from energy levels mostly between 82 and 107 kcal/mole above its zero point level. This energy range is compared to that of the DEE that dissociates to radical products from a group of energy levels mostly between 87 and 110 kcal/mole above its zero point level.

D. Branching Ratio and Total Product Yield Dependence on Laser Power

The integrated TOF signal at m/e = 26 as a function of laser power is shown in Fig. 12. In spite of the large error bars, one can see the signal still increased with laser power at the higher powers used in this experiment. Quantitative interpretation of this data is, however, quite difficult in this case. There are two dominant factors which would cause our signal level to rise in this measurement. The first is simply that more molecules absorb enough photons during the laser pulse to reach energy levels above one or both dissociation limits. The second factor arises from our experimental arrangement. An excited DEE molecule will spend at most 2.7 μsec in the viewing region of the detector. Because the lifetimes for dissociation to molecular or radical products at an energy level of 98 kcal/mole above the ground state are ~13 and ~180 μsec, respectively, we detect only a small fraction of the total number of dissociations. With increasing laser power, the average energy level a molecule will reach above the dissociation limit increases. At the higher excitation levels, the dissociation rate constants become higher and a greater fraction of the molecules will dissociate within the region viewed by the detector. Even when most of the molecules are already above the dissociation limit and no increase in the number of molecules above the dissociation limit is expected, higher laser intensity will still give a larger signal. For instance, the fraction of dissociations forming radical products that occur within the viewing region of the detector increases by a factor of 3, from ~1 percent to ~3 percent, if the molecules dissociate from an energy

level 19.63 kcal/mole compared to 16.64 kcal/mole above the dissociation limit.

A crude determination of a branching ratio between these two channels was made by comparing the total signal at m/e = 14, 15, 26, 27, 28, and 29 ascribed to C_2H_5 with the total signal at all the masses counted ascribed to C_2H_5OH. If the branching ratio were 1:1, and the ionization cross sections are the same we would expect the total ion signal from C_2H_5 to be 10.8 times that of C_2H_5OH due to the differences in laboratory angular and velocity distribution of these two products. The observed total ion signal for C_2H_5 is 3.0 times that for C_2H_5OH, giving a branching ratio of 78 percent molecular channel and 22 percent radical channel. The analysis of the total ion signals of C_2H_5 compared to C_2H_4 gives a similar branching ratio. However, the ion signal of C_2H_5O compared to C_2H_5OH gives a branching ratio of 95 percent : 5 percent. Our lack of data at m/e = 45 may be the source of the discrepancy, but as this would only shift the branching ratio in favor of the molecular channel in the comparison of the C_2H_5 and C_2H_5OH counts and would not affect the C_2H_4:C_2H_5 ratio, we may arrive at a <u>lower bound of ~70 percent molecular channel</u> (2). The branching ratio predicted from the rate parameters is critically dependent on the mean energy level from which the molecules dissociate for each channel. In a calculation where the molecular products are formed from energies peaked at 107 kcal/mole above the ground state of DEE and the radical products are formed from 3 kcal/mole higher energies, the branching ratio is 85.3 percent and 14.7 percent in qualitative agreement with

our crude estimate.[17] Our best estimate of the energy levels from which dissociation occurred, based on the translational energy distribution obtained from the m/e = 44 TOF, was ~9 kcal/mole lower; at these lower energies the radical channel would be <5 percent of the dissociation yield.

DISCUSSION

The effect that an exit channel barrier has on the asymptotic translational energy distribution of the products has been treated theoretically by Marcus[18] and Hase et al.[19] Hase et al.[19] studied ethyl radical decomposition to H + C_2H_4 with Monte Carlo classical trajectories on potential energy surfaces with different exit channel barrier heights. The exit channel barrier results from the C-C single bond in the reactant shortening to a C=C double bond in the ethylene product. He found that the shape of the product translational energy distribution at the top of the barrier agreed with the predictions of RRKM theory, but that the distribution broadened and shifted to higher translational energies as the reaction was allowed to proceed beyond the top of the exit channel barrier. The effect was larger for a 3.5 kcal/mole barrier than it was for a 0.1 kcal/mole barrier. Marcus[18] demonstrated the application of RRKM theory to prediction of final product translational energy distributions when the reaction proceeds through a tight transition complex which involves an exit channel barrier. He showed that one should allow for the evolution of the RRKM

transition state as the reaction proceeds down the exit channel barrier. In his example case, the bending vibrations excited in the tight transition state are coupled into translation and rotation of the products as they recoil from each other.

The concerted reaction forming ethanol and ethylene has a large exit barrier estimated at ~50 kcal/mole. The measured product translational energy distribution shown in Fig. 11 has an average of ~24 kcal/mole translational energy. At an RRKM critical configuration calculated from the István and Péter A-factor and activation energy only 1.5 to 2.5 kcal/mole is in the relative motion of the products, if the molecule dissociates from energies averaging around 14, and 39 kcal/mole respectively above the dissociation limit, so one might conclude that the interactions between the products as they descend the exit barrier considerably alters their energy distribution at the top of the barrier. Their final translational energy is measured to be almost 1/2 of the exit barrier height.

The fraction of the exit channel barrier energy released to translation in this four-center elimination reaction is significantly higher than that measured for the four-center HCl elimination from halogenated hydrocarbons by Sudbo et al.,[3] but considerably smaller than the 70 percent released to translation in the IRMPD dissociation of ethyl vinyl ether to $CH_3CHO + C_2H_4$.[2] The latter comparison is particularly interesting as both involve hydrogen atom transfer and breaking of a C-O bond, as here both bonding electrons move away from the CO bond in a concerted reaction, the C-O interaction becomes repulsive, and the

translational energy of the product molecules is mainly due to the repulsive energy release of this interaction. Although the fractions of the exit barriers appearing in translational energy are somewhat different for EVE and DEE, they have a similar average translational energy release, 31 and 24 kcal/mole respectively. In concerted reactions with large exit barriers, the structure of the transition state will determine the energy partitioning to a large extent. If the chemical bonds in the products which are to be formed are extensively stretched in the transition state, significant vibrational excitation is expected. On the other hand the longer the bond which is to be broken is extended, the less important the repulsive energy release will be. In the four-center HCl elimination reactions, the C-Cl bond to be broken must be significantly extended, but in EVE or DEE, in view of the enormous translational energy release it is likely that the C-O bonds to be broken are not significantly extended when the interaction suddenly becomes repulsive.

The shape of the product translational energy distribution (Fig. 9) for the radical channel (1) was in agreement with RRKM theory for reactions proceeding through a loose transition state. We accounted for the fact that in an IRMPD experiment, the reactant molecules dissociate from a distribution of energy levels above the dissociation limit by using an averaged RRKM P(E') to fit the data. The exact form of this distribution was described in the Results and Analysis Section. The best fit P(E') was calculated with molecules dissociating to radicals from a spread of energy levels peaked at 16.64 kcal/mole above

the dissociation limit. The average energy released to translation of the radical products detected was 1.6 kcal/mole.

Because the photon absorption and stimulated emission cross sections as a function of energy for a highly energized molecule are not generally known, one is usually uncertain in an IRMPD experiment as to what mean energy level the absorbing molecule will reach before it dissociates. An attempt was made in this study to reduce this uncertainty considerably. Assuming (1) that the thermochemical A-factor and activation energy reported for the dissociation channel are correct and (2) that the translational energy distribution of the products is correctly predicted by RRKM theory, one can determine the approximate mean energy level from which the molecules dissociated to radicals by attempting to fit the data with various predicted RRKM P(E')'s. The mean total available energy for the RRKM P(E') that fit the measured velocity distribution determines the mean energy level from which the molecules dissociated. The method is only weakly dependent on the assumed shape of the distribution of energies of the dissociating levels. If the radical product TOF were measured carefully at several laser fluences, one might also expect to gain some information on how the mean energy of the dissociating levels increases with photon intensity.

REFERENCES

1. Aa. S. Sudbo, P. A. Schulz, E. R. Grant, Y. R. Shen and Y. T. Lee, J. Chem. Phys. 70, 912 (1979).
2. F. Huisken, D. Krajnovich, Z. Zhang, Y. R. Shen and Y. T. Lee, J. Phys. Chem. 78, 3806 (1983).
3. Aa. S. Sudbo, P. A. Schulz, Y. R. Shen and Y. T. Lee, J. Chem. Phys. 69, 2312 (1978).
4. D. Krajnovich, F. Huisken, Z. Zhang, Y. R. Shen and Y. T. Lee, J. Chem. Phys. 77, 5977 (1982).
5. C. R. Quick, Jr. and C. Wittig, J. Chem. Phys. 72, 1694 (1980).
6. D. S. King and J. C. Stephenson, Chem. Phys. Lett. 51, 48 (1977); J. C. Stephenson and D. S. King, J. Chem. Phys. 69, 2485 (1978).
7. K. J. Laidler and D. J. McKenney, Proc. Roy. Soc. London, Ser. A, 278, 517 (1964).
8. S. Istvan and H. Peter, Mag. Kem. Foly. 81, 120 (1975).
9. S. W. Benson and H. E. O'Neal, Kinetic Data in Gas Phase Unimolecular Reactions, NSRDS-NBS 21 (1970).
10. Y. T. Lee, J. D. McDonald, P. R. LeBreton and D. R. Herschbach, Rev. Sci. Instrum. 40, 1402 (1969).
11. H. Wieser, W. G. Laidlaw, P. J. Krueger and H. Fuhrer, Spectrochim. Acta, Part A, 24, 1055 (1967).
12. See, for example, ref. 3.
13. E. Stenhagen, S. Abrahamsson and F. W. McLafferty, Ed., Atlas of Mass Spectral Data (John Wiley and Sons, New York) 1969.
14. P. A. Schulz, Ph.D. thesis, University of California, Berkeley 1979.

15. P. J. Robinson and K. A. Holbrook, Unimolecular Reactions (Wiley, New York) 1972.

16. Or if all these levels are not above the dissociation limit, as for the case when 10.68 kcal above the dissociation limit, we used a narrower distribution: 8, 20, 60, 80, 60, 20, 8.

17. For this calculation, the spread of energy levels from which dissociation in the viewing region of our detector occurred was comparable to that described in Part 3C. We used a ground state photon absorption cross section of 1×10^{-18} cm^2 which fell exponentially to 3.2×10^{-19} at the radical dissociation limit. The excitation level described was reached at a photon fluence of 1.83 J/cm^2; this was the average excitation of the molecules that dissociated in the collision region. The average excitation of all the molecules at the end of the laser pulse was ~80 kcal/mole. These parameters predicted a larger increase in signal with increasing laser power than our data showed.

18. R. A. Marcus, J. Chem. Phys. 62, 1372 (1975).

19. W. L. Hase, R. J. Wolf and C. S. Sloane, J. Chem. Phys. 71, 2911 (1979).

FIGURE CAPTIONS

Fig. 1. The low energy dissociation channels of $C_2H_5OC_2H_5$. ΔH^o_{300} values were calculated from values tabulated in Rosenstock et al., J. Phys. Chem. Ref. Data 6, Supp. 1, (1977) for the ethanol and acetaldehyde channels and estimated to be 85 kcal/mole for the $C_2H_5OCH_2$ channel using group additivity rules (S. W. Benson, Thermochemical Kinetics, Wiley Interscience, New York, 1976) and the heat of formation of CH_3OCH_2. The energetics of the $C_2H_5O + C_2H_5$ radical channel are those of Ref. 9. The barrier in the ethanol channel, 66 kcal/mole from the reactant, was reported in Ref. 8.

Fig. 2. TOF distribution of m/e = 31, (CH_3O^+, CH_2OH^+) at 10° from the molecular beam. • Experimental points, ——— best fit, obtained by adding the individual contributions of C_2H_5OH (——— • ———) and C_2H_5O (—— —— ——). The C_2H_5OH contribution was calculated using the P(E') in Fig. 11. The C_2H_5O contribution was calculated using the P(E') in Fig. 9. The relative intensities were varied to obtain the best fit and an isotropic center of mass angular distribution was used. Photon energy fluence = 2.4 J/cm^2.
Note that the time scale in this and all subsequent TOF spectra include the transit time of the ion through the mass spectrometer. (For our operating conditions, the ion transit time in μsec is 2.0 $\sqrt{M}$ where M is the detected ion mass in amu.) To convert to laboratory velocity, the displayed flight times

must be corrected for the ion transit time and divided into the flight path, 20.7 cm. For an example of this transformation, see Figures 3(a) and 3(b).

Fig. 3. a) TOF distribution of m/e = 30, (CH_2O^+, $CHOH^+$) at 10° from the molecular beam. • Experimental points, ———— best fit, obtained by adding the individual contributions of C_2H_5OH (——— · ———) and C_2H_5O (—— —— ——). The individual contributions were calculated as in Fig. 2. Photon energy fluence = 2.4 J/cm^2.

b) Laboratory velocity flux distribution of m/e = 30 derived from the TOF distribution between 360 and 70 μsec. The c.m. velocity may be approximately obtained by subtracting 1120 m/sec x cos 10° from the laboratory velocity.

Fig. 4. TOF distribution of m/e = 29 ($C_2H_5^+$, COH^+), at 10° from the molecular beam. Data is shown with a 5 point polynomial smooth. • Experimental points, ———— best fit, obtained by adding the individual contributions of C_2H_5OH (—— · ——) and C_2H_5 (—— — ——). The C_2H_5OH contribution was calculated as in Fig. 2. The C_2H_5 contribution was calculated from the P(E') shown in 9 which is derived from the C_2H_5O TOF distribution (Fig. 6). Photon energy fluence = 2.4 J/cm^2.

Fig. 5. TOF distribution of m/e = 28, (CO^+, $C_2H_4^+$), at 10° from the molecular beam. • Experimental points, ———— best fit obtained by adding the individual contributions of C_2H_4 (—— · · ——), C_2H_5OH (—— · ——) and C_2H_5

(—— — ——). The shape of each individual TOF distribution is fixed by the P(E') that fit the m/e = 44 and 31 TOF's (Fig. 6 and 2). The relative intensity of each contribution was varied to obtain best fit.

Fig. 6. TOF distribution of m/e = 44, $C_2H_4O^+$, at 10° from the molecular beam. • Experimental points, ———— fit calculated using the P(E') in Fig. 9 and an isotropic center of mass angular distribution. Photon energy fluence = 2.4 J/cm^2.

Fig. 7. TOF distribution of m/e = 27, $C_2H_3^+$, at 10° from the molecular beam. • Experimental points. ———— best fit obtained by adding the individual contributions of C_2H_4, C_2H_5OH and C_2H_5 as in Fig. 7. Photon energy fluence = 2.4 J/cm^2.

Fig. 8. TOF distribution of m/e = 26, $C_2H_2^+$, at 10° from the molecular beam. • Experimental points. ———— best fit obtaining by adding the individual contributions of C_2H_4 (—— · · ——), C_2H_5OH (—— · ——) and C_2H_5 (—— — ——). The shape of each individual TOF distribution is fixed by the P(E') that fit the m/e = 44 and 31 TOF's (Fig. 6 and 2). The relative intensity of each contribution was varied to obtain best fit. Photon energy fluence = 1.8 J/cm^2.

Fig. 9. Center-of-mass translational energy distribution for the radical dissociation channel DEE → C_2H_5O + C_2H_5 derived from the m/e = 44, $C_2H_4O^+$, TOF distribution (Fig. 6). This P(E') was used to obtain the calculated fits shown in all

other TOF distributions which contained contributions from C_2H_5O or C_2H_5.

Fig. 10. RRKM rate constant curves for DEE decomposition assuming E_a = 66 kcal/mole and $\log_{10}A$ = 13.9 for the reaction producing $C_2H_5OH + C_2H_4$ and E_a = 81.8 and $\log_{10}A$ = 16.3 for the reaction producing $C_2H_5O + C_2H_5$.

Fig. 11. Center-of-mass translational energy distribution for the molecular elimination channel DEE $\rightarrow C_2H_5OH + C_2H_4$ derived from the ethanol contribution to the m/e = 31 TOF distribution (Fig. 2). This P(E') was used to obtain the calculated fits shown in all other TOF distributions which contained contributions from C_2H_5OH or C_2H_4.

Fig. 12. Integrated signal at m/e = 26 as a function of photon energy fluence. • Experimental points. Error bars represent plus or minus one standard deviation of the statistical counting error. The laser pulse shape is constant, so intensity increased with fluence.

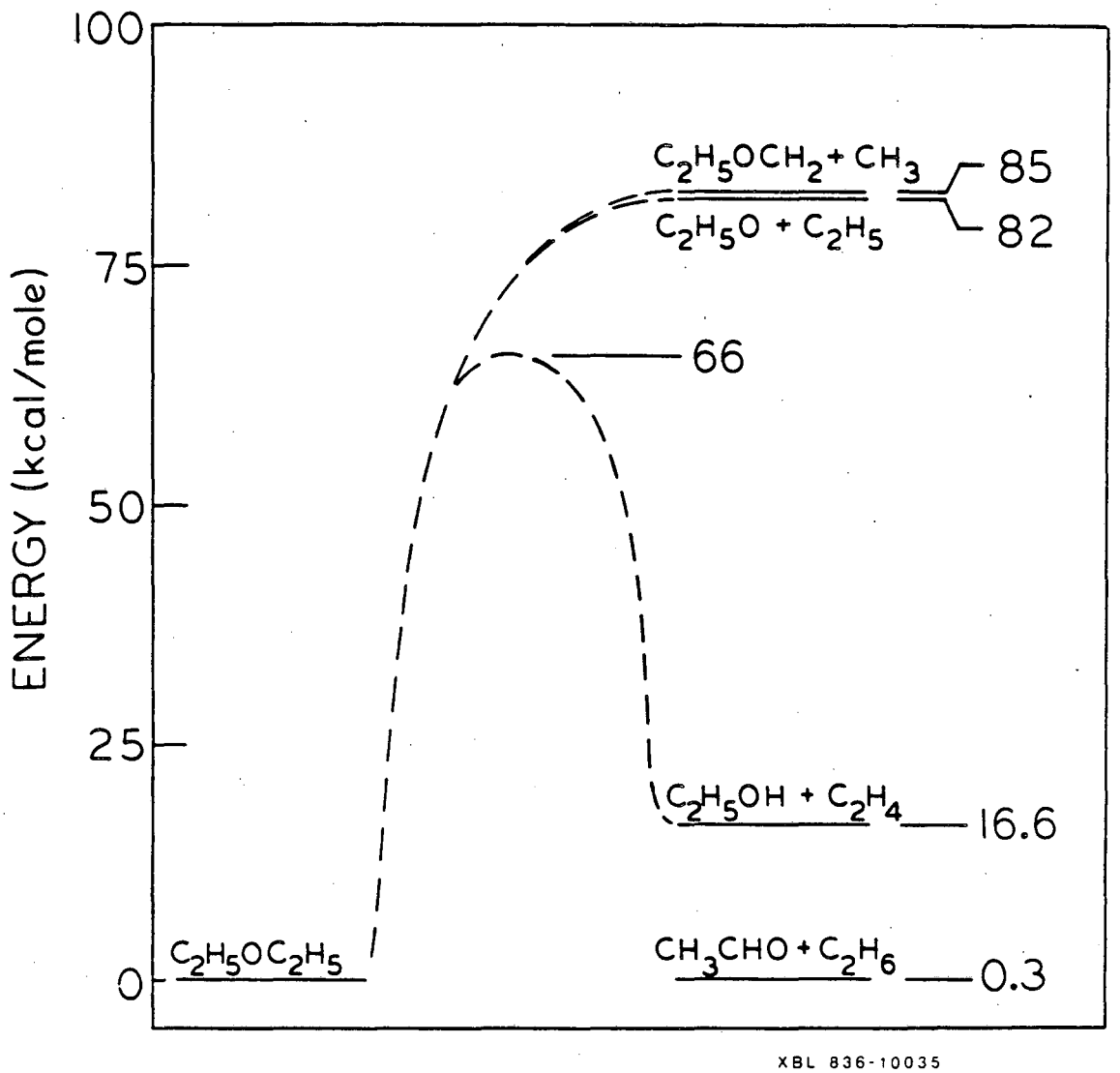
100
75
50
25
0
ENERGY (kcal/mole)
$C_2H_5OCH_2 + CH_3$
85
$C_2H_5O + C_2H_5$
82
66
$C_2H_5OH + C_2H_4$
16.6
$C_2H_5OC_2H_5$
$CH_3CHO + C_2H_6$
0.3
XBL 836-10035

Fig. 1

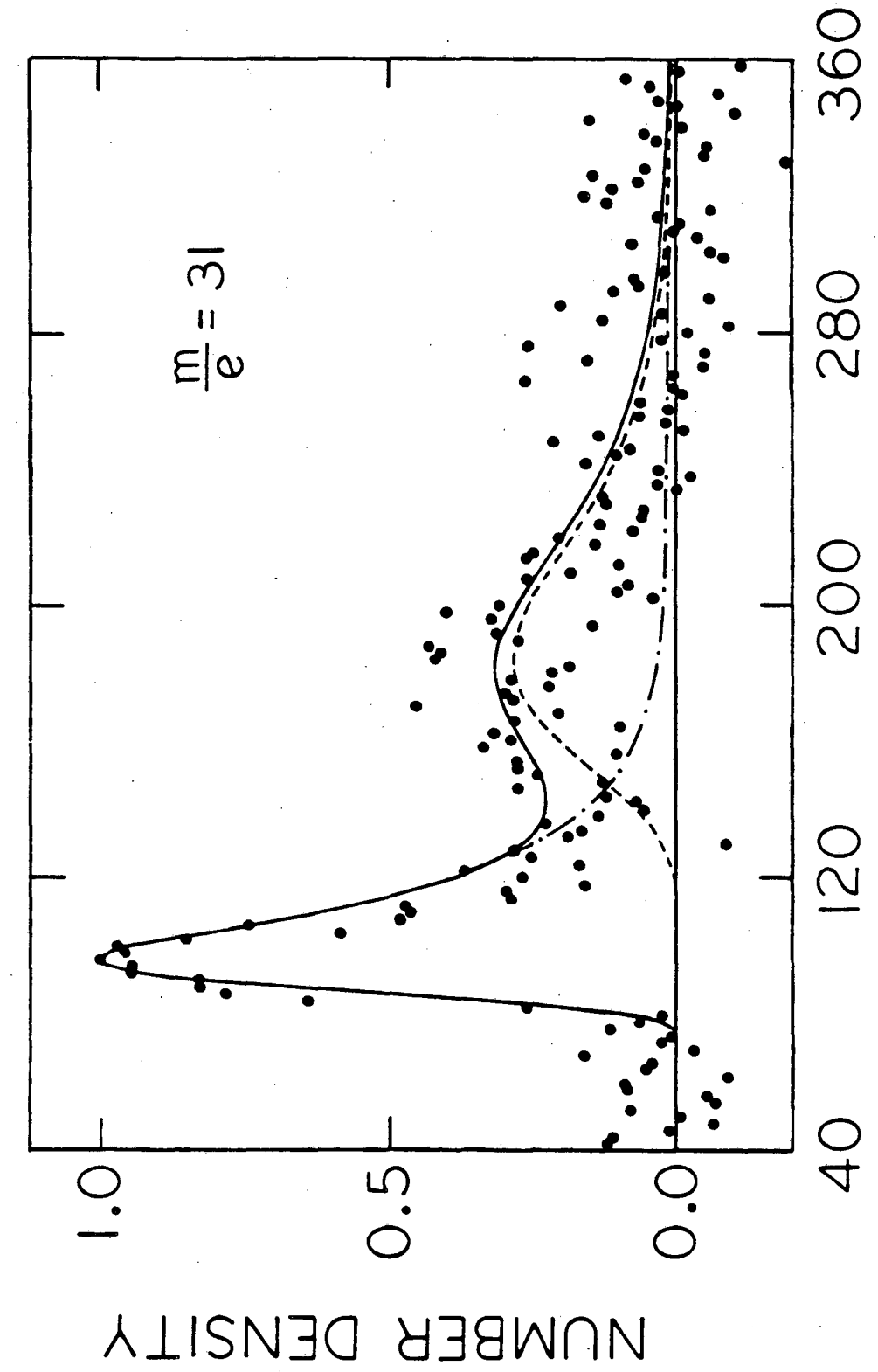

XBL 836-9989

Fig. 2

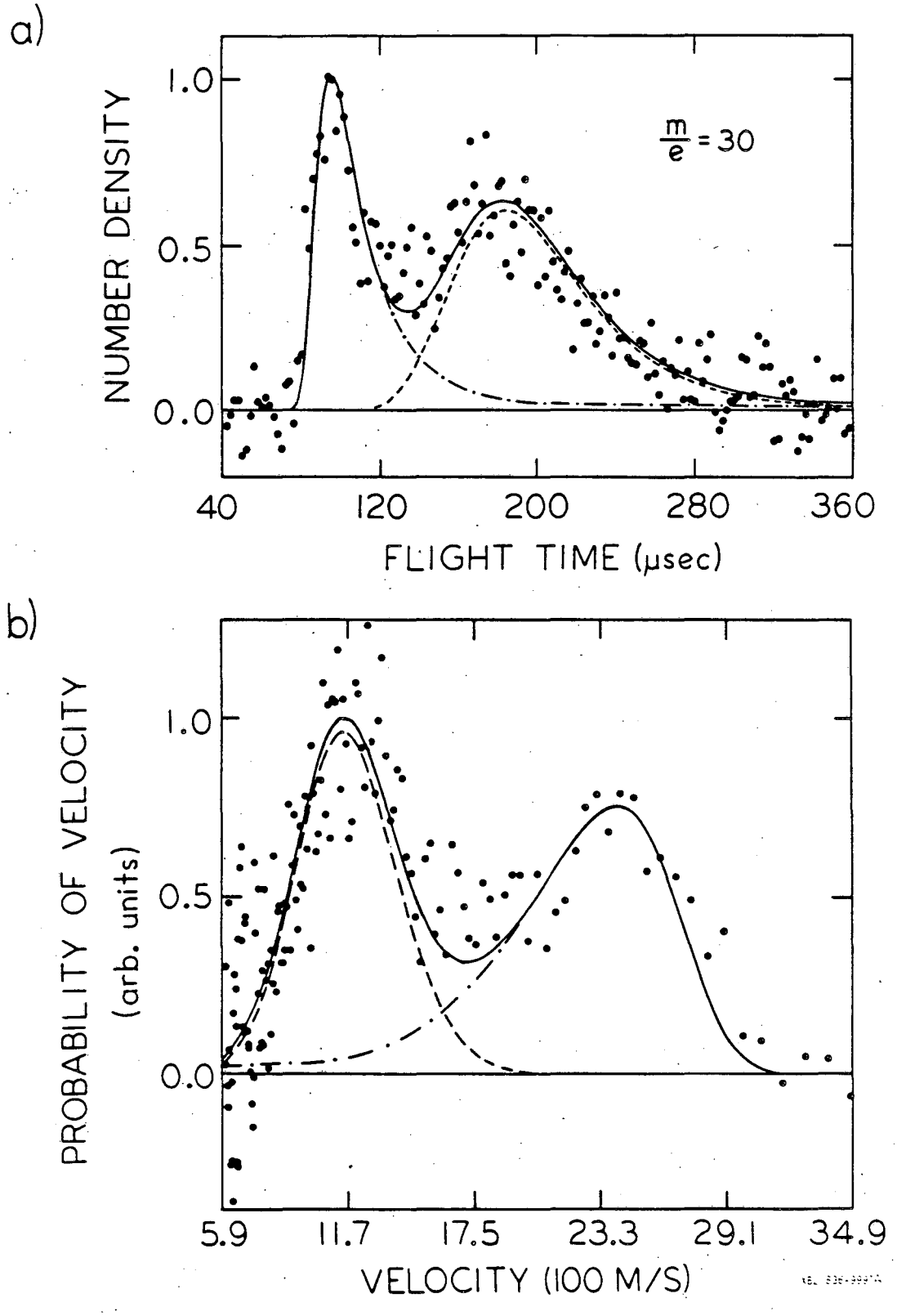
a)
NUMBER DENSITY
1.0
0.5
0.0
$\frac{m}{e}$ = 30
40
120
200
280
360
FLIGHT TIME (μsec)
b)
PROBABILITY OF VELOCITY
(arb. units)
1.0
0.5
0.0
5.9
11.7
17.5
23.3
29.1
34.9
VELOCITY (100 M/S)

Fig. 3

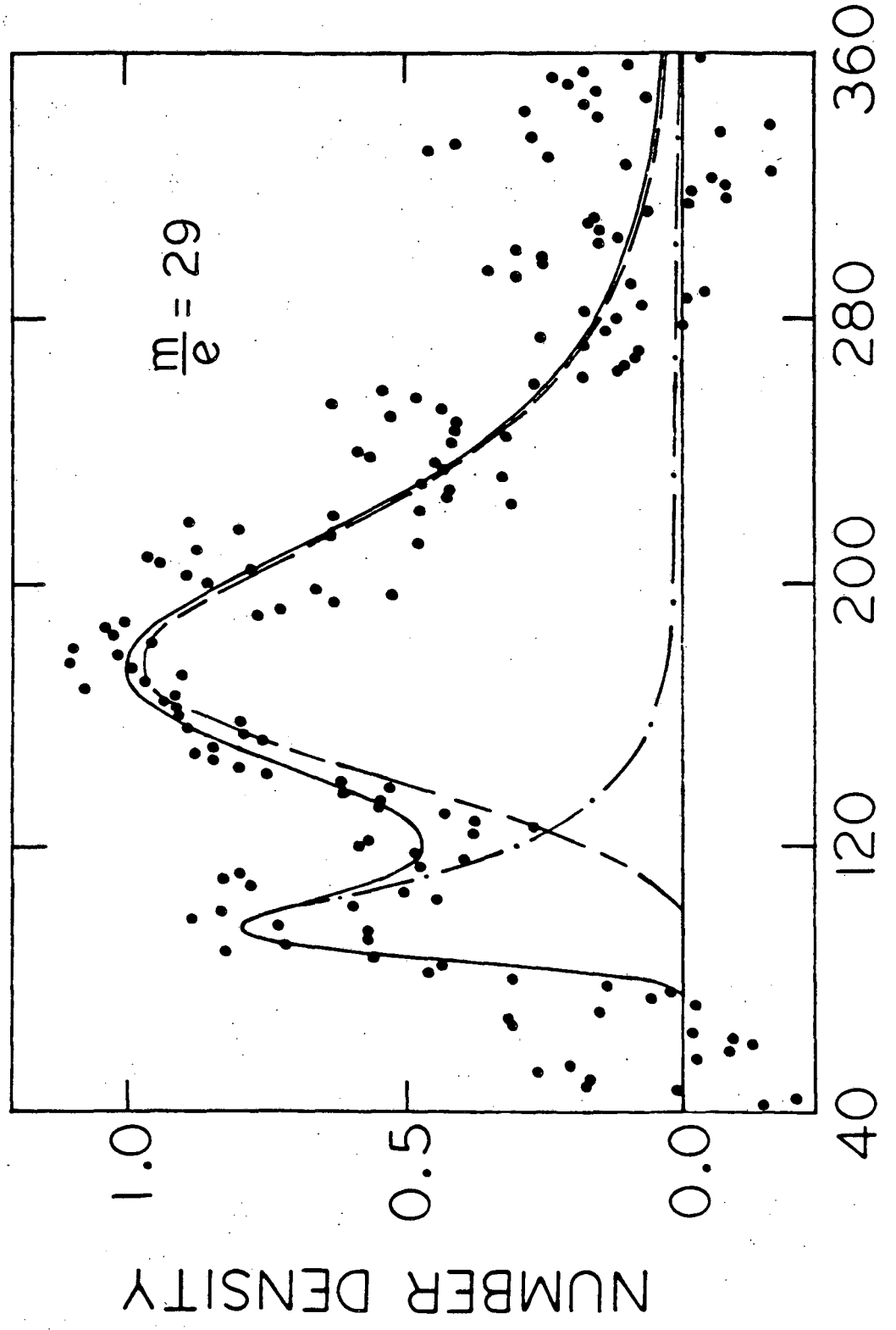

XBL 836-9988

Fig. 4

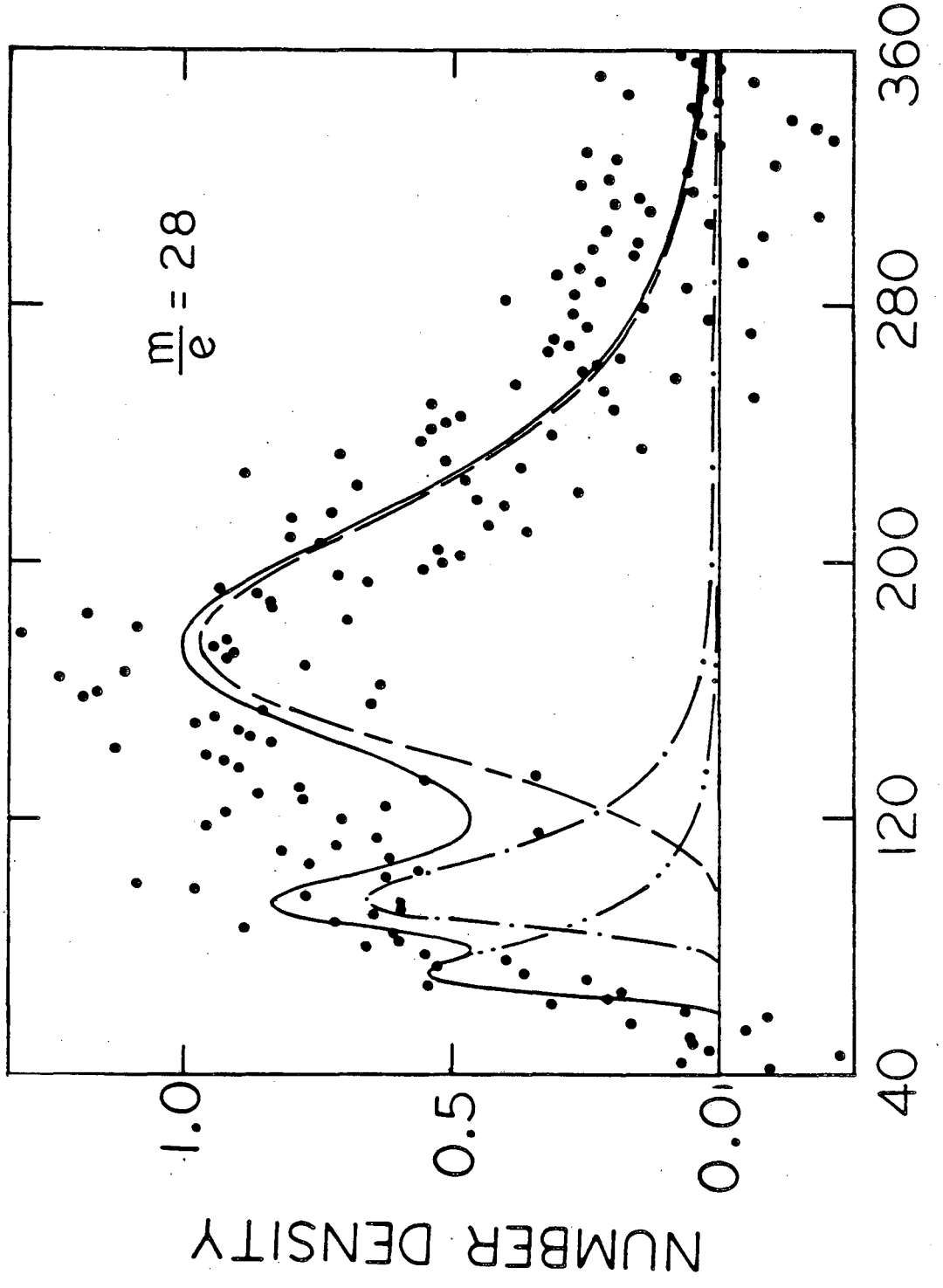

XBL 836-9986

Fig. 5

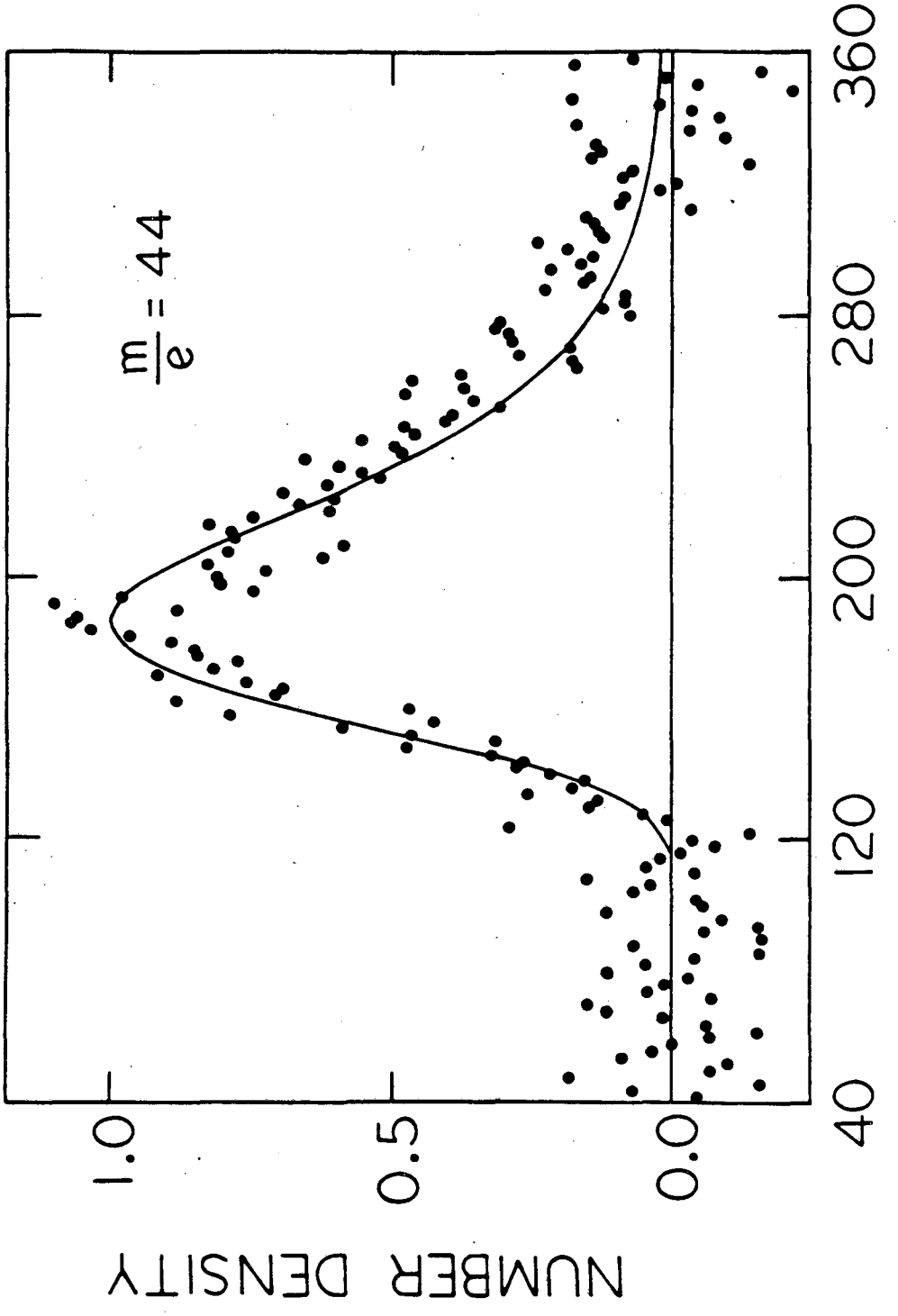

XBL 836-10034

Fig. 6

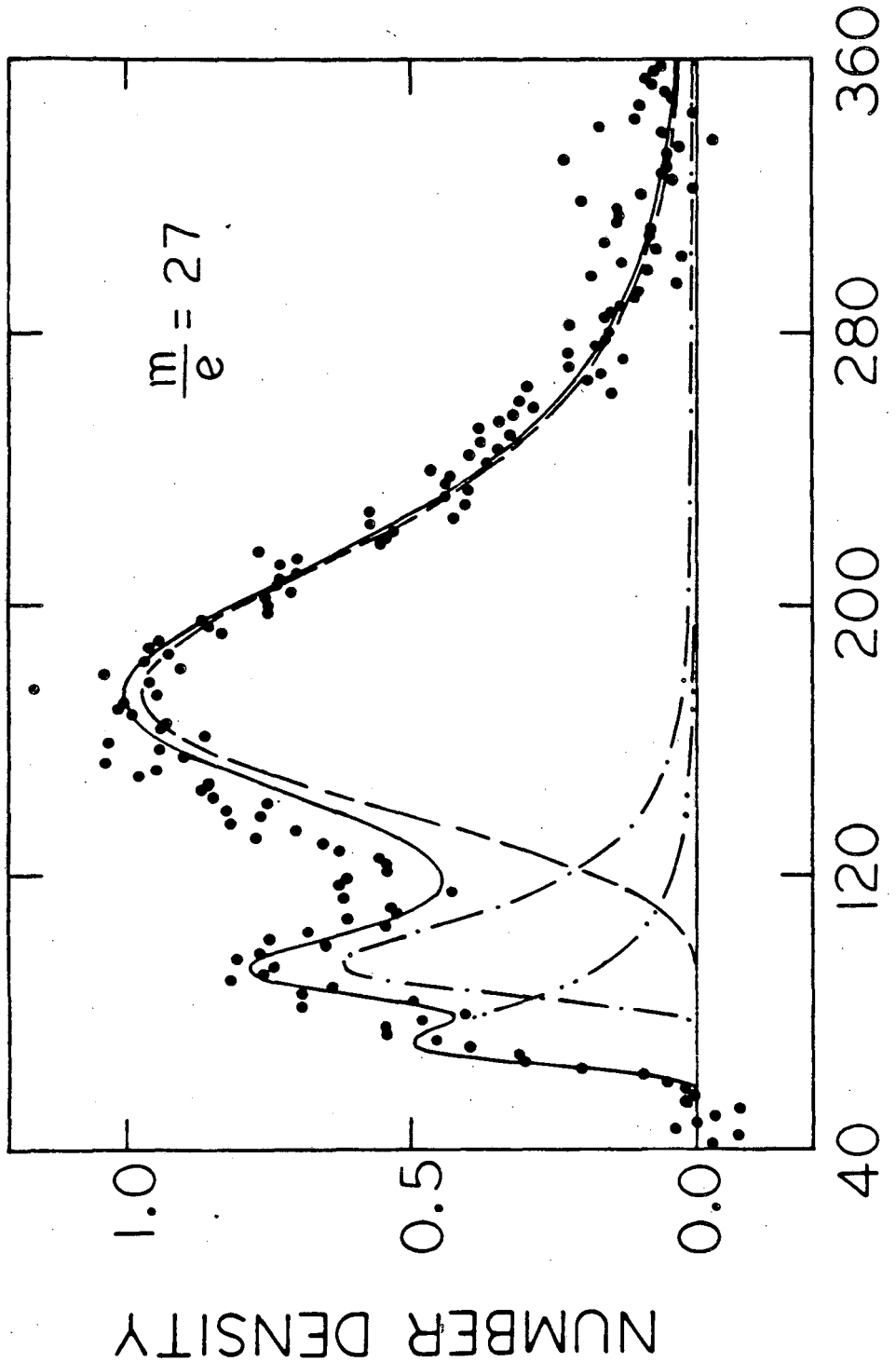

XBL 836-9990

Fig. 7

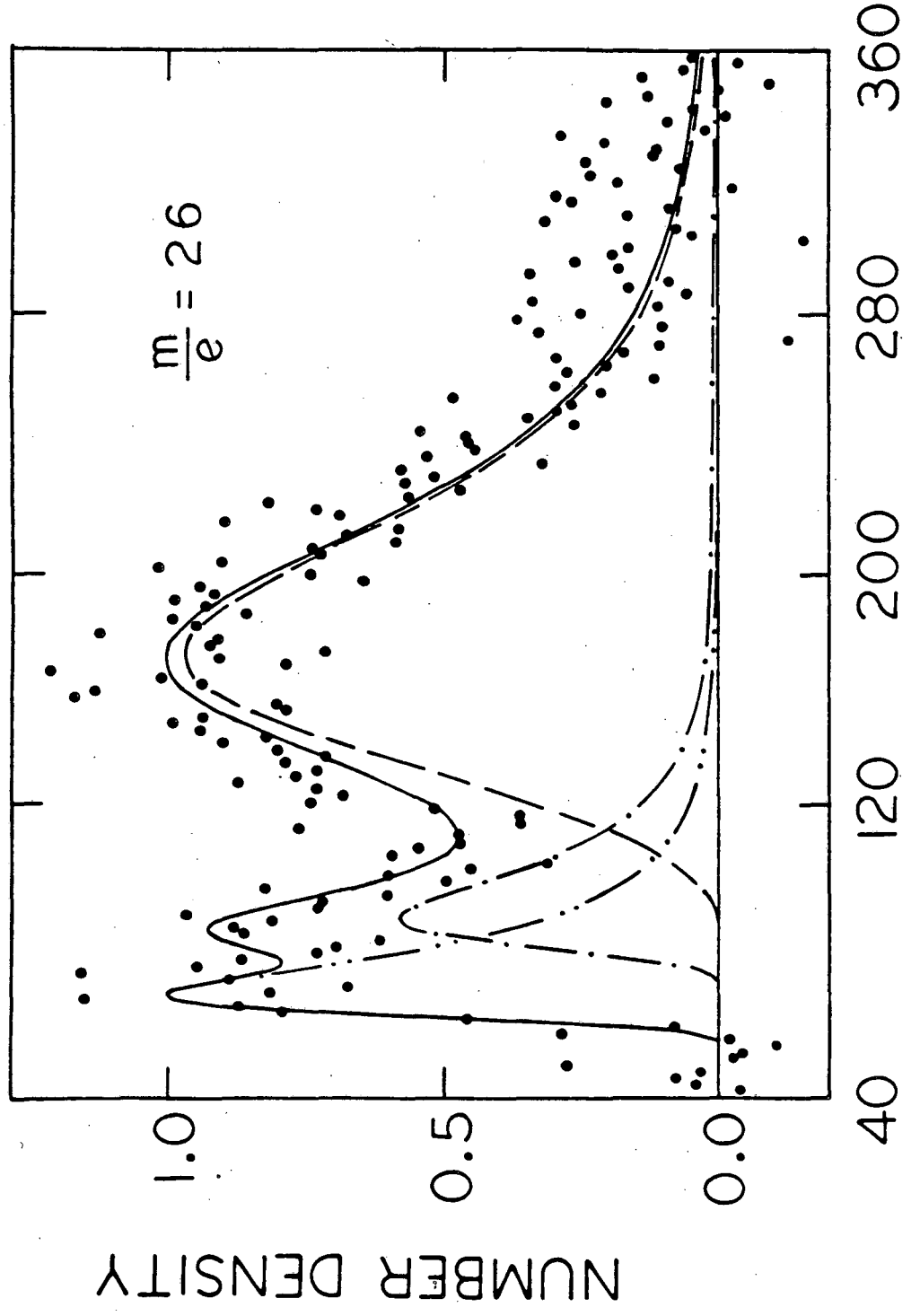

XBL 836-9992

Fig. 8

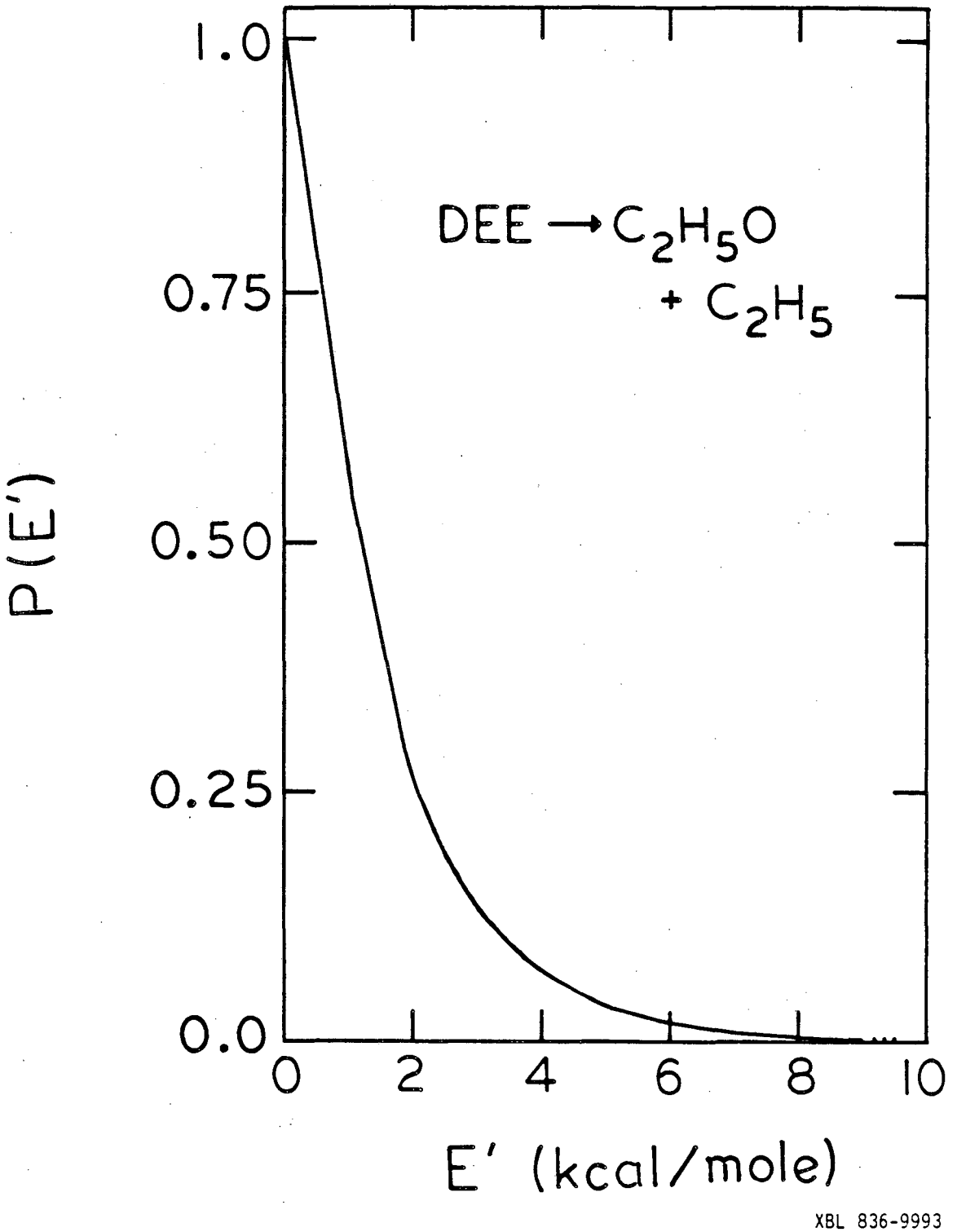

XBL 836-9993

Fig. 9

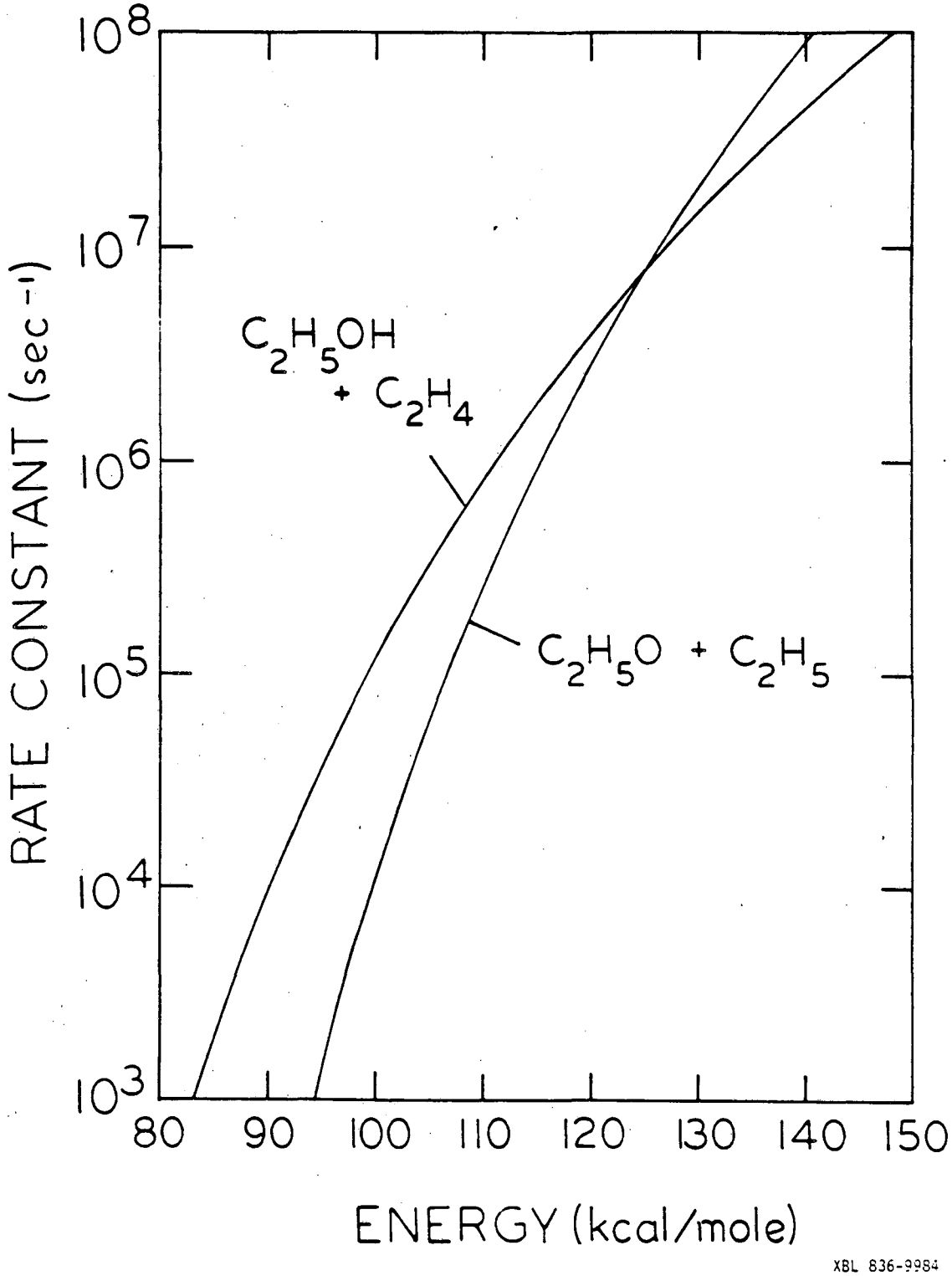

XBL 836-9984

Fig. 10

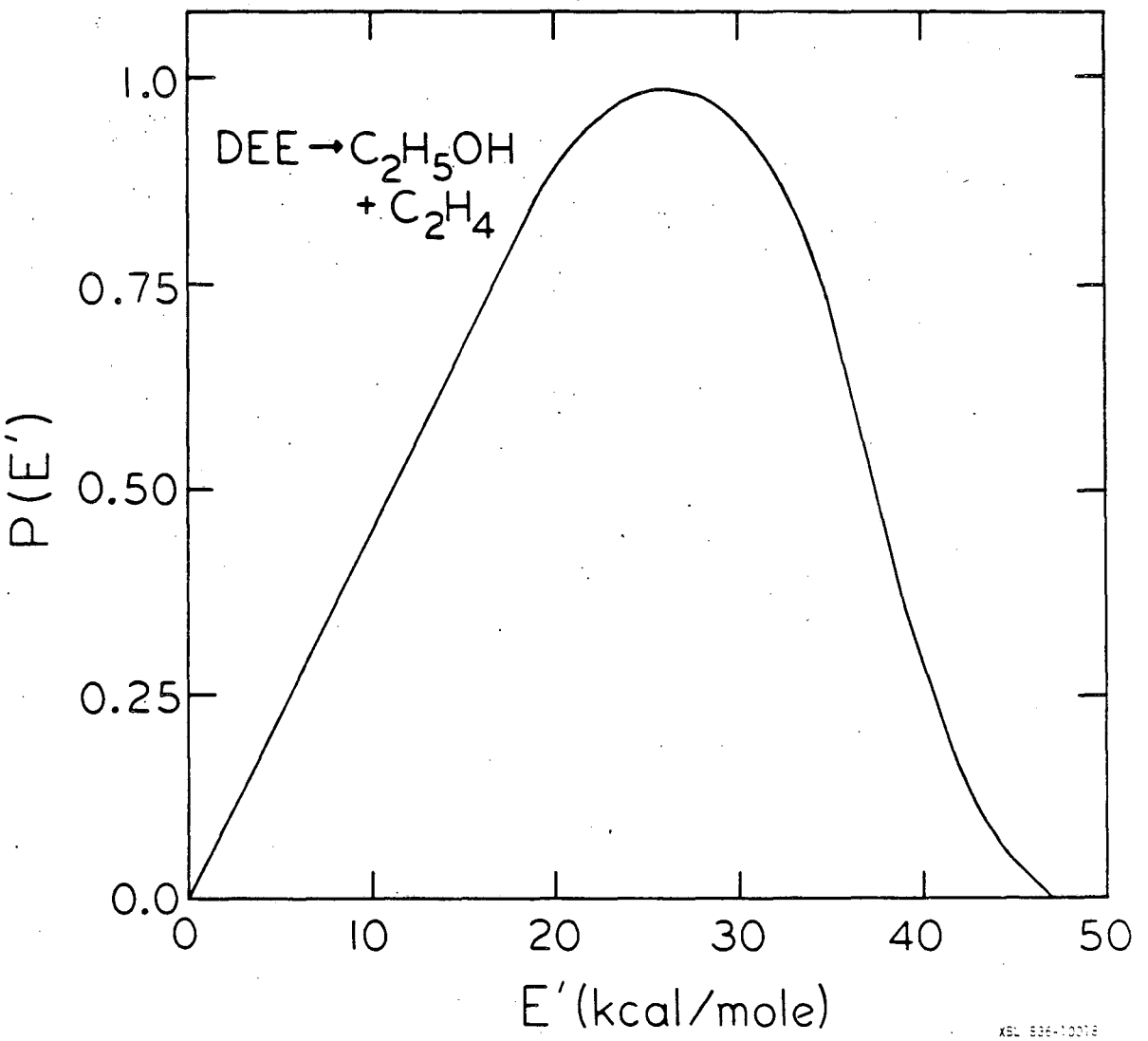

Fig. 11

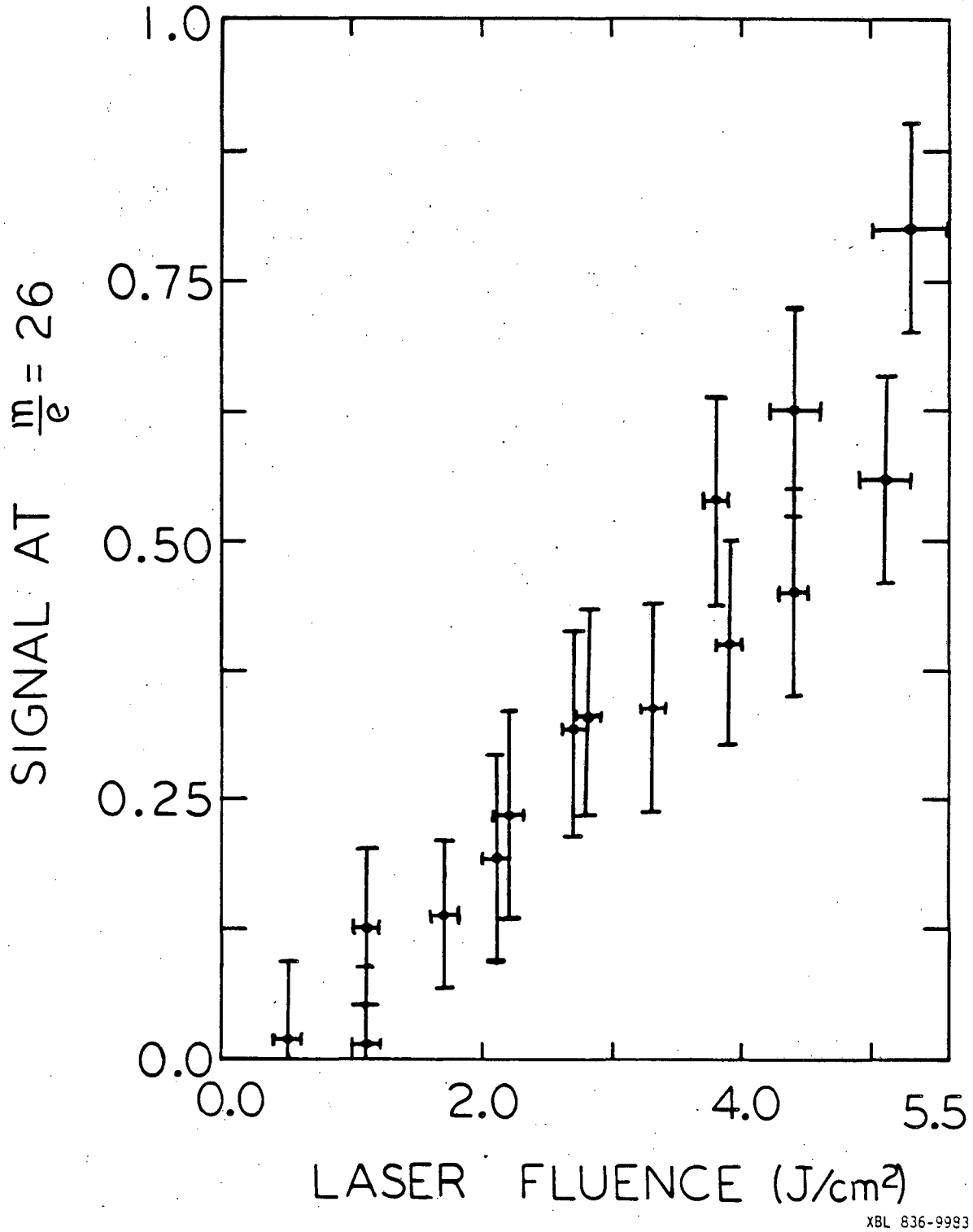
1.0
0.75
0.50
0.25
0.0
SIGNAL AT m/e = 26
0.0
2.0
4.0
5.5
LASER FLUENCE (J/cm²)
XBL 836-9983

Fig. 12

APPENDIX A: Rotating Source Machine Detector Interlock - Description and Operation

General Description

The detector interlock's primary function is to protect the magnetic turbomolecular pump and ionizer filament in the case of an extended normal and emergency power failure. It also provides for TMP 360 (small turbopump) restart and ionizer protection in the case that the normal power fails but emergency power engages within five minutes, thus requiring operator intervention only to restart the magnetic turbopump. The wiring diagram is shown in Figure 1 and the front control panel is shown in Figure 2. The interlock's response to several cases of power or turbopump failure are outlined below. Maintenance requirements and suggested improvements are also outlined.

Interlock Response to Power and Turbopump Failures

Note: The operation requires that the TMP 360 small turbopumps are set up in the automatic start mode. To be restarted after a failure in this mode, power need only be shut off to them and turned back on after a short delay.

A. Normal Power Failure Which is Relieved by Emergency Power Takeover Within Five Minutes

Immediately following the normal power failure the power to the ionizer (filament and optics), quadrupole, doorknob and photomultiplier

(hereafter referred to as ionizer and other detector components) are latched off. This is to prevent damage to those components in case of subsequent power failure or surges. When the emergency power takes over or normal power resumes (this must occur within five minutes) the TMP 360 turbopumps automatically restart as do the foreline pumps. The magnetic turbopump must be restarted by pressing the START button on the frequency converter. Because this turbo is magnetically suspended the operator need not be present to restart it immediately, it will pump for several hours. The bell will ring when power resumes indicating there has been a power failure and the red ionizer light (L1, see Figures 1 and 2) will light on the front panel indicating the power to the ionizer and other detector components is latched off. The bell may be shut off temporarily by turning the bell set switch (S7) to the OFF position. Once good detector pressure is verified by the operator, the power to the ionizer and other components may be turned on again by pressing the reset pushbutton (PB1) for the ionizer on the front panel of the interlock box. It is suggested that the ionizer filament current supply and high voltage (HV) supplies be turned down prior to pressing the reset button as the output of the supplies will surge immediately to reach their preset values. When reset, the bell will stop ringing, the light indicating power to the ionizer (L4) will light, and the red light (L1) will go off. The bell set switch (S7) should be turned to the ON position so it is ready to signal subsequent power or turbopump failure.

B. Normal Power Failure Which is Not Relieved by Emergency Power Takeover Within Five Minutes

In the event of a power failure, the magnetic turbopump is suspended by a small battery supplied by Leybold Heraeus. The battery, even if fully charged, can only suspend the pump for thirty minutes. The magnetic turbo must be slowed down by air friction by venting the detector to dry nitrogen before the battery runs out. The venting and slowdown requires twenty minutes so the magnetic turbopump is interlocked to vent five minutes after a power failure if power is not restored.

When the power initially fails, the power to the ionizer and other detector components is latched off as in failure case A. When the magnetic turbo interlock powers the vent vales, the interlock uses the same voltage source to initiate three responses. The power for the vent valve which the detector interlock uses is supplied across pins 1 and 3 of the magnetic turbopump control (see Figure 1, right center). The voltage source powers a relay which connects the car battery to power three relays (see Figure 1). These three relays, when powered, cut off power to 1) the small turbopumps, 2) the foreline pumps and liquid nitrogen, and 3) the ionizer and other detector components, which should already be latched off. The relays are latched so even when the small battery which powers the vent valve and initial detector interlock response relay is depleted, the car battery still powers the relays which keep the ionizer from turning on again in the vented chamber. Likewise,

the foreline and turbopumps do not restart and pump out the vented chamber.

Thus the magnetic turbopump is slowed down via the venting so it will not crash onto its bearing at full rotational speed when the small battery runs out and the ionizer and other pumps are latched off after venting has begun.

Caution--do not press the reset of the ionizer (PB1) after such a venting. The ionizer will turn on in atmosphere! To pump the detector down after the emergency venting, first consider waiting 6 hours after power has been restored to the magnetic turbopump battery pack so it may recharge fully (see Fig. 9 in the 560M manual from Leybold Heraeus). Then 1) turn all the small turbopump switches, S1, S2, and S3, to the OFF position, 2) prepare to use the mechanical pump to pump out the diffusion pump by setting S6 to the OFF position (this positions the butterfly valves so the foreline pumps do not yet pump on the turbo foreline but the mechanical pump is open to the D.P. foreline), 3) simultaneously press the turbo reset and foreline reset pushbuttons PB3 and PB2 to turn the mechanical pump and diffusion pump on; 4) wait for the mechanical pump to evacuate the diffusion pump, then switch S6 to the mechanical pump position so the butterfly valve shifts to let the mechanical pump evacuate the turbo foreline and seals the D.P. foreline (S5 must be in the ON position for S6 to power either butterfly valve), and 5) start the turbomolecular pumps by switching S1, 2 and 3 to the ON position and pressing the START button on the magnetic turbo frequency converter. When the foreline reaches a low enough pressure S6 may be switched to the diffusion pump position so the diffusion pump

evacuates the turbo foreline instead of the mechanical pump. The ionizer reset PB1 should not be pressed until the detector has been baked out sufficiently and/or the ionizer and other detector power supplies turned off. Otherwise they will surge on unexpectedly when the reset is pressed.

C. Small Turbopump Failure

If any of the small turbopumps fail, pins 5 and 4 on the back of the respective frequency converter become shorted. The detector interlock uses this to 1) turn off the ionizer and quadrupole, etc., as a precaution, 2) ring the turbo failure bell indicating there has been a turbo failure, and 3) attempt to restart the failed turbo once by cutting the power off to the turbo and turning the power on again. Once the failure is corrected the turbo will restart automatically and the ionizer and other detector voltages may be restored by the operator by pressing the reset button PB1. Turn down the ionizer and high voltage power supplies before resetting.

The detector will not be vented in the event of small turbopump failures as the pump can often be restarted before the UHV is significantly contaminated.

D. Magnetic Turbopump Failure

If the magnetic turbopump fails, pins 5 and 6 on the back of its frequency converter will no longer be shorted. The detector interlock

uses this to latch the ionizer off as in the other failures. No automatic restart try is available. The operator should attempt to restart the pump by pressing the STOP then the START buttons on the frequency converter. Even if the pump will not restart, we have encountered times when just a transistor in the frequency converter has blown and can be replaced. The pump may then be restarted before it spins down and fails to maintain UHV conditions. The detector is only vented in the case of power failure to the magnet levitating the turbopumps; the detector is not automatically vented if the turbopump itself indicates failure on the frequency converter.

E. Operator Error in Venting and Normal Venting Procedure

If the vent button is pushed and any of the pumps or the ionizer are still on, the detector interlock will shut off and the bell will ring. This method is not recommended as the ionizer filament will not cool off instantly.

For normal venting, 1) turn the ionizer and other HV power supplies off well ahead of time, 2) turn the bell set switch S7 to OFF, 3) press STOP on the magnetic turbo frequency converter, 4) turn off the small turbo's with S1, 2 and 3, 5) isolate the foreline by switching the butterfly switch S5 OFF (be certain there is sufficient air pressure in the pneumatic butterfly valves to turn them), 6) turn the mechanical and diffusion pump off with switch S4, and 7) press the vent valve button on the magnetic turbopump control.

The detector interlock cannot distinguish this from emergency venting so the restart procedure is as outlined in failure part C.

Suggested Improvements

1) Run the A-B connection shown on the return of the KRP14AG ionizer relay (Fig. 1, bottom left) through a connection which is only made if the detector ion gauge is in the 10^{-8} torr range. Then the ionizer will be protected in the case of a slow leak or foreline failure.
2) Run the diffusion pump heater through a relay which switches the heater off when the cooling water flow is interrupted.

Maintenance

1) The ±12V car battery must be kept charged. It is located on top of the detector rack; a car battery recharger is stored next to it. Hook it up to the recharger for 12 hours every 6 months and after each power failure. If this battery is not adequately charged the interlock system will not work properly, e.g., if the turbopumps fail the ionizer will not be shut off.
2) The only normally powered relay is the KRP14AG relay that controls power to the ionizer, quadrupole and other detector components. This relay is thus the only one likely to wear out with time. If it does, power will not be transmitted to the ionizer and other

power supplies but the pumping of the detector will not be affected. The relay is mounted in a socket and is LBL stock. The relay may be replaced and the ionizer reset button (PB1) reset to restore normal operation. Again, the bell will ring following replacement of the relay before the reset button is pushed unless the bell set switch (S7) is set to OFF. The filament heater power supply (and high voltage power supplies) should be turned off prior to pressing reset to prevent them from surging to full current/ voltage values.

3) The indicator lights on the front panel occasionally burn out and may be replaced by removing them from their socket without interrupting detector operation. L1 and L4 are 115 VAC. L2 and L3 are 12 VDC.

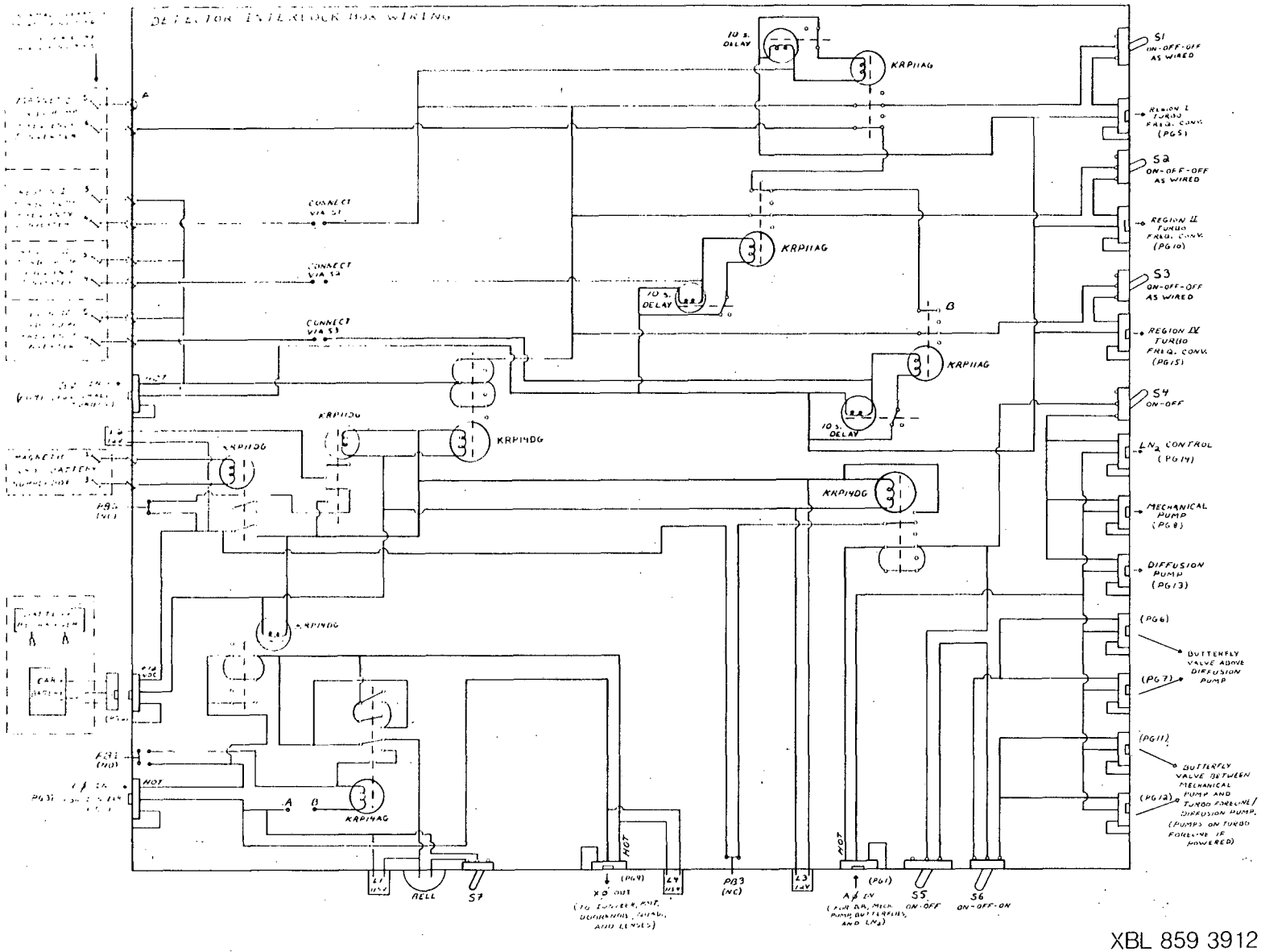

XBL 859 3912

Fig. 1. Detector interlock wiring diagram

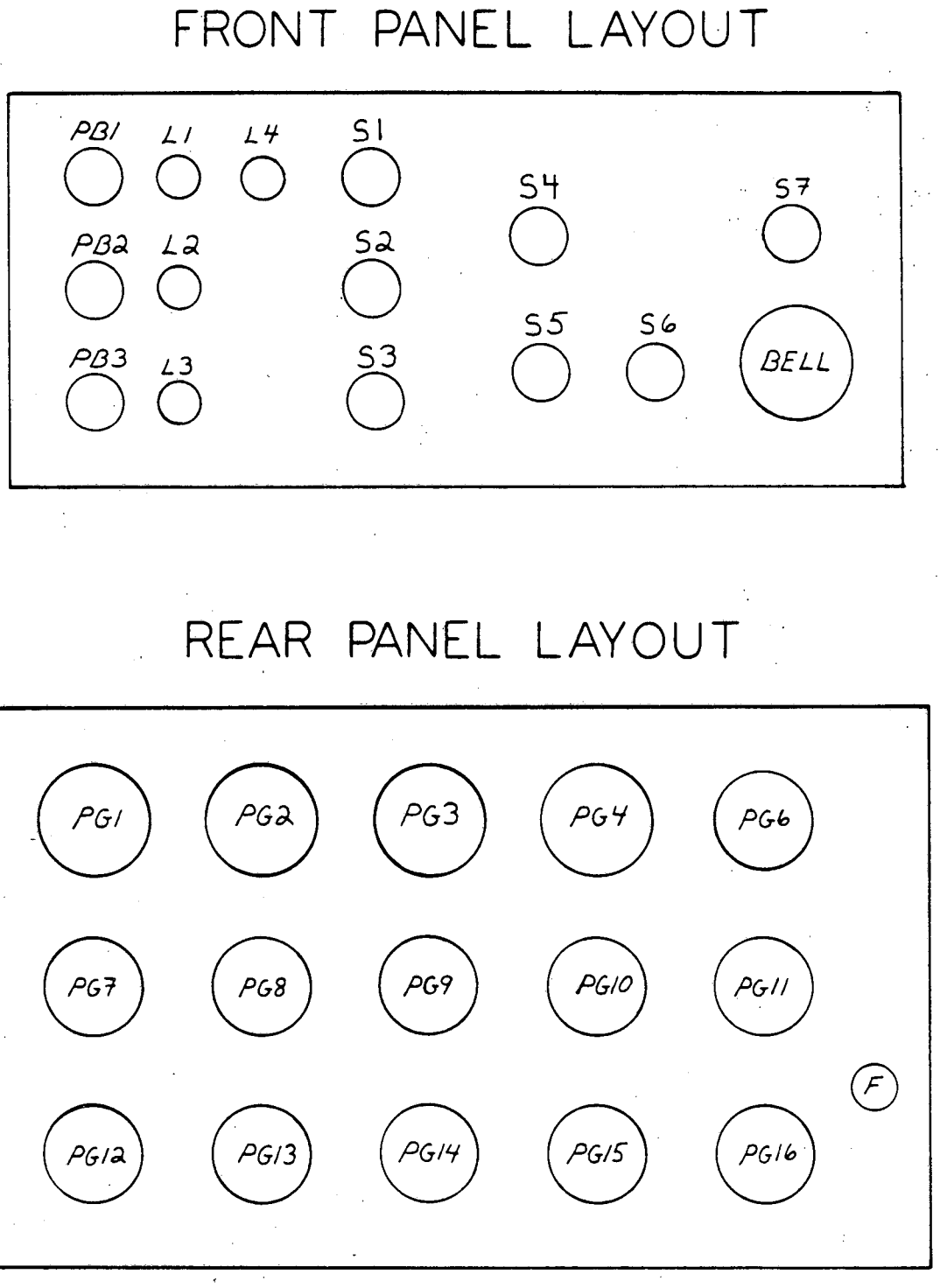

XBL 859 3911

Fig. 2. Detector interlock box panel layouts: (top) front panel indicator light and control switches, (bottom) power input and output plugs. F equals connector to turbopump frequency convertor indicator pins.

APPENDIX B: Fluorescence Detection Assembly

Purpose

The fluorescence detection assembly for the rotating source machine was designed to allow one to obtain a fluorescence excitation spectrum of the parent molecules in the molecular beam. For state-selective preparation of the parent molecule in a photofragmentation experiment, one would tune the excitation laser to the desired transition and record the laser-induced fluorescence signal concurrently with the time-of-flight data to measure the relative number of molecules being excited for each product time-of-arrival spectrum.

The fluorescence detection assembly is totally enclosed in the vacuum apparatus and monitors fluorescence from the laser-molecular beam interaction region. Alternately, with a simple adaptation of the mount and baffling, it may monitor fluorescence from a point away from the interaction region, should one desire to introduce a probe laser to interrogate the internal states of product molecules as a function of their laboratory velocity.

The description of the fluorescence detection assembly includes 1) details of the photomultiplier tube (PMT), voltage divider, and collection and filtering optics, 2) suggestions for assembly and improvement, and 3) a parts list for the fluorescence collection and signal processing components and voltage divider electronics.

Description

The photomultiplier tube is an RCA model C31000M. The tube is an experimental version of the RCA 8850 used commonly in the Daly detectors and may be used with the same voltage divider. As the 8850, the C31000M has a sensitive bialkali photocathode and a high-gain gallium-phosphide first dynode. The GaP dynode amplifies pulses from the photocathode so that these photoelectron pulses have a larger height than the dark count pulses originating in the later dynodes. Thus the tube is optimal for photon counting applications as one can discriminate effectively between dark counts and photon counts. The significant advantages of the C31000M over the 8850 are 1) it has a fused silica window which extends the spectral response of the tube far below 300 nm and 2) it has a lower dark pulse summation than the 8850. The relative spectral sensitivity of the C31000M at 200 nm is ~55% while that of the 8850 is << 1%. The spectral response of the tubes is the same between 300 and 650 nm.

The voltage divider used with the C31000M is the same as that for the 8850 pictured in C. Ng's Ph.D. thesis, University of California, Berkeley (LBL 21X227 S-1) with a few differences and/or clarifications. Thank you to Paul Weiss for his helpful suggestions in the fabrication of the voltage divider; three clarifications of the C. Ng drawing he pointed out were 1) pin 3, the 5th dynode, is to be connected on the socket to pin 10, the PMT's internal shield, while pin 14 is dynode 6, 2) the unlabeled capacitor in the drawing is C_1, and 3) a mu-metal

shield wrapped around the PMT doubles as both a magnetic and an electrostatic shield and is to be floated at the photocathode potential. The use of the 51Ω resistor in C. Ng's thesis which is drawn in series with the signal from the anode is unclear. Its only purpose as shown might be to limit the rate of discharge of an accidentally charged anode. If the resistor were meant to be from signal to ground to provide termination at the PMT end of the signal cable it would necessarily reduce the pulse height at the measurement end of the signal cable by a factor of 2 (assuming anode current is measured across a second 50Ω terminator). The divider I fabricated has the resistor wired in series with the anode, as shown in C. Ng's thesis, so voltage should not be applied to the tube unless the signal cable is terminated. For future voltage dividers, I would take a sugestion made by Ralph Page and replace the 51Ω in series resistor with a 1kΩ resistor to ground at the anode pin so the anode could not charge up if the signal cable were disconnected. As an additional improvement, the noise pickup from, for instance, the firing of the excimer laser, could be reduced if the signal cable from the anode had both a shielded signal cable and a shielded ground wire. In practice with the existing design we just kept the signal cable short. The voltage divider components were mounted on a PC board (LBL 21X1111-PI) in a water-cooled box and potted with vacuum epoxy. A parts list of the electrical components and the relevant distributors follow and Appendix C lists drawings for the voltage divider box.

An assembly sketch of the fluorescence collection and filtering setup is shown in Fig. 1. All the optics and filter are mounted directly on the PMT housing so alignment only requires positioning the one complete assembly. The assembly is mounted so the 1" diameter 1" focal length lens is 2" below the interaction region of the laser and molecular beam. A cone of fluorescence from the interaction region is focused by the lens to a point 2" below the lens, at which an iris with an ~5 mm aperture is positioned (thanks, Y.T.). Before the iris there is the option of inserting a long wave pass filter. If the fluorescence is sufficiently red-shifted from the excitation laser light one may use the filter to attenuate the signal from scattered light. (A small selection of filters has been obtained; more are stocked by Schott or Corion. Care should be taken to use absorption filters, not interference filters, as the light is converging as it passes the filter.) The fluorescence diverges after the iris onto the face of the PMT. All the light impinges on the 1.7" diameter sensitive surface of the photocathode. With this arrangement we verified experimentally that the PMT only sees significant laser light which is scattered from surfaces in the conical viewing region above the interaction region.

Assembly Notes and Suggestions for Improvement

A. Voltage Divider

Of the voltage divider components, the .0047 μfd capacitors and anode resistor are mounted directly on the PMT socket while the rest are mounted on a PC board (21X1111-PI) and potted in the water cooled box.

Two suggested improvements are the inclusion of a 1 kΩ resistor to ground at the anode pin instead of the 51Ω resistor in series and a shielded BNC cable with both signal and isolated ground wires protected by the shield for the entire length of the cable from the anode.

Note that there is an additional wire coming from the voltage divider in addition to the ones attached to the PMT socket. This wire is carefully electrically insulated as it is connected to the photocathode potential. It is to be connected to the wire attached to the magnetic shield of the PMT and should not be disconnected unless the PMT is off.

B. Photomultiplier Tube and Housing

The C31000M does not come with a magnetic shield. A mu-metal shield floated at the photocathode voltage was added. A wire soldered to a copper tab which is bent around the bottom overlapped edge of the mu-metal shield is attached to the appropriate wire from the voltage

divider. The tube with mu-metal shield is wrapped in insulating tape. The housing is lined with .030" thick teflon to provide further insulation. The PMT housing has a groove to allow the mu-metal float wire to extend out to the voltage divider. Care should be taken that the wire is attached near pin 16 or 17 so the final orientation of the PMT socket and housing does not restrict the rotation of the molecular beam source.

Space is very tight in the rotating source machine so the PMT fits snugly in the housing and one side of the outside surface of the housing is flattened to allow the molecular beam source to rotate to 0°. The assembly of the housing is straightforward with the space restriction in mind. The curved outer surface of every piece is flattened to clear the differential wall of the source at 0°. From the bottom up one assembles the following pieces (see drawing list in Appendix C): socket tube cap, socket tube, socket tube ring (welded to cap), fins of socket, base ring, tube. When assembled, the face of the PMT reaches to near the top of the housing.

The assembly of the fluorescence collection and filtering optics to the top of the photomultiplier housing are shown in Fig. 1. (The drawings for the small metal mating pieces were not saved.) The drawings for the mount to hold the PMT housing and optics in the machine are listed in Appendix C and are self explanatory. A threaded rod is screwed into the mount and facilitates the vertical positioning of the PMT; the small ring which slips around the socket tube and holds the PMT vertically slides up and down this threaded rod and is secured at

the final height with nuts on the threaded rod and screws into vertical grooves on the housing mount. The entire mount bolts into holes in the bottom center of the main chamber. The upper ring of the mount is oversized for the PMT housing; three screws thread through the ring inward to the PMT allowing easy adjustment of the tilt of the housing and optical assembly so the interaction region is viewed.

A potential improvement might be made in the collection efficiency of the focusing lens. Insertion of a 1-1/2" diameter 1" focal length lens may be possible depending on what angle one plans to rotate the source to during data accumulation. Care must be taken to assure that the molecular beam does not hit the lens or mount and scatter back to the nearby interaction region and that the liquid helium cooled slit mounted on the source clears the lens assembly at all positions of the source.

Parts List

A. Photomultiplier Tube, Collection Optics, and Electronics

RCA C31000M photomultiplier tube

(Replacement pins Amp Inc., Harrisburg, PA, No. 201328-1 Type II socket 24-20)

Suprasil lens, 1" diameter, 1" focal length

Biconvex lens ordered from Optics for Research does not have the specified focal length.

Plano-concave lens supplied by Howard Nathel achieves good spatial filtering (glass). Mount plano side toward interaction region.

Long wave pass filters, 1" diameter

Purchased from Corion Corp., Hollistor, MA, filters LG350, 420, 505, 595, and 670 -F, 2-3 mm thick, numbers list λ at 50% transmittance, transmittance curves shown in Corion catalog. Schott sells a greater variety.

Ilex mechanical shutter with iris

From Melles Griot, Irvine, CA, No. 04IMS001. Shutter may be cable operated with 5-44 Asa standard cable (from any camera store). Aperture of iris is adjustable between 1.6 to 25.4 mm diameter. Thread for mounting to lens assembly is .5 mm, not 50 TPI as quoted in catalog.

Lens and filter mounts for 1" optics

Klinger Scientific, Richmond Hill, NY, adaptor mounts type B No. 178348. 1" mount for optics to mm thread.

Boxcar

Stanford Research Systems, Palo Alto, CA, SR 250, nin bin compatible with small gate width achievable (~2 nsec).

Analog Processor

Stanford Research Systems SR 225, nin bin compatible, used for normalizing to laser power (A·B, A÷B, A-B, etc.).

B. Voltage Divider (Wiring diagram similar to one in C. Ng thesis as noted.)

Box

Mechanical drawings: listed in Appendix C

Vacuum epoxy: Emmerson and Cummings skycast 2850FT blue epoxy and catalyst 24LV from C.V. Roberts (213) 870-9561.

High voltage chassis feedthrough: Kings SHV 1704-1, LBL stock 5935-58226

BNC chassis feedthrough: salvage

Electrical components

P.C. board: design on file at LBL 21X1111-P1

Resistors:

R_1 60 kΩ ± 1 wire-wound, Newark Electronics, Oakland, CA (hereafter, Newark) No. 18F143R60K

R_{2-9} 40 kΩ ± 1 , Newark, No. 13F143R40K

R_{10} 51Ω carbon composition LBL stock No. 5905-16458 (suggest replace with 1kΩ to ground)

Zener diodes:

$Z_{1-15,19,20}$	IN3041B, 75 volt, replaced with Sylvania No. ECG5093A, 75 volt 1 Watt.
Z_{16-18}	IN3037B, 51 volt, Newark No. 08T1N3037B

Capacitors:

C_{1-12}	.0047 μF HI-Q ceramic disc, LBL stock 5910-44369
C_{13-15}	.01 μF 1 kV buffer ceramic disc, LBL stock 5910-24572
C_{16-17}	.05 μF 600 WVDC, HI-K ceramic disc, Newark No. 19F539
C_{18-19}	.1 μF 600 WVDC, HI-K ceramic disc, Newark No. 67F5018

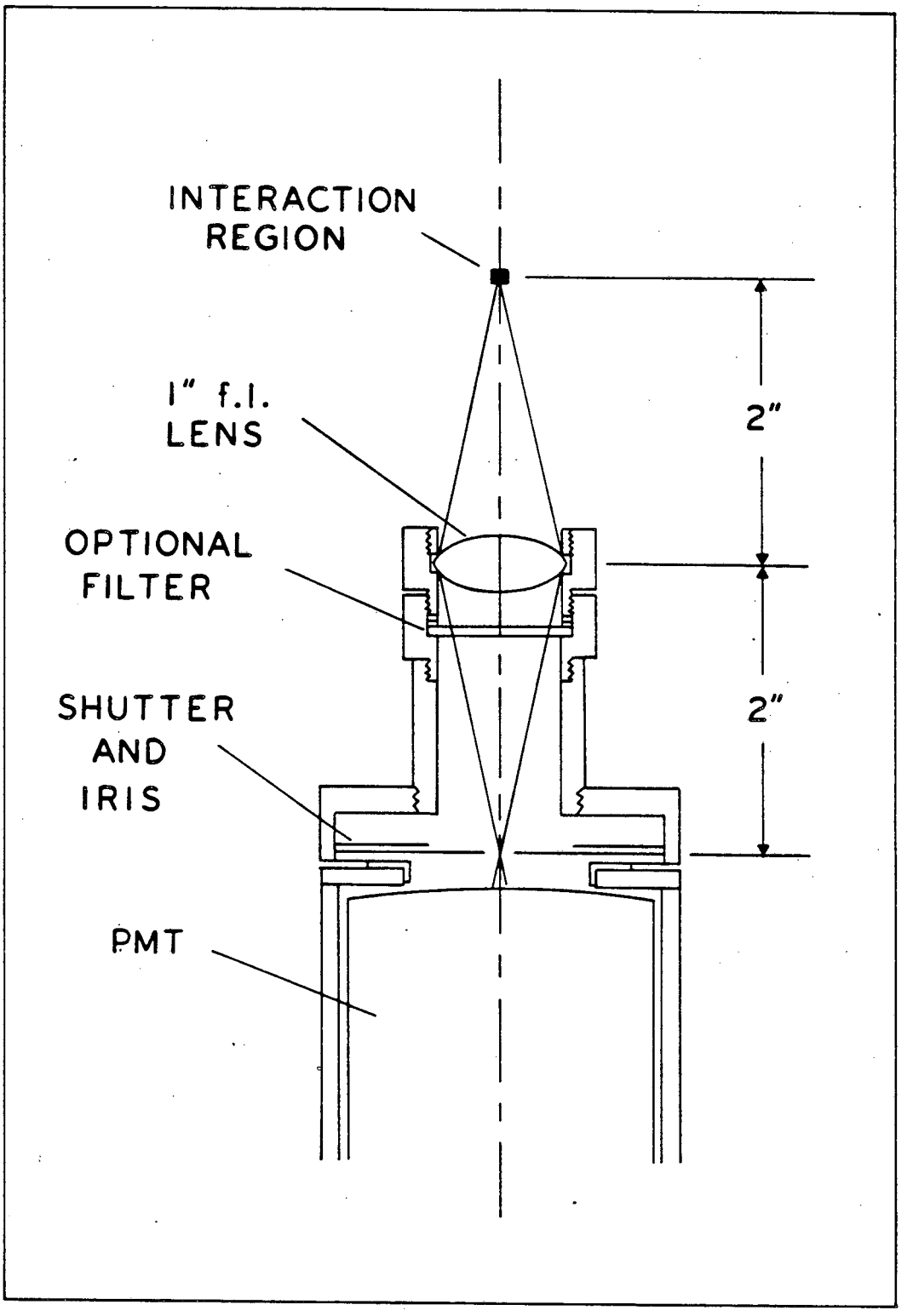

XBL 8510-4295

Fig. 1. Fluorescence Collection and Filtering Assembly

APPENDIX C: Compilation of Mechanical Drawing Contributions to Rotating Source Machine

The mechanical drawings for portions of the rotating source machine listed below are filed with the mechanical engineering print room at Lawrence Berkeley Laboratory and may be obtained by writing to Professor Lee. The portions of the machine designed by the two other students are not listed here but are also easily obtained. Each drawing is listed by drawing number-size and title. The drawings shown here are for construction of the fluorescence detection system, time-of-flight wheel assembly, source chamber nozzle assembly, laser lens and window flanges and adaptors, detector gate valve and photomultiplier tube accessories, and source chamber additions (for rotation of source). Many thanks to Professor Lee for the fine example of his many previous designs.

A. Fluorescence Detection System

21N009-3 Photomultiplier housing mount, part 1 of 5

21N010-1 Photomultiplier housing mount, part 2 of 5

21N011-1 Photomultiplier housing mount, part 3 of 5

21N012-1 Photomultiplier housing mount, part 4 of 5

21N013-1 Photomultiplier housing mount, part 5 of 5

21N014-3 RCA C31000M (or 8850) divider heat sink box

21N015-1 Divider heat sink box end

21N016-1 Divider heat sink box cover

21N017-3 Photomultiplier tube housing - tube (C31000M)

21N018-1 Photomultiplier tube housing - base ring

21N019-1 Photomultiplier tube housing - socket tube

21N020-1 Photomultiplier tube housing - socket tube ring

21N021-1 Photomultiplier tube housing - socket tube cap

B. TOF Wheel Assembly

20D925-3 Rough assembly sketch

20D926-3 TOF square keyed flange

20D927-2 Square flange to tube welding

20D928-3 TOF motor mount

20D929-3 TOF wheel moveable cylinder

20D930-2 TOF flange to cylinder mating plate

20D931-2 TOF height adjust mating plate

20D932-2 Photodiode mount

20D933-2 Motor cooling block

20D934-2 TOF wheel - thin

20D935-1 Motor casing modification

20D936-1 Conical spacer to rest on bearing

20D937-1 Thin wheel holder - first half

20D938-1 Thin wheel holder - second half

20D939-1 Thin wheel spacer

C. Source Chamber Nozzle Assembly

20D940-2 Nozzle tube with 0.005" hole

20D941-2 Self aligning nozzle support cage

20D942-1 Sliding key between nozzle and support cage

20D943-1 Nozzle clamp

20D944-1 Nozzle feedthrough flange - epoxy glass

20D945-1 High temperature nozzle feedthrough flange

20D946-2 2-1/2" dia. port nozzle feedthrough flange

20D947-3 7-1/2" dia. port flange with electrical feedthrough

20D948-3 4" dia. port nozzle feedthrough flange

20D983-1 Source skimmer 0.020" dia. hole

20D984-1 Differential wall skimmer for 3 mm collision

D. Laser Lens and Window Flanges and Adaptors

20D949-3 Laser feedthrough flange tube - part. plate

20D950-1 Laser feedthrough flange tube retaining ring
(see 20D556-2 Laser feedthrough flange - part plate under Source Chamber Heading)

20D951-1 Laser lens holder - part 1

20D952-1 Laser lens holder - part 2

20D953-2 Laser entrance adaptor flange for 3" dia. port

20D954-1 Laser exit flange for 1-1/2 dia. port - Brewster

20D955-2 Laser entrance adaptor flange for excimer

20D956-1 Laser entrance and exit flanges for excimer

E. Detector: Gate Valve and PMT Accessories

20D959-1 Gate valve rod handle

20D960-1 Gate valve closed position stop - parts 1 and 2

20D977-1 Gate valve large hole stop

20D978-1 Gate valve small hole stop

20D980-2 Gate valve rod

20D982-3 Gate valve rod feedthrough flange with conn.

20D264-3 Voltage divider box for 8850

20D265-1 End to voltage divider box for 8850

20D267-1 PMT socket retainer ring - 8850

20D268-1 PMT capacitor cover - 8850

20D269-2 PMT voltage divider box holder

F. Source Chamber Additions

20D919-4 Support stand addition - for water and rotating source lever

20D920-3 Plate mount for drive sprocket mount

20D921-1 Drive sprocket mount

20D922-1 Sprocket for 25" rotating ring

20D923-1 Lever to drive sprocket adaptor

20D957-2 90° rotation source stop

20D958-2 0°rotation source stop

G. Main Chamber Additions

20D979-1 Cold shield heater housing

20D981-3 Main chamber ion gauge cover

APPENDIX D: Publications from Graduate Work

1. L. J. Butler, D. Krajnovich, Y. T. Lee, G. Ondrey, and R. Bersohn, "The Photodissociation of Nitromethane at 193 nm", J. Chem. Phys., 79, 1708 (1983).

2. L. J. Butler, R. J. Buss, R. J. Brudzynski, and Y. T. Lee, "Energy Partitioning to Product Translation in the Infrared Multiphoton Dissociation of Diethyl Ether", J. Phys. Chem., 87, 5106 (1983).

3. J. W. Hepburn, R. J. Buss, L. J. Butler, and Y. T. Lee, "Molecular Beam Study of the Photochemistry of S_1 Glyoxal", J. Phys. Chem., 87, 3638 (1983).

4. D. Krajnovich, Z. Zhang, L. Butler, and Y. T. Lee, "Photodissociation of CF_2Br_2 at 248 nm by the Molecular Beam Method", J. Phys. Chem., 88, 4561 (1984).

5. D. Krajnovich, L. J. Butler, and Y. T. Lee, "U.V. Photodissociation of C_2F_5Br, C_2F_5I, and 1,2-C_2F_4BrI", J. Chem. Phys., 80, 3031 (1984).

6. L. J. Butler, E. Hintsa, S. Shane, and Y.T. Lee, "The Electronic State-Selective Photodissociation of CH_2BrI at 248, 210, and 193 nm," in preparation.

LAWRENCE BERKELEY LABORATORY
TECHNICAL INFORMATION DEPARTMENT
UNIVERSITY OF CALIFORNIA
BERKELEY, CALIFORNIA 94720